MnDOT Contract, No. 1003325, Work Order No. 56

NRRA Long-term Research Project

Performance Benefits of Fiber-reinforced Thin Concrete Pavement and Overlays

Task-2: Third Year Annual Cell Performance Report (2019-2020)

Prepared by:
Souvik Roy, Manik Barman, Amarjeet Tiwari, UMD
and
Tom Burnham, Minnesota Department of Transportation

UMD
UNIVERSITY OF MINNESOTA DULUTH
Driven to Discover

DEPARTMENT OF TRANSPORTATION

2021

DISCLAIMER

This report represents the results of research conducted by the authors and does not necessarily represent the views or policies of the National Road Research Alliance, Local Road Research Board, Transportation Research and Innovation Group of the Minnesota Department of Transportation, or the University of Minnesota Duluth. This report does not contain a standard or specified technique.

The authors, The National Road Research Alliance, the Local Road Research Board, the Minnesota Department of Transportation, Transportation Research and Innovation Group and the University of Minnesota Duluth do not endorse products or manufacturers. Any trade or manufacturers' names that may appear herein do so solely because they are considered essential to this report.

LIST OF CONTENTS

LIST OF TABLES

LIST OF FIGURES

1 INTRODUCTION

The Minnesota Department of Transportation (MnDOT) constructed several fiber reinforced concrete (FRC) test cells at MnROAD in 2017. These cells were constructed as a part of a National Road Research Alliance (NRRA) funded research study on fiber reinforced concrete. The main research objective of these cells is to identify and quantify the contribution of structural synthetic fibers in mitigating different distresses that typically occur in thin concrete pavements and overlays. The location of the 2017 FRC research cells at the MnROAD test facility is shown in

Figure 1-1~~Figure 1-1~~. Table 1 presents a summary of the designs and materials used in these test cells. A total of eight cells were constructed, among which seven cells were constructed with FRC, and one control cell was constructed with plain concrete (Cell 506). Cells 139 and 239 were constructed as ultra-thin (3-inch) and thin (4-inch) concrete pavement on an un-stabilized gravel base (matching with typical city street design). An enhanced fiber dosage (@30% RSR; see Table 1 for the dosage information) was used in these two cells. Cells 705 and 805 were constructed as thin un-bonded concrete overlays on an existing concrete pavement varying the panel size; a standard fiber dosage (@20% RSR) was used in these two cells. Cells 506 through 806 were constructed as thin concrete pavement on an un-stabilized gravel base mainly varying with fiber content (0% to 0.75% volume fraction). Table 2

~~Table 2~~ presents the paving dates of the different cells. Figure 1-2 shows a photograph of the fiber used in all the seven FRC cells during the 2017 construction. Table 3 presents the concrete mixture related information for the FRC research cells. All eight cells were equipped with different types of sensors for measuring responses such as (i) dynamic strain due to wheel load, (ii) static strain induced by the environmental forces, (iii) pavement temperature and gradient, and (iv) joint movement. Periodical distress (cracks, spalling, and faulting) surveys were conducted to keep track of the distresses. Falling weight deflectometer (FWD) tests are periodically conducted to determine joint performance in different seasons.

This report provides a summary of the distresses observed in the above-mentioned 2017 FRC research cells and an analysis and discussion of the responses measured by different sensors up to the third year of service.

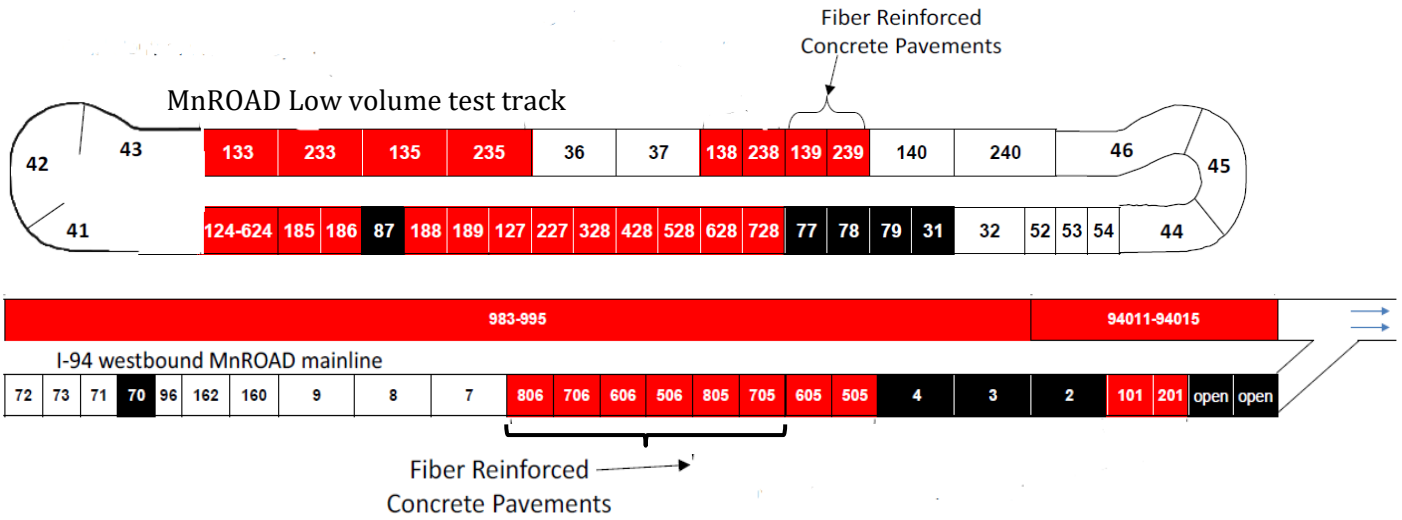

Figure 1-1: Location of the 2017 FRC Research cells at the MnROAD test facility (MnDOT, 2018).

Table 1. Summary of the 2017 NRRA MnROAD test cells constructed under FRC study.

Cell number	Length (ft.)	Pavement/ overlay Type	Underlying layer (constr. year)	Type of concrete/ fiber dosage*	Panel size W ft. x L ft.	Panel thickness (inch)
506	144	Thin pavement on gravel base	11 in. class 5Q aggregate base (2017)	*Plain concrete*	6 x 6	5
606**	138			*FRC/ standard*		
706				*FRC/ enhanced*		
806				*FRC/ high*		
139	270	Ultra-thin Pavement on gravel base	6 in. class 5 aggregate base (2017)	FRC/ enhanced	6 x 6	*3*
239	273	Thin Pavement on gravel base			6 x 6	*4*
705	144	Thin un-bonded overlay on concrete pavement (w/fabric interlayer)	Concrete (1993)	FRC/ standard	*Driving: 14 x 12 Passing: 12 x 12*	5
805	124				*Driving: 6 x 12 and 8 x 12 Passing: 6 x 12 and*	5

					6 x 12	

** Fiber dosages: standard - corresponding to 20% residual strength ratio (ASTM C1609); enhanced - corresponding to 30% residual strength ratio (ASTM C1609); high – corresponding to 0.75 fibers volume fraction.*

*** Even though the design thickness was 5 inches, the actual measured thickness was found to be 6 inches*

Table 2. Paving dates and times of MnROAD 2017 FRC research cells.

Cell	Date	Approximate Time
139	7/17/2017	9:15:00 AM
239	7/17/2017	9:15:00 AM
506	6/26/2017	9:20:00 AM
606	6/27/2017	9:15:00 AM
706	6/29/2017	8:45:00 AM
806	6/30/2017	8:00:00 AM
705	9/5/2017	2:00:00 PM
805	9/5/2017	3:00:00 PM

Figure 1-2: Photograph of the Forta Ferro fibers used in MnROAD 2017 FRC research cells.

Table 3. Mix designs for FRC Cells (includes control mix with no fibers) (MnDOT, 2018).

Mix/Cell	Air (%)	Water (lbs)	Cement (lbs)	Fly ash (lbs)	Fly ash (%)	W/C Ratio	FA #1 (lbs)	CA #1 (lbs)	Fiber (lb/cy)	Fiber (% of conc. vol.)	Target RSR (%)	Slump range (in.)
MR-3A21FC/ 506	7.0	239	400	170	30	0.42	1222	1798	0	0	0	0.5-3
MR-3A21F1/ 705,805,606		248	413	177			1204	1773	5	0.33	20	
MR-3A21F2/ 139,239,706		252	420	180			1196	1761	8	0.52	30	
MR-3A21F3/ 806		258	430	185			1184	1743	11.66	0.75	NA	

2 PAVEMENT DISTRESSES

2.1 Cracks and Spalling

The distresses such as cracks, spalling, and faulting were documented through periodical distress surveys. Table 4 provides the dates of the crack and spalling surveys and the corresponding equivalent standard axle load (ESAL). Distress surveys were conducted by visually observing and documenting the distresses on MnDOT's distress survey sheets. A summary of the distresses (cracking and spalling) documented in the third year of service (until March 2020) is provided in Figure 2-1~~Figure 2-1~~. This figure, however, does not include the unique distresses that developed in Cell 139. The following section elaborates on the distresses observed in each cell. The distress map for all the cells, collected from MnDOT, can be found in APPENDIX A~~APPENDIX A~~. *It shall be noted that all the data and pictures presented in this report for the distresses and different sensors are collected by MnDOT and provided to the research team*.

Table 4. List of distress survey dates.

Cell	Construction Dates in 2017	Distress Survey Dates in 2018/ ESALs	Distress Survey Dates in 2019 / ESALs	Distress survey Dates in 2020/ESALs
139	Jul 17	May 1/ 49K	Mar 18/ 82K; Dec 4/ 114K	Mar 24/ 195K
239	Jul 17	May 1/ 38K	Mar 18/ 62K; Dec 4/ 122K	Mar 24/ 146K
705	Sep 5	Mar 13/ 750K Apr 25/ 825K	Mar 18/ 1,800K; Oct 23/ 2,400K	Mar 5/2700K
805	Sep 5	Mar 13/ 750K; Apr 25/ 825K	Mar 18/ 1,800K; Oct 23/ 2,400K	Mar 5/2700K
506	Jun 26	Mar 14/ 750K	Mar 19/ 1,800K; Oct 25/ 2,400K	Mar 5/2700K
606	Jun 27	Mar 14/ 750K	Mar 19/ 1,800K; Oct 25/ 2,400K	Mar 5/2700K
706	Jun 29	Mar 14/ 750K	Mar 19/ 1,800K; Oct 25/ 2,400K	Mar 5/2700K
806	Jun 30	Mar 14/ 750K	Mar 19/ 1,800K; Oct 25/ 2,400K	Mar 5/2700K

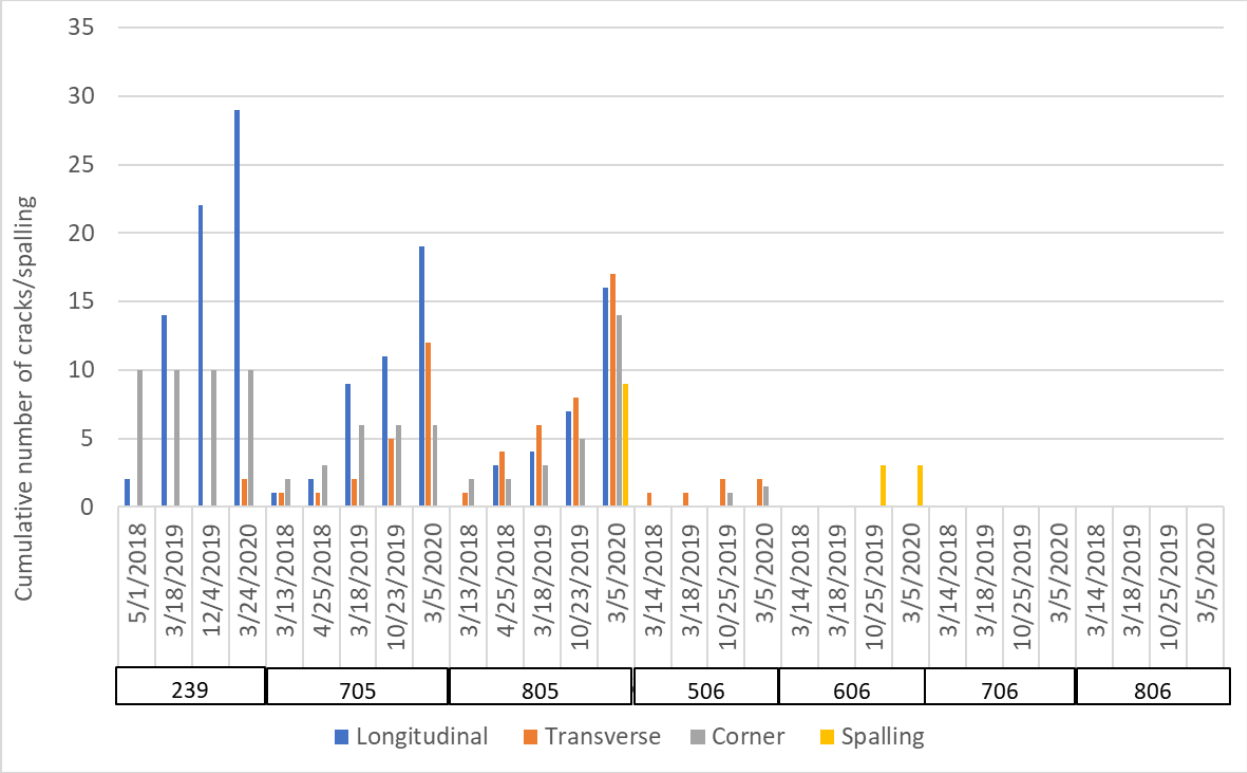

Figure 2-1. Summary of distresses observed at the MnROAD FRC research cells until the third year of service period (Cell 139 not shown).

2.1.1 Cells 139 and 239

Cell 139 was constructed with three-inch-thick (ultra-thin) concrete slabs on an un-stabilized gravel base at the low-volume test track. The size of the slabs of this cell was 6ft x 6ft, and the number of the total slabs was 180. Cell 139 was inadvertently exposed to early loads from construction trucks that were using the crossover segment to access other cells under construction, which resulted in many early-age cracks. Figure 2-2~~Figure 2-2~~ shows a picture of a couple of such early-age cracks in this cell. These types of cracks continued to develop, propagate throughout the first year of service, and eventually, many slabs of this cell were shattered by the end of the summer of 2018. Besides that, there was a considerable amount of depression along the outer wheel path at some locations; this distress looked like rutting that occurs in asphalt pavements. Figure 2-3~~Figure 2-3~~ and Figure 2-4~~Figure 2-4~~ show photographs of the above-mentioned distress.

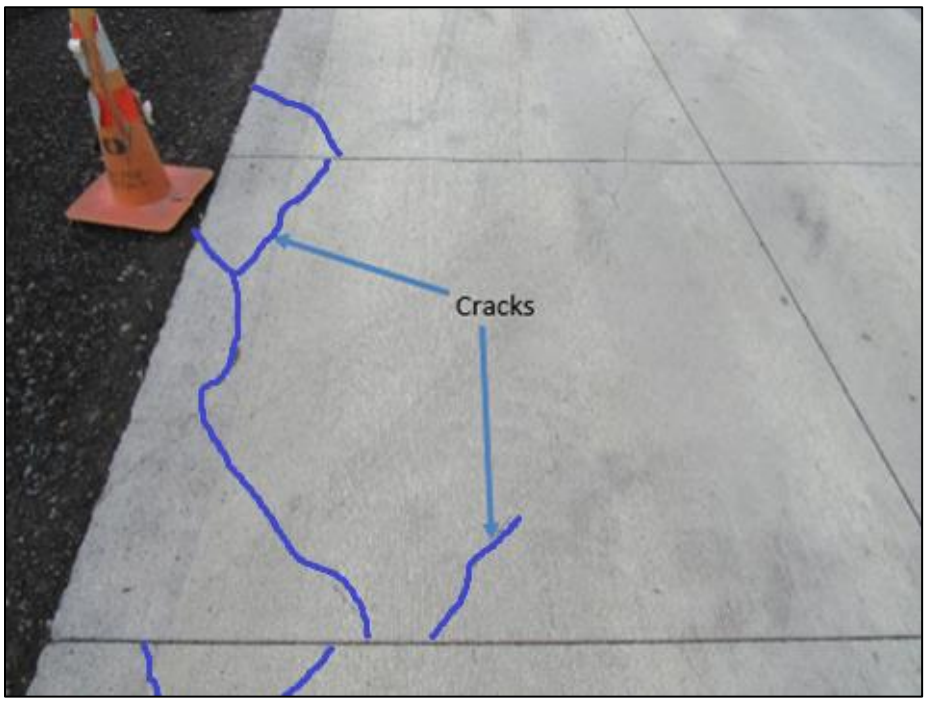

Figure 2-2. Cell 139 after exposure to construction trucks.

Figure 2-3. Shattered slabs in Cell 139 .

Figure 2-4. Depression along the wheel path in Cell 139 .

Because of the occurrence of the high severity of the distresses (slab shattering and depression along the wheel path), as many as 14 of the 44 slabs of the inside lane were replaced on September 27, 2018. Figure 2-5 shows a few photos collected during the removal of broken slabs and the construction of the replacement slabs. The replacement slabs were 4-inch thick, with eight of them containing fiber reinforced concrete and the other six with plain concrete. The fibers used in the replacement slabs were different and laterally stiffer than those used in 2017, as shown in Figure 2-6~~Figure 2-6~~a. The dosage of the fiber was 5.5 lb/cy, which corresponds to a 30% residual strength ratio. Figure 2-6~~Figure 2-6~~b shows the ASTM C1609 test results for the two numbers of beam samples prepared at the site during the construction of replacement slabs in Cell 139. The replacement slabs have performed well; the distress survey conducted in the spring of 2020 showed only one crack in one of the fiber-reinforced replacement slabs. The location of this crack was at the transition joint of the new 4 inch thick replacement slabs and old 3 inch thick slabs. The reason behind this crack is more due to the repetitive impact of the wheel load than fatigue stresses.

(2.5 a) Removal of broken slabs for Cell 139

(2.5b) Close shot of the broken concrete pieces

(2.5c) Fibers on the fractured face of a concrete piece.

(2.5d) Preparation of the base layer for reconstruction of the broken slabs.

Figure 2-5. Photographs of the replacement and reconstruction on Cell 139 (outer slabs, inside lane).

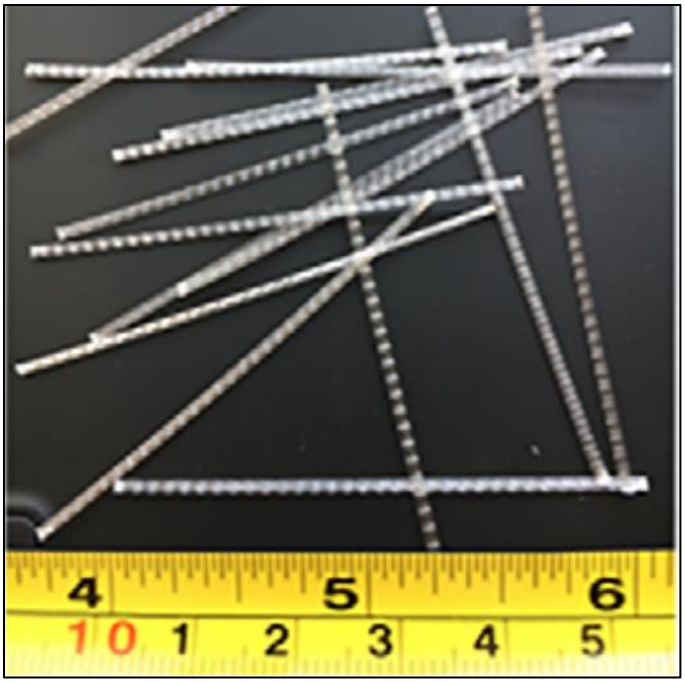

(2.6a) Fibers used in new slabs of Cell 139.

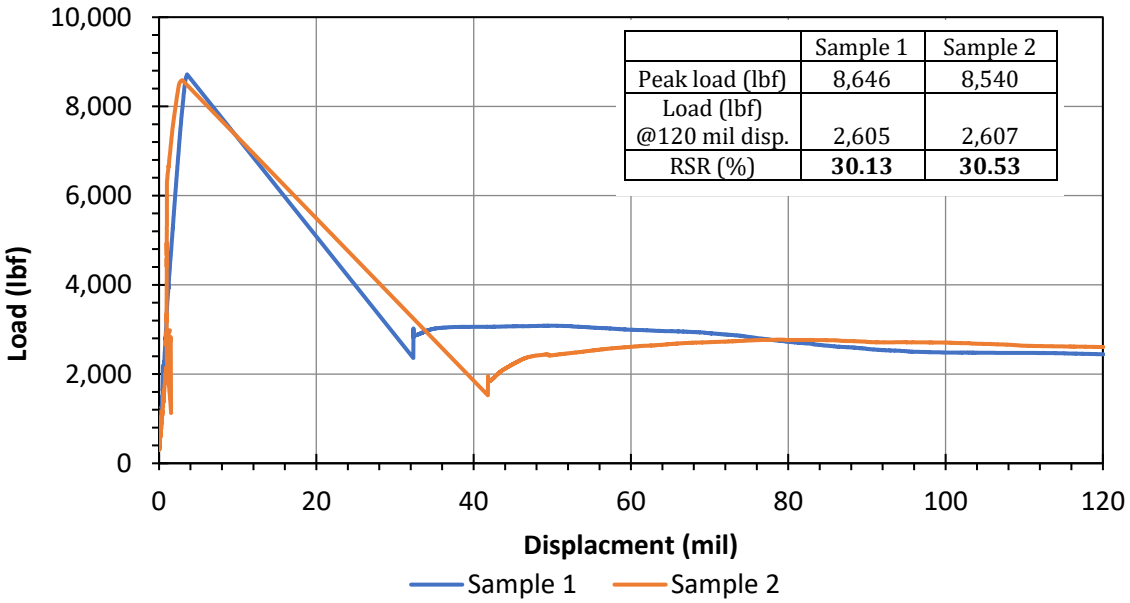

	Sample 1	Sample 2
Peak load (lbf)	8,646	8,540
Load (lbf) @120 mil disp.	2,605	2,607
RSR (%)	**30.13**	**30.53**

(2.6b) ASTM C1609 test results of the FRC concrete samples prepared during the construction of replacement slabs for Cell 139.

Figure 2-6. Photograph of fibers used in the reconstruction of Cell 139 and ASTM 1609 test results for the FRC samples.

On the other hand, unrepaired (original) slabs continued to be distressed with traffic load and age, with primary longitudinal and secondary transverse and diagonal cracks. Based on the December 2019 distress survey data, it was found that as much as 75% of the slabs have cracked in Cell 139 after 114,000 ESALs applied to them. Figure 2-7 shows four photographs of Cell 139 taken in October 2019. The unrepaired slabs eventually failed and became undrivable in the middle of the third year of service (2020).

Figure 2-7. A few photographs of Cell 139 during October 2019.

While the slab thickness limitation (only 3-inch thick) of this cell and early-age loading were the main reasons for the initiation of the distresses of Cell 139, a relatively weak base layer and some drainage issues were believed to have aggravated the distress of this cell.

Cell 239 on the low-volume test track is a 4-inch thick concrete pavement on an un-stabilized gravel base with 6ft x 6ft slabs. The total number of slabs in this cell is 176. This cell experienced longitudinal and corner cracks. Figure 2-8~~Figure 2-8~~ shows a photograph of typical corner cracks that formed in Cell 239. Figure 2-9 shows a photograph of longitudinal cracks that occurred in Cell 239.

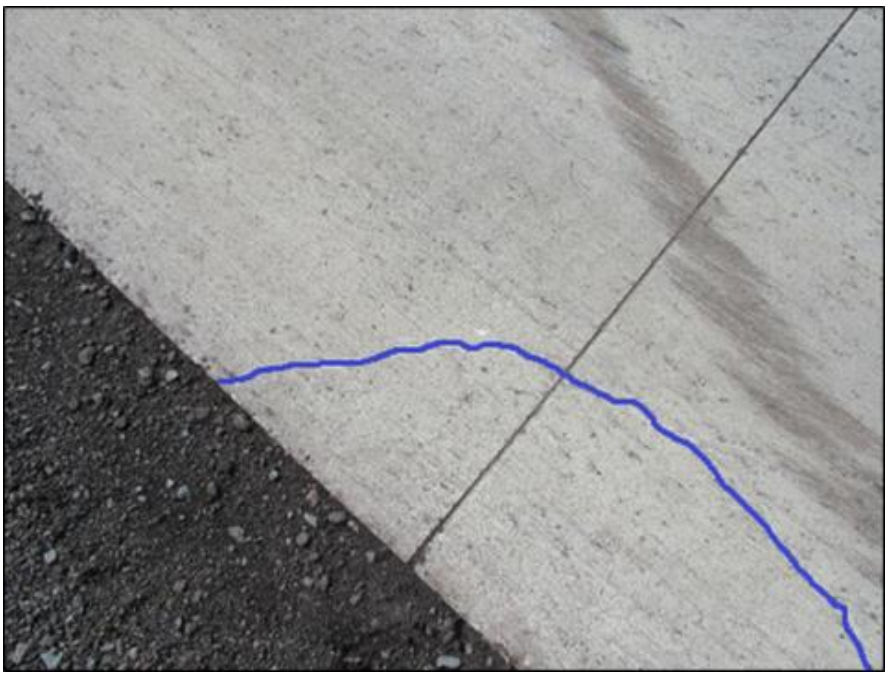

Figure 2-8. Corner cracks in Cell 239 (2018)

Cell 239 performed way better than Cell 139 throughout the last three years. Based on the distress survey data until March 2020, a total of 35 panels have cracked in this cell, with 27 in the inside lane. A total of 20% of slabs have cracked after 145,000 ESALs in this cell compared to more than 75% cracked slabs in Cell 139 with a similar traffic load. The severity of the cracks in Cell 239 was also much less than those in Cell 139. It should be noted that this cell also had much less early construction traffic loadings than Cell 139.

Figure 2-9. Longitudinal cracks in Cell 239 (April 2019)

2.1.2 Cells 705 and 805

Cell 705 was constructed as a 5-inch thick unbonded concrete overlay placed over a nonwoven geotextile fabric secured to an existing 7.5-inch-thick concrete pavement constructed in 1993. Cell 705 was constructed with large slabs, 12 ft x 12 ft (passing lane), and 14 ft W x12 ft L (driving lane), with a total of 22 slabs. Figure 2-10 to Figure 2-12 show photographs of typical longitudinal, transverse, and corner cracks that occurred in Cell 705 in 2018. Figure 2-13 and Figure 2-14 show additional cracking in Cell 705 was observed in April 2019 and September 2020.

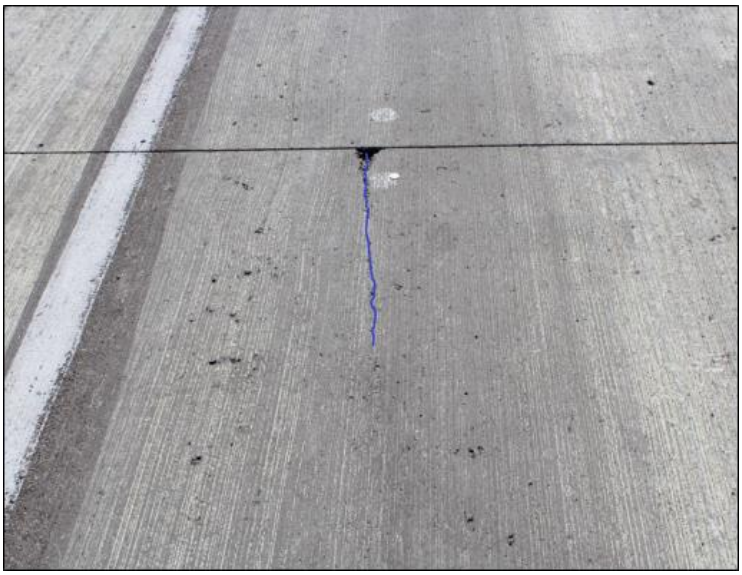

Figure 2-10. Longitudinal crack in Cell 705 (2018)

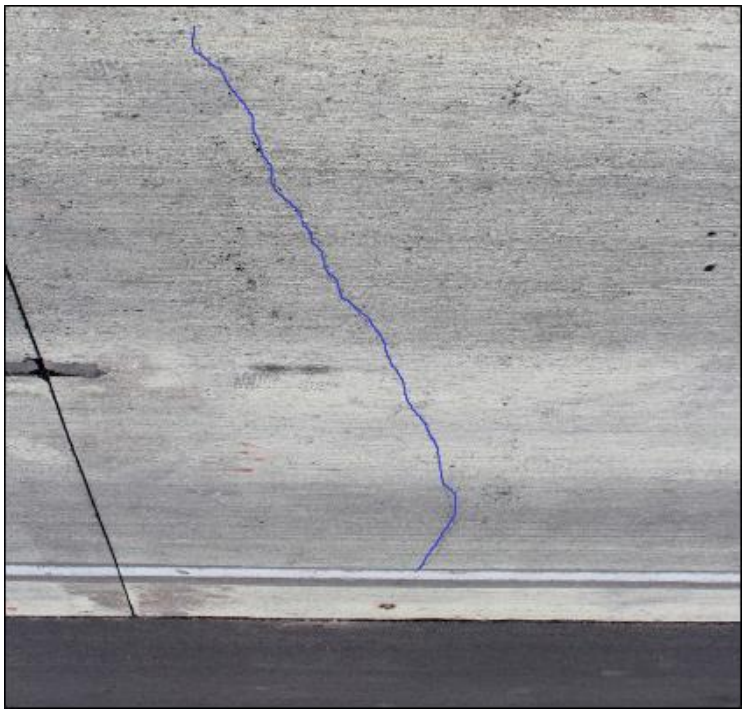

Figure 2-11. Transverse crack in Cell 705 (2018)

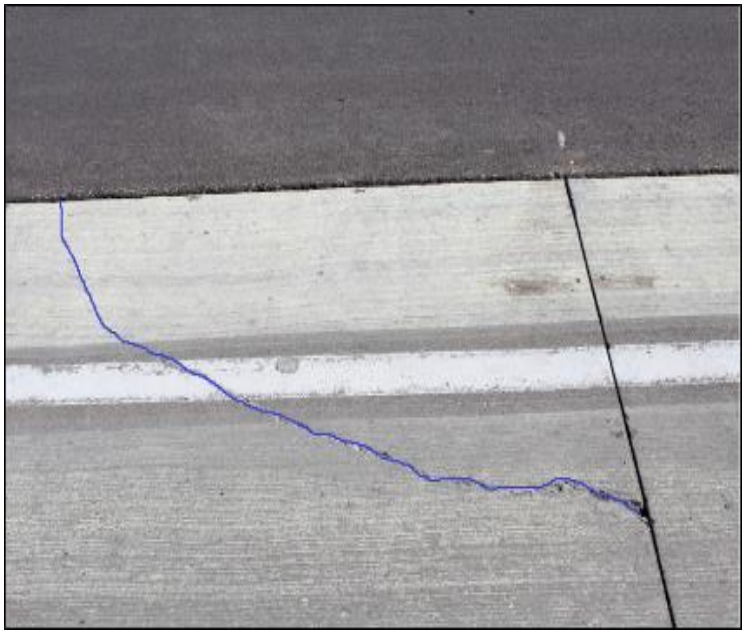

Figure 2-12. Corner crack in Cell 705 (2018)

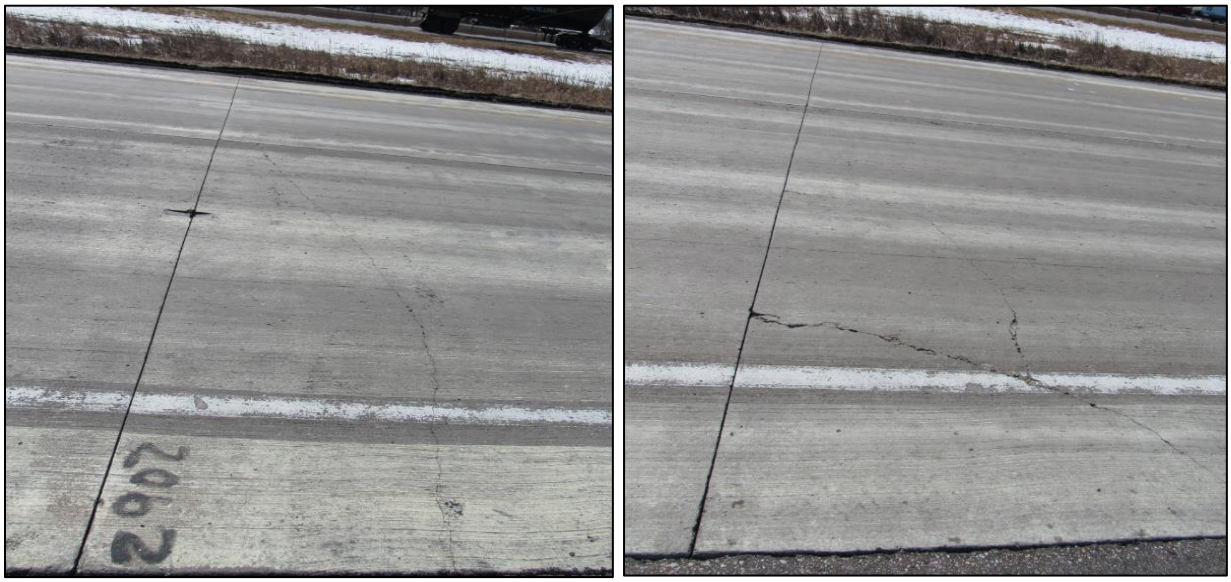

Figure 2-13. Photographs of transverse and corner cracks in Cell 705 as observed during April 2019

Figure 2-14. Photograph of Cell 705 before replacement on September 2020

Cell 805, which was also constructed as a 5-inch thick unbonded concrete overlay, has narrower slabs compared to Cell 705, as shown in Table 1. Cell 805 has a total of 40 slabs. This cell also experienced longitudinal cracks, transverse cracks, and corner cracks. Figure 2-15 to Figure 2-17 show photographs of typical cracks in Cell 805 in 2018. Figure 2-18 and Figure 2-19 show additional cracks observed in Cell 805 in April 2019 and September 2020.

Based on the distress survey data until March 2020, a total of 11 out of 22 panels were cracked in Cell 705, of which eight were in the driving lane; a total of 50% slabs have cracked after 2.7 million ESALs. For Cell 805, 14 out of 40 slab panels were cracked, of which 13 were in the driving lane; 65% of the slabs in the driving lane and 35% of total slab panels were cracked after 2.7 million ESALs.

Figure 2-15. Longitudinal crack in Cell 805 (2018)

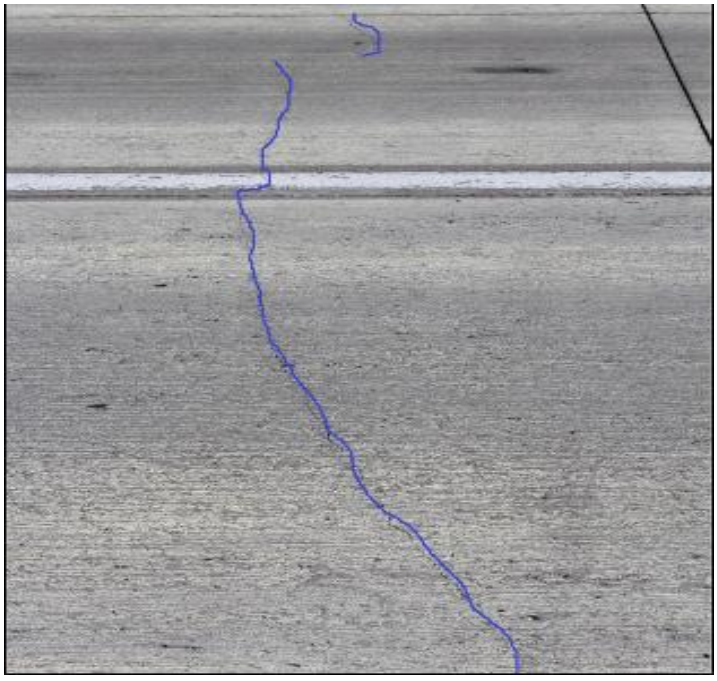

Figure 2-16. Transverse crack in Cell 805 (2018)

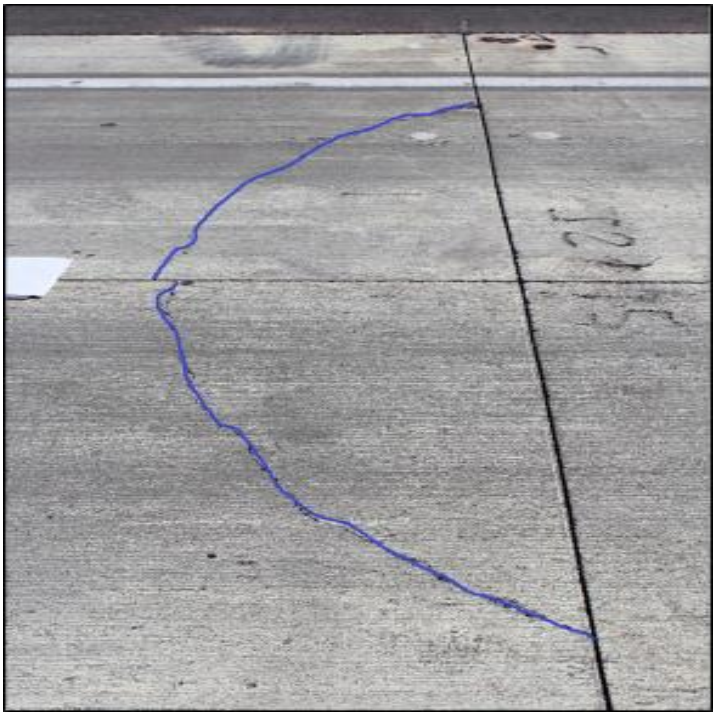

Figure 2-17. Corner crack in Cell 805 (2018)

Figure 2-18. Photographs of observed cracks in Cell 805 during April 2019.

Figure 2-19. Photograph of Cell 805 before removal on September 2020

2.1.3 Cells 506 through 806

Cells 506, 706, and 806 were constructed with 5-inch thick 6ft x 6ft size slabs on an un-stabilized gravel base (not overlay). Cell 606 was constructed with 6-inch thick 6ft x 6ft size slabs. All of these cells were constructed on the mainline test track (I-94 westbound). Cells 506, 606, 706, and 806 have 96, 92, 76, and 88 numbers of slabs, respectively.

Cell 506, which is the control cell constructed without any fibers, experienced one transverse crack, and spalling on 15 numbers of transverse joints before April 2018. The October 2019 distress survey reveals that Cell 506 experienced one diagonal crack and two more transverse cracks in addition to the cracks observed in 2018. Figure 2-20 and Figure 2-21~~Figure 2-21~~ show photographs of the transverse crack and joint spalling documented in April 2018. Figure 2-22 shows the photograph of the cracks in 2019. All three cracks developed in three adjacent slabs which is a probable indication that the underlying base layer or subgrade support was weaker in this location. These cracks have deteriorated with the traffic severely and had to be replaced in the summer of 2020. Figure 2-23~~Figure 2-23~~ shows a photograph of distressed slabs of Cell 506 before they were replaced in June 2020.

Formatte

Regarding the spalling in Cell 506, upon looking closer at multiple spalling locations, it was found that joint areas were filled with hardened saw-cut residue. The residue was not cleaned out of the joints after sawing. There was a clear correlation between the spalling and the presence of the residue. It was up to ¼" deep and completely spanned the saw cut. Thus, when the joints closed in the summer, the spalls formed in these locations. Figure 2-24 shows two photographs of hardened saw-cut residue found at the spalled joints of Cell 506. No visible saw-cut residue was not noticed at the joints of other cells. As the occurrence of the spalling in Cell 506 was not primarily because of the weaker concrete, the spalling statistics are not included in the distress summary in Figure 2-1~~Figure 2-1~~.

Figure 2-20. Transverse crack in Cell 506 (control, non-FRC) observed in the year 2018.

Figure 2-21. Spalling in Cell 506 (control, non-FRC) observed in the year 2018.

Figure 2-22. Photographs of transverse and diagonal cracks in Cell 506 (October 2019)

Figure 2-23. Cell 506 before replacement in June 2020

Figure 2-24. Hardened saw-cut residue found within the spalled joints of Cell 506.

Cell 606, which was constructed with 5 lbs./cy (20% residual strength) of structural fibers, experienced one corner crack prior to April 2018. This corner crack was the only crack as observed during the 2019 distress survey as well. Figure 2-25~~Figure 2-25~~ shows

photographs of the crack in April 2018 and October 2019. It can be seen that the severity of this crack did not change much as compared to what has happened for the cracks in Cell 506 (Figure 2-20 vs. Figure 2-22). As this crack is in the last panel next to a cell transition joint, it can be assumed that this crack is not a typical fatigue-related crack; it occurred because of a construction issue. The distress survey conducted on March 2020 found one joint spalling and two additional low severity corner cracks.

Cells 706 and **806**, which were constructed with fiber dosages of 8 and 11.7 lbs/cy, respectively, did not experience any cracks or spalling prior to October 2019 except for a couple of narrow cracks in Cell 806 originated at the location of a joint opening sensor (Figure 2-26~~Figure 2-26~~). March 2020 distress survey did not report any additional cracks for these two cells.

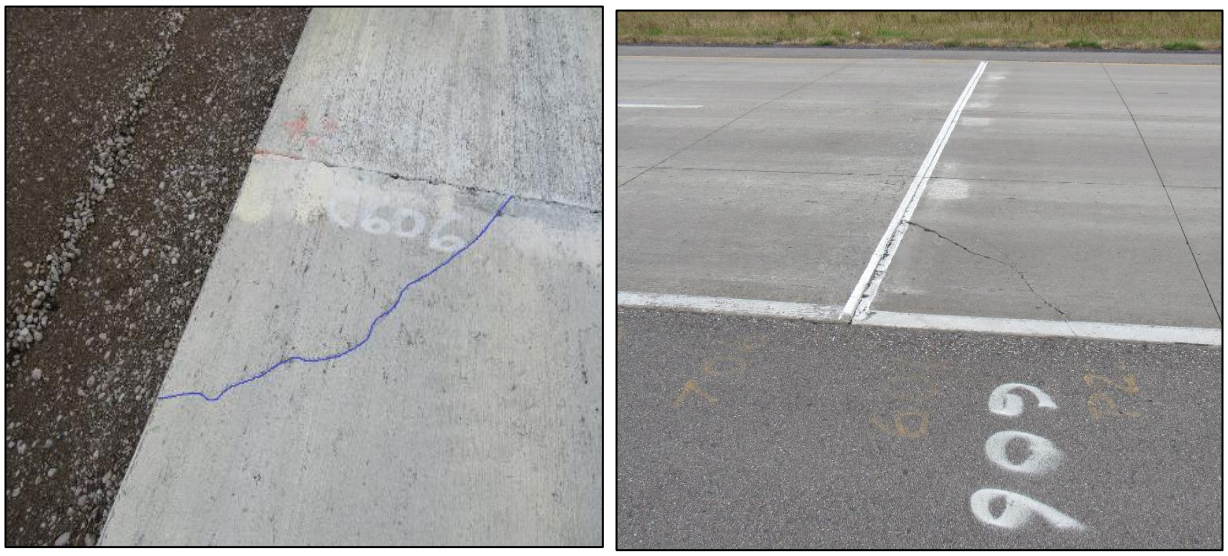

(a) (b)

Figure 2-25. Corner crack (construction issue) in the last panel of Cell 606 observed (a)in the year 2018 and (b) 2019

Figure 2-26. Narrow cracks in Cell 806, originated at the location of the joint opening sensor

One a different note, MnROAD researchers had studied thin (5 to 6.5 inches thick; Cells 113-513) concrete pavement test cells on a comparable underlying support, but with large size slabs, 12 -15 ft. long x 12 ft wide. These cells were constructed in the year 2008 with round or plate dowels in the transverse joints. These cells were also on the MnROAD Mainline like Cells 506 through 806. Approximately 1 million ESALs were applied per year. Burnham & Izevbekhai (2012) reported that these cells developed punchout failures in the driving lane and longitudinal cracks in the passing lane during the third year of service. The improved performance of Cells 506 through 806 compared to Cells 113 and 513 indicate that the short size panels (6ft x 6ft) can delay the formation of fatigue cracking in thin concrete pavements.

2.2 Joint Faulting

Joint faulting was measured at ten different transverse joints in each cell, marked as Joint 1 through 10. It shall be noted that the joint number in these plots is just the serial number of joints where faulting was measured and different from the MnDOT's assigned joint numbers. Joint faulting was measured using a modified Georgia DOT style fault-meter (MnDOT, 2018). It should be noted that the surface texture depth is usually around 1 mm

on average; therefore, any faulting readings below 1 mm may not be indicating any notable faulting. Faulting for each cell is the average of all the faulting readings taken in a cell. As discussed earlier, faulting values below 1 mm are not considered significant and the joints are not considered faulted joints. So, when we consider the average of 10 joints to report faulting, the question remains whether all the 10 joints are faulted joints. A proposed concept of "Faulting Index" is under consideration to address this issue and will be presented in the final report for this project.

2.2.1 Cells 139 and 239

Figure 2-27~~Figure 2-27~~ shows the faulting measured at various transverse joints of Cells 139 and 239. As previously mentioned, Cell 139 had experienced depression along the wheel path, so it may not also be appropriate to compare the faulting results between Cells 139 and 239. Interestingly, faulting results for Cell 239 showed mostly negative values. In general, a negative faulting value indicates that the leave side of the joint is at a higher elevation than the approach side. Negative faulting is usually not typical (Selezneva et. al., 2000), but since the magnitude of the faulting in Cell 239 is below -1 mm, it can be stated that there was not any notable faulting until the third year of service, at least at the joints where the faulting values were recorded. This shows that only three years of data (approximately 150,000 ELALs) is not enough to comment on the joint faulting trends of Cells 139 and 239. It can also be stated that the joint faulting was not the dominant distress for Cell 239; the fatigue cracking was the dominant distress by far. The other important fact is that the FWD measured deflections for the Cell 139 were significantly higher than the Cell 239 and all other cells considered in this study, which indicates that the lower thickness of the Cell 139 was just not enough to distribute the load on a wider area.

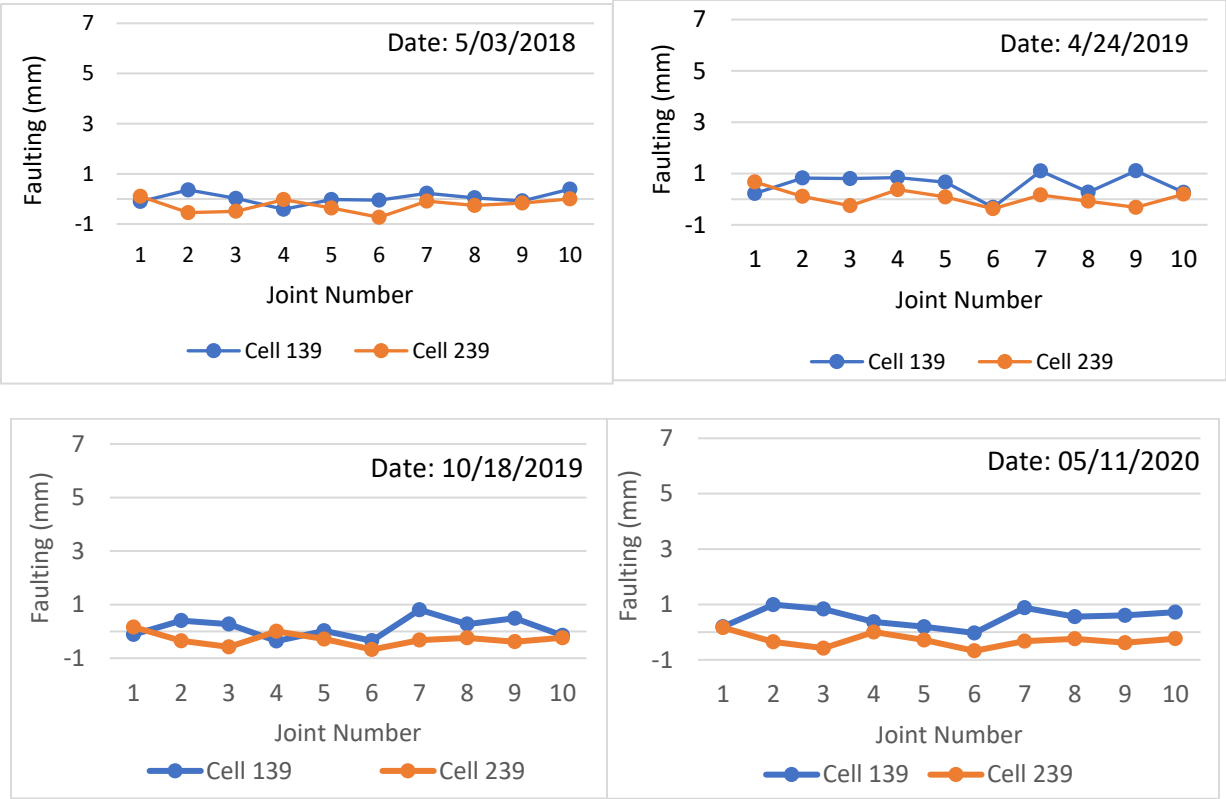

Figure 2-27. Faulting summary of Cells 139 and 239 at four different dates until May 11, 2020.

2.2.2 Cells 705 and 805

Figure 2-28~~Figure 2-28~~ shows the faulting for Cells 705 and 805 until May 2020. Both Cells 705 and 805 had shown mostly positive faulting. One noticeable observation was that the faulting at Joint number-2 and- 4 of Cell 705 was higher in April 2019 (spring) than what was measured in October 2019. May 2020 showed Joint 4 having more faulting than the previous year's measurement, but Joint number 2 surprisingly reported the same faulting measurement as in October 2019. Even though the faulting values in these cells were around 1 to 2 mm, Cell 805 experienced a slightly higher amount of faulting. It may happen that the narrower and lighter slabs in Cell 805 compared to Cell 705 move relatively more under the wheel load. Faulting values may also have been affected by the large number of cracked panels in these cells.

2.2.3 Cells 506 through 806

Figure 2-29~~Figure 2-29~~ shows the faulting measured in Cells 506, 606, 706 and 806 until May 2020. Cell 506, which was constructed with plain concrete, experienced the highest faulting (up to 5 mm) among the four cells. Figure 2-30~~Figure 2-30~~ shows a photograph of noticeable faulting in Cell 506 (note that there is a sunken corner crack in the leave slab, which exaggerated the faulting in the photo). Figure 2-31~~Figure 2-31~~ shows the trend of average faulting versus fiber dosage. Cell 606, which was 6-inch thick (higher aggregate interlock) and constructed with a fiber dosage of 5 lbs./cy experienced approximately 82% less faulting than Cell 506 until May 2020. Cell 706, with a fiber dosage of 8 lbs./cy, also experienced less faulting than Cell 506. Cell 806 which had the highest fiber dosage at 11.7 lbs./cy, experienced lower faulting compared to any other FRC cell. The faulting in the Cell 806 indicates that 0.75 volume fraction fiber still could not completely arrest the faulting. It may be stated that the interstate type traffic loadings on a 5 inches thick pavement are extreme (3 million ESALs in 3 years in this case) and should therefore be considered as an accelerated loading situation. Normal traffic levels associated on a 5 inches thick concrete pavement (on a gravel base) would be lower, and therefore may not have resulted in this level of faulting so soon.

Compared to these 5-inch thick cells, Cell 113- 513 (Burnhum & Izevbekhai, 2012) did not report any considerable joint faulting. It suggests that the doweled Cells 113 and 513 perform better than the Cells 506- 806 when it comes to transverse joint faulting.

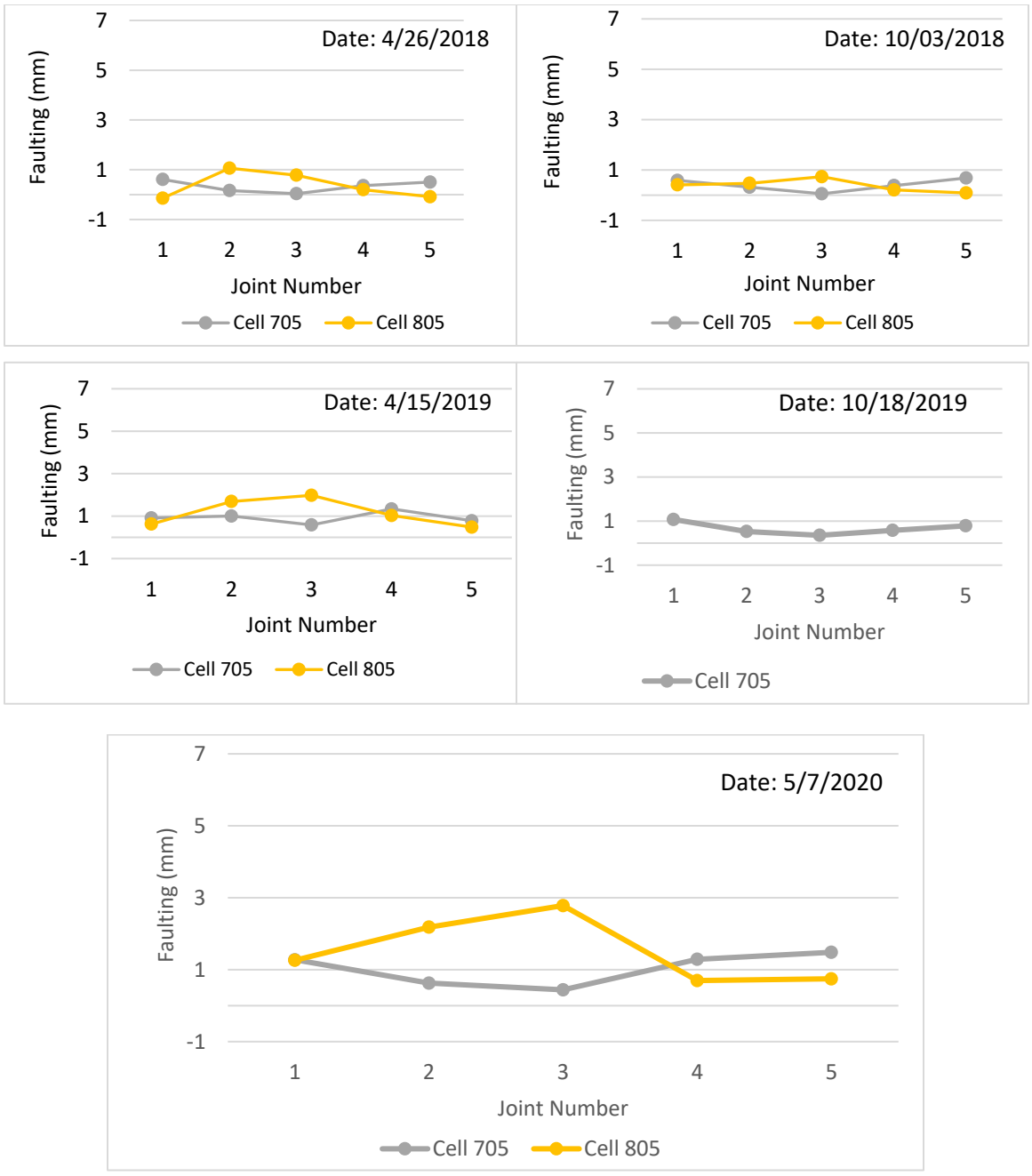

Figure 2-28. Faulting summary of Cells 705 and 805 until May, 2020.

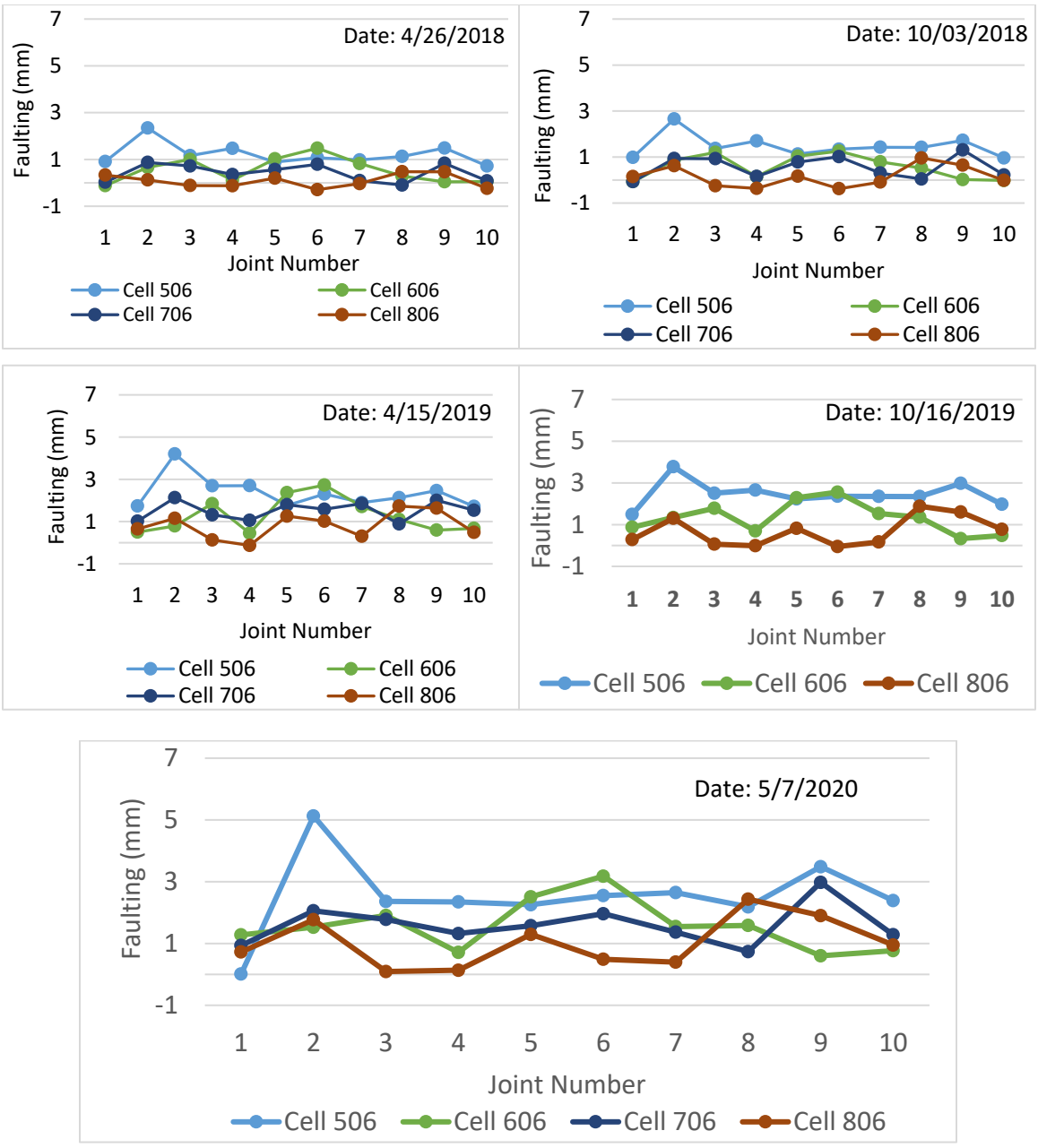

Figure 2-29. Faulting summary of Cells 506 through 806 until May, 2020.

Figure 2-30. Photograph of faulting of Cell 506 (non-FRC). Note that faulting is exaggerated due to the broken corner in leave slab.

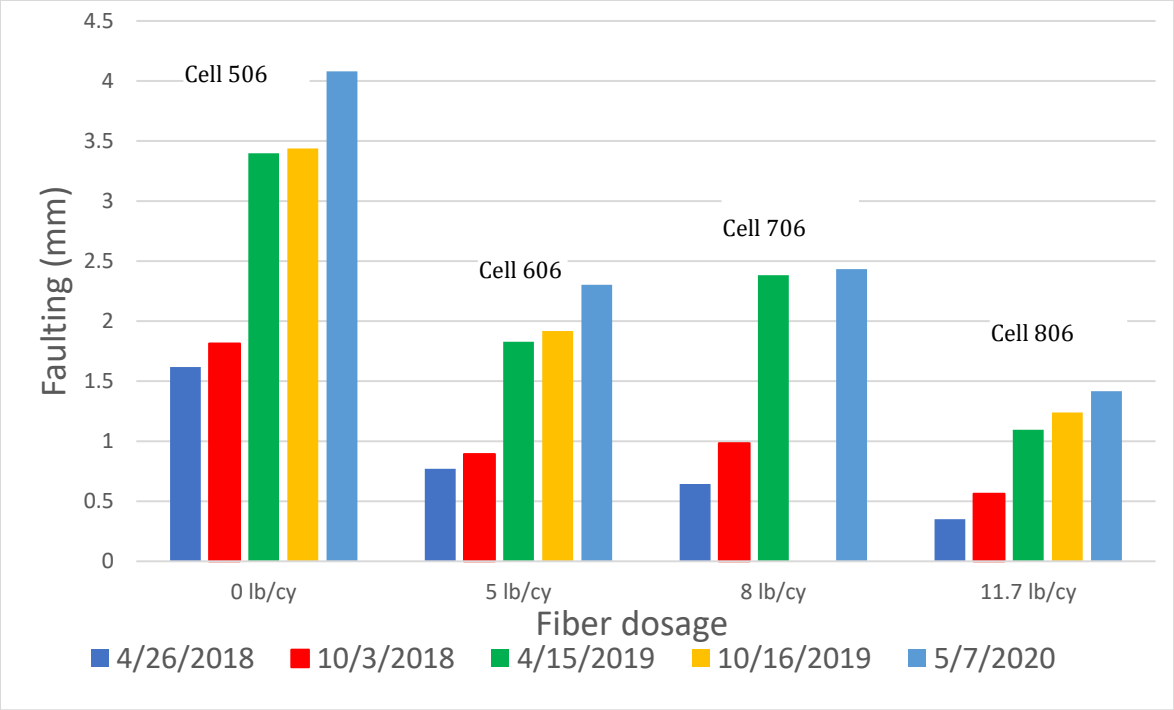

(a)

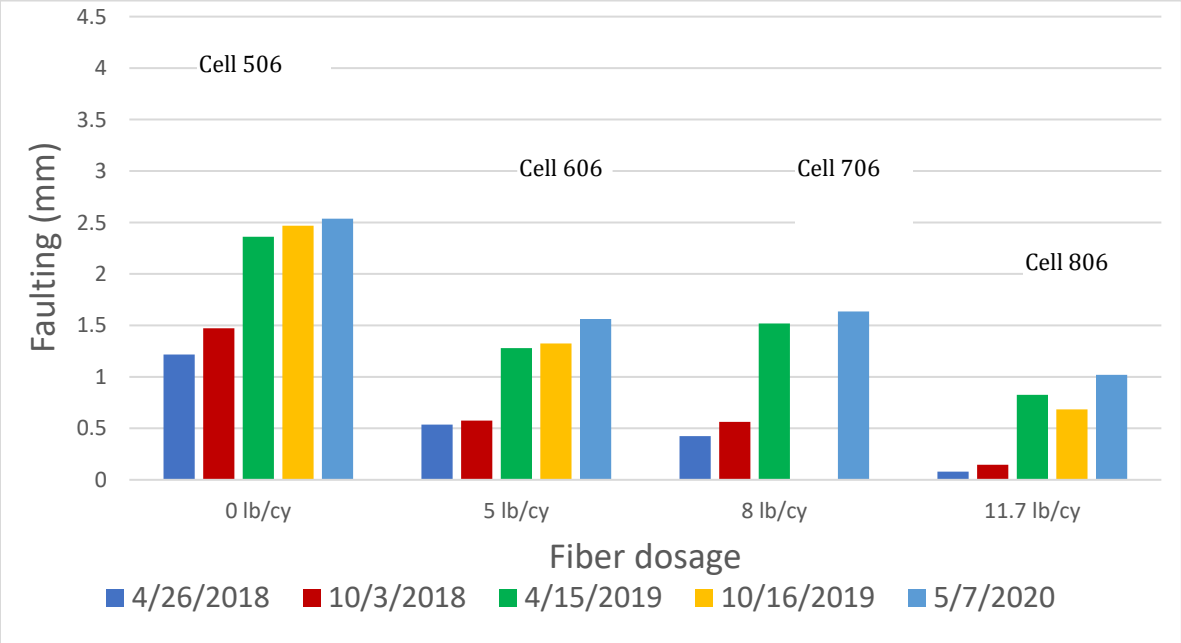

(b)

Note: Faulting for each cell is the average of all the faulting readings taken in a cell. Faulting data of Cell 706 for the April 2019 was erroneous, so discarded.

Figure 2-31. Faulting for Cells 506 through 806 with respect to fiber dosage (a) Only driving lane joints (b) average of the driving and passing lane joints.

3 ANALYSIS OF SENSOR DATA

MnROAD 2017 FRC research cells were instrumented with four types of sensors: joint opening, dynamic strain gauge, vibrating wire strain gauge, and temperature sensors (thermocouples). Figure 3-1~~Figure 3-1~~ through Figure 3-8~~Figure 3-8~~ shows the sensor plans for all eight cells. This section provides an analysis of the data collected from various sensors.

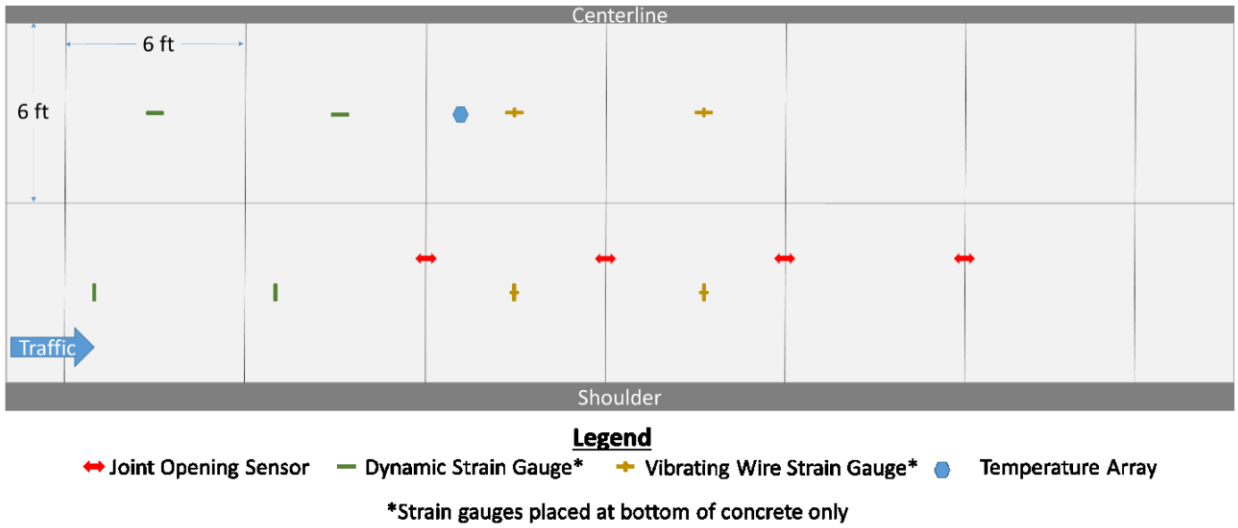

Figure 3-1. Sensor plan for Cell 139, inner lane (MnDOT, 2018).

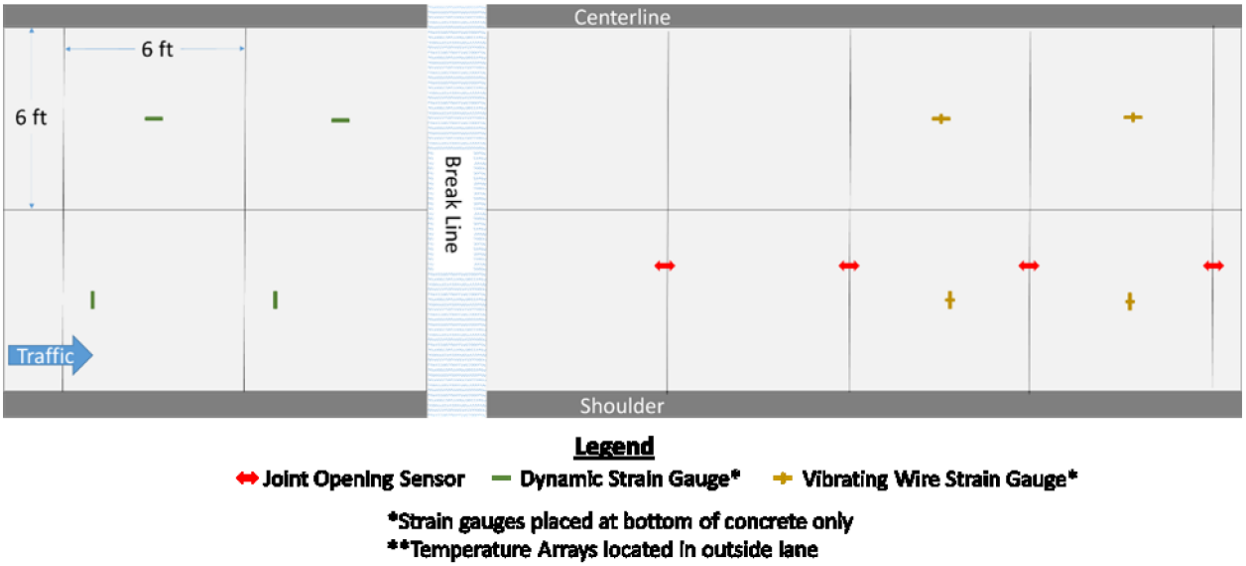

Figure 3-2. Sensor plan for Cell 239, inner lane (MnDOT, 2018).

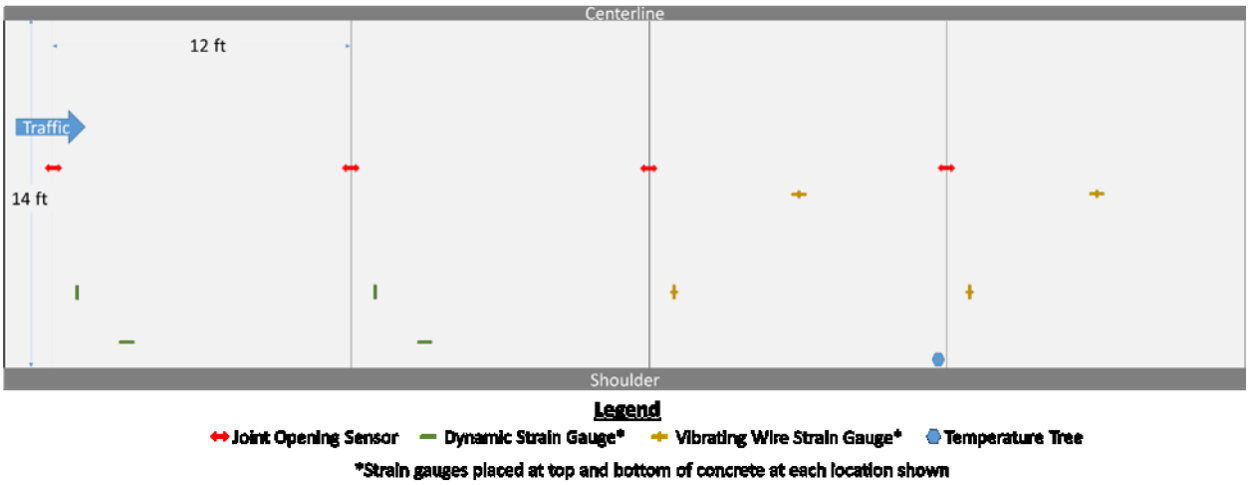

Figure 3-3. Sensor plan for Cell 705, driving lane (MnDOT, 2018).

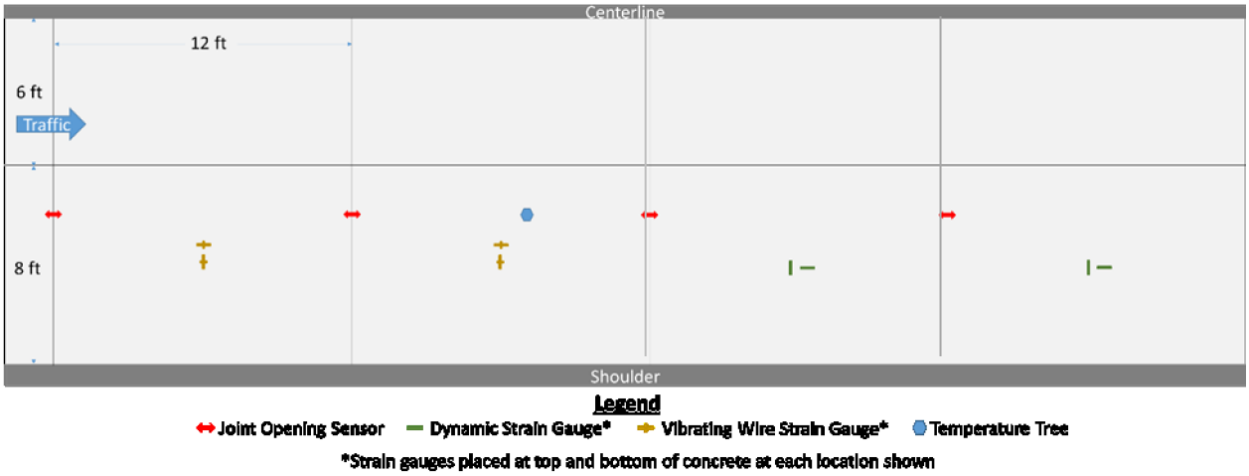

Figure 3-4. Sensor plan for Cell 805, driving lane (MnDOT, 2018)

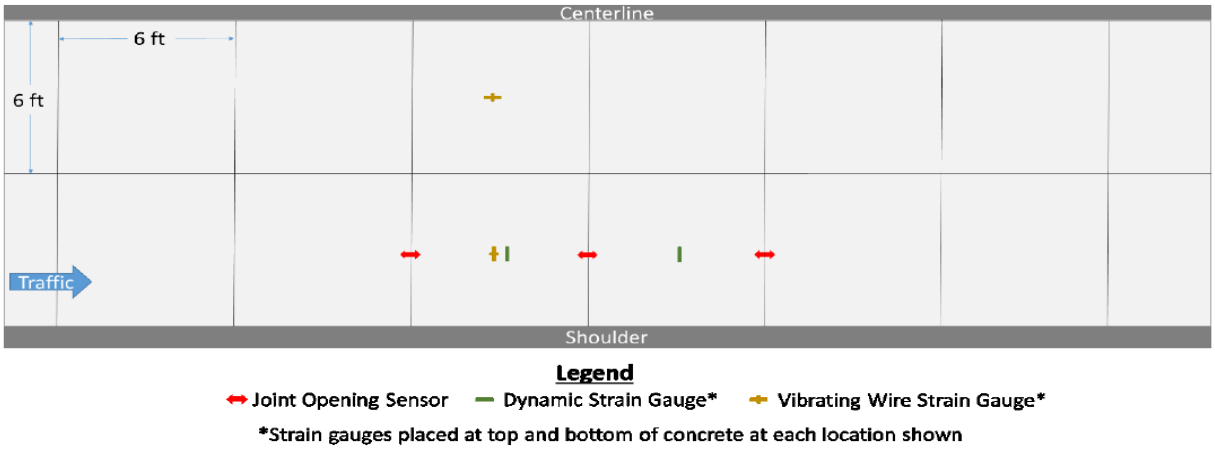

Figure 3-5. Sensor plan for Cell 506, driving lane (MnDOT, 2018).

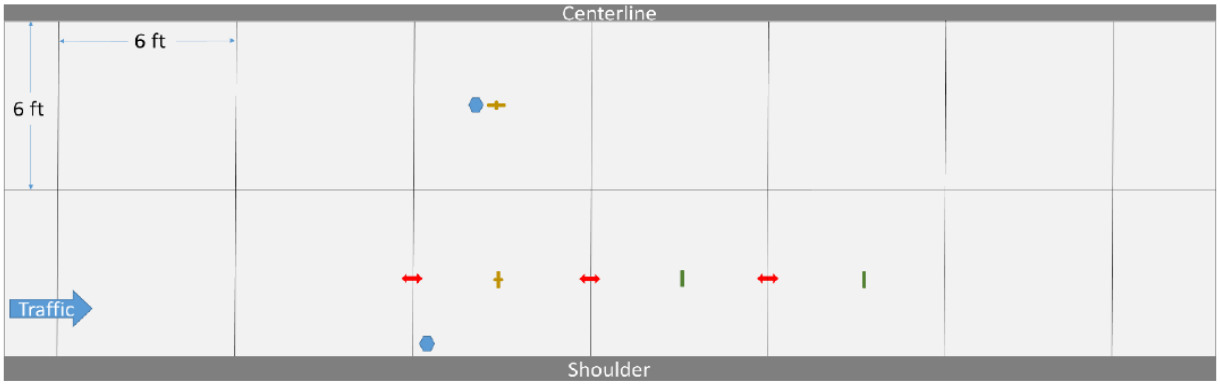

Figure 3-6. Sensor plan for Cell 606, driving lane.

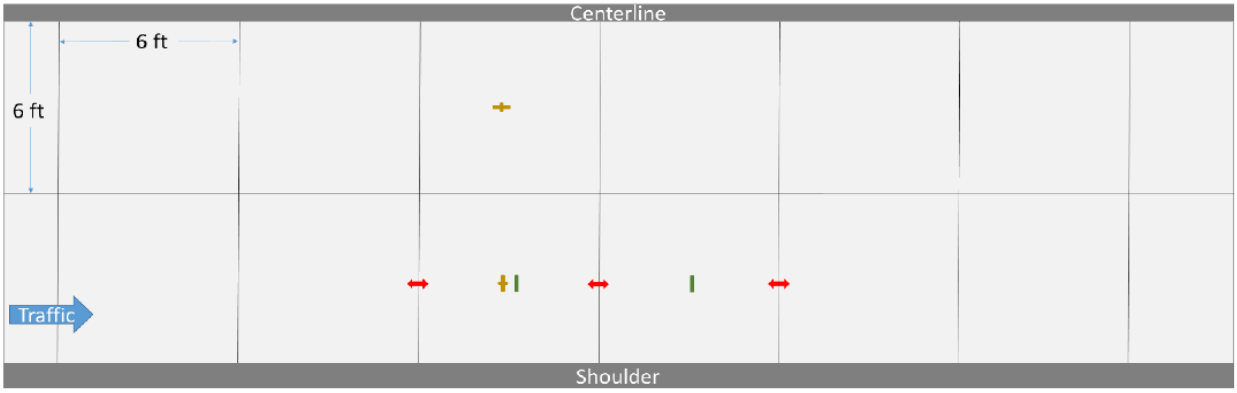

Figure 3-7. Sensor plan for Cell 706, driving lane.

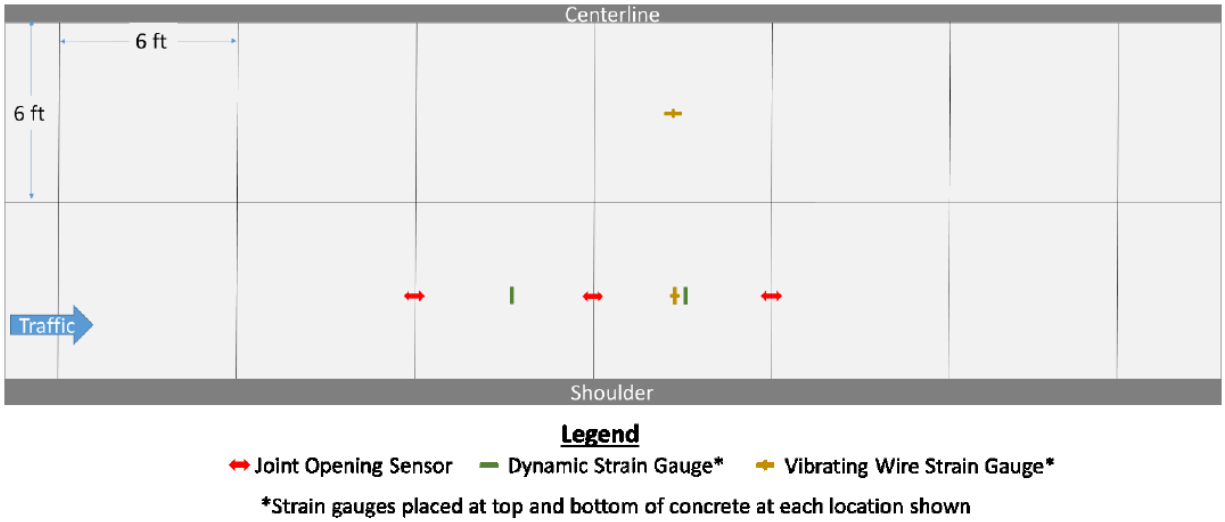

Figure 3-8. Sensor plan for Cell 806, driving lane.

3.1 Temperature

Thermocouple sensors were installed at MnROAD 2017 FRC research cells to capture the variations of temperature as well as temperature-gradient in the concrete slab. Thermocouples were installed at different depths within and beneath the slabs. Figure 3-9~~Figure 3-9~~ shows an example of a thermocouple sensor tree installed in Cells 139, 239, 705, 805, and 606. One sensor tree was installed in each of the Cells 139, 705, and 805; two trees were installed in Cells 239 and 606, located at different offsets from the centerline. For this report, to distinguish between the two sensor trees in Cells 239 and 606, the farthest sensor tree from the centerline was designated as the outer sensor and the sensor tree closest to the centerline as the inner sensor. All the thermocouple sensors were programmed to record temperature data every 15 minutes. In addition to collecting pavement temperature data, ambient temperature data was also collected at MnROAD using an external weather station, which is capable of collecting other ambient parameters like, precipitation, relative humidity, wind speed, wind direction, etc. Figure 3-10~~Figure 3-10~~ shows the variation of the ambient temperatures collected from mid-June 2017 to November 2020. As shown in this figure, January 29, 2019, was the coldest day with a temperature of -34.2^{o}C and December 31, 2017, was the second coldest day at MnROAD with -29.5^{o}C temperature. On the other side, May 28, 2018, was the warmest day with a temperature of 37^{o}C. The variation of the relative humidity at the MnROAD Project site from 2017 summer to 2020 winter is provided in Figure 3-11. As anticipated, the relative humidity during the winter months was less than the rest of the year.

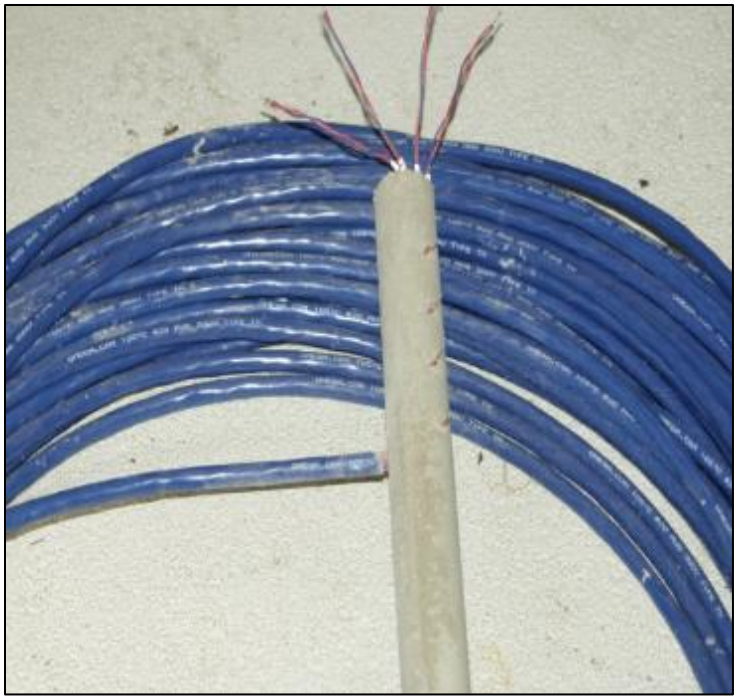

Figure 3-9. Example of a thermocouple sensor tree.

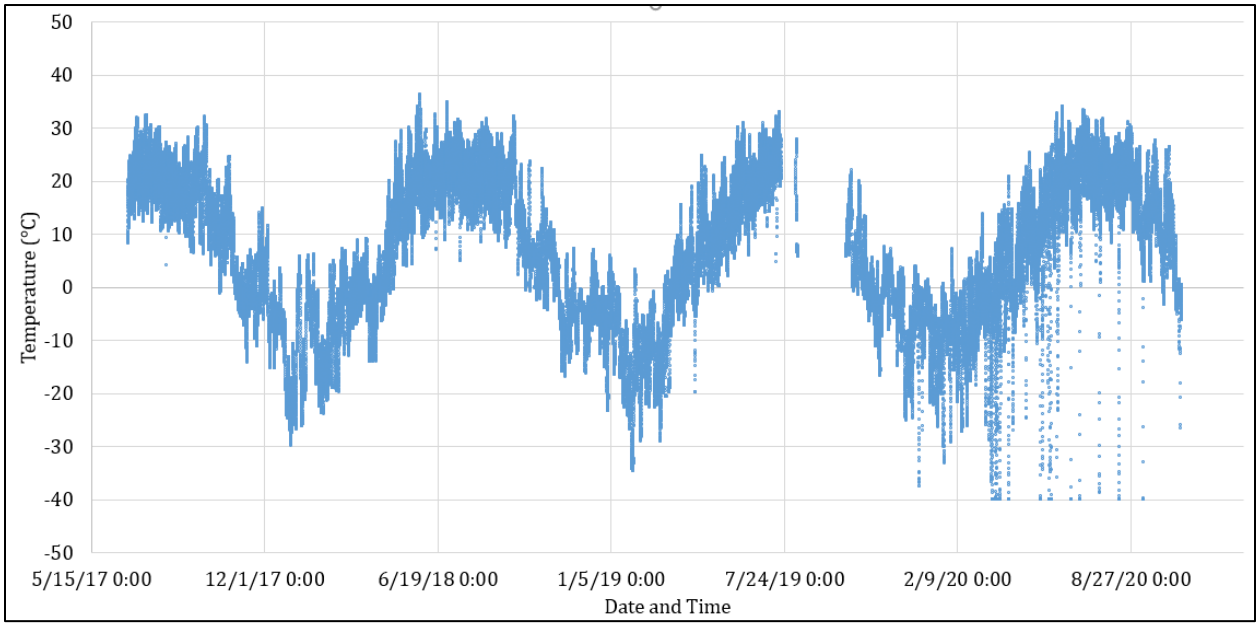

Figure 3-10. The ambient temperature at the MnROAD Project site.

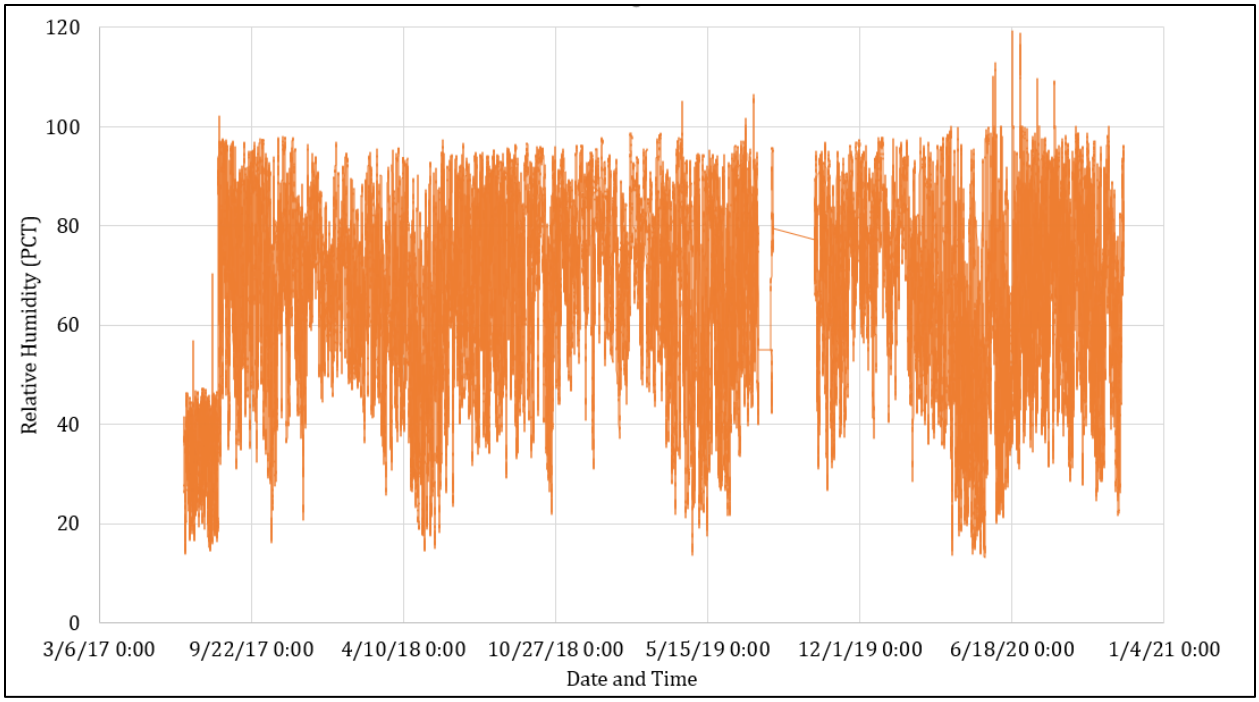

Figure 3-11. Relative humidity variation at the MnROAD Project site.

3.1.1 Pavement Temperature

The pavement slab temperature data for the cells equipped with thermocouples are shown in Figure 3-12~~Figure 3-12~~ through Figure 3-18~~Figure 3-18~~. These figures contain several plots, each with temperatures recorded at different depths of the slab. As expected, the general trends of the seasonal temperature variations are similar for all the cells and align well with the ambient temperature trend, shown in Figure 3-10~~Figure 3-10~~. The maximum and minimum temperatures recorded for each cell and their respective dates of occurrence and times are summarized in Table 5~~Table 5~~. The dates of the coldest temperatures for all the cells were recorded on January 30, 2019 except for Cells 705 and 805, which recorded the coldest temperature on December 31, 2017. Cell 239 outer sensor and Cell 805, experienced their warmest day on May 28, 2018. Cell 139 experienced the warmest day on the date of its paving, i.e. July 17, 2017. The inner thermocouple tree of Cell 239 also experienced the warmest temperature on July 17, 2017, on its paving date. These observations indicate that Cells 139 and 239 were constructed on a relatively warmer day, and the recorded highest temperatures probably were influenced by the heat of hydration of the cement. Two thermocouple sensors of Cell 705 stopped working after October 2019.

Although the sensor trees beneath the Cell 705 slab continued to work, they were outside the boundary of interest and hence not added in Figure 3-15~~Figure 3-15~~.

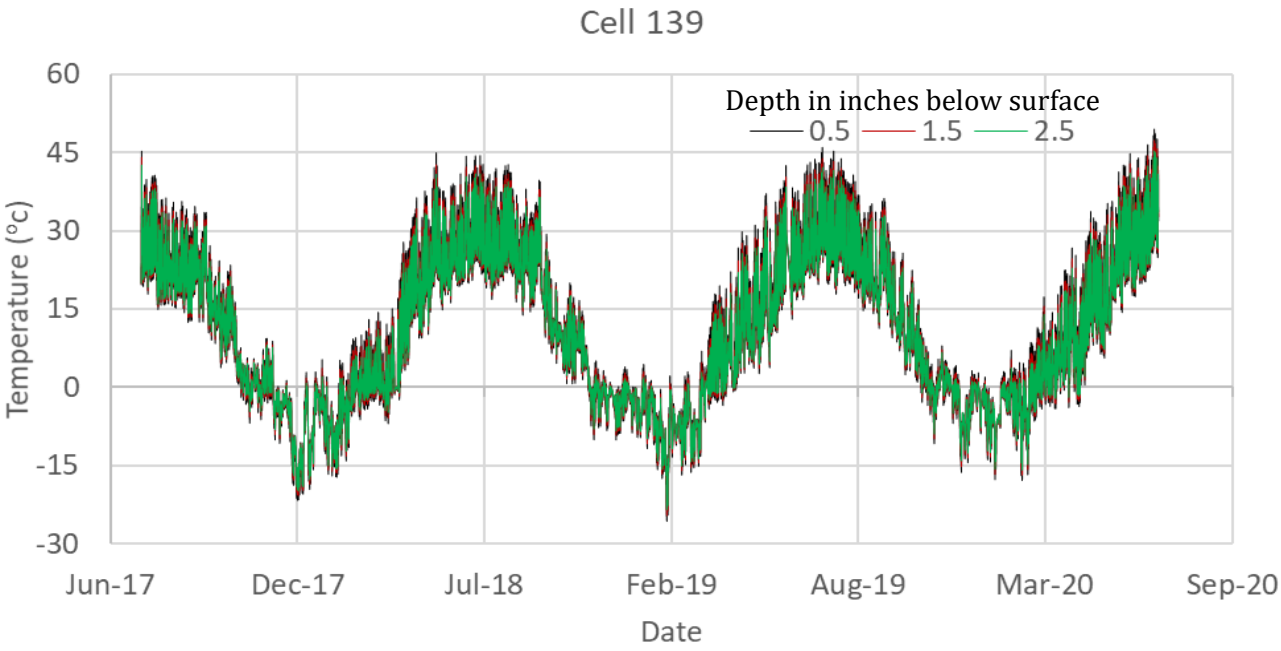

Figure 3-12. Temperature profile of Cell 139.

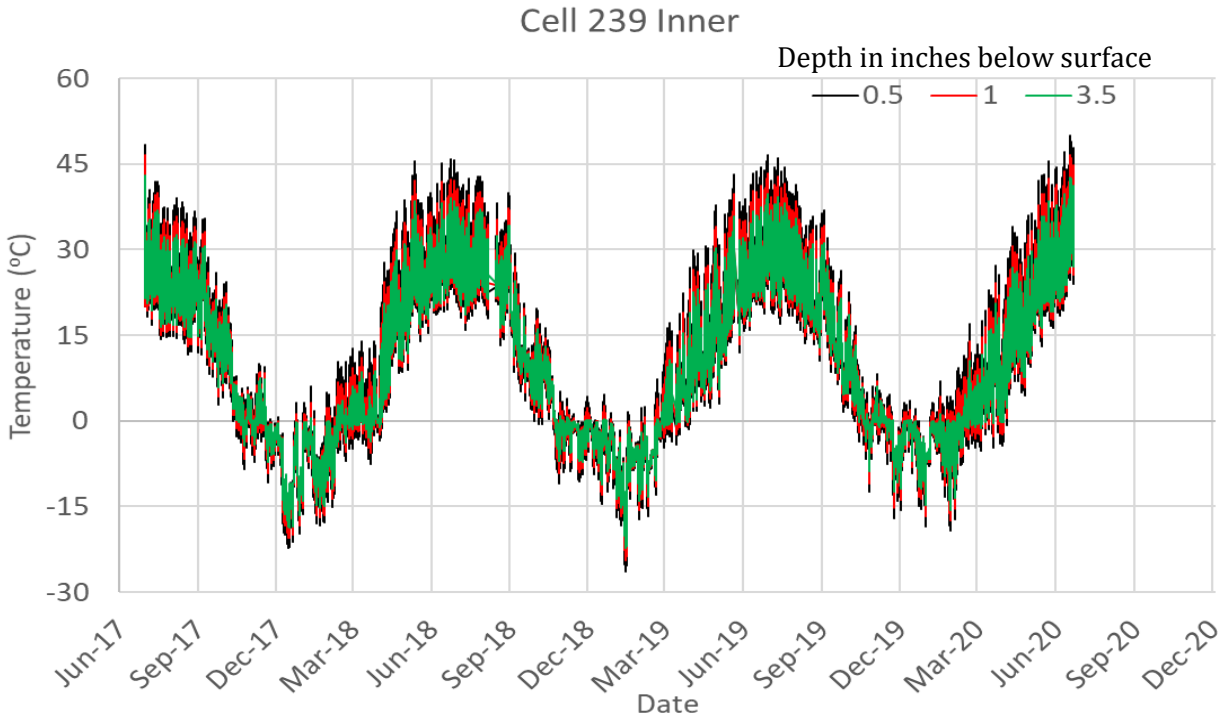

Figure 3-13. Temperature profile of Cell 239 inner lane.

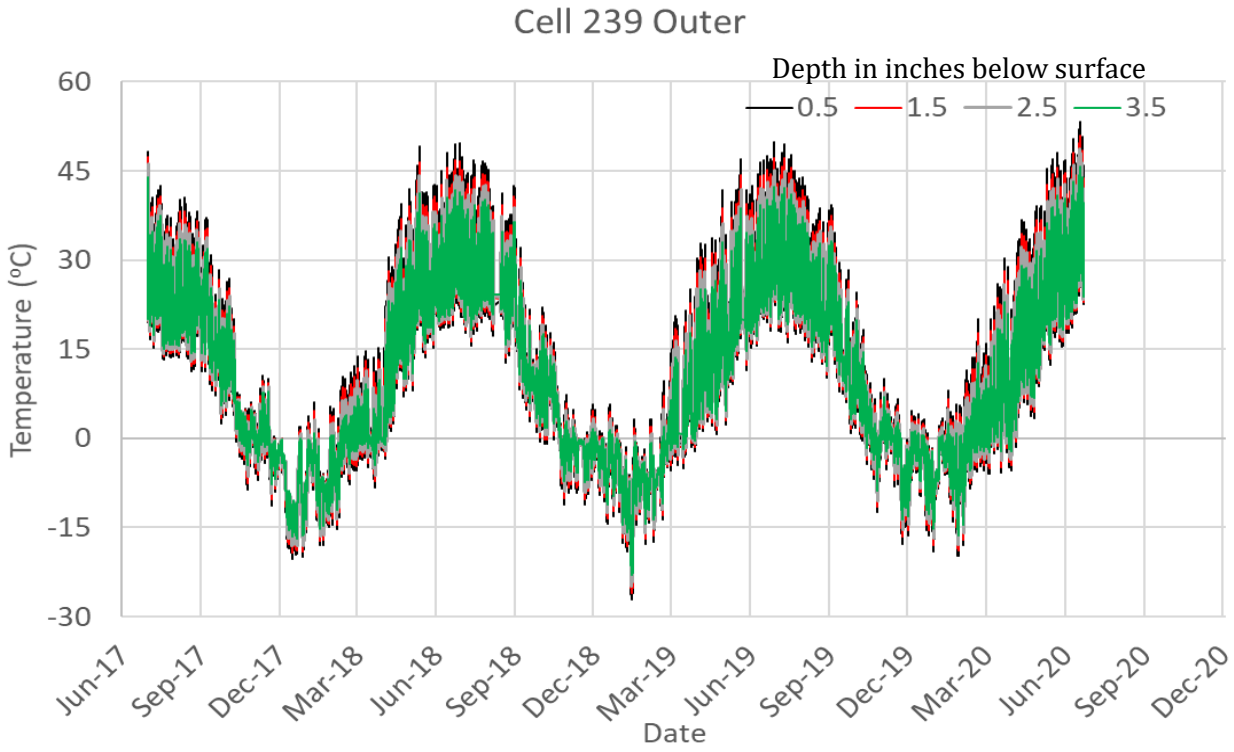

Figure 3-14. Temperature profile of Cell 239 outer lane.

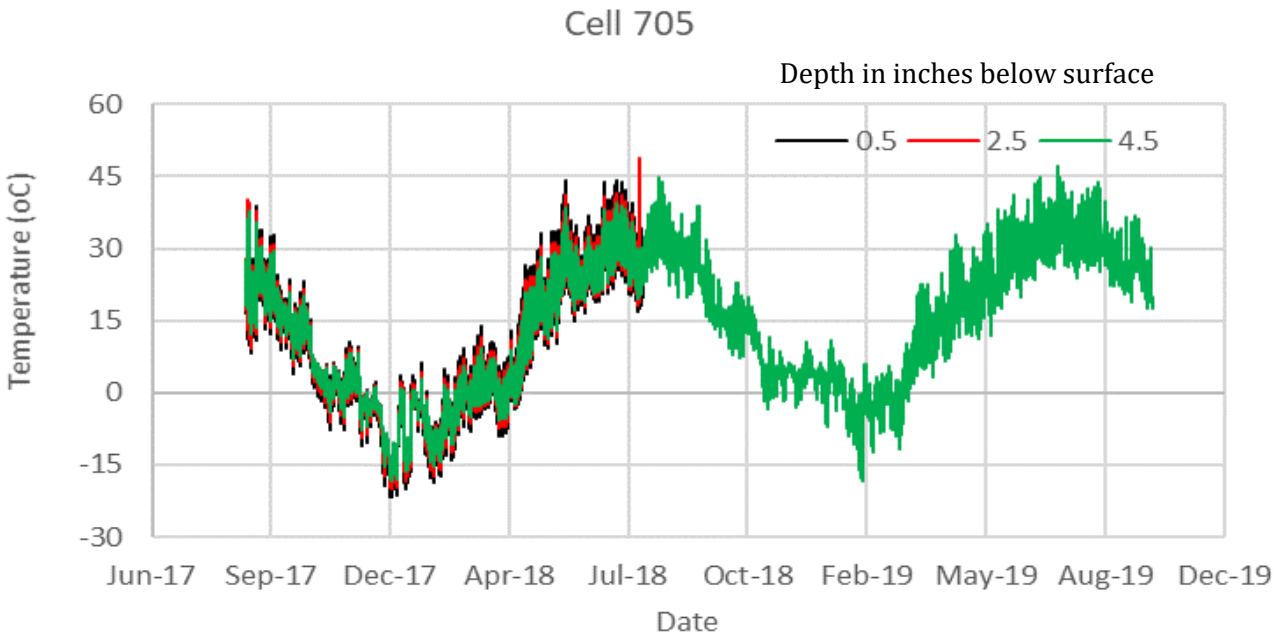

Figure 3-15. Temperature profile of Cell 705.

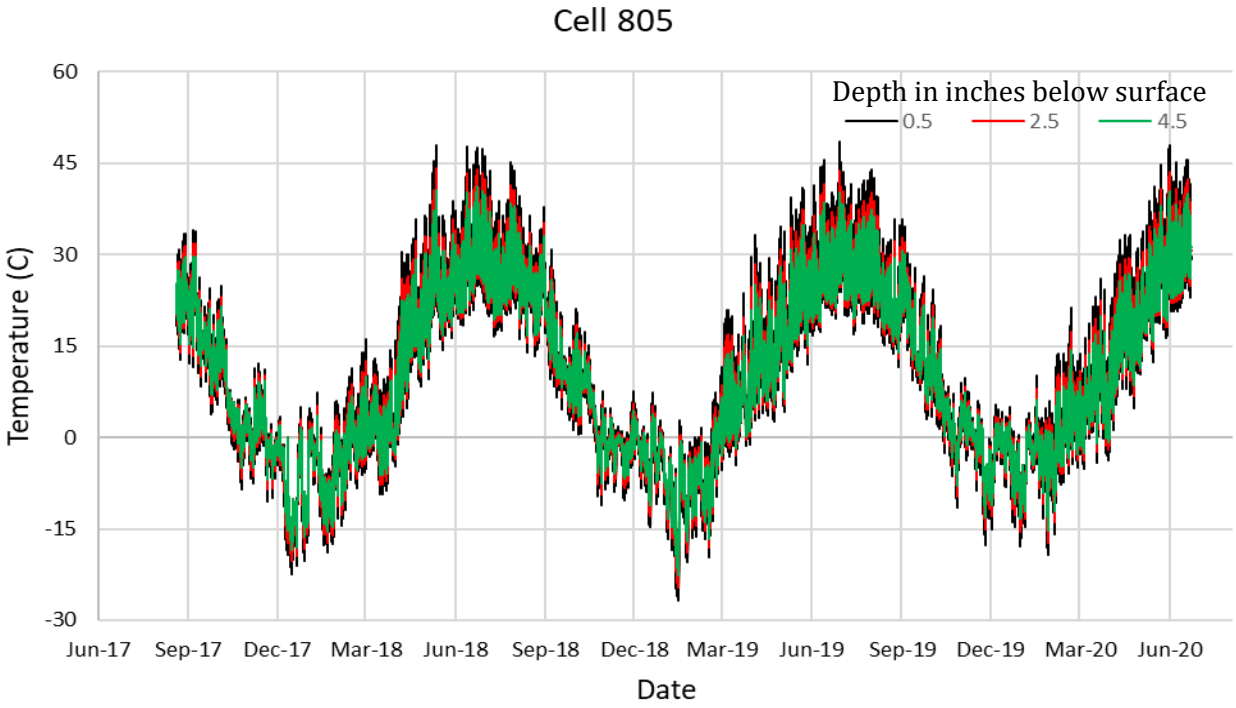

Figure 3-16. Temperature profile of Cell 805.

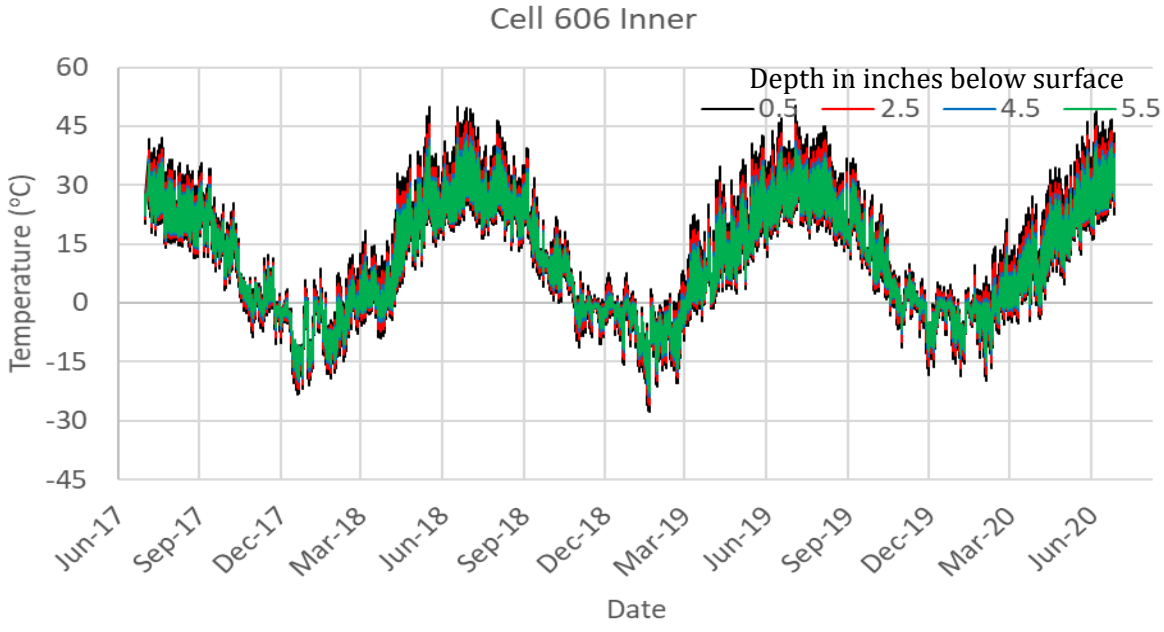

Figure 3-17. Temperature profile of Cell 606 inner lane.

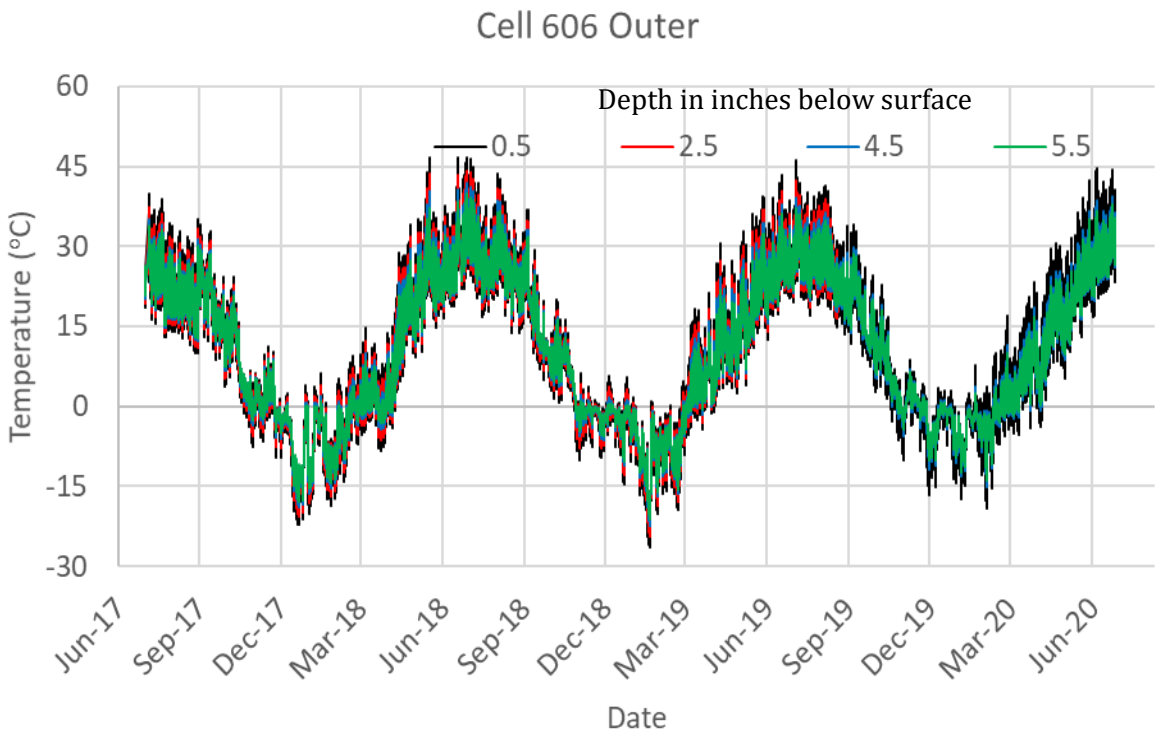

Figure 3-18. Temperature profile of Cell 606 outer lane.

Table 5. Cell extreme temperatures and respective dates and times.

Cell		Temperature ° C	Date	Time
139	Max	49.51	7/4/2020	2:45 PM
	Min	-25.68	1/30/2019	7:45 AM
239	Max Outer	49.77	5/28/18	2:15 PM
	Min Outer	-27.21	1/30/19	7:30 AM
	Max Inner	48.33	7/17/17	2:45 PM
	Min Inner	-26.43	1/30/19	7:00 AM
705	Max	47.2	7/15/19	3:45 PM
	Min	-21.82	12/31/17	8:45 AM
805	Max	47.92	5/28/18	2:45 PM
	Min	-22.42	12/31/17	8:45 AM
606	Max Outer	46.71	7/9/2018	3:45 PM
	Min Outer	-26.41	1/31/2019	7:30 AM
	Max Inner	50.25	7/15/2019	3:15 PM
	Min Inner	-27.7	1/31/2019	7:30 AM

Note: Temperature readings collected at different depths of slabs are considered.

The relationship between the temperature and depth of the slab was studied to determine the nature of the temperature variation (either linear or non-linear). Figure 3-19~~Figure 3-19~~ and Figure 3-20~~Figure 3-20~~ show the temperature profiles of various cells during their coldest and warmest temperature events, respectively. Temperature profiles for various cells at an intermediate temperature, observed on April 24, 2019, are studied as well, as shown in Figure 3-21. The general nature of the temperature variation with respect to the depth of the slab was linear, except for Cell 239, which showed a slightly non-linear nature; the reason for a distinct trend of the temperature variation in Cell 239 is not known. One possible reason could be that the thermocouple attached to the tree at one-inch depth moved downwards because of the construction-related issue. The relatively lower thickness of the slabs in this study compared to the conventional concrete pavements may be the reason for the linear temperature gradients in all other cells. As the cells (except Cell 239) experienced linear temperature gradients, the analysis has been restricted to the linear temperature gradient only.

3.1.2 Linear Temperature Gradient (LTG)

The linear temperature gradient (LTG) was determined by subtracting the temperature of the bottommost sensor from the temperature of the topmost sensor of a slab and then divided by the vertical distance between these sensor locations in question. A negative temperature gradient indicates that the pavement is colder at the top and warmer at the bottom, and a positive temperature gradient indicates the opposite scenario. At negative and positive temperature gradients, slabs experience upward and downward curling, respectively. In this work, temperature gradients were calculated every 15 minutes, then the monthly extreme positive and negative LTGs were determined as shown in Table 7~~Table 7~~ and Table 8~~Table 8~~.

Table 6~~Table 6~~ shows the monthly maximum and minimum LTGs for Cells 139 and 239. Cell 139 had the highest positive LTG of 2.68^{o}C/cm in December 2019. The highest negative LTG for cell 139 was -0.99 ^{o}C/cm in July 2019. The outer sensor tree of Cell 239 had the highest LTG of 1.79 ^{o}C/cm in June 2020 and the highest negative LTG of -2.53^{o}C/cm in

December 2019, while the inner sensor tree had the highest positive LTG of 1.81°C/cm in September 2019 and the lowest LTG of -2.49 °C/cm in December 2019.

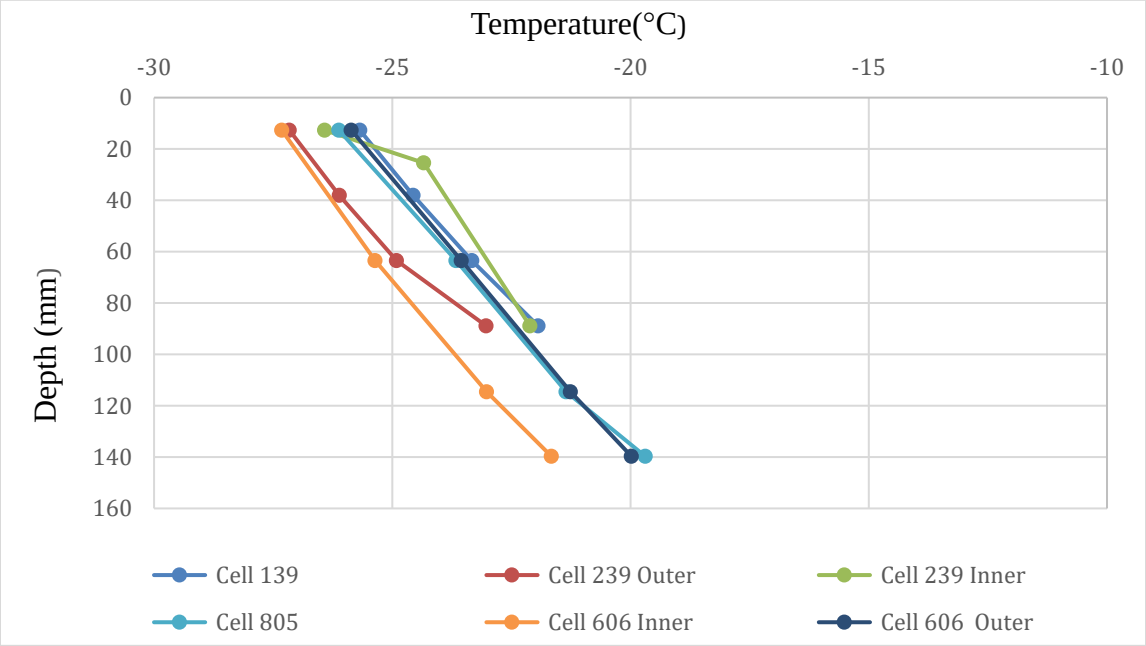

Figure 3-19. Temperature vs. slab depth on the coldest day, January 30, 2019, 7:45 AM.

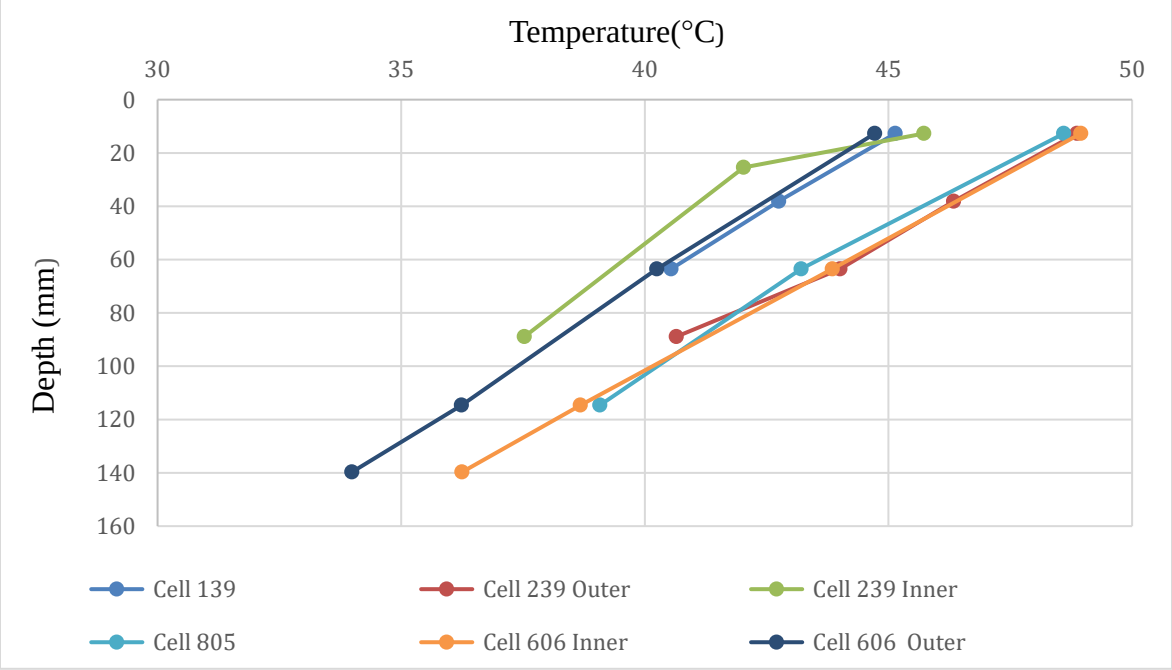

Figure 3-20. Temperature vs. slab depth on the warmest day, July 15, 2019, 2:30 PM.

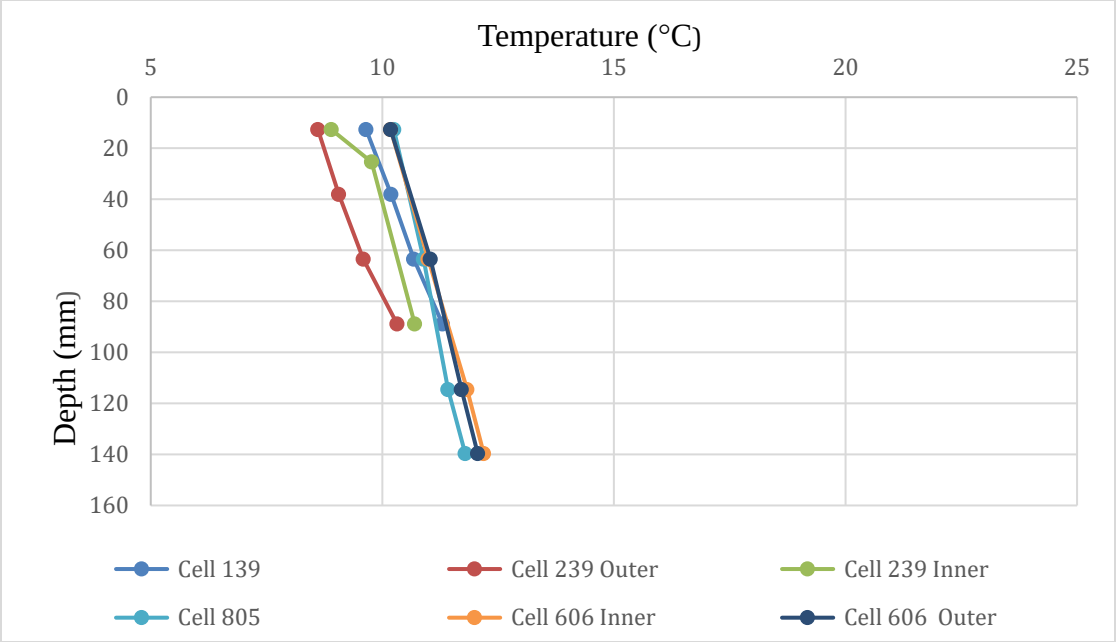

Figure 3-21. Temperature vs. slab depth at an intermediate temperature on April 24, 2019, 4:15 AM.

Table 6. Max. and Min. linear temperature gradient results for Cells 139 and 239.

Temperature Gradient (°C/cm)						
	Cell 139 (3-inch)		Cell 239 (4-inch)			
	Inner		Outer		Inner	
Month	Negative	Positive	Negative	Positive	Negative	Positive
Jul-17	-0.65	0.81	-0.91	0.95	-0.59	1.07
Aug-17	-0.58	0.87	-0.68	1.25	-0.61	1.14
Sep-17	-0.52	0.79	-0.85	1.08	-0.49	0.98
Oct-17	-0.38	0.72	-0.45	0.94	-0.41	0.88
Nov-17	-0.49	0.60	-0.59	0.80	-0.51	0.75
Dec-17	-0.48	0.41	-0.58	0.40	-0.52	0.59
Jan-18	-0.51	0.68	-0.67	0.72	-0.47	0.82
Feb-18	-0.51	0.98	-0.64	1.06	-0.51	1.17
Mar-18	-0.43	1.04	-0.52	1.15	-0.47	1.29
Apr-18	-0.52	1.09	-0.66	1.61	-0.56	1.34
May-18	-0.62	1.09	-1.07	1.41	-0.53	1.35
Jun-18	-0.76	1.16	-0.63	1.56	-0.49	1.32
Jul-18	-0.92	1.19	-0.91	1.41	-0.63	1.10
Aug-18	-0.86	1.18	-0.91	1.54	-0.62	1.18

Temperature Gradient (°C/cm)						
	Cell 139 (3-inch)		Cell 239 (4-inch)			
	Inner		Outer		Inner	
Month	Negative	Positive	Negative	Positive	Negative	Positive
Sep-18	-0.95	1.19	-0.81	1.24	-0.50	0.89
Oct-18	-0.95	0.89	-0.54	0.90	-0.68	0.99
Nov-18	-0.81	0.95	-1.08	0.74	-0.91	0.67
Dec-18	-0.82	1.04	-0.57	0.63	-0.62	0.54
Jan-19	-0.61	0.92	-0.88	0.65	-0.62	0.47
Feb-19	-0.51	0.70	-0.71	0.84	-0.61	0.62
Mar-19	-0.44	1.04	-0.47	1.24	-0.45	1.12
Apr-19	-0.91	1.19	-0.71	1.45	-0.38	1.18
May-19	-0.62	1.16	-0.63	1.45	-0.57	1.16
Jun-19	-0.55	1.11	-0.83	2.22	-0.57	1.35
Jul-19	**-0.99**	1.12	-1.63	1.43	-1.15	1.15
Aug-19	-0.72	1.06	-1.06	1.41	-0.73	1.06
Sep-19	-0.51	0.76	-0.72	1.34	-0.65	**1.81**
Oct-19	-0.47	0.99	-1.22	1.55	-1.17	0.98
Nov-19	-0.74	0.61	-2.21	0.68	-1.05	0.75
Dec-19	-0.79	**2.68**	**-2.53**	1.12	**-2.49**	0.64
Jan-20	-0.44	0.43	-0.90	0.60	-0.56	0.46
Feb-20	-0.63	0.98	-0.81	1.13	-0.74	1.22
Mar-20	-0.44	1.12	-0.55	1.43	-0.62	1.35
Apr-20	-0.35	0.48	-0.55	1.48	-0.82	1.32
May-20	-0.46	1.26	-1.13	1.60	-0.59	1.51
Jun-20	-0.78	1.11	-1.24	**1.79**	-0.90	1.31

* Data collection for Cells 139 and 239 started on July 17th, 2017

Cells 705 and 805 are thin unbonded fiber reinforced concrete overlays on concrete pavements. Table 7~~Table 7~~ shows the monthly maximum and minimum LTGs for both Cells 705 and 805. From the available data for Cell 705, the maximum positive LTG was found as 1.00 °C/cm, and the maximum negative was -0.74 °C/cm. Cell 805 had a maximum positive LTG of 1.11 °C/cm and a maximum negative LTG of -0.90 ° C/cm. For Cell 705, the maximum positive LTGs occurred in July 2018, and for Cell 805, the same occurred in April and November 2019. The maximum negative LTG for Cell 705 occurred in September 2017,

and for Cell 805, it occurred in September 2018 and November 2019. Overall, the maximum LTGs for Cell 805, which were constructed with 6 ft wide slabs, were slightly higher than Cell 705 that had 12 ft wide slabs.

Table 7. Linear temperature gradient results for Cells 705 and 805.

Temperature Gradient (°C/cm)				
	Cell 705 (5-inch)		Cell 805 (5-inch)	
Month	**Negative**	**Positive**	**Negative**	**Positive**
Sep-17	**-0.74**	0.53	-0.39	0.57
Oct-17	-0.35	0.41	-0.38	0.57
Nov-17	-0.40	0.35	-0.41	0.48
Dec-17	-0.45	0.19	-0.47	0.30
Jan-18	-0.48	0.44	-0.50	0.56
Feb-18	-0.44	0.53	-0.46	0.66
Mar-18	-0.37	0.64	-0.43	0.83
Apr-18	-0.39	0.74	-0.43	1.01
May-18	-0.35	0.81	-0.48	1.04
Jun-18	-0.38	0.77	-0.25	-0.24
Jul-18	-0.62	**1.00**	-0.70	1.08
Aug-18			-0.67	1.05
Sep-18			**-0.90**	1.02
Oct-18			-0.82	0.64
Nov-18			-0.88	0.58
Dec-18			-0.88	0.61
Jan-19			-0.57	0.40
Feb-19			-0.53	0.80
Mar-19			-0.46	0.93
Apr-19			-0.76	**1.11**
May-19			-0.45	1.10
Jun-19			-0.39	0.97
Jul-19			-0.60	0.98
Aug-19			-0.44	0.92
Sep-19			-0.35	0.87
Oct-19			-0.36	0.61
Nov-19			**-0.90**	**1.11**

Temperature Gradient (°C/cm)				
	Cell 705 (5-inch)		Cell 805 (5-inch)	
Month	Negative	Positive	Negative	Positive
Dec-19			-0.52	0.44
Jan-20			-0.49	0.40
Feb-20			-0.61	0.83
Mar-20			-0.32	0.89
Apr-20			-0.36	0.89
May-20			-0.45	0.86
Jun-20			-0.57	1.03

* Data collection for cell 805 started on September 5th 2017

Out of the four Cells 506 through 806 in the mainline test track, only Cell 606 has thermocouples. Two sensor trees were included in this cell. The LTGs for both sensor trees are provided in Table 8~~Table 8~~. For the inner sensor tree, the maximum positive LTG was 2.77 °C/cm, and the maximum negative TG was -4.16 °C/cm. The outer sensor tree has maximum positive and negative LTGs of 1.59 °C/cm and -1.56 °C/cm, respectively. For outer and inner sensor trees, the positive maximum LTG occurred in September and November 2019, respectively, whereas the negative maximum LTGs for the outer and inner sensor trees occurred in December 2019 and November 2019, respectively.

Table 8. Linear temperature gradient results for Cell 606.

Temperature Gradient (°C/cm)				
	Cell 606 Inner (5-inch)		Cell 606 Outer (5-inch)	
Month	Negative	Positive	Negative	Positive
Jul-17	-0.38	0.74	-0.28	0.62
Aug-17	-0.50	0.74	-0.33	0.62
Sep-17	-0.37	0.64	-0.33	0.61
Oct-17	-0.34	0.55	-0.34	0.42
Nov-17	-0.43	0.52	-0.41	0.39
Dec-17	-0.47	0.33	-0.43	0.22
Jan-18	-0.49	0.61	-0.47	0.49
Feb-18	-0.47	0.72	-0.43	0.56
Mar-18	-0.47	0.91	-0.39	0.72

Temperature Gradient (°C/cm)				
	Cell 606 Inner (5-inch)		Cell 606 Outer (5-inch)	
Month	**Negative**	**Positive**	**Negative**	**Positive**
Apr-18	-0.47	1.06	-0.44	0.84
May-18	-0.53	1.12	-0.34	0.92
Jun-18	-0.40	1.04	-0.36	0.85
Jul-18	-0.40	0.99	-0.38	0.77
Aug-18	-0.35	0.93	-0.35	0.73
Sep-18	-0.48	0.71	-0.38	0.56
Oct-18	-0.39	0.68	-0.37	0.54
Nov-18	-0.47	0.55	-0.48	0.45
Dec-18	-0.43	0.54	-0.41	0.43
Jan-19	-0.56	0.56	-0.55	0.43
Feb-19	-0.47	0.61	-0.44	0.47
Mar-19	-0.46	0.98	-0.43	0.80
Apr-19	-0.33	1.17	-0.33	0.97
May-19	-0.45	1.17	-0.35	0.93
Jun-19	-0.41	1.04	-0.38	0.82
Jul-19	-0.64	1.03	-0.38	0.86
Aug-19	-0.45	0.99	-0.39	0.76
Sep-19	-0.56	1.25	-0.44	**1.59**
Oct-19	-0.80	0.68	-1.14	0.60
Nov-19	**-4.16**	**2.77**	-1.41	0.45
Dec-19	-1.40	0.51	**-1.56**	0.36
Jan-20	-0.49	0.38	-0.48	0.32
Feb-20	-0.58	0.94	-0.59	0.71
Mar-20	-0.35	0.95	-0.34	0.75
Apr-20	-0.36	0.96	-0.38	0.76
May-20	-0.45	0.92	-0.44	0.73
Jun-20	-0.54	0.90	-0.40	0.77

*Data collection started July 7th, 2017

3.1.3 Frequency Distribution of Linear Temperature Gradients

In order to determine the common LTG ranges, the frequency distributions of the LTGs were plotted for each cell, as shown in Figure 3-22~~Figure 3-22~~. The LTG ranges and the corresponding frequencies were plotted in this figure. The frequency distributions of Cells

139 and 239 did not show a significant difference. In Cell 239, the trends between the two sensor trees were similar, with the exception that the outer sensor tree had a higher number of frequencies for an LTG range of -0.5 to -0.25 °C/cm than the inner one. The Cell 239 inner sensor tree and Cell 139 provided very similar LTGs. The maximum frequency for Cell 139 and the inner tree in Cell 239 occurred in the LTG range of -0.15 to 0 °C/cm. The maximum frequency for the outer sensor tree in Cell 239 occurred in the range of -0.5 and -0.25 °C/cm. Cell 705 and 805 have similar trends, with the maximum for both cells occurring between -0.15 and 0 °C/cm. The trends of the LTGs measured at the inner and outer trees of Cell 606 were also the same, with the maximum frequency occurring between -0.15 and 0 °C/cm.

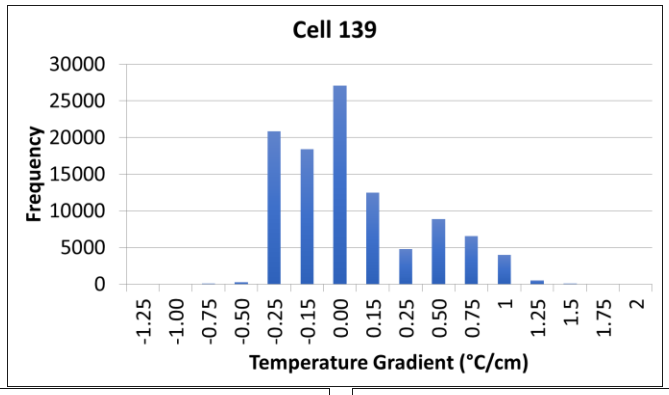

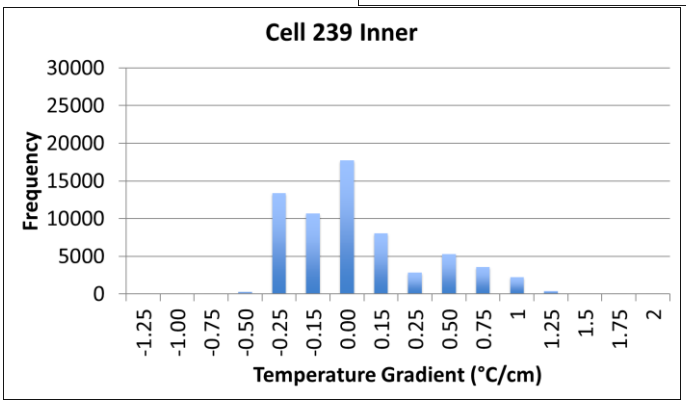

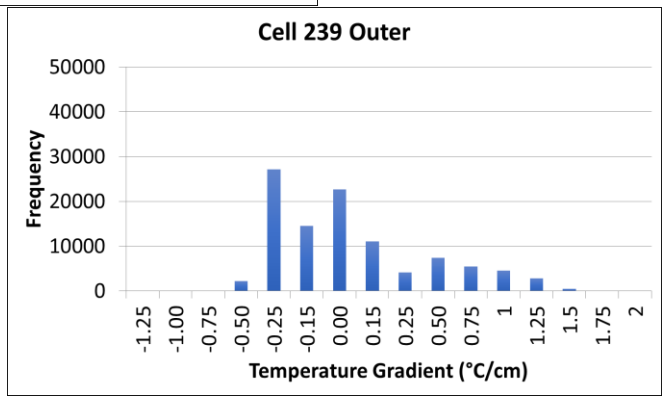

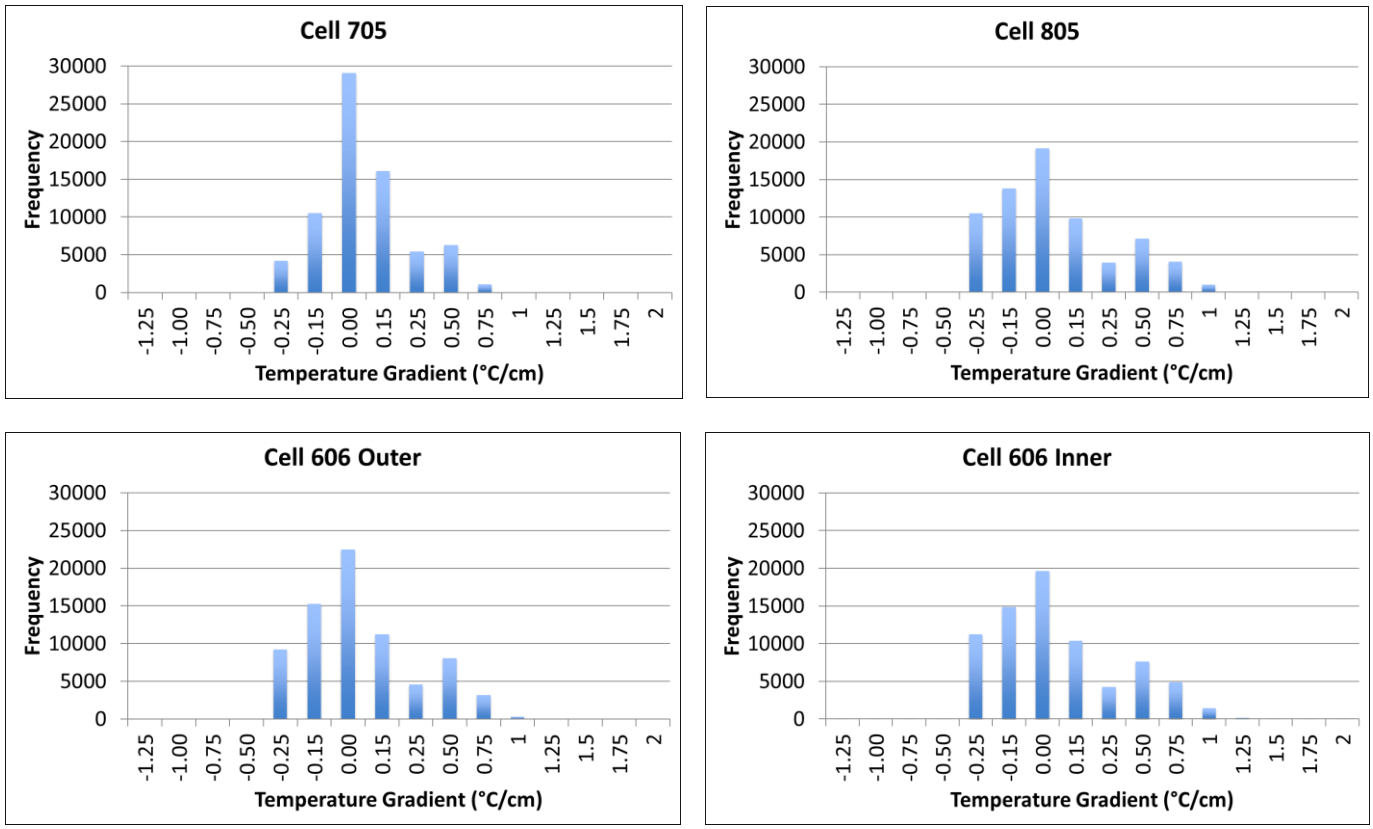

Figure 3-22. Frequency distributions of the linear temperature gradient for various cells.

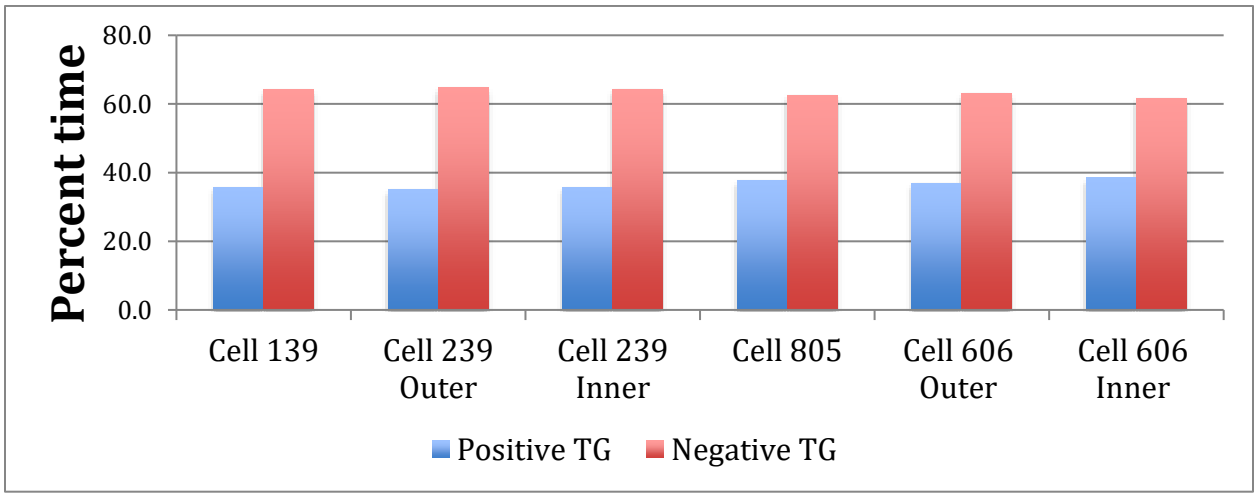

Figure 3-23. Percent times of positive and negative LTGs.

Figure 3-23~~Figure 3-23~~ shows the percent time that the LTG was positive and negative. Overall, the percent time that the LTG was positive or negative was consistent between the

cells. It appeared that all the cells experienced negative temperature gradients for more than 60 percent time.

3.2 Environmental Strain

Vibrating wire sensors were installed in all the cells to measure the environmental strain that occurs in the slabs and to investigate the trends of this strain with respect to fiber dosage and pavement design features. A photograph of a vibrating sensor is shown in Figure 3-24~~Figure 3-24~~. The raw data from this type of sensor are converted to estimate the environmental strain that is exerted on the concrete as a result of the change in the moisture state, temperature and temperature gradient, freezing of underlying layers, and joint locking. MnDOT has an established procedure for converting the raw vibrating wire data into a meaningful strain. One of the important steps in the vibrating wire data analysis procedure is to determine the initial strain value, which corresponds to the first reading when the concrete has hardened sufficiently to fully engage the sensor, and the temperature difference between the nearby top and bottom temperature sensors is approximately '0'. The initial strain value serves as the baseline value for subsequent readings. In order to determine the above-mentioned initial strain value, temperatures at the top and bottom of the slab and the raw frequency data are plotted together. An example of such plots is provided in Figure 3-25~~Figure 3-25~~; these plots are related to one of the vibrating sensors of Cell 139 (Sensor 1, longitudinal direction). Using these plots, the time of the first 0-temperature gradient is determined, after the raw frequency data started proper cycling; the corresponding strain at this time is considered as the initial strain value. In Figure 3-25~~Figure 3-25~~, it can be seen that the initial strain value was achieved around 8:30 AM of July 18, 2017 (approximately 11 hours after the paving) when the temperature gradient was nearly 0.

Figure 3-24. Photograph of a vibrating wire sensor.

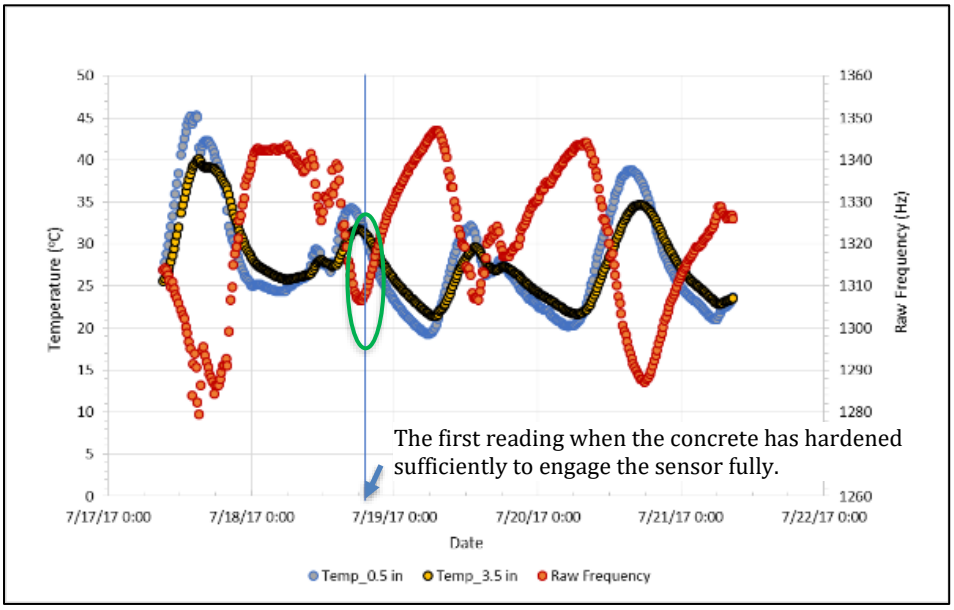

Figure 3-25. Temperature vs. raw frequency, Cell 139, Sensor 1.

3.2.1 Cells 139 and 239

In Cell 139, four vibrating wire sensors were installed, two in the longitudinal direction and two in transverse directions, all at the bottom of the slab, at a depth of 2.5 inches (a half-inch from the bottom of the concrete). Figure 3-26~~Figure 3-26~~ shows the environmental

strains measured by the four sensors; sensor data is available until July 2019. Three out of four sensors showed a similar trend, while the fourth sensor, which was in the transverse direction, showed a completely different and higher negative (tensile) strain compared to the other three. The less variation between the two sensors in the transverse direction and one longitudinal direction may be attributed to the small panel size and somewhat similar boundary conditions along three sides of each slab.

Nevertheless, all the sensors have provided negative strains, indicating that slabs were in a state of contraction. A close look at all these plots indicates that the negative strains in all the sensors sharply increased from July 18, 2017, until the mid of August 2017. Although the temperature declined during this period, the drying shrinkage could have played an influencing role. After that, the strains in all the sensors followed the temperature variation, recording higher tensile strain during the winter, and lower tensile strain at warm temperatures.

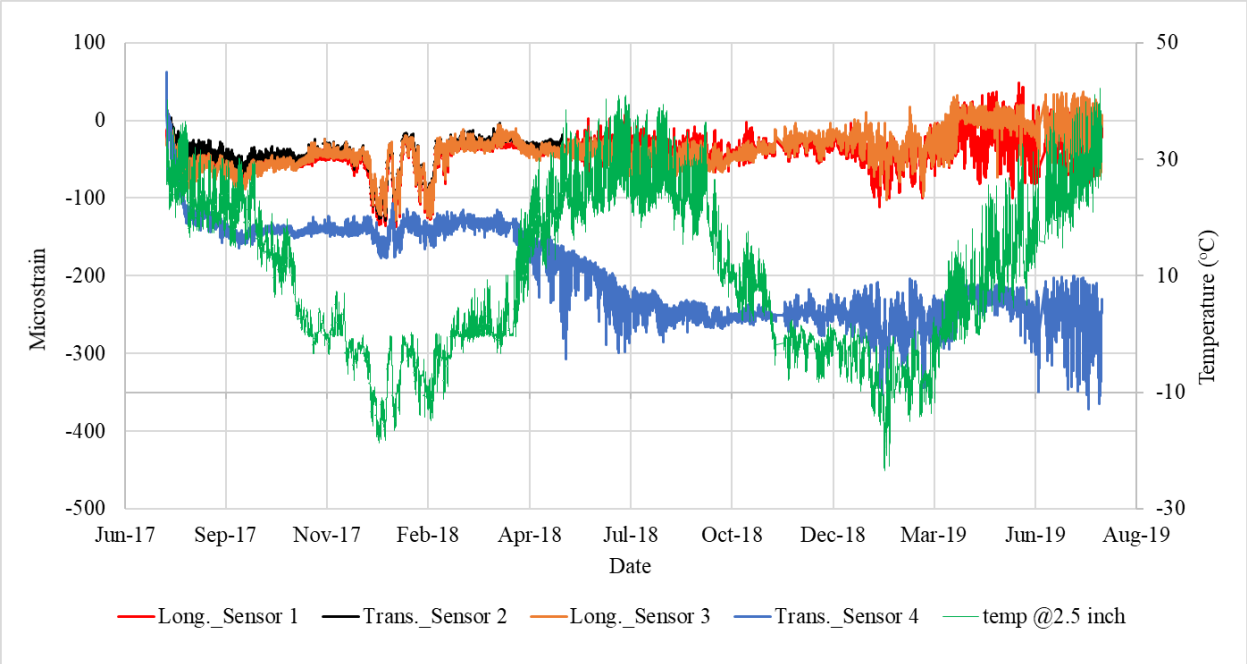

Figure 3-26. Environmental strains and slab temperature for Cell 139.

Figure 3-27~~Figure 3-27~~ shows plots for the environmental strains and temperature at the 3.5-inch depth of the slab for Cell 239. Like Cell 139, vibrating wire sensors were installed only at the bottom of the slab because of the thickness limitation. As can be seen in Figure 3-27~~Figure 3-27~~, the strains varied with the seasonal temperature and also experienced a sharp increase in negative strain until the mid of August 2017. The strain measured during the winter was relatively high, in general. Sensor 7, which was placed along the longitudinal direction shown a higher amount of strains than the other three sensors in the cell. The overall trend of the strains measured in Cell 239 was similar to what was observed in Sensor 4 of Cell 139, indicating an increase in the strain values with the age of the pavement. Compared to the sensors in the transverse directions, the sensors in the longitudinal direction experienced greater strains. The difference in magnitude of the environmental strains in both Cells 139 and 239 was not large.

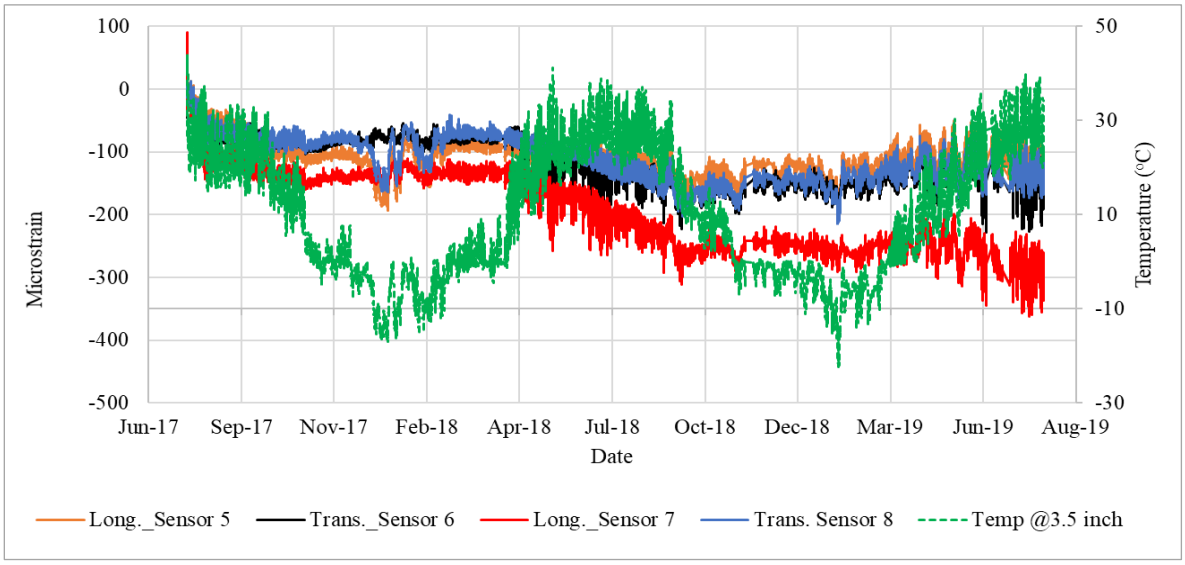

Figure 3-27. Environmental strains and slab temperature for Cell 239.

3.2.2 Cells 705 and 805

In Cell 705, eight vibrating wire sensors were installed in two slabs, four in each slab. In each slab, sensors were installed in the longitudinal and transverse directions. The longitudinal sensors were located at the center of the slab, and the transverse sensors were

adjacent to the transverse joints, as shown in Figure 3-3~~Figure 3-3~~. Two sensors were installed at each location, one at the top and the other at the bottom of the slab, one-half-inch inside the concrete. Figure 3-28~~Figure 3-28~~ and Figure 3-29~~Figure 3-29~~ show the strains measured in the first slab and second slab, respectively. Like the other two cells discussed above, the sensors in this cell also showed a correlation with the seasonal temperature. In the first slab, it appeared that the sensors placed at the top of the slabs experienced more strains irrespective of their location, with all the sensors recording higher negative strain values in the cold temperatures. Two sensors (6 and 7) in the second slab recorded higher tensile strain compared to all the other six sensors in this cell. Sensor 6, which was placed at the bottom of the slab along the longitudinal direction, recorded high tensile strain from an early age, whereas Sensor 7 picked up the high strain since summer 2018. The strain measured in these two sensors ranged from 350 to 450 micro strain from September 2018 until August 2019, when the readings were collected for the last time.

Like Cell 705, a total of eight vibrating wire sensors were installed in Cell 805. All the sensors were installed at the center of the slabs, both near the top and bottom of the slab, half-inch inside the concrete. This report included the results of three sensors installed in the first slab. The results of the three sensors in Cell 805, as can be seen in Figure 3-30~~Figure 3-30~~, also showed a great correlation with the seasonal temperature variation. Sensor 1, which was placed in the transverse direction, recorded the highest strain, around 300 to 375 micro-strain during the winter (including the strain due to the shrinkage at during the initial period).

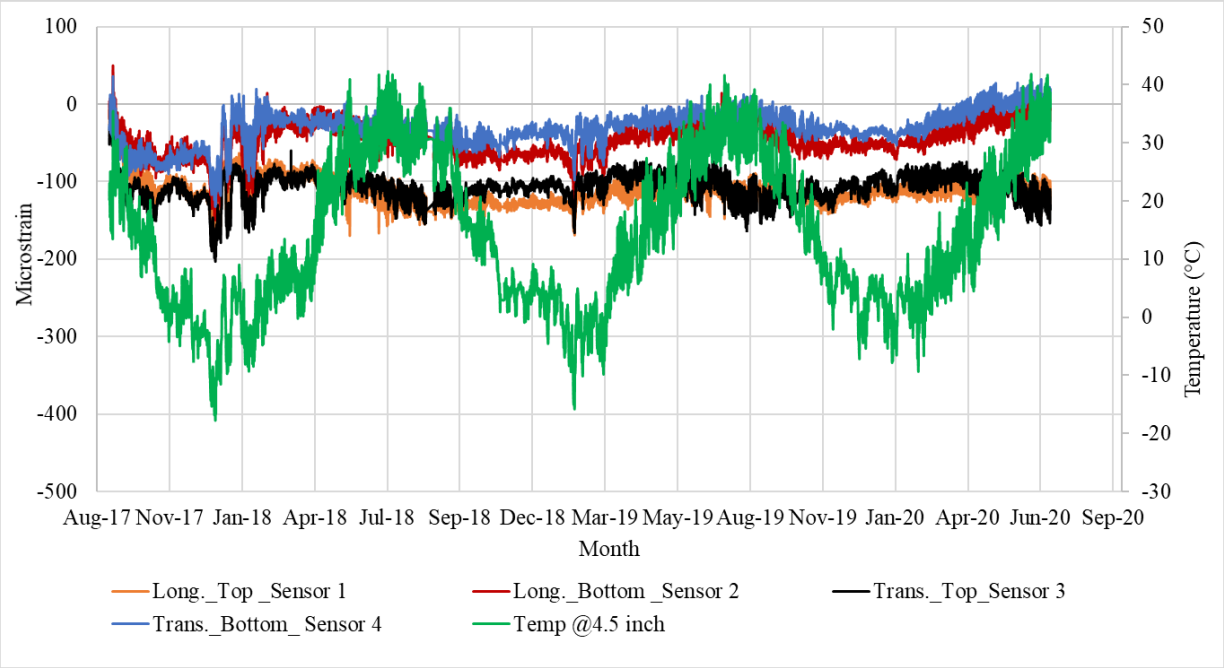

Figure 3-28. Environmental strains and slab temperature for Cell 705, first slab.

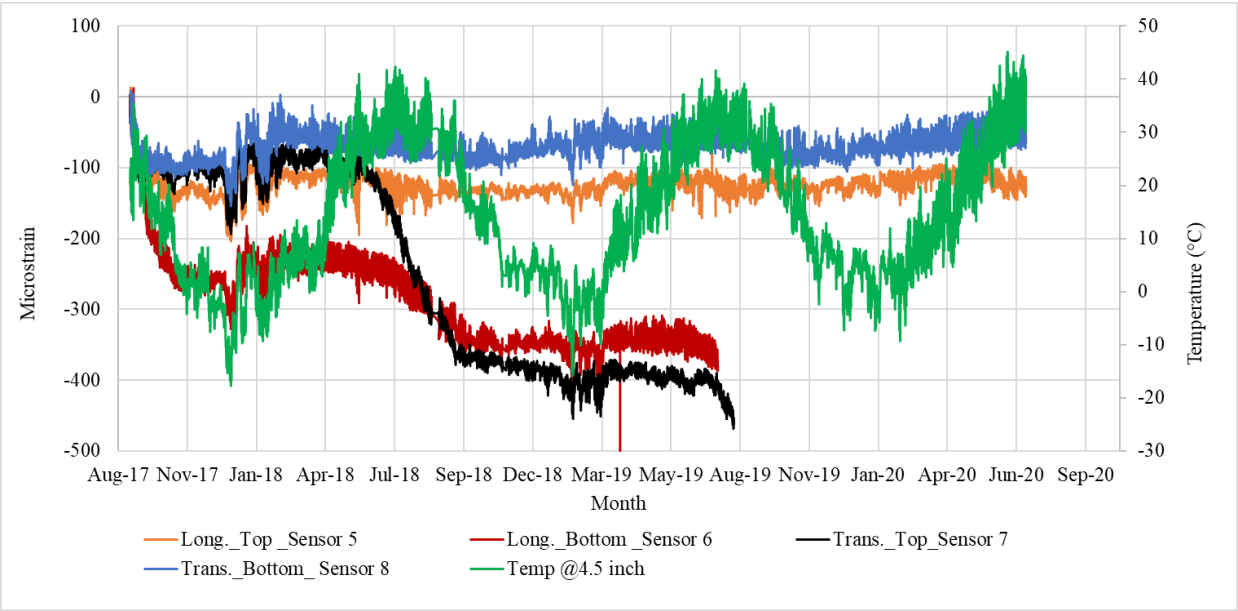

Figure 3-29. Environmental strains and slab temperature for Cell 705, second slab.

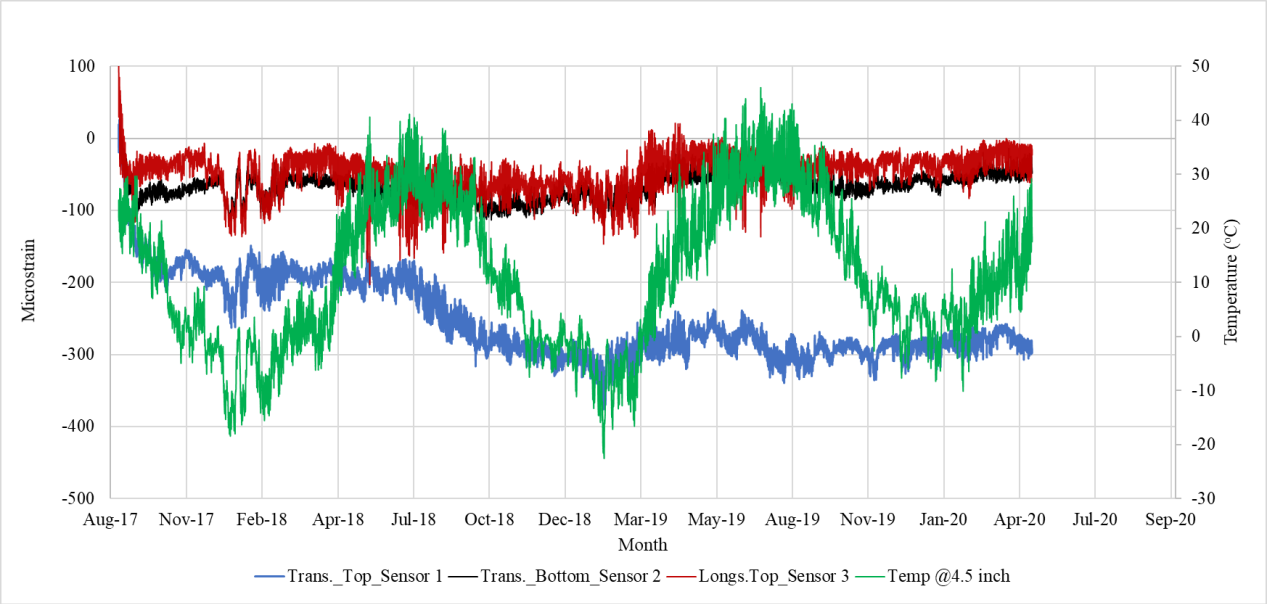

Figure 3-30. Environmental strains and slab temperature for Cell 805, first slab.

3.2.3 Cells 506 through 806

As previously mentioned, the vibrating wire and temperature data for the initial period are used to zero out the subsequent strain values. For these cells, some vibrating wire data for the first couple of weeks were not available. The vibration wire and temperature data for other cells were thereby studied, and their trends were used to populate the initial strain values for these cells. Figure 3-31~~Figure 3-31~~through Figure 3-34~~Figure 3-34~~ show the environmental strains calculated for these cells. Each of these cells has four sensors, two in the transverse direction in one slab and the other two in the longitudinal direction in another slab. The strains measured in all these cells are relatively low compared to the other four cells discussed above. The strain values have shown a correlation with the slab temperature, and values were high during the winter months as anticipated.

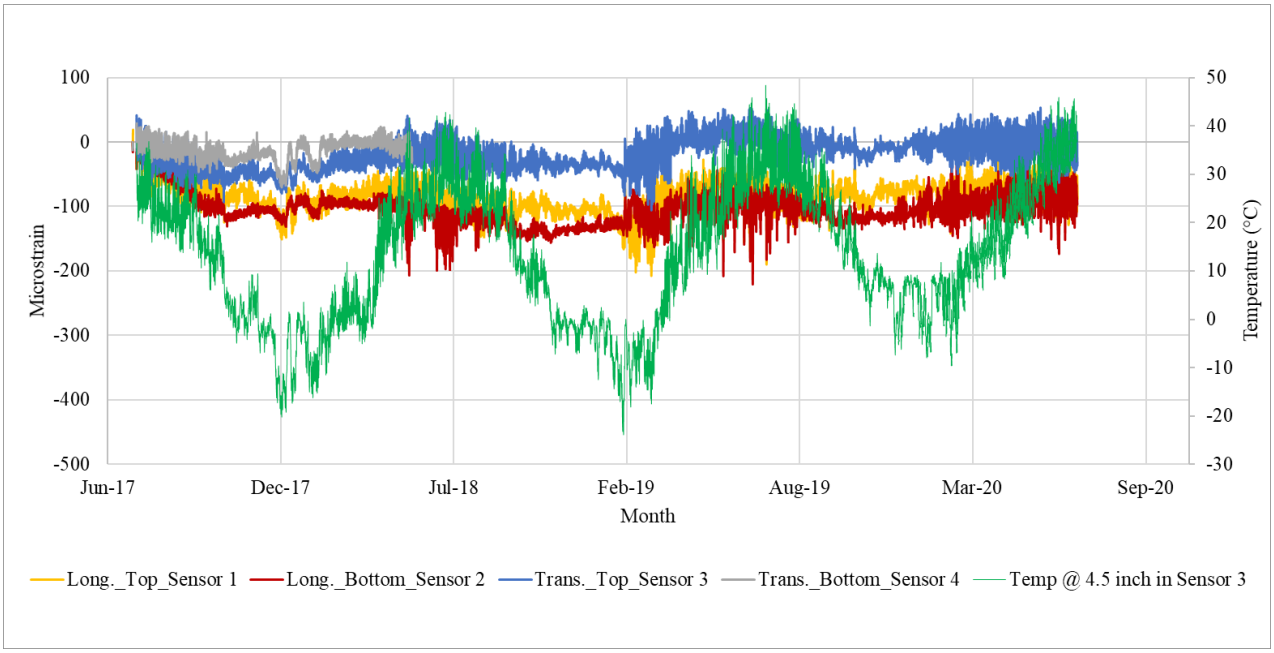

Figure 3-31. Environmental strains and slab temperature for Cell 506.

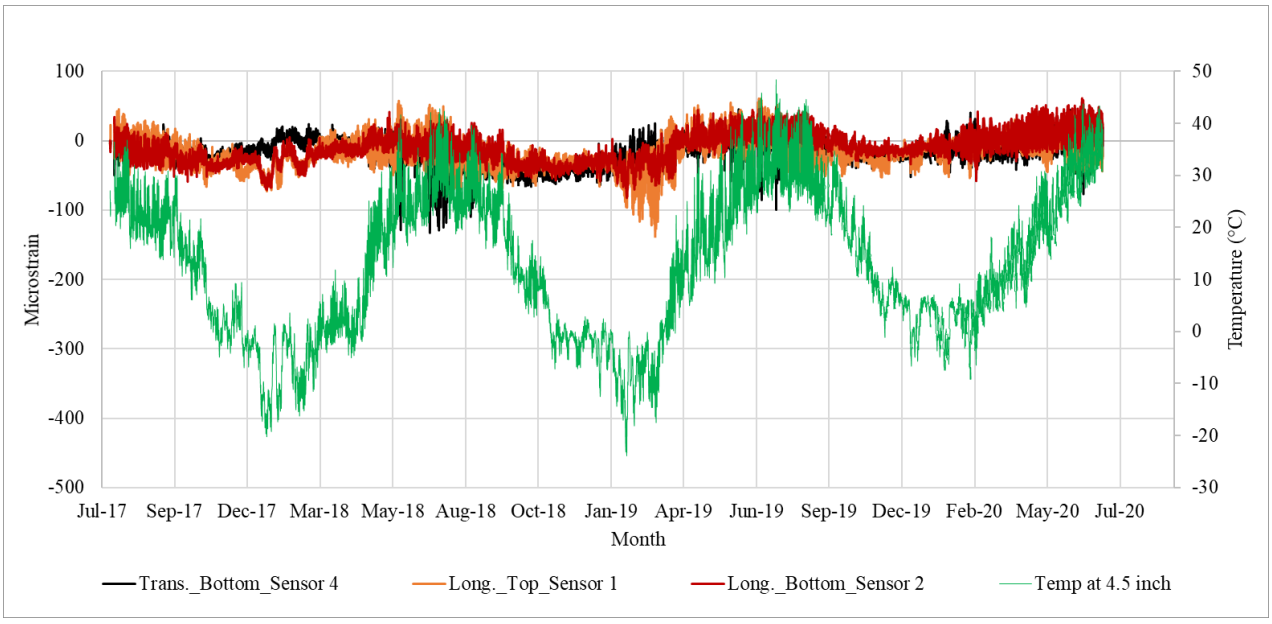

Figure 3-32. Environmental strains and slab temperature for Cell 606.

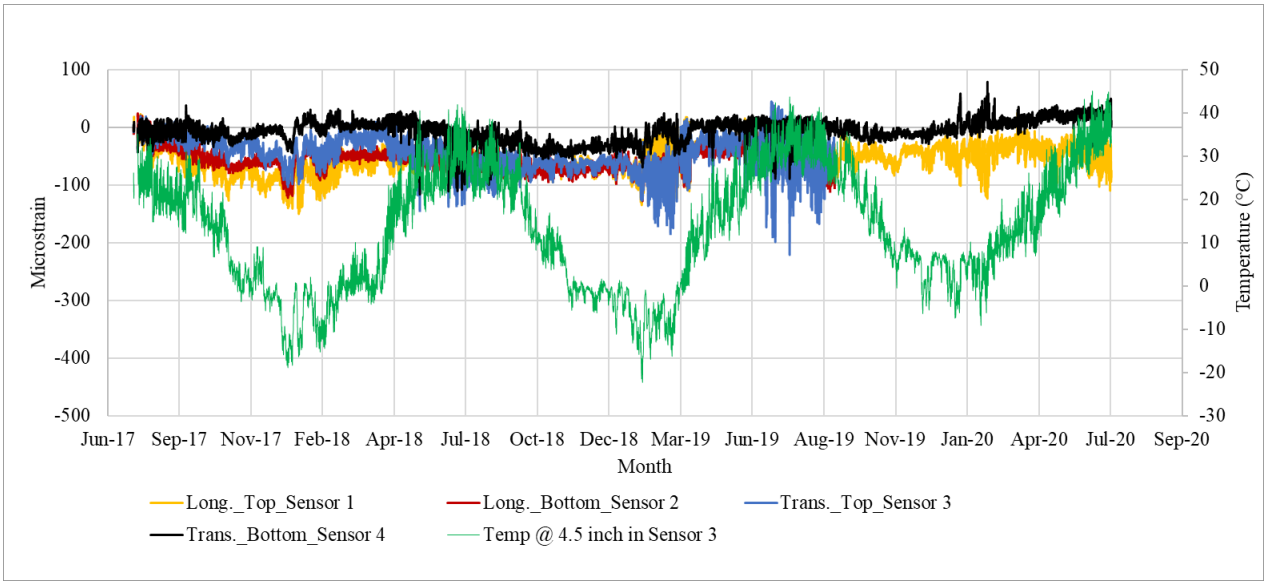

Figure 3-33. Environmental strains and slab temperature for Cell 706.

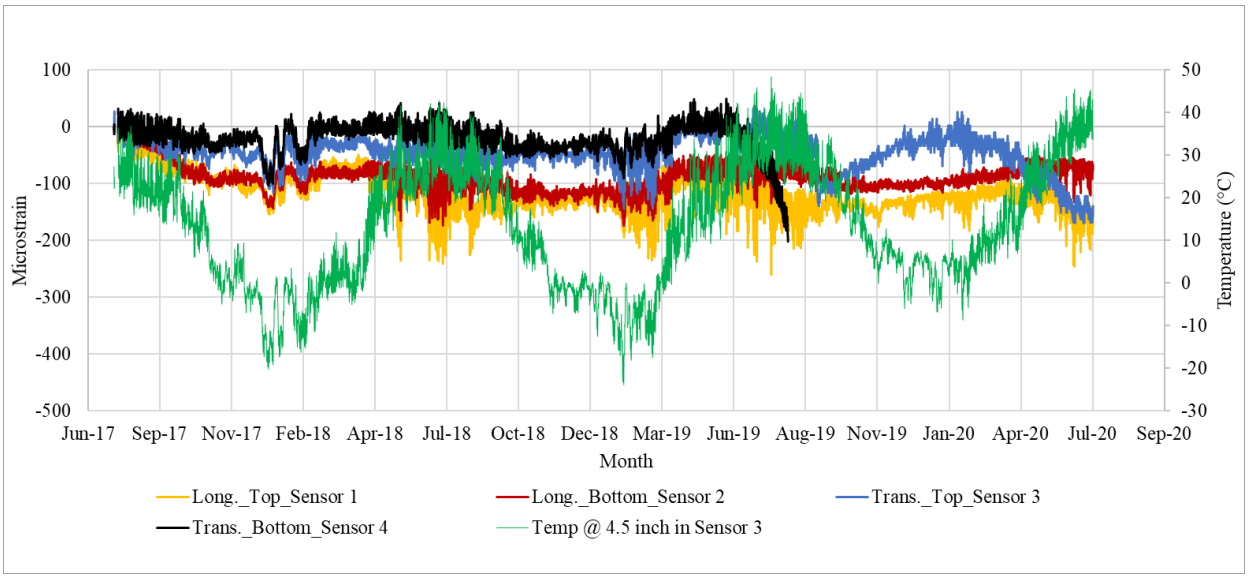

Figure 3-34. Environmental strains and slab temperature for Cell 806.

In summary, it can be stated that the strain recorded by almost all of the sensors were influenced by the seasonal temperature; strains were high during the winter and low in summer. Some sensors also have shown increasing strains with the age of the pavement,

probably because of the fatiguing of the slabs and damage accumulation in the overall structure. Strains in ultra-thin (3-and 4-inch thick) concrete pavements were relatively higher than the thin concrete pavements (Cells 506-806). This may be because of more curling and warping effect. The difference in the strains between the sensors placed either in the transverse or longitudinal directions and the top and bottom of the slabs could not be clearly established from the data analyzed. A distinct influence of the fibers has not been observed from the data and the analysis presented in this report.

3.3 Dynamic Strain

Dynamic strain sensors record the dynamic strain in the slab when a vehicle, MnDOT's five-axle truck, in this case, passes over them. As the tire offset (distance of the wheel from the sensor) affect the readings, MnDOT's truck was run multiple times for each date of data collection. The raw data collected from the sensors are processed, and peaks, valleys, and baseline (Figure 3-35~~Figure 3-35~~) are determined using the MnDOT's Peak-Pick Program (Burnham and Tewfik, 2007) for each run. Figure 3-35~~Figure 3-35~~ is an example of the plots with the peaks and valleys noted. As the truck has five axles, each sensor documents five peaks and five valleys. MnDOT has provided such plots and excel spreadsheets with the values of peaks, baseline, and valleys to the research team. These plots and excel spreadsheets were used to determine the strain experienced by each sensor under each of the five axle loads. The difference between the peaks and baseline is considered as the strain. The maximum of five strain values from all the runs are compared with each other, and the greatest value of them is reported as the dynamic strain for the sensor in question for a specific test date.

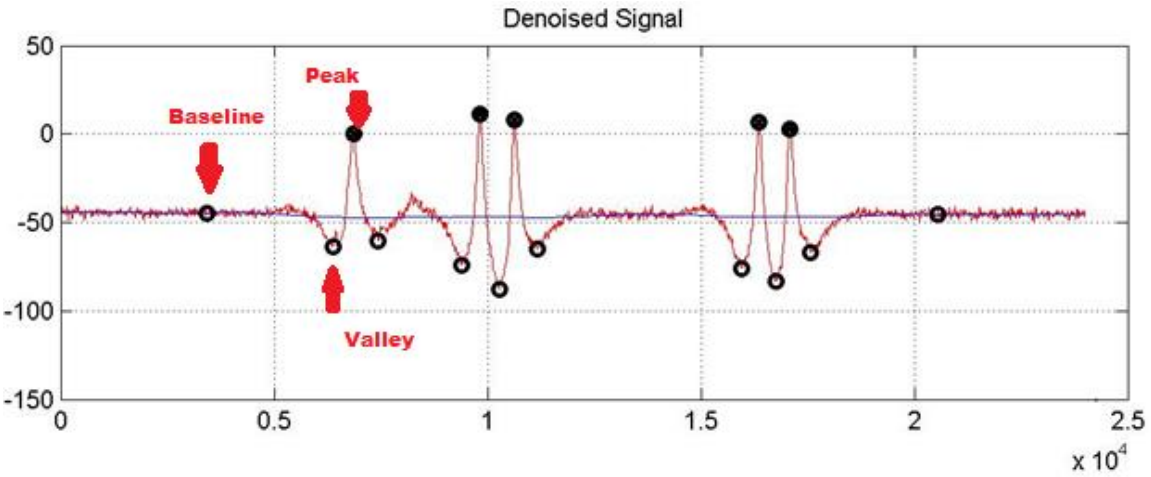

Figure 3-35. An example of a plot of strain due to the dynamic load exerted by the MnDOT truck.

Figure 3-36~~Figure 3-36~~ shows the dynamic strains recorded by the sensors in longitudinal and transverse directions for Cells 139 and 239. Some strain values are missing at multiple dates because of the malfunction of some sensors, also no data were collected for these two cells in 2020. Overall, the magnitude of the strains in Cell 139 was higher than that was recorded in Cell 239. One sensor in Cell 139, placed in the longitudinal direction, showed that the magnitude of the strain increased with time. Other sensors did not show any trend. Figure 3-37~~Figure 3-37~~ shows the comparison of dynamic strains between Cells 705 and 805. Compared to Cells 139 and 239, Cells 705 and 805 experienced far lower strains. The strain measured in 2020 was almost double of the previous reading. The strains recorded in the Cell 705 and 805 did not show a significant difference, with slightly higher strain recorded for Cell 705 for some dates.

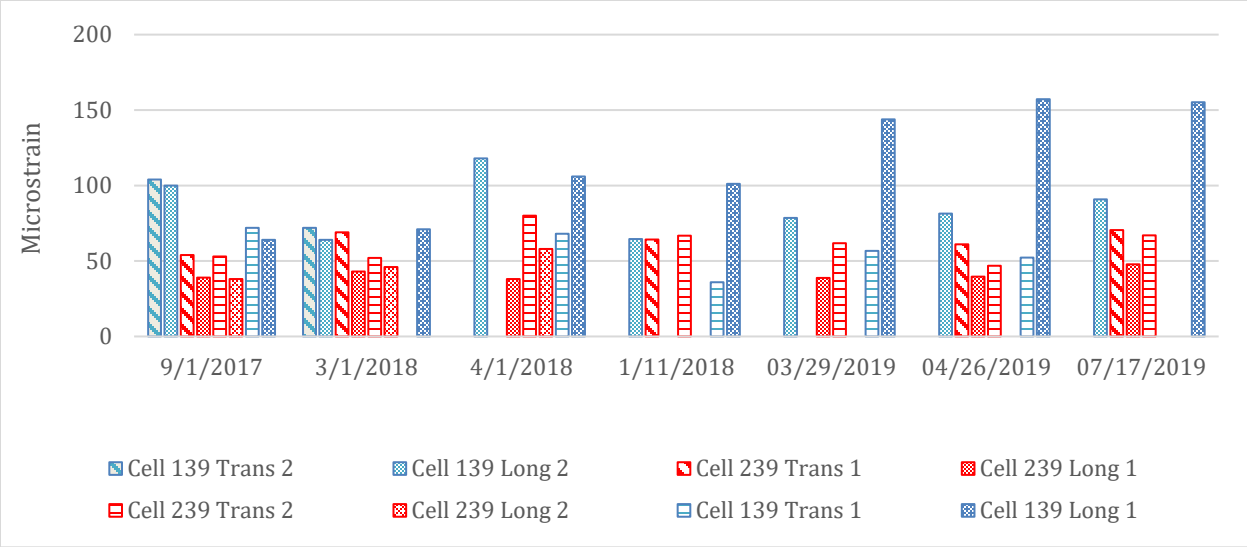

Figure 3-36. Dynamic strains recorded in Cells 139 and 239.

Cells 506, 606, 706, and 806 are the cells that compare the performance for different dosages of fibers. Dynamic sensors in these cells were laid along with the transverse directions only. The magnitudes of the dynamic strains in these cells are comparable. Data collected in 2020 shows that Cell 506 recorded slightly higher strain value compared other cells.

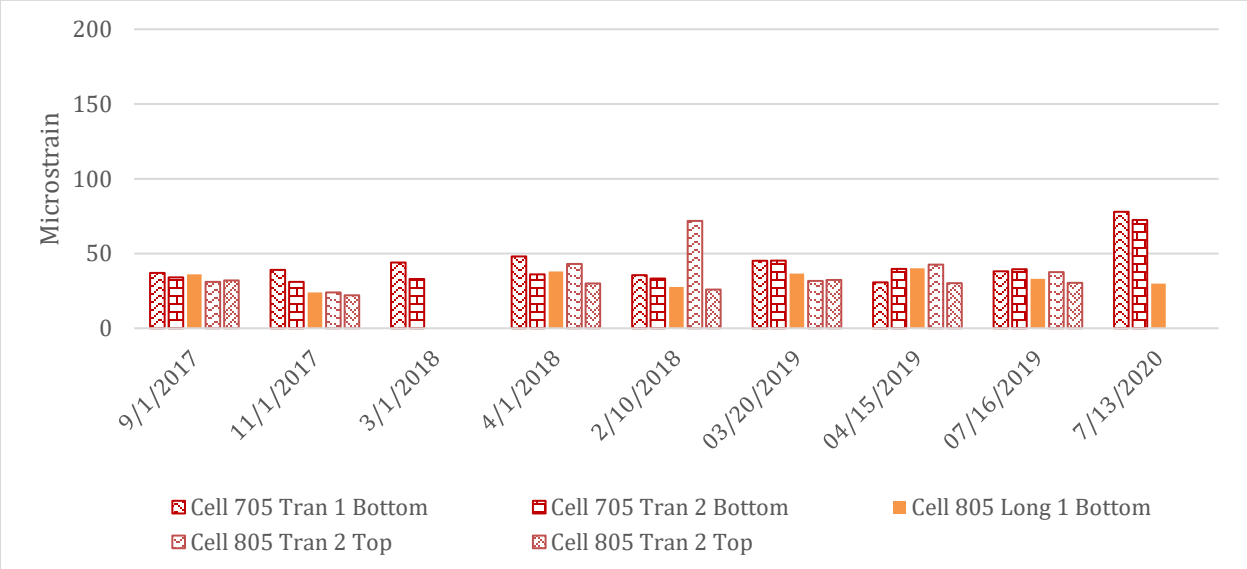

Figure 3-37. Dynamic strains recorded in Cells 705 and 805.

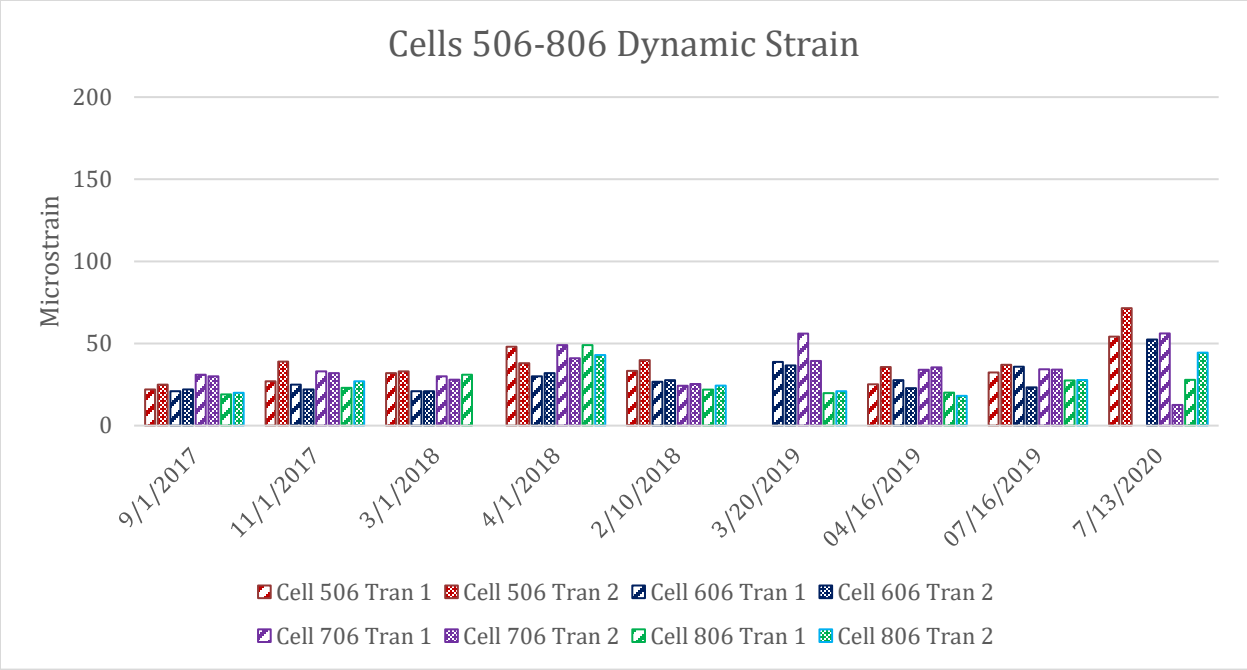

Figure 3-38. Dynamic strains recorded in Cells 506 through 806.

3.4 Joint Movement

A new type of joint opening sensor (spring-loaded potentiometer) was installed in MnROAD 2017 FRC research cells. A sketch and two photographs of such a joint opening sensor are provided in Figure 3-39~~Figure 3-39~~. The goal of using this type of sensor is to track joint movement constantly throughout the year rather than manually measuring at certain time intervals. Figure 3-40 shows a plot of relative joint opening recorded by a joint opening sensor in Cell 506. The first joint opening reading was used to zero the subsequent joint opening readings. In this figure, there are two jumps in joint movement data, one in August of 2017 and the other one around October 2017. The first jump in Figure 3-41~~Figure 3-41~~ is assumed to be related to the joint deployment. When the joints deploy, the sensor readings are supposed to show a jump. Some sensors didn't record any jump. The reason for this is either the deployment occurred before collecting the initial reading, the jump was not recognizable because of a minimal crack width change, or joint did not deploy at all. The second jump is related to the reinstallation of the sensor.

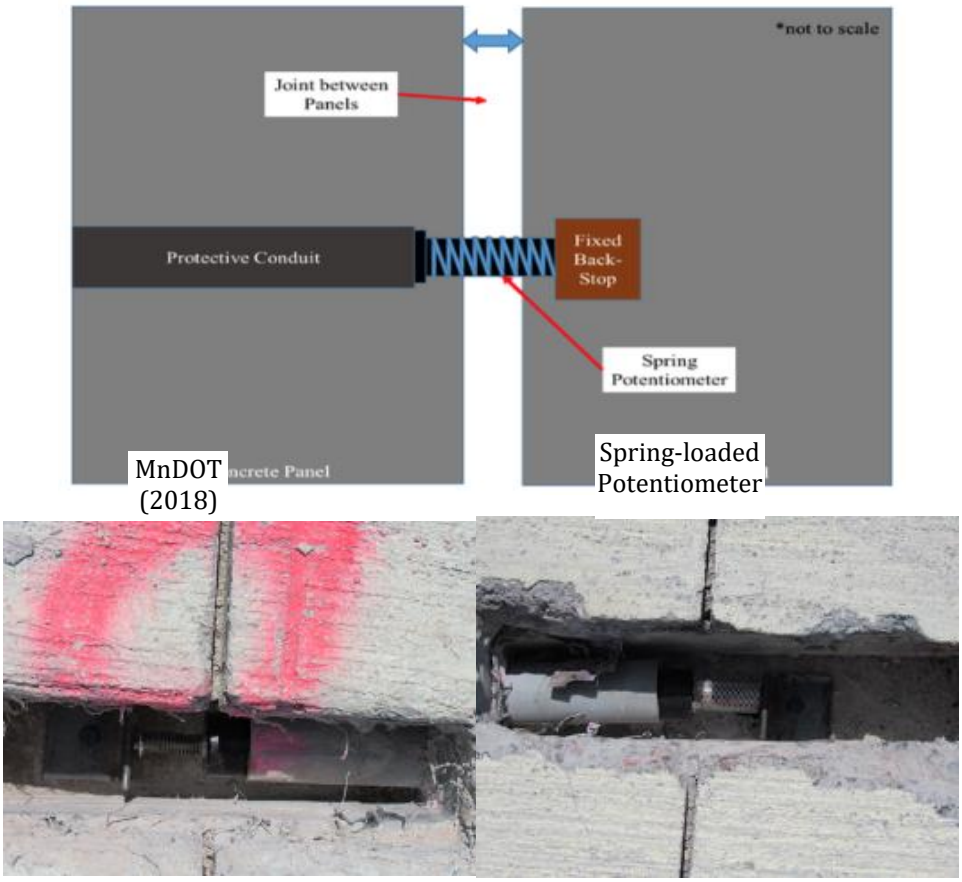

Figure 3-39. Sketch and photographs of joint opening sensors before installation of protective covering.

Most of the joint opening sensors had to be re-installed after their first installation; protection for the sensor was applied during the reinstallation time. For the sensors that were reinstalled, data were adjusted to neutralize the re-installation related jump (Figure 3-41~~Figure 3-41~~). For the sensor data presented in Figure 3-41~~Figure 3-41~~, it can also be seen that some erroneous data was recorded for some duration between September 2018 through January 2019. Figure 3-42~~Figure 3-42~~ provides an example of joint movement readings collected by Sensor 3 of Cell 706; in this case, the joint in question probably did deploy before the collection of the first reading. This plot provides a good example of a relative joint opening with respect to the first reading. It can be seen that the joint opening was maximum during the winter months, after which the joint opening reduced with the temperature increase. Some sensor readings were discarded because of erroneous data, where the crack opening readings fluctuated significantly.

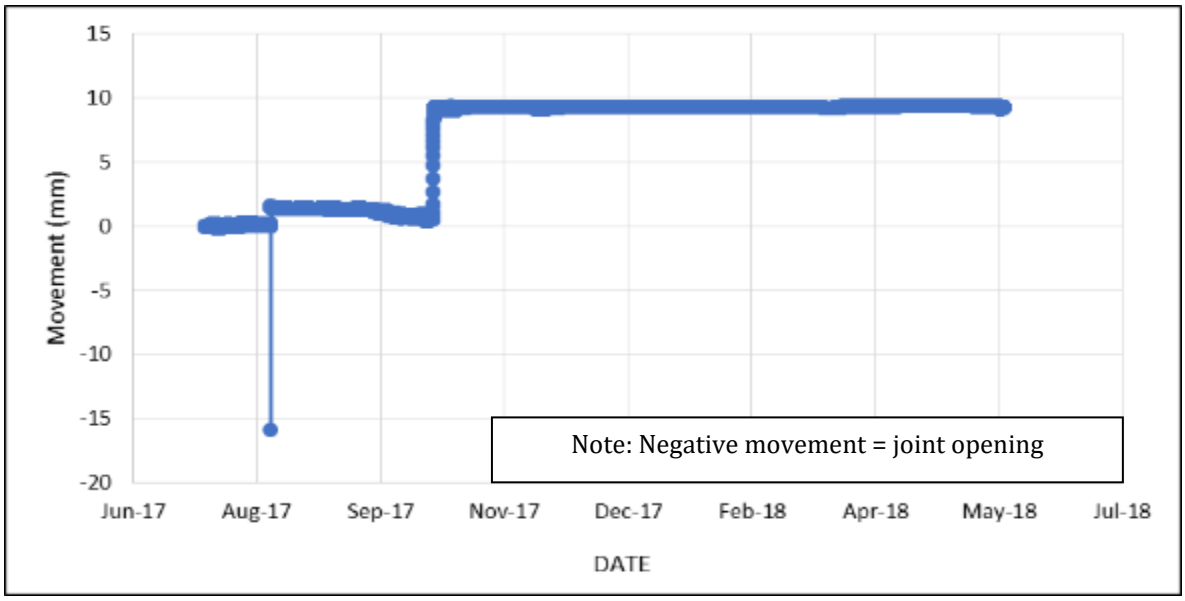

Figure 3-40. Joint movement recorded by Sensor 1 of Cell 506, before adjustment for re-installation was made.

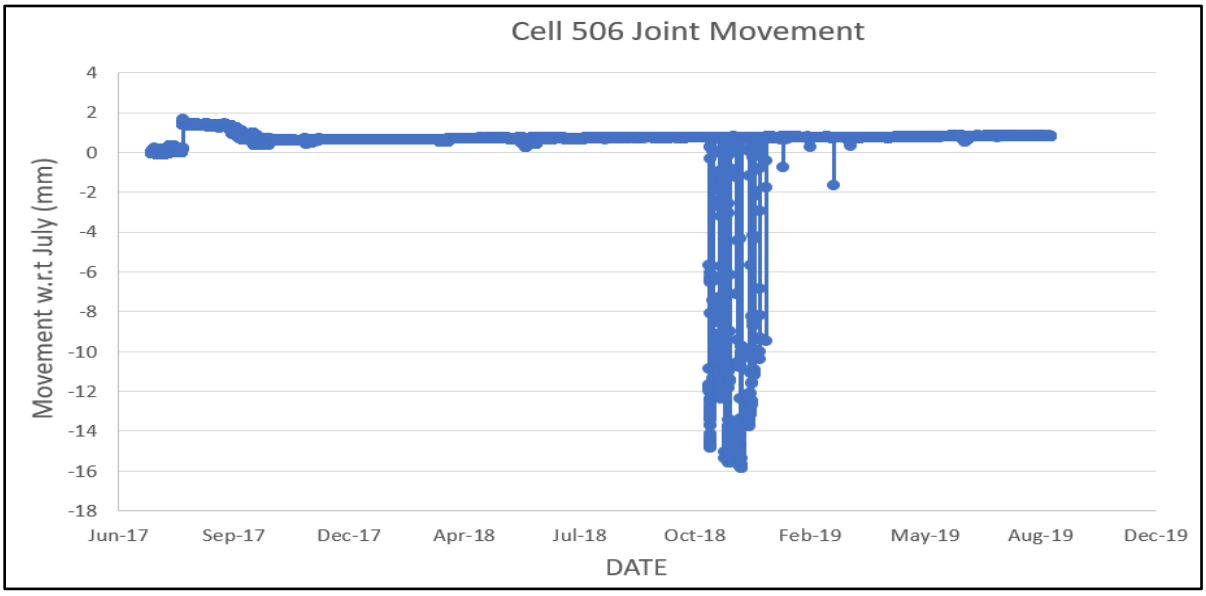

Figure 3-41. Joint movement recorded by Sensor 1 of Cell 506, after adjustment for re-installation was made. (Note- diff. scale in the y-axis)

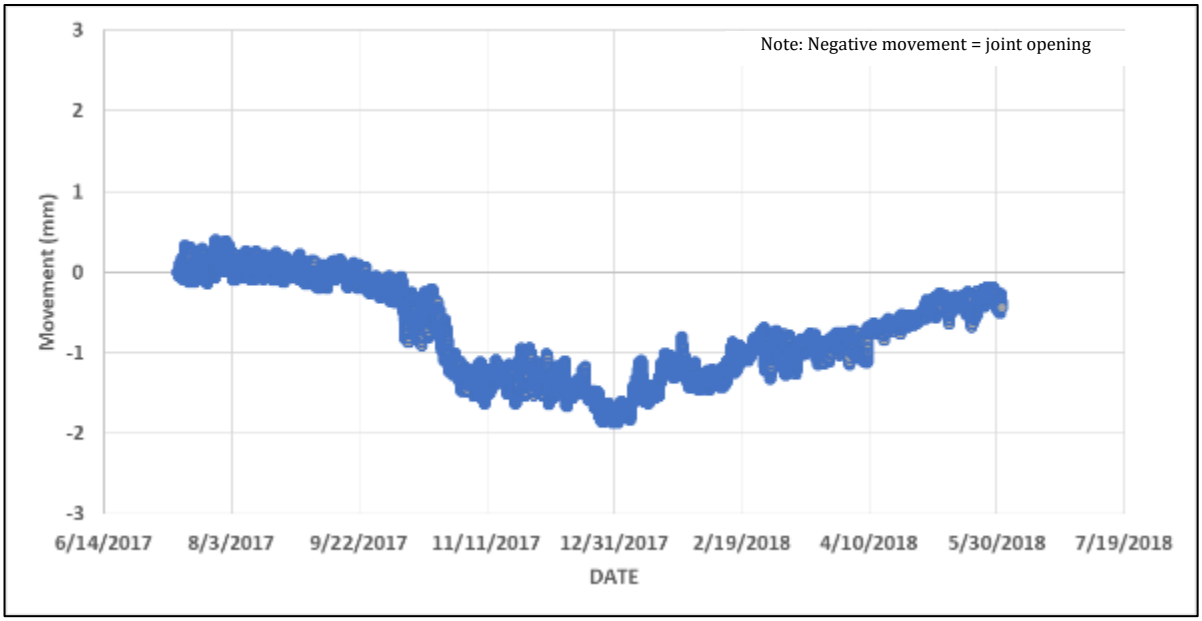

Figure 3-42. Movement recorded by Sensor 3 of Cell 706, no adjustment was required.

(Note diff. scale in y-axis)

APPENDIX B includes joint movement plots for all the cells. Because of the considerable variations in the data quality in some sensors, very convincing trends could not be achieved for all the cells, but the results of many sensors are reasonable. In order to investigate the seasonal variation of joint opening, the monthly average relative joint opening was calculated for each cell and plotted in Figure 3-43~~Figure 3-43~~ through Figure 3-50~~Figure 3-50~~. The averages for Cells 705 and 805 were zeroed with respect to September 2017, and all the other cells were zeroed with respect to July 2017. Cells 705 and 805 were zeroed using the later month because they were constructed later than the other cells. In Cell 139, two sensors did not show a great variation in the joint opening, but the Sensor 1 showed that the joint opening increased during the winter months compared to the first reading taken in July 2017. Based on the data, the joints of the Cell 239 (at least where the sensors were installed) remained relatively dormant for most of the year with slight expansion recorded by Sensor 3 in the winter months. Cells 705 and 805 had experienced the largest joint opening movement among all the eight cells and a difference in the jointg movements between these two cells is not apparent. While a few sensors installed in these two cells remained dormant, others showed significant movements and did not show a meaningful

correlation with seasonal temperature change. The cells are unbonded concrete overlays and have unwoven geotextile at the interface which might have influenced the slab movements. It may happen that some slabs are being migrated with the traffic load.

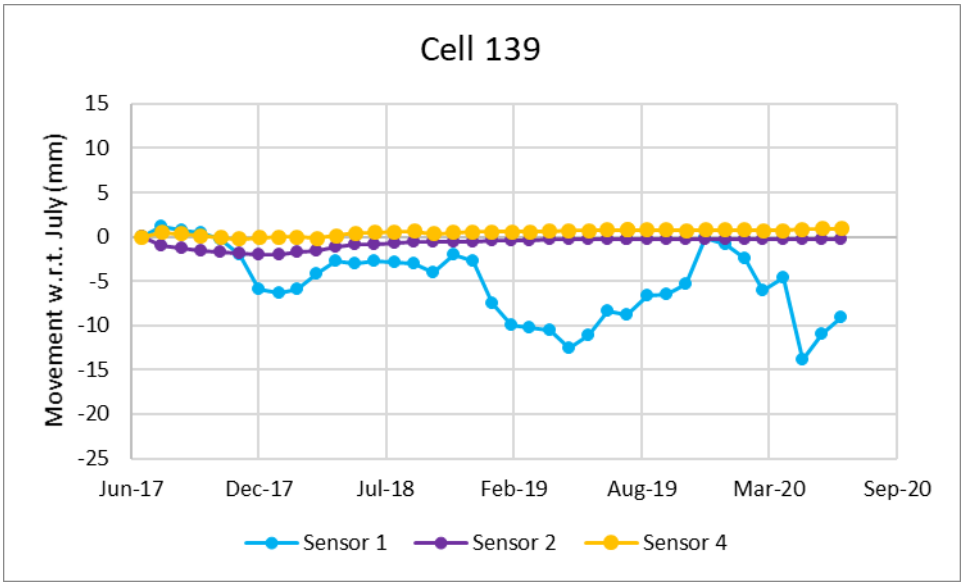

Figure 3-43. Monthly average relative joint movement for Cell 139.

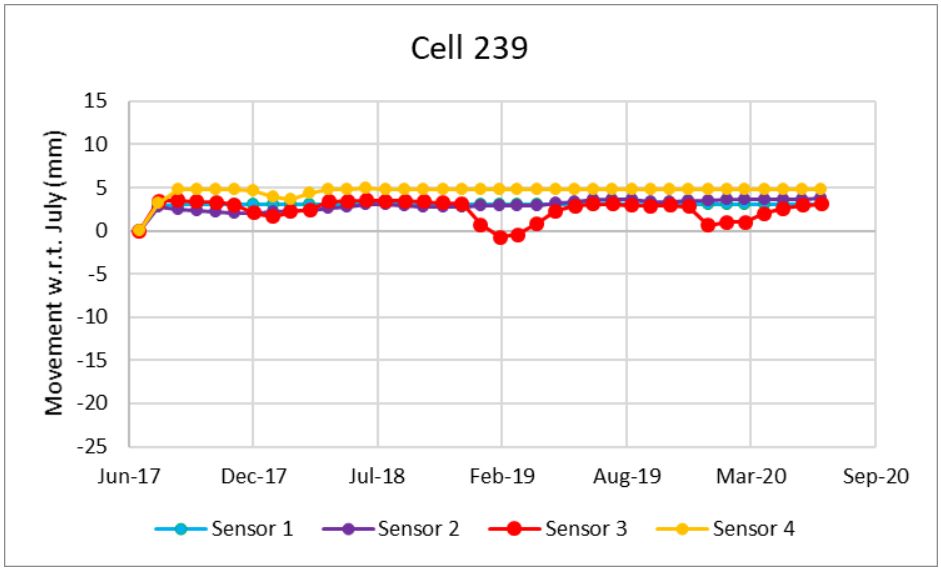

Figure 3-44. Monthly average relative joint movement for Cell 239.

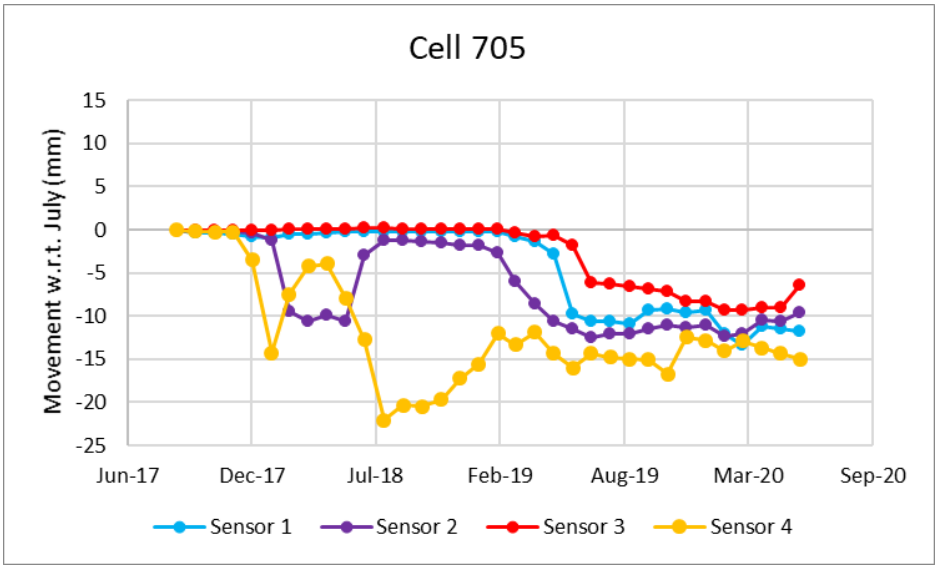

Figure 3-45. Monthly average relative joint movement for Cell 705.

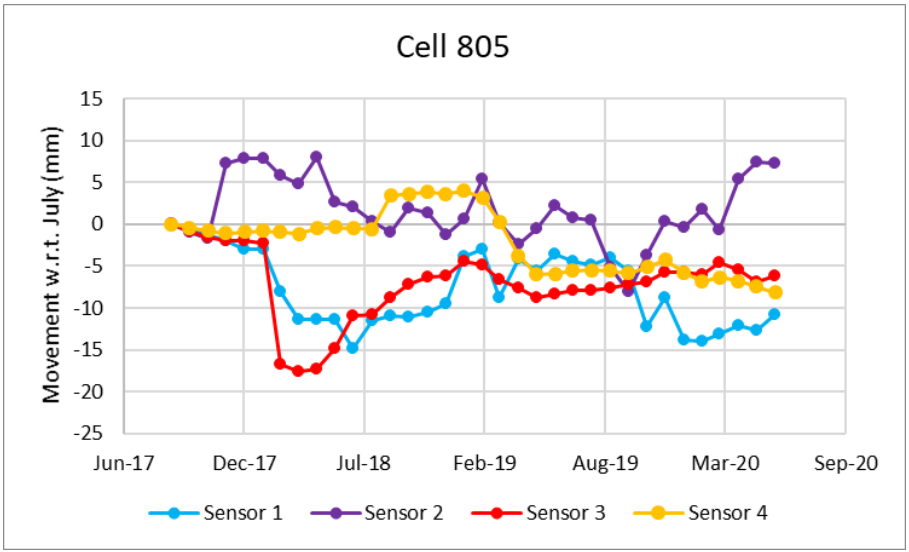

Figure 3-46. Monthly average relative joint movement for Cell 805.

Cell 506 does not contain fibers, and it was anticipated that larger joint openings would be observed in this cell compared to its counterparts (Cells 606 to 806). One sensor in this cell remained dormant throughout the three service years. Cell 606 contained 5 lbs./ cy fibers. Two sensors in this cell indicate that the joints did not close in summer once they opened in the first winter. The other sensor of Cell 606 shows joint opening in fall of 2019. Joints of Cells 706 and 806 showed movement after 2019-2020 winter.

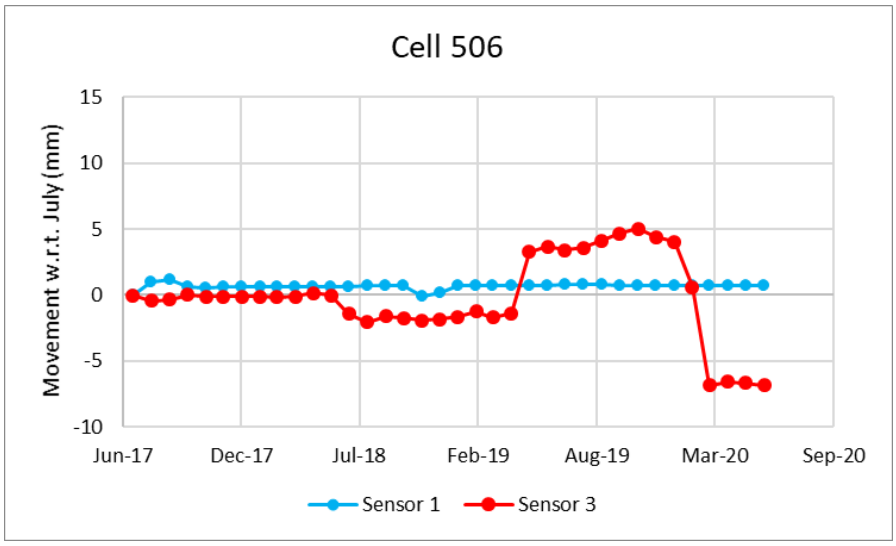

Figure 3-47. Monthly average relative joint movement for Cell 506.

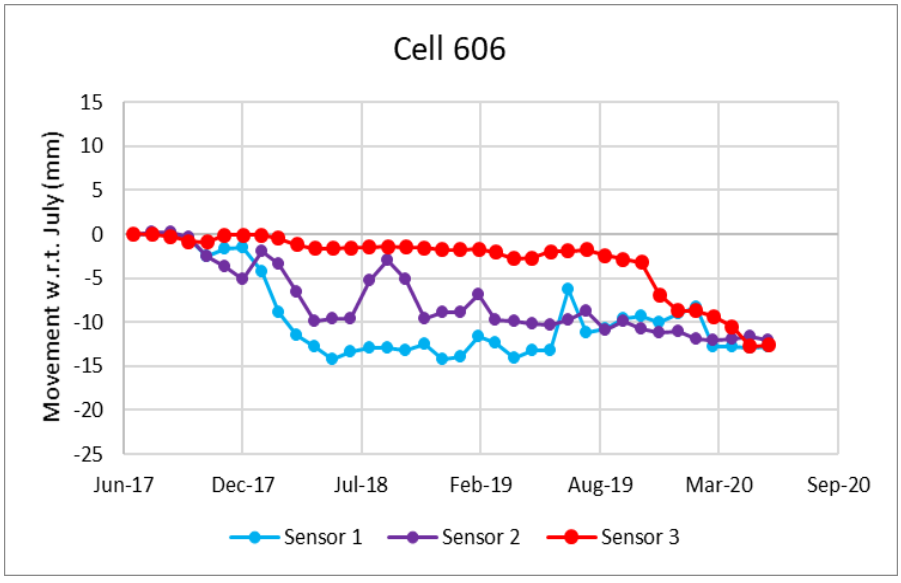

Figure 3-48. Monthly average relative joint movement for Cell 606.

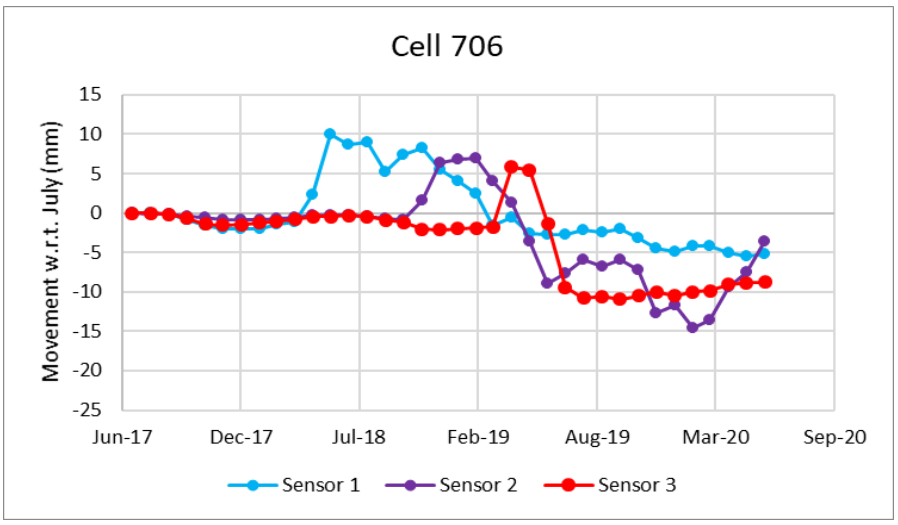

Figure 3-49. Monthly average relative joint movement for Cell 706.

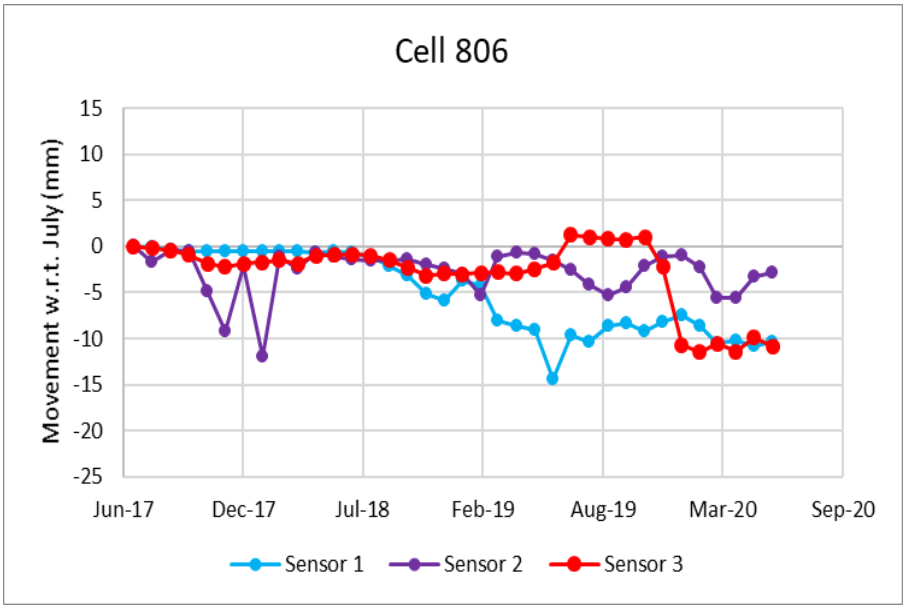

Figure 3-50. Monthly average relative joint movement for Cell 806.

4 JOINT PERFORMANCE

This section discusses the joint performance data. The results of the falling weight deflectometer (FWD) test conducted at selected transverse joints were used to determine the load transfer efficiency (LTE), differential displacement, and loaded-side displacement. The LTE is the ratio of the deflections at the unloaded side to the loaded side and expressed as a percentage. The differential displacement is the arithmetic difference between the loaded-side deflection and unloaded-side deflection.

4.1 Load Transfer Efficiency (LTE)

Figure 4-1~~Figure 4-1~~through Figure 4-16~~Figure 4-16~~ show the LTE of all the cells. The LTE data of the Cells 139 and 239 were comparable when the first test was conducted on September 6, 2017 and it ranged between 85 and 94%. The LTE of these two cells then continued to drop with the traffic load. The outside lane of both the cells, where traffic load is not applied, showed consistent higher LTE values than the inner lane, even though the Cell 139 experienced some LTE drops with age. In the year 2020, the Cell 139 inner lane showed more LTE when it was expected to be lesser than the previous years. The slab ID 23 showed the maximum LTE which is understandable because this slab was replaced by September 2018 and since then it has been performing better when compared to the other slabs of Cell 139 which were not replaced. Although, slab ID 7, 15 and 40 were not replaced. Hence their increase in LTE is not understood.

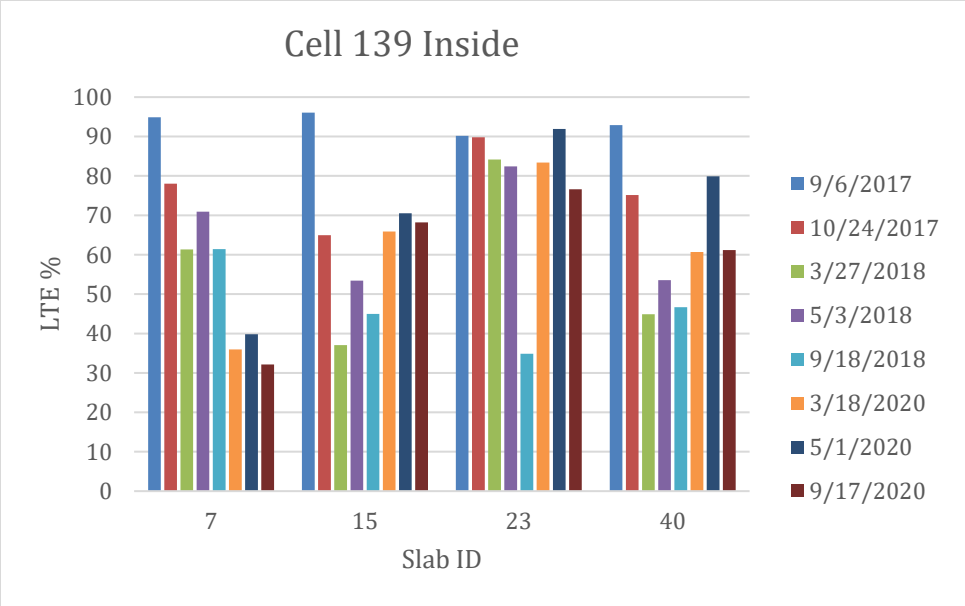

Figure 4-1. LTE of Cell 139 inside lane.

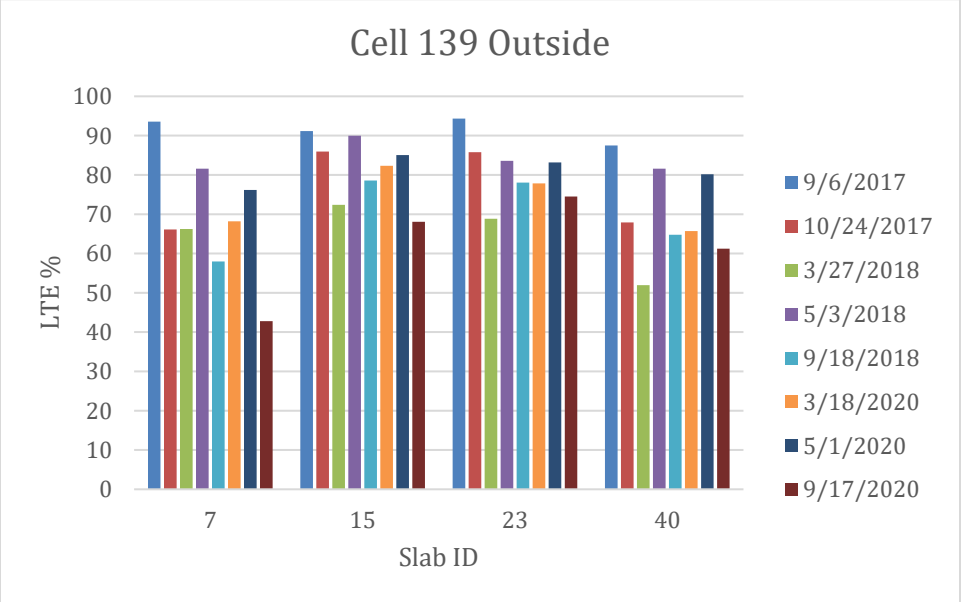

Figure 4-2. LTE of Cell 139 outside lane.

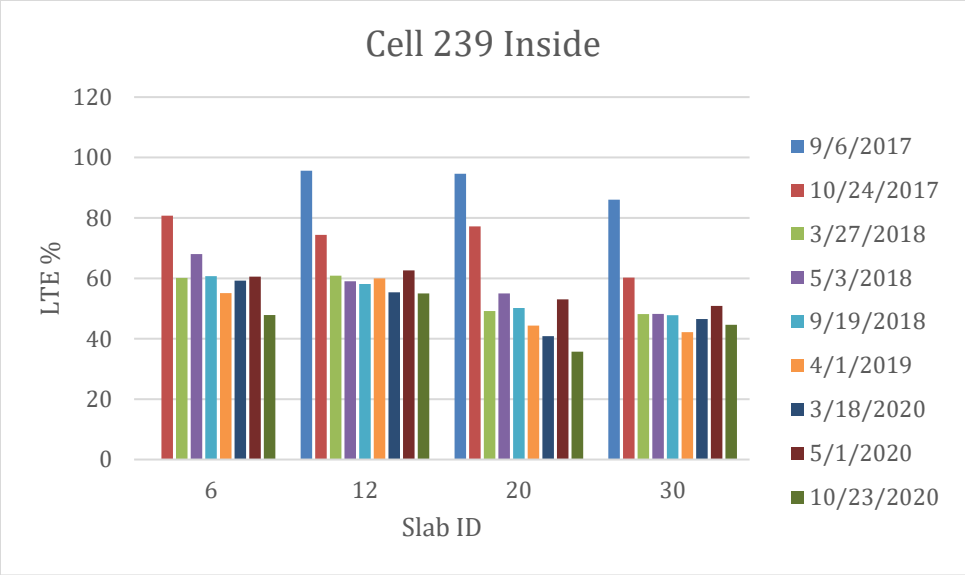

Figure 4-3. LTE of Cell 239 inside lane.

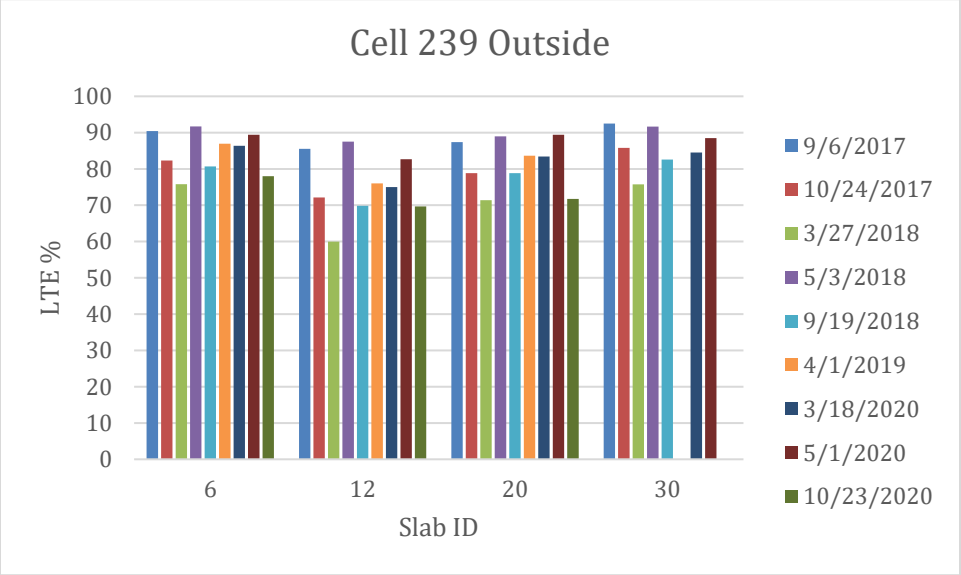

Figure 4-4. LTE of Cell 239 outside lane.

The wide joint opening of Cells 705 and 805, as discussed in Section 4.5, appeared to have influenced the LTE significantly. Contrary to the low faulting results, these two cells exhibited surprisingly very low LTE, at least in the joints considered in FWD testing. Based on the joint opening sensor data, some of the cracks were wider than 10 mm. The LTE of

concrete pavement at such wide joint opening is usually very low. The FWD test conducted during the April and June 2019 however shown some increase in the LTE in the driving lane of these two cells. The exact reason for this increase is not known; however, upon investigating the joint movement data, it was found that one joint movement sensor (Sensor 3) of Cell 506 (Figure 3-50~~Figure 3-50~~) detected significant joint contraction (~5mm) during April 2019. It might happen that the thawed water in the spring expanded slabs leading to joint contraction. One of the co-authors of this report, Mr. Tom Burnham, mentioned observing such joint contraction during spring at much lower temperatures than the recommended FWD testing cutoff limit of 75°F in the summer. The LTE for these cells again dramatically decreased in 2020. Some of the panels in Cells 705 and 805 were cracking up, possibly effecting the slab support condition near several joints. The driving lane of these two cells were completely replaced with a 5 inch thick Hot Mix Asphalt (HMA) layer on October 10, 2020.

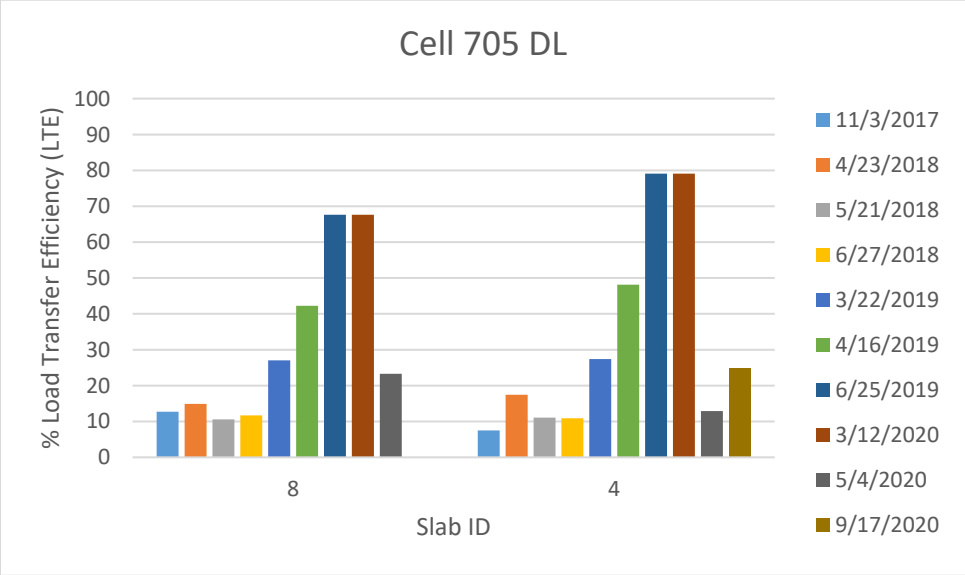

Figure 4-5. LTE of Cell 705 driving lane.

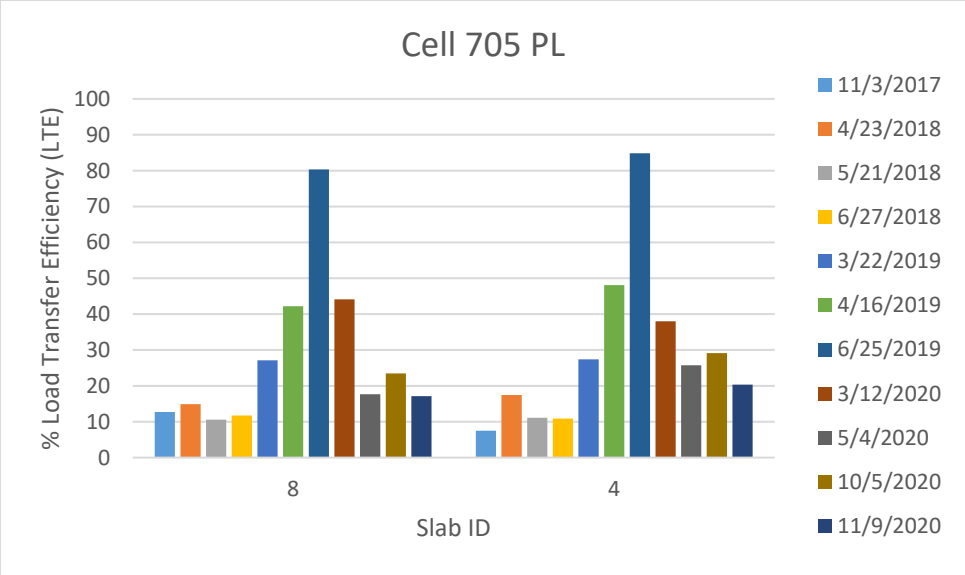

Figure 4-6. LTE of Cell 705 passing lane.

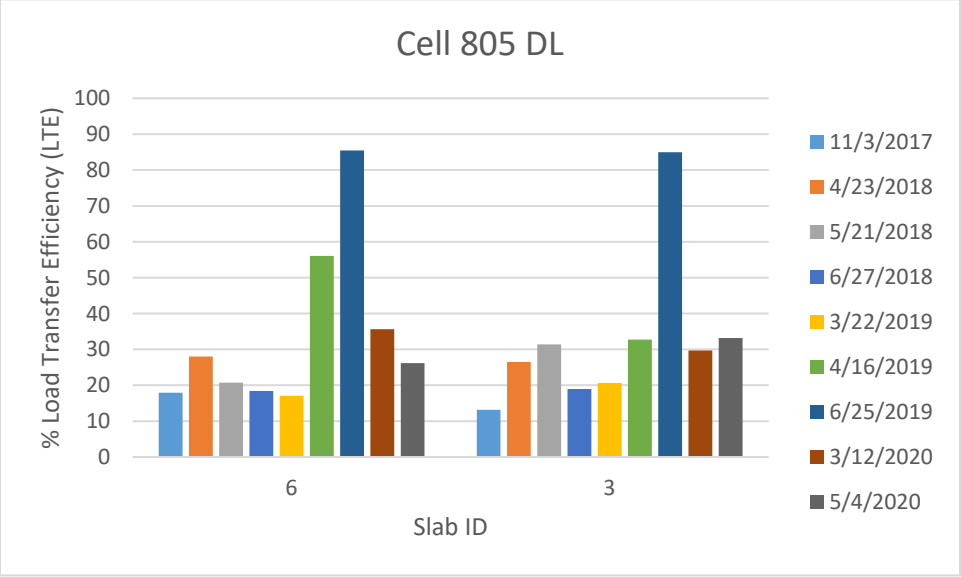

Figure 4-7. LTE of Cell 805 driving lane.

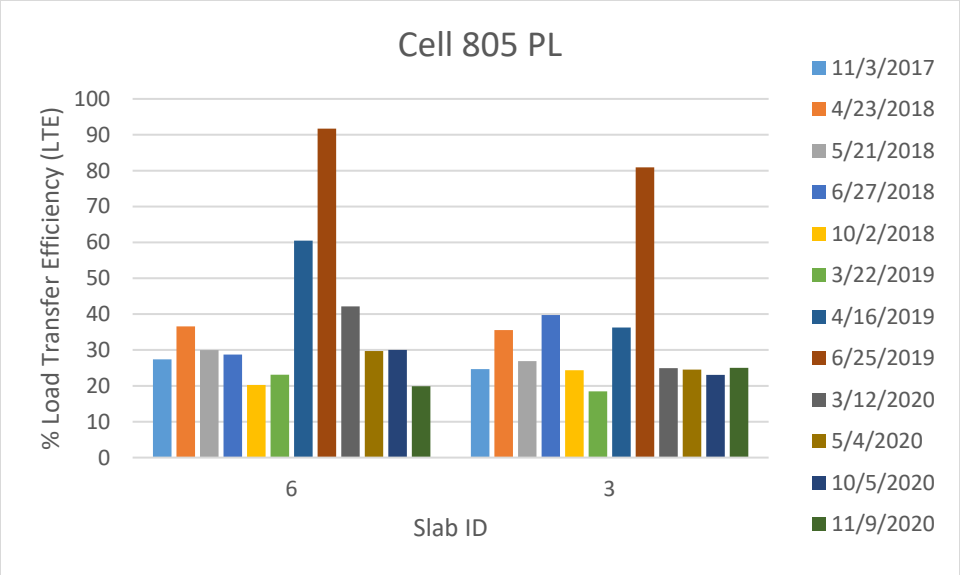

Figure 4-8. LTE of Cell 805 passing lane.

The LTE results of Cells 506 through 806 clearly reveals the contribution of structural fibers in keeping the LTE high. For Cell 506, even though the FWD test conducted on the driving lane in September 2017 showed a range of LTEs between 75 and 85%, the LTE afterwards significantly decreased overall. Surprisingly, the FWD tests conducted during the April 2019, shown relatively higher LTE at all the three joints considered. The reason for this may be similar to what happened in the Cells 705 and 805. The LTE in the passing lane of Cell 506 was always low, with a maximum of around 50%. The 2020 FWD test results show a considerable and steady decrease in LTE for Cell 506.

The LTE results of Cell 606, which is 6-inch thick, were at or above 90% when measured in September 2017, except one joint in the passing lane which always did show a low LTE (around 25 to 50%). The LTE for this cell had dropped significantly over the time. The FWD tests conducted on Cell 606 over the third year of service showed a gradual decrease in LTE for all the joints, which was expected. The LTE in the passing lane has also dropped significantly.

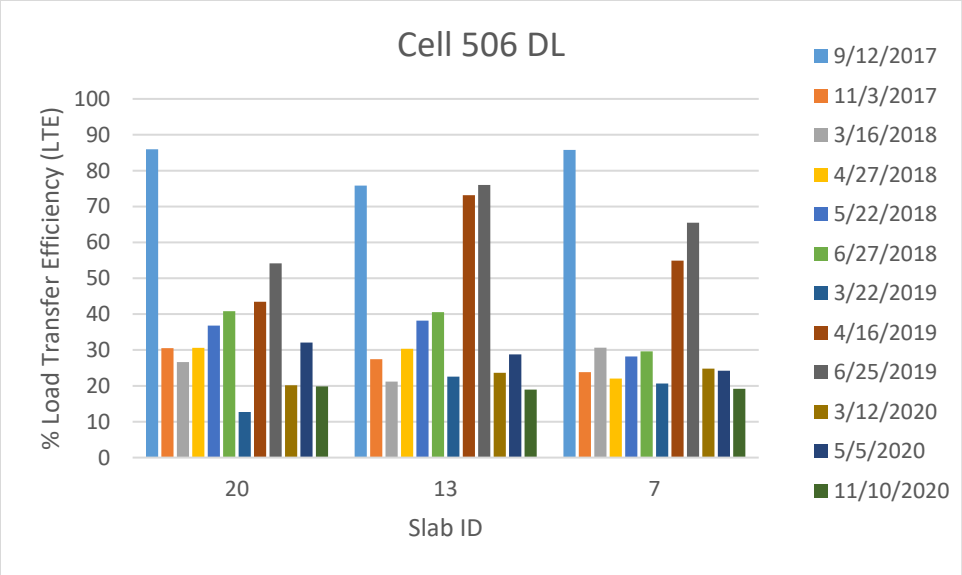

Figure 4-9. LTE of Cell 506 driving lane.

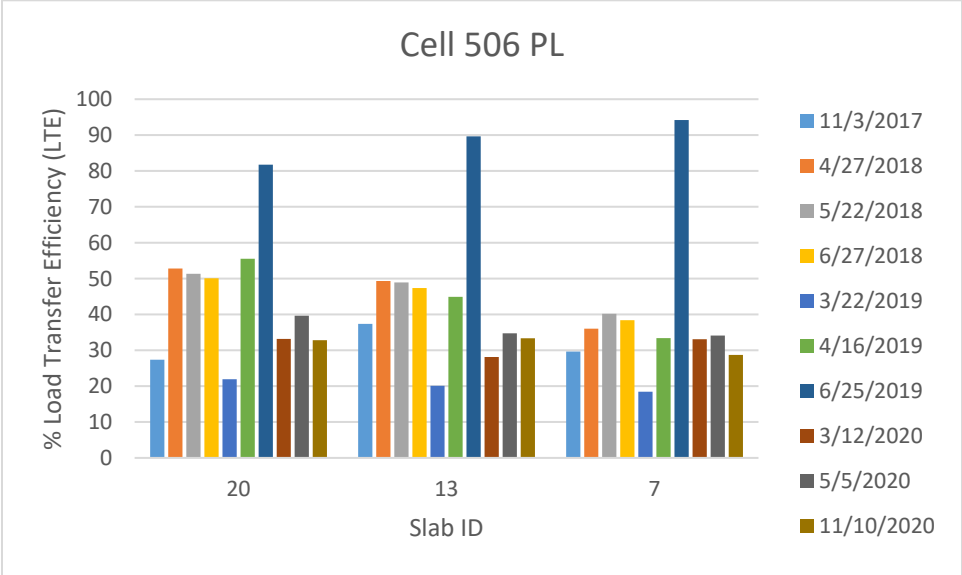

Figure 4-10. LTE of Cell 506 passing lane.

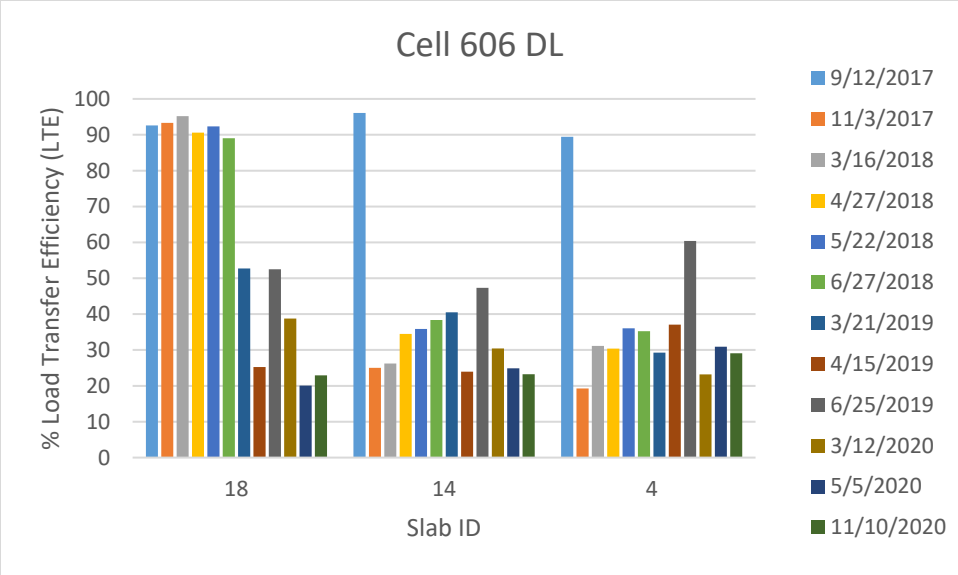

Figure 4-11. LTE of Cell 606 driving lane.

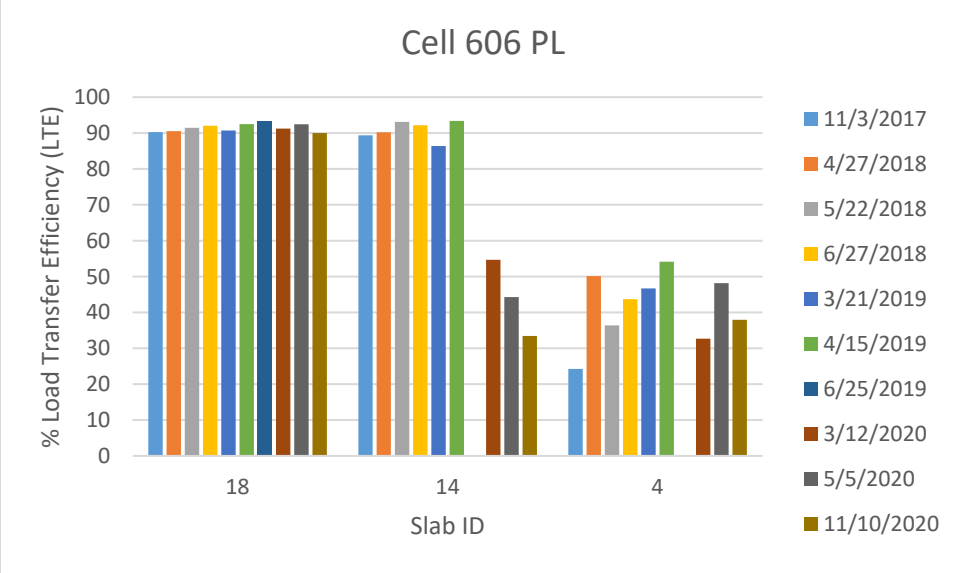

Figure 4-12. LTE of Cell 606 passing lane.

The LTE of Cell 706, which is 5-inch thick and contains 8 lbs./cy fibers, was initially high at three joints (at the driving lane) out of total of six joints measured. However, when measured at later dates, these joints exhibited 40 to 56% LTE.

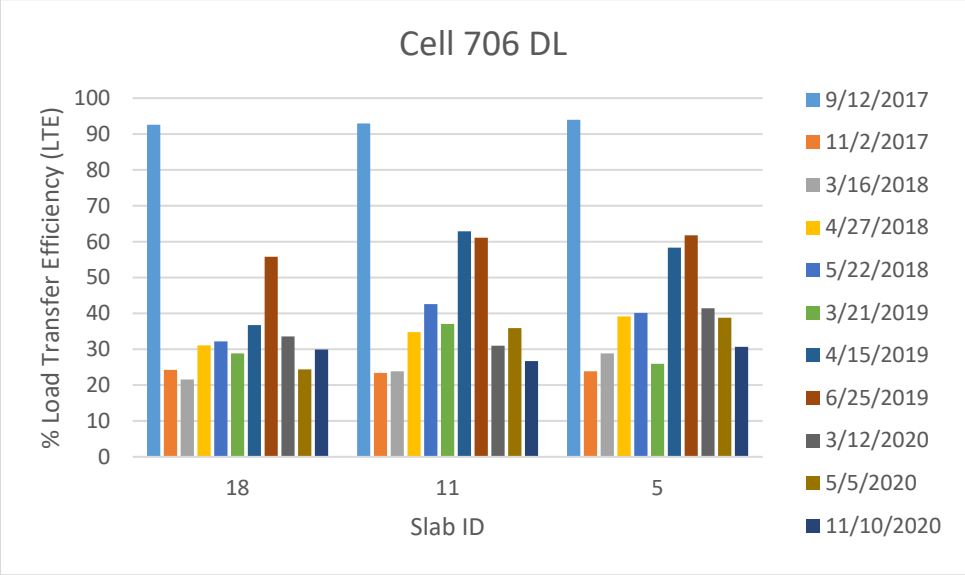

Figure 4-13. LTE of Cell 706 driving lane.

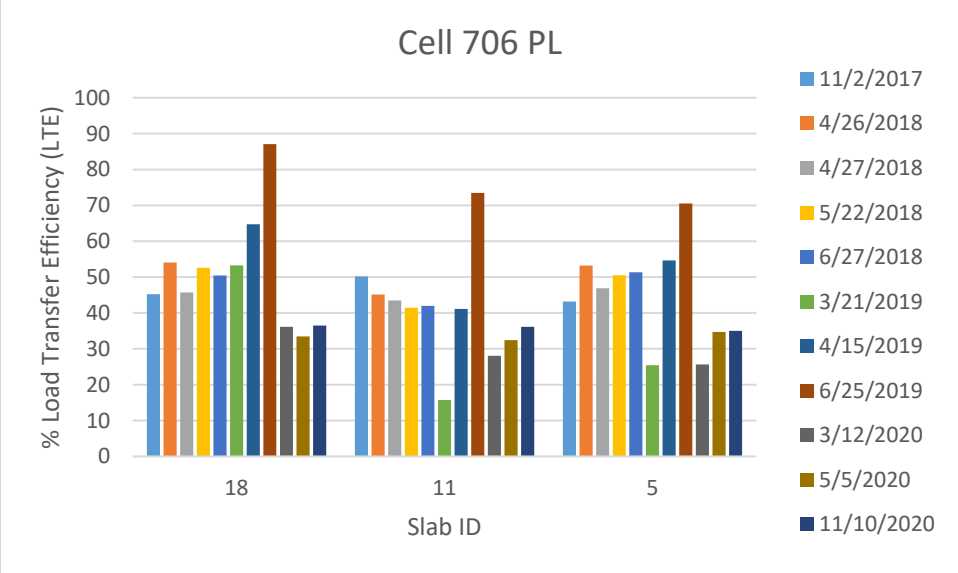

Figure 4-14. LTE of Cell 706 passing lane.

Cell 806, which is 5-inch thick and contains 11.7 lbs./cy of fibers, consistently exhibited the highest LTE among all the cells, until 2019. Notably, all the joints were able to maintain a

very good LTE between 88 to 94% throughout the first two years of service life. The higher LTE of this cell helped in keeping the faulting to the lowest among all the eight cells. Third year data for Cell 806 showed that for the driving lane, the LTE decreased overall to an average of 30%. However, the passing lane LTE showed an average value of 90%, which was significantly higher when compared to all the other cells. The dramatic decline in the LTE values for the Cell 806 driving lane indicates that the contribution of fibers and/ or aggregate interlock have significantly reduced after approximately 2.5 million ESALs.

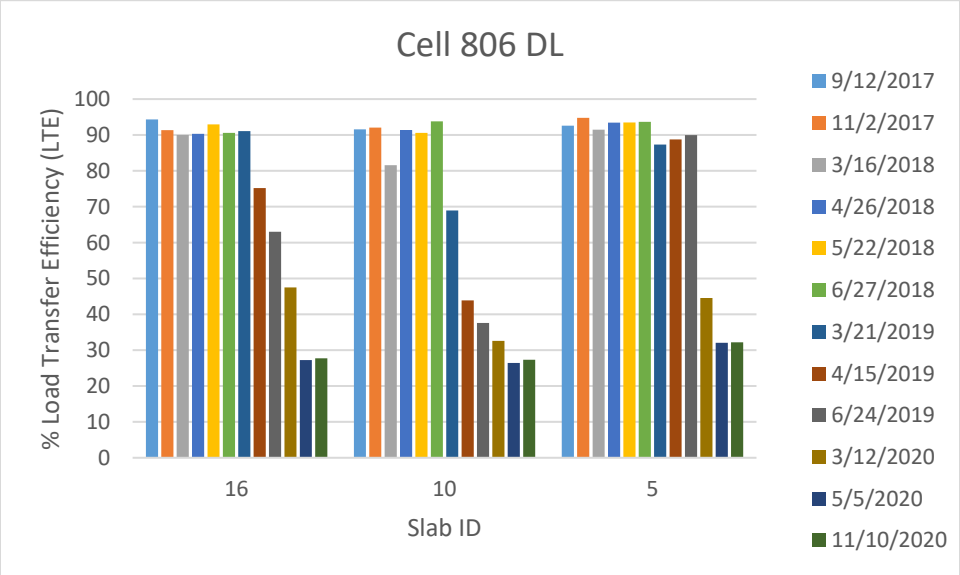

Figure 4-15. LTE of Cell 806 driving lane.

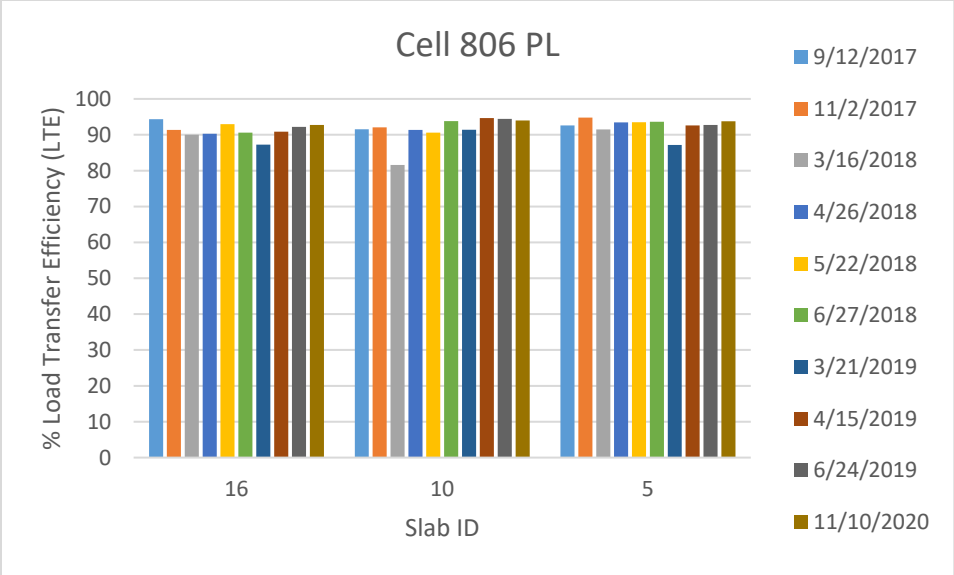

Figure 4-16. LTE of Cell 806 passing lane.

Regarding the MnROAD's old Cells 113 -513, these cells had variable LTE values between them. Cell 113 which had round dowels had better LTE as compared to Cell 513 which had plate dowels. Overall, the LTE for Cell 113 did not change much over the 3 years of service life and was almost 90% throughout. Whereas, Cell 513 LTE decreased from 85% to 65% in the same 3 years. Based on these LTE values, it appears that the doweled Cells 113 and 513 had comparable LTE values to Cell 806. Cell 506-706 having less, or no fiber dosage do not have better LTE values when compared to doweled Cells 113 and 513.

4.2 Differential Displacement

Figure 4-17~~Figure 4-17~~ through Figure 4-32~~Figure 4-32~~ show the plots for differential displacements for all the cells. The general trend of the differential displacement is similar to the trends observed for the LTE. The differential displacements for both Cells 139 and 239 continously increased with the traffic load. The FWD test result for the Joint 23 of cell 139 resulted in a very high value of differential displacement, also the 2020 data shows excessive differential displacement in most of the joints of Cell 139. For the Cell 239, as anticipated, the driving lane shown higher differential displacement compared to the passing lane and overall significantly lower than Cell 139.

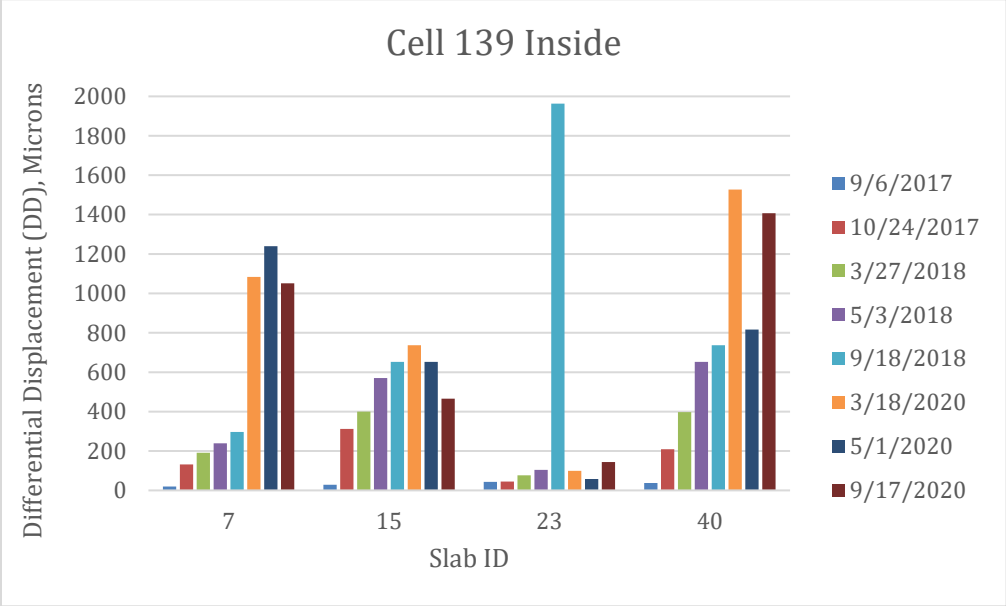

Figure 4-17. Differential displacement of Cell 139 inside line.

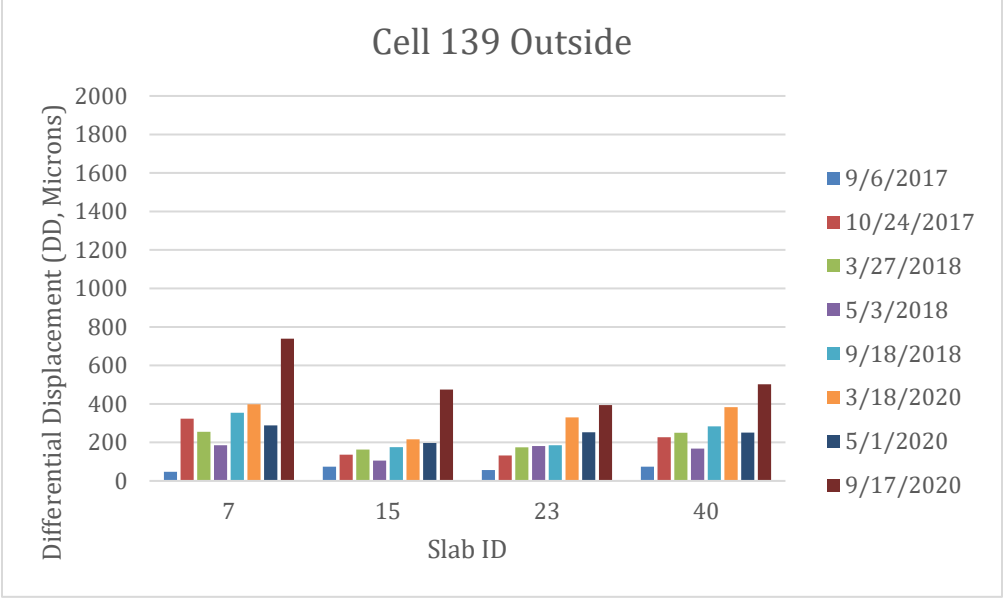

Figure 4-18. Differential displacement of Cell 139 outside line.

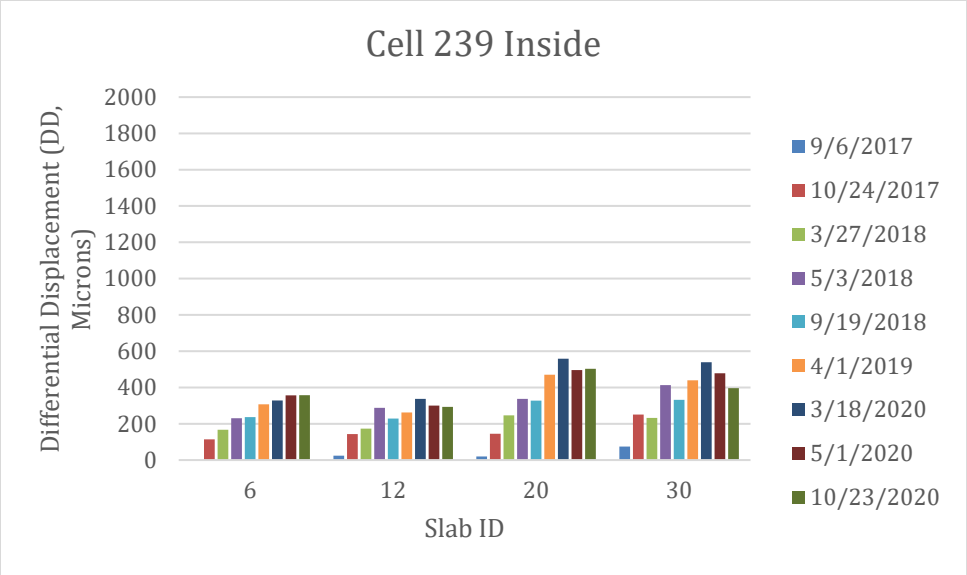

Figure 4-19. Differential displacement of Cell 239 inside line.

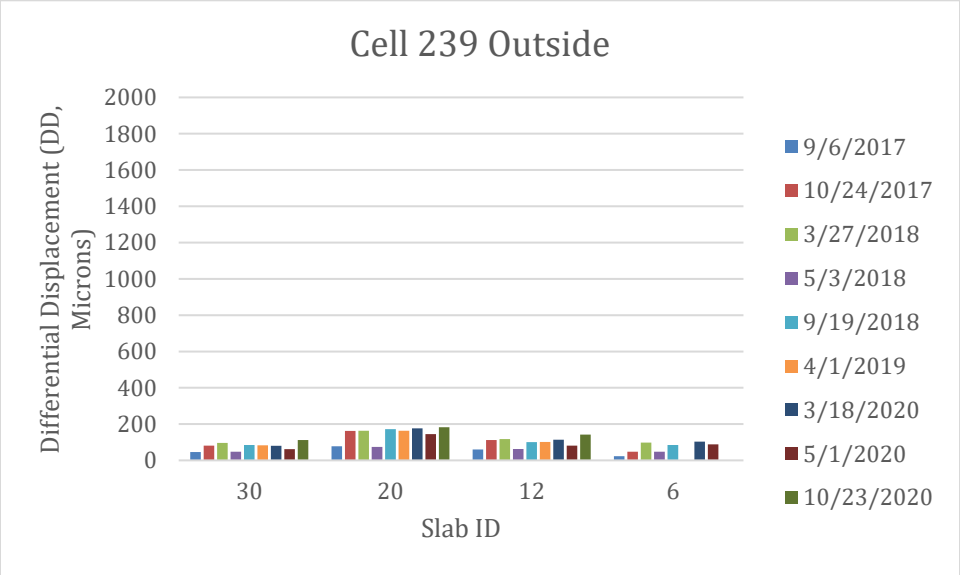

Figure 4-20. Differential displacement of Cell 239 outside line.

Cells 705 and 805 both have experienced high differential displacements at the transverse joints; the differential displacements of Cell 705 (~1000 micron) was almost twice of the Cell 805 (~460 microns). Even though the differential displacements was relatively high, the fabric interlayer provided in these cells is expected to limit the faulting. The other notable observation is that the differential displacement for Cell 705 decreased with traffic,

this is surprising, but it may be possible if the joint support condition weakend and both the slabs experience higher overall displacement. The driving lane of Cell 805 shown steady increase on the differential displacement, while the passing lane shown somewhat similar values over the years.

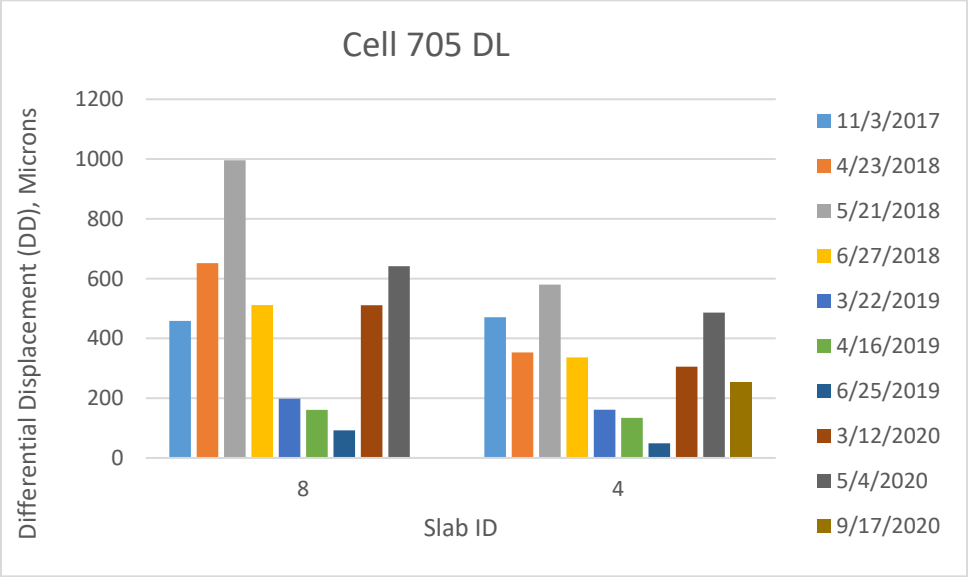

Figure 4-21. Differential displacement of Cell 705 driving lane.

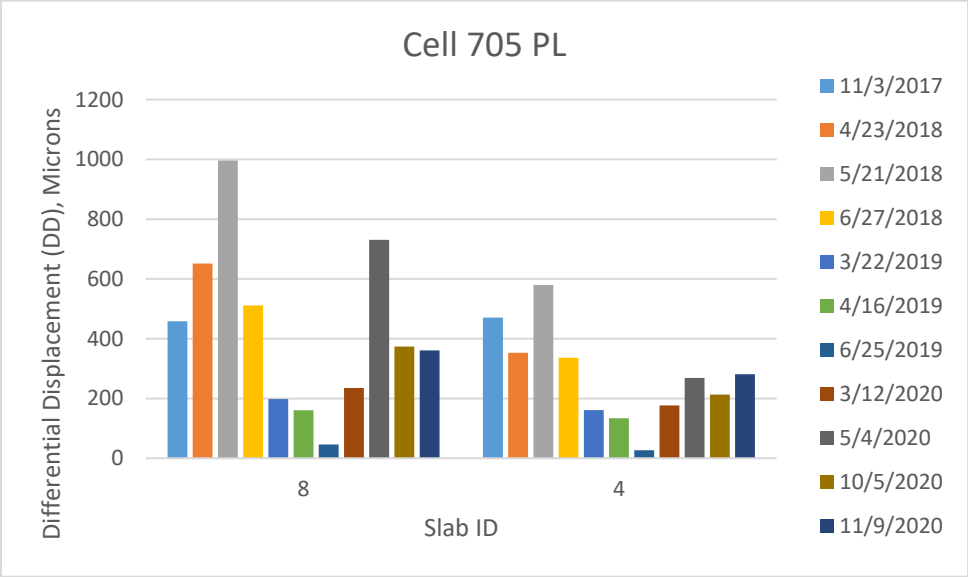

Figure 4-22. Differential displacement of Cell 705 passing lane.

Note: the y-axis is different than Cells 139 and 239

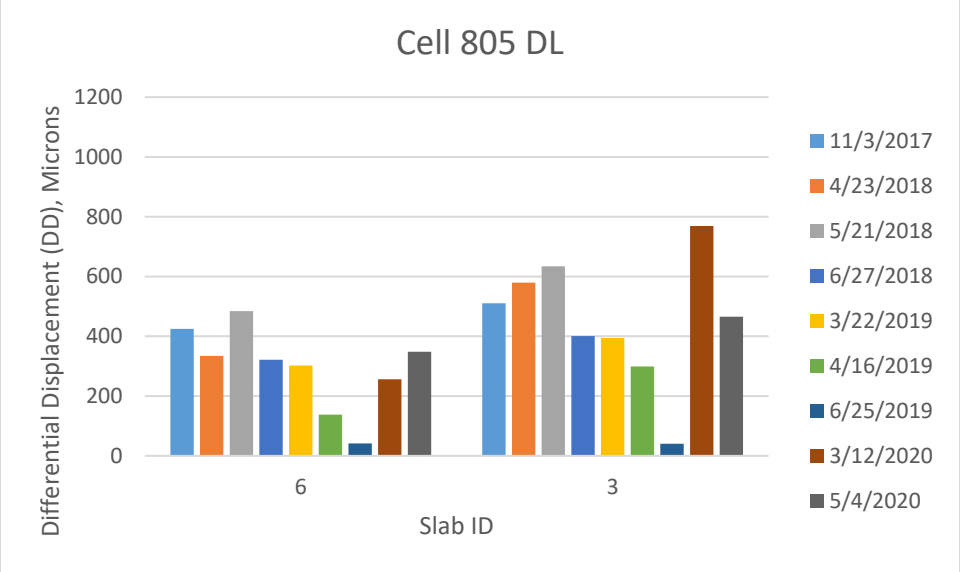

Figure 4-23. Differential displacement of Cell 805 driving lane.

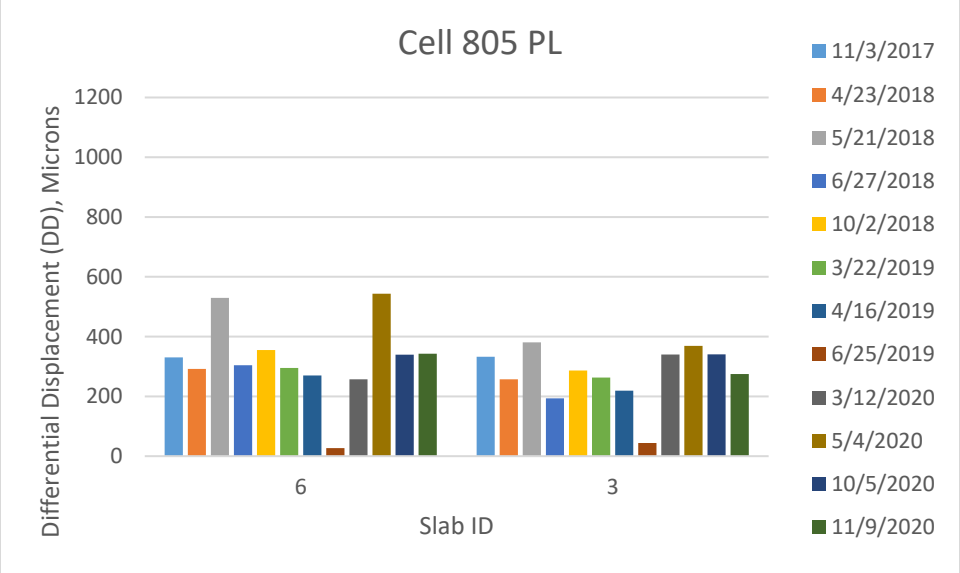

Figure 4-24. Differential displacement of Cell 805 passing lane.

The contribution of fibers in joint performance can also be seen in the differential displacement plots for Cell 506 through 806. The driving lanes of Cells 506, 606 and 706 exhibited higher differential displacements than Cell 806. Cell 506 showed hgher

differential deflection initially, but then decreased with traffic and then again increased in 2020. The Cell 806 driving lane had neglegible differential deflection compared to aother cells, until spring of 2020 when it started increasing with the traffic (matches with the LTE observations).

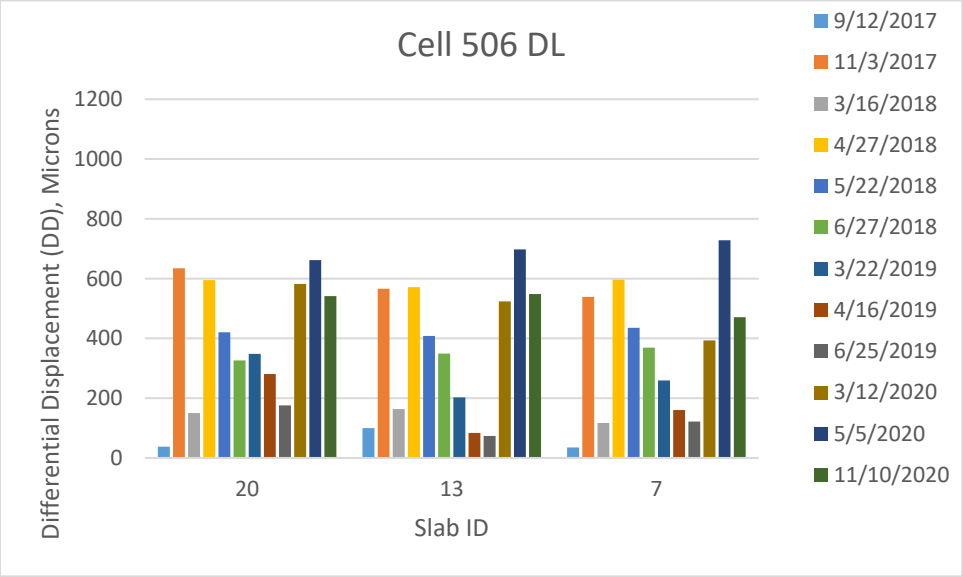

Figure 4-25. Differential displacement of Cell 506 driving lane.

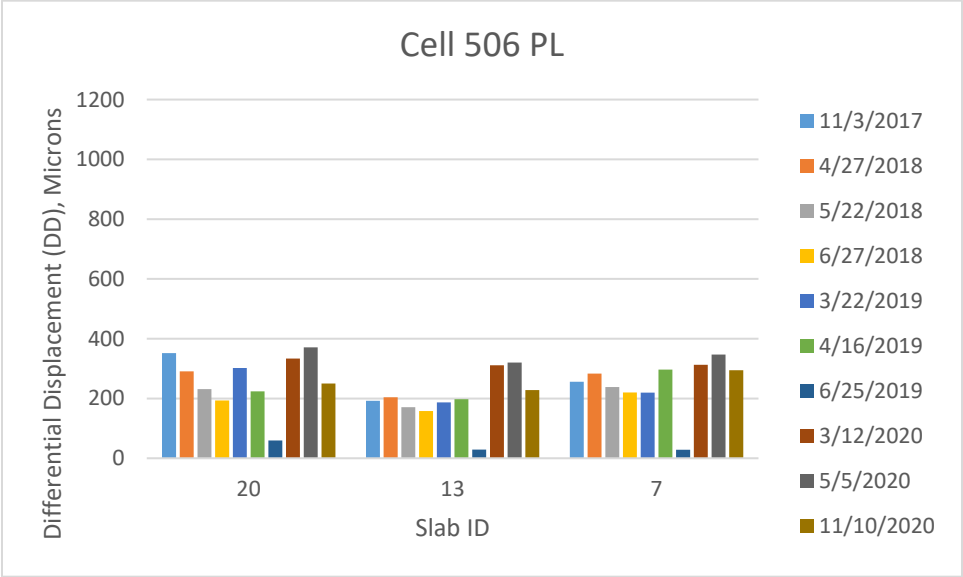

Figure 4-26. Differential displacement of Cell 506 passing lane.

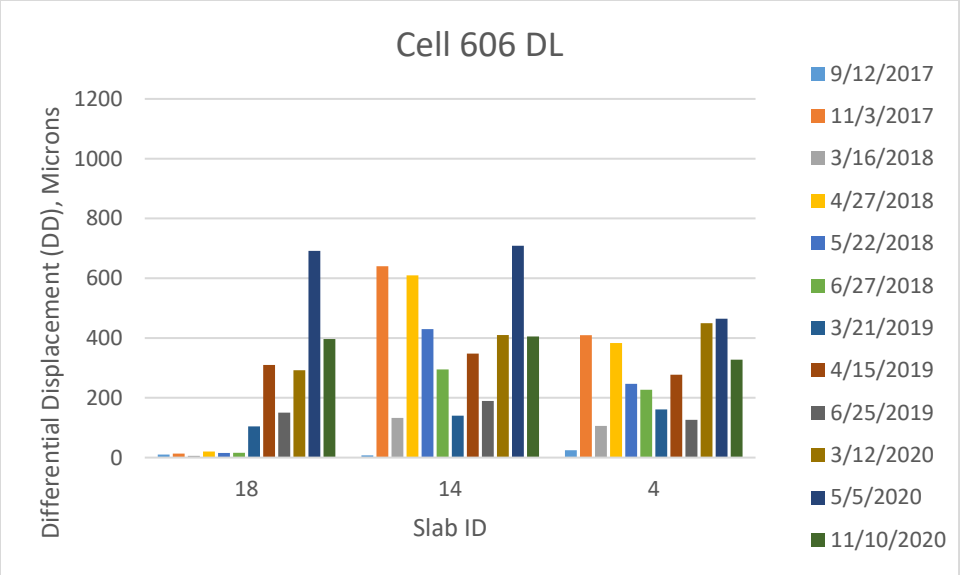

Figure 4-27. Differential displacement of Cell 606 driving lane.

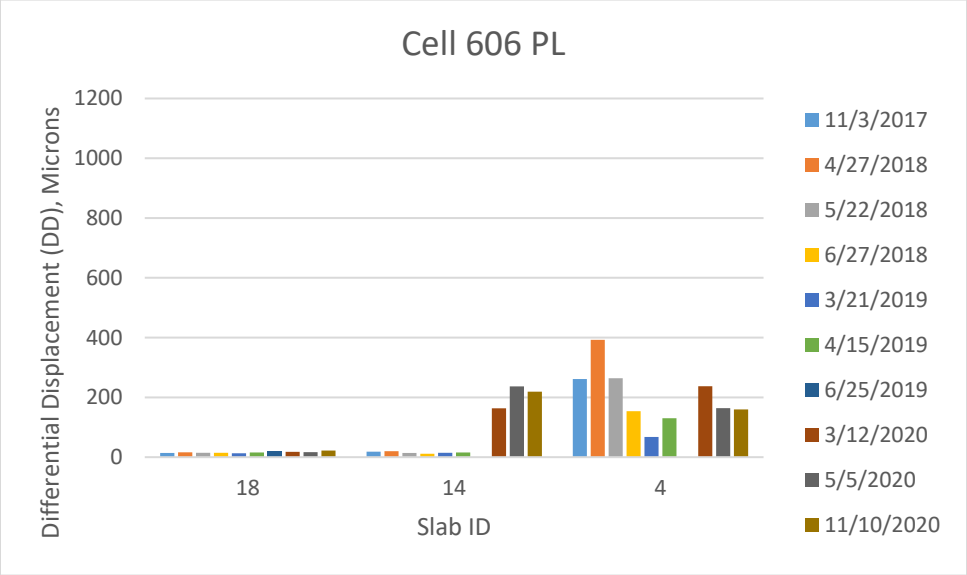

Figure 4-28. Differential displacement of Cell 606 passing lane.

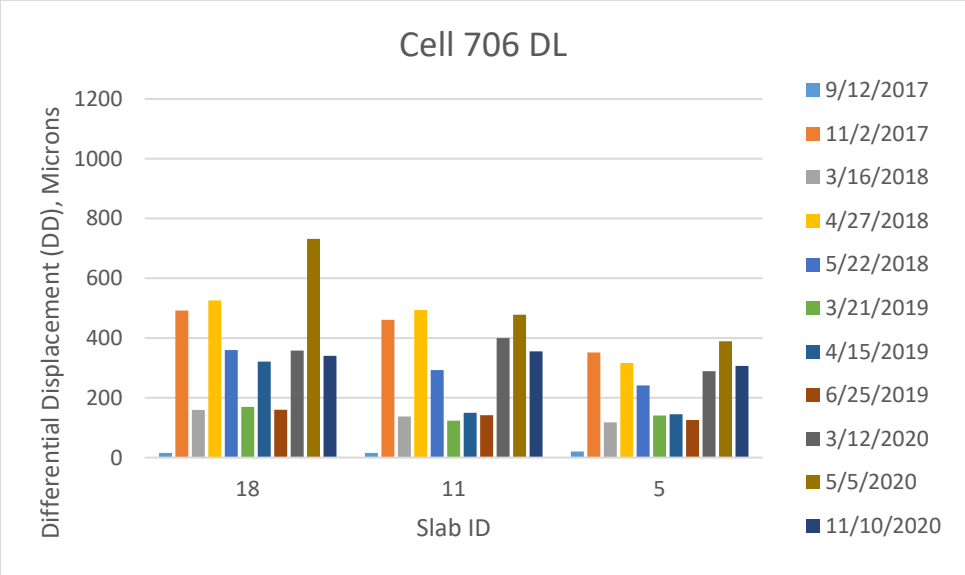

Figure 4-29. Differential displacement of Cell 706 driving lane.

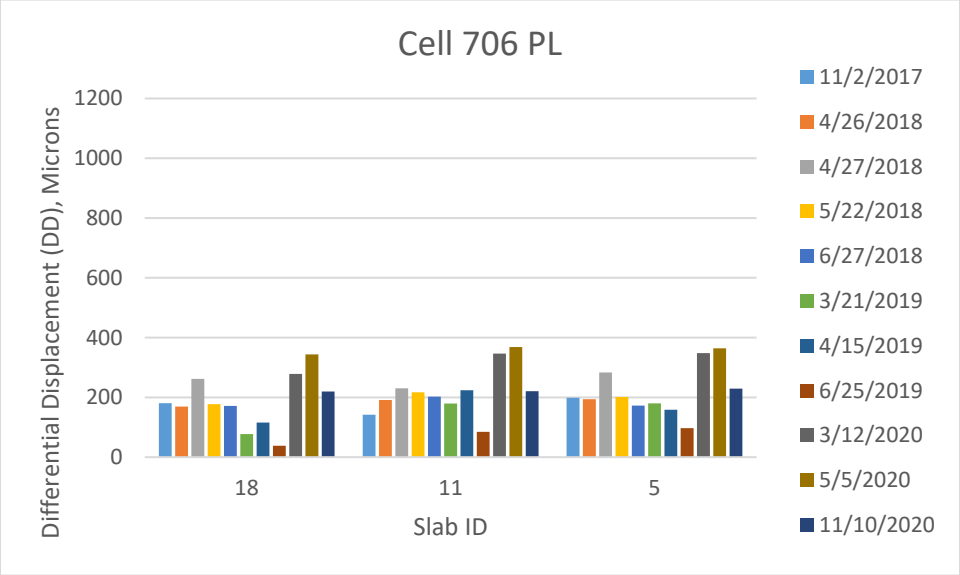

Figure 4-30. Differential displacement of Cell 706 passing lane.

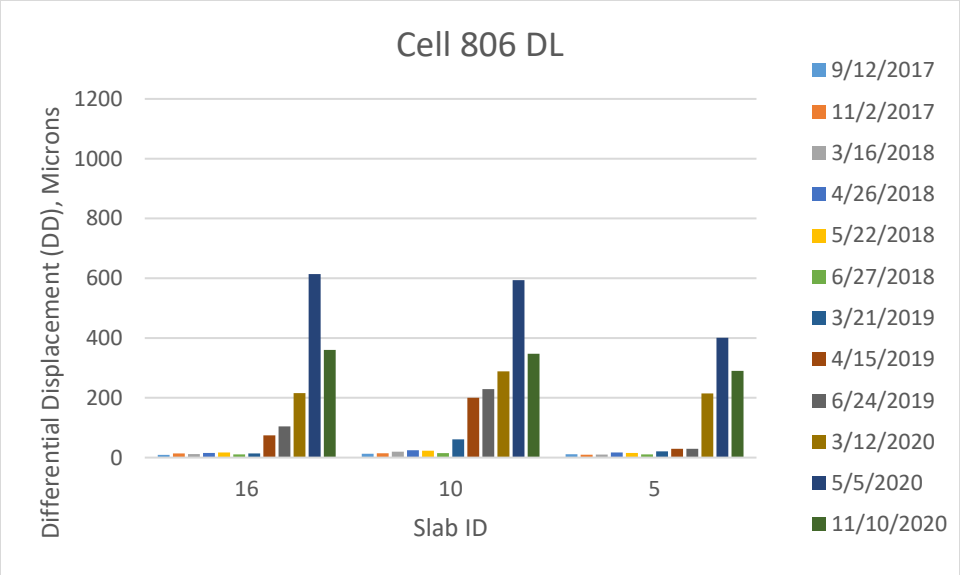

Figure 4-31. Differential displacement of Cell 806 driving lane.

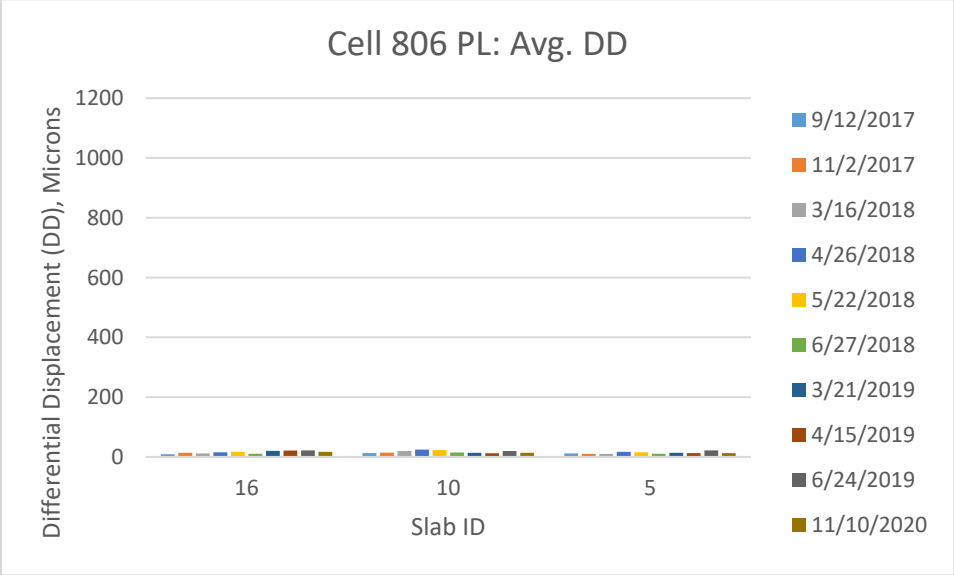

Figure 4-32. Differential displacement of Cell 806 driving lane.

4.3 Loaded-side Displacement

Figure 4-33~~Figure 4-33~~ through Figure 4-48~~Figure 4-48~~ shows loaded-side displacement, which is a good indicator of joint performance. Even though the LTEs and differential displacements for the Cells 139 and 239 were somewhat comparable, the Cell 139 had significantly higher loaded-side displacement. This clearly indicates that cell 139 had poorer joint stiffness or weaker support compared to Cell 239.

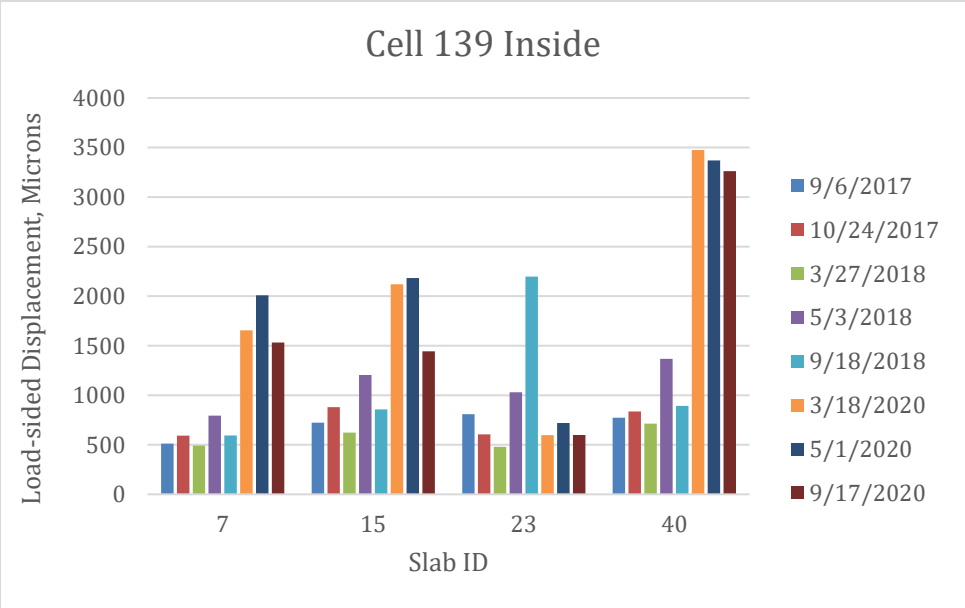

Figure 4-33. Loaded-side displacement of Cell 139 inside lane.

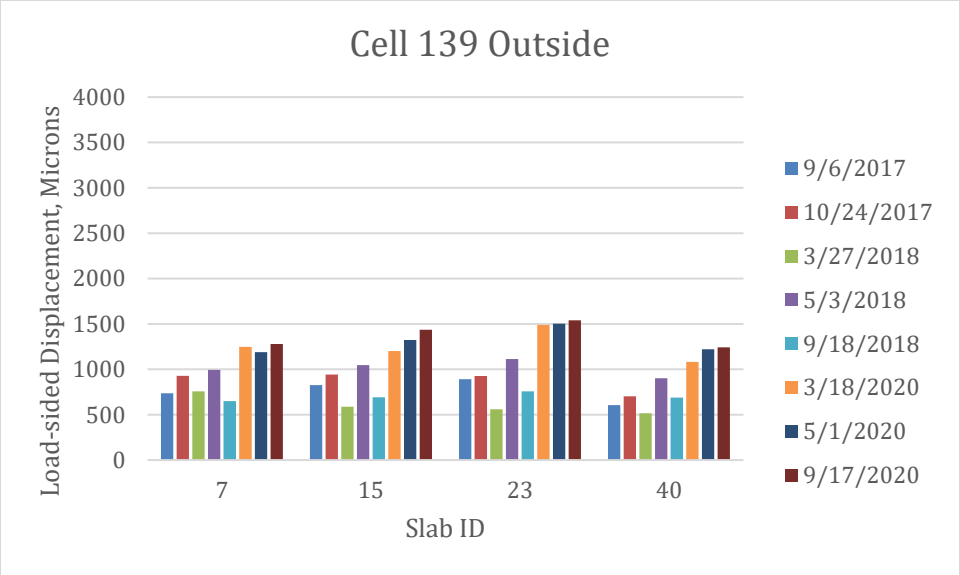

Figure 4-34. Loaded-side displacement of Cell 139 outside lane.

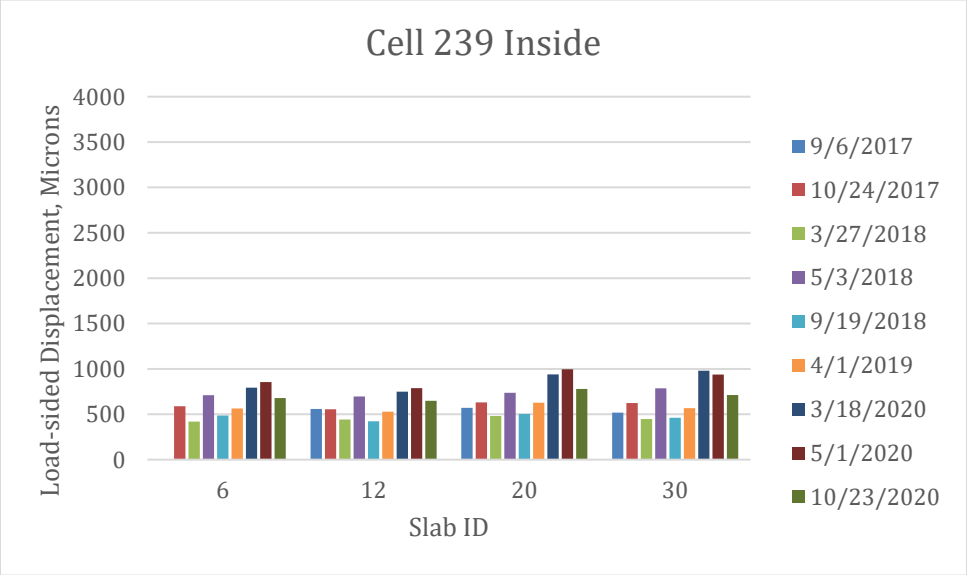

Figure 4-35. Loaded-side displacement of Cell 239 inside lane.

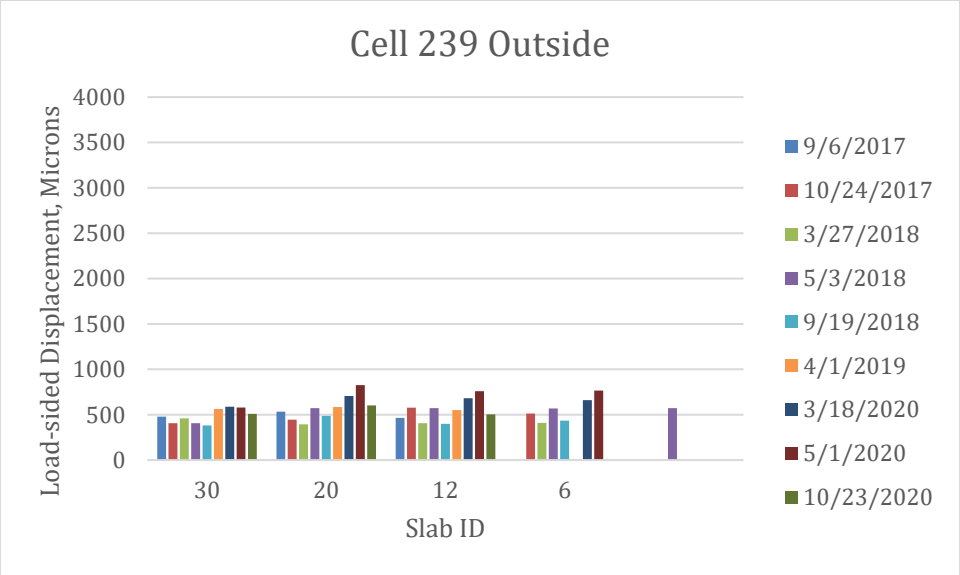

Figure 4-36. Loaded-side displacement of Cell 239 outside lane.

Between these Cells 705 and 805, the Cell 705 compared to Cell 805 had experienced higher, and as much as twice, the loaded-side displacements initially. But then the 2020 readings indicate that Cell 805 has higher loaded-side displacement. The loaded-side displacement of Cells 506 through 806 also showed that the 806 performed better than the other three cells initially until approximately 2.5 million ESALs. The 2020 readings (beyond 2.5 million ESALs) indicate that all four cells have similar loaded-side displacement, with Cell 506 (no fiber) slightly higher than the other three. Overall, it can be stated that the influence of fibers has diminished after 2.5 million ESALs.

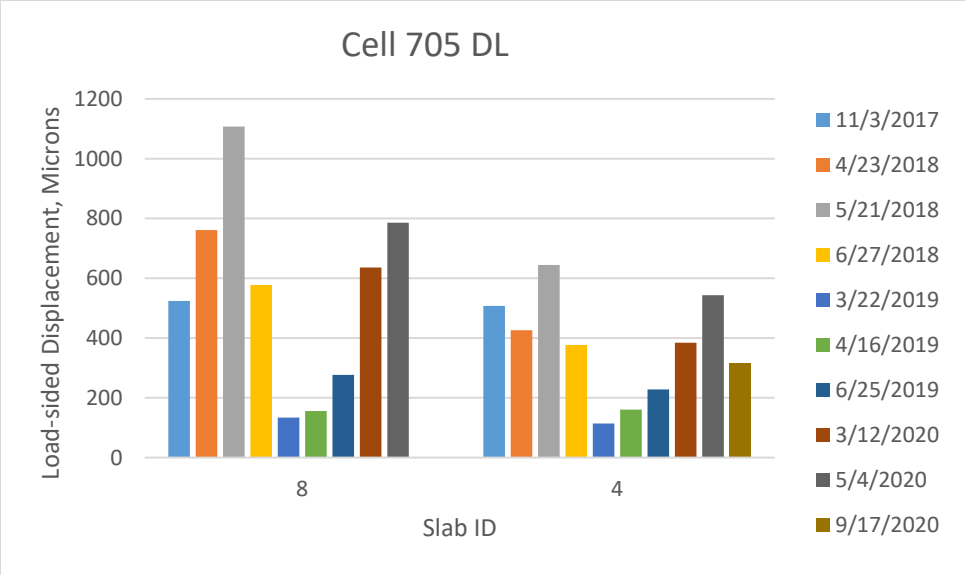

Figure 4-37. Loaded-side displacement of Cell 705 driving lane.

Note: the y-axis is different than Cells 139 and 239

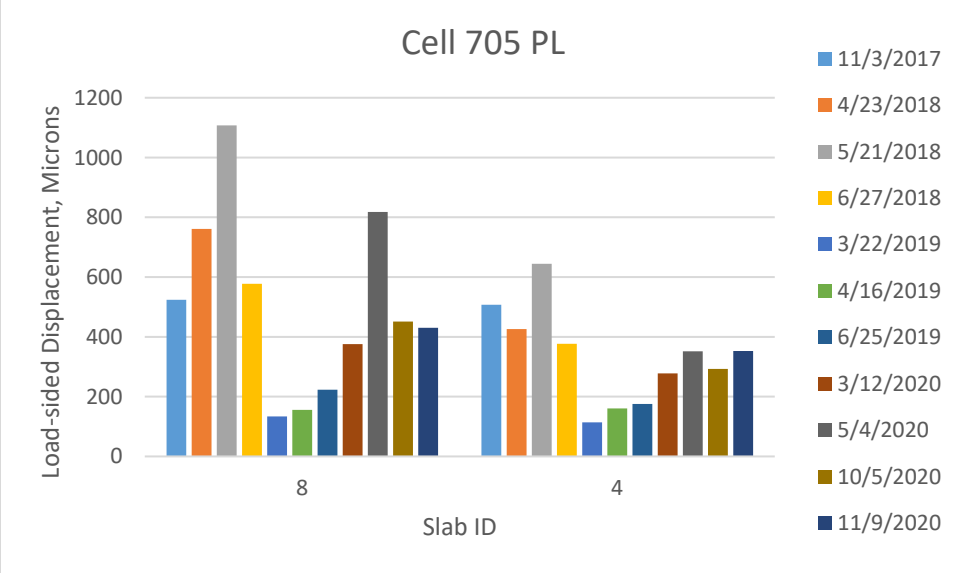

Figure 4-38. Loaded-side displacement of Cell 705 passing lane.

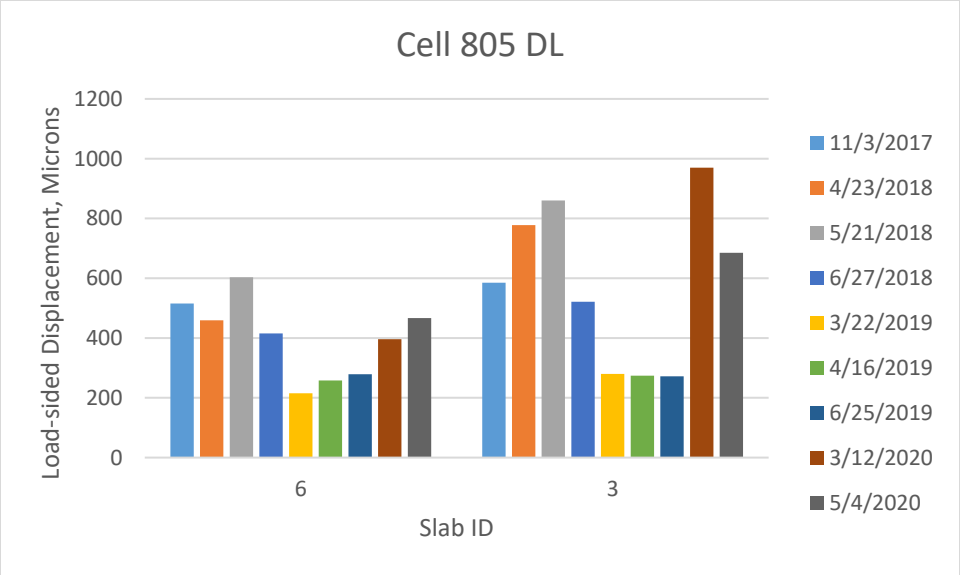

Figure 4-39. Loaded-side displacement of Cell 805 driving lane.

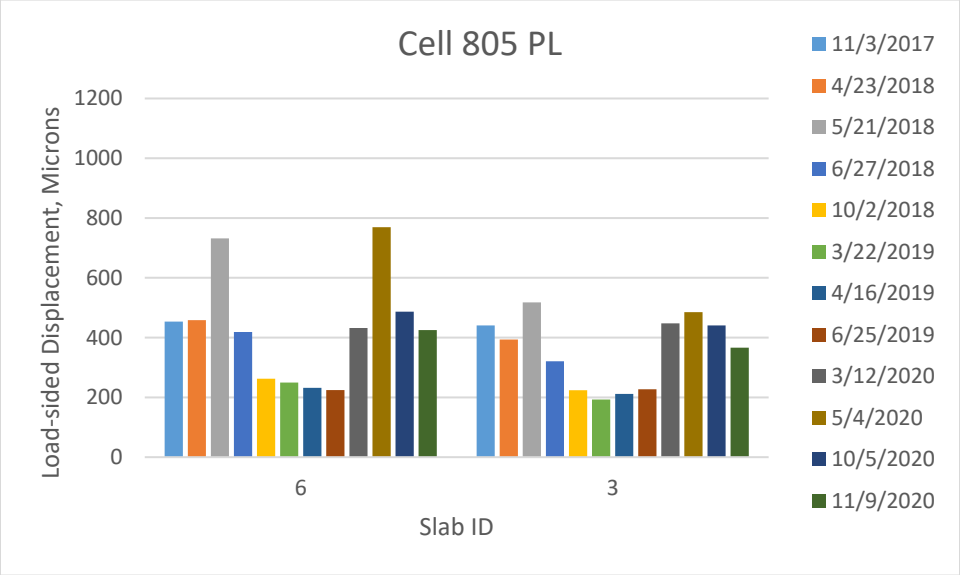

Figure 4-40. Loaded-side displacement of Cell 805 passing lane.

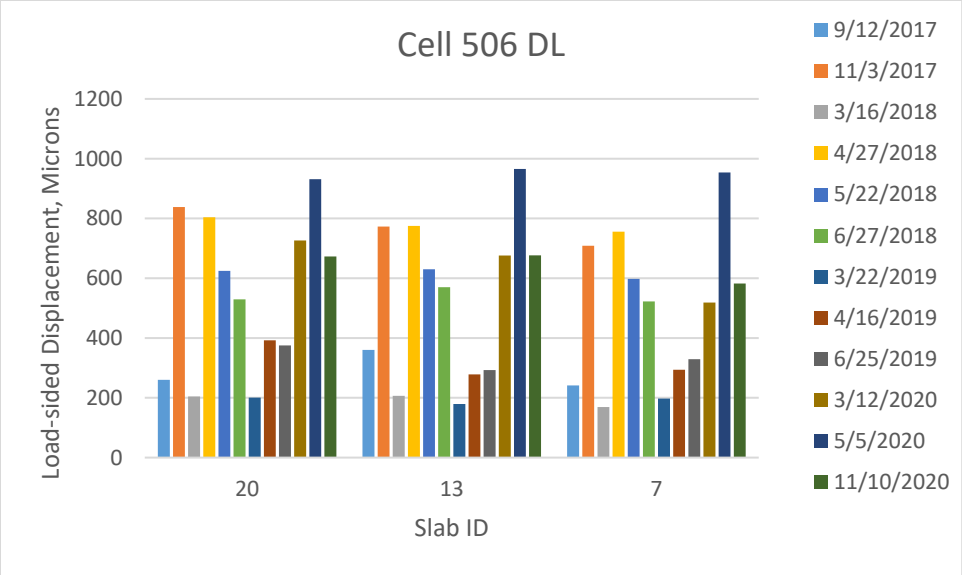

Figure 4-41. Loaded-side displacement of Cell 506 driving lane.

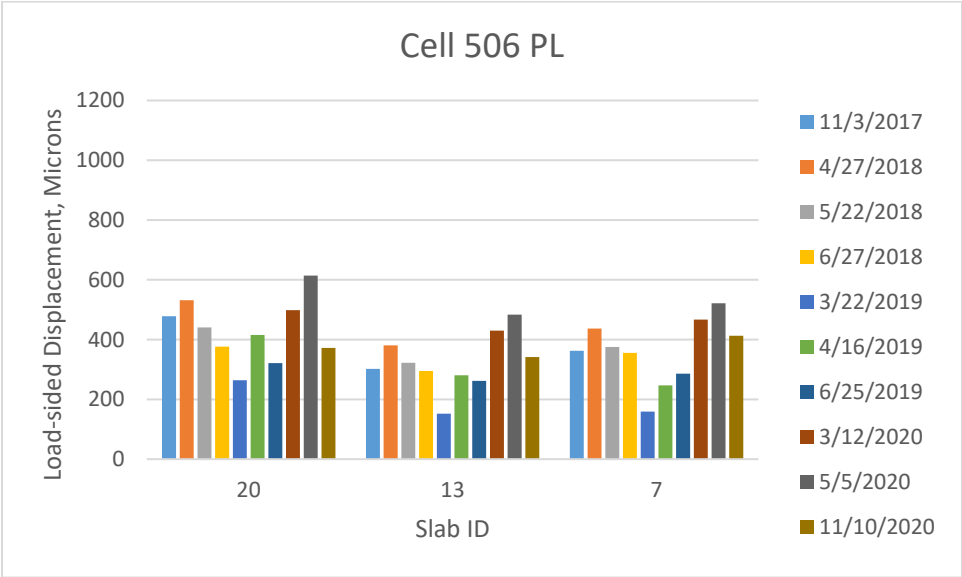

Figure 4-42. Loaded-side displacement of Cell 506 passing lane.

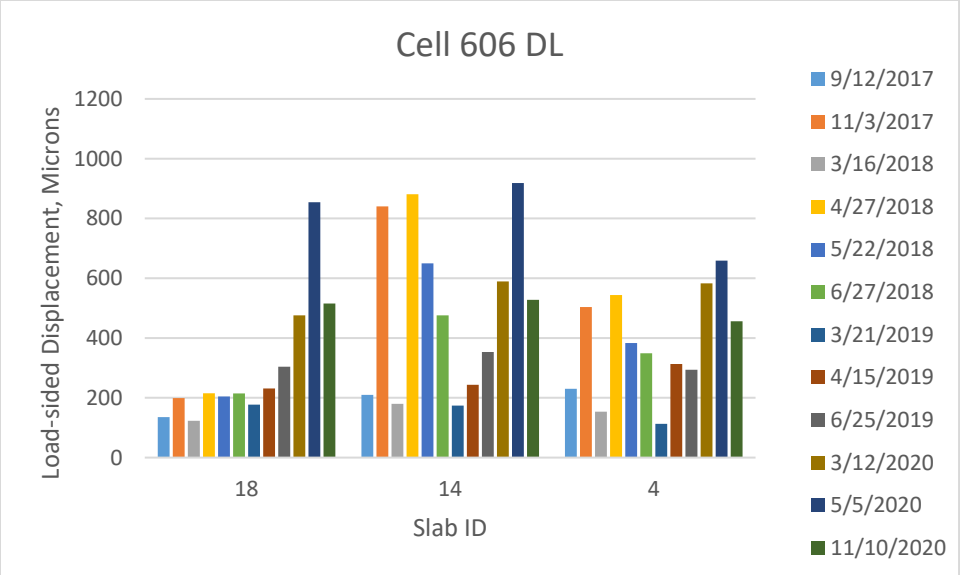

Figure 4-43. Loaded-side displacement of Cell 606 driving lane.

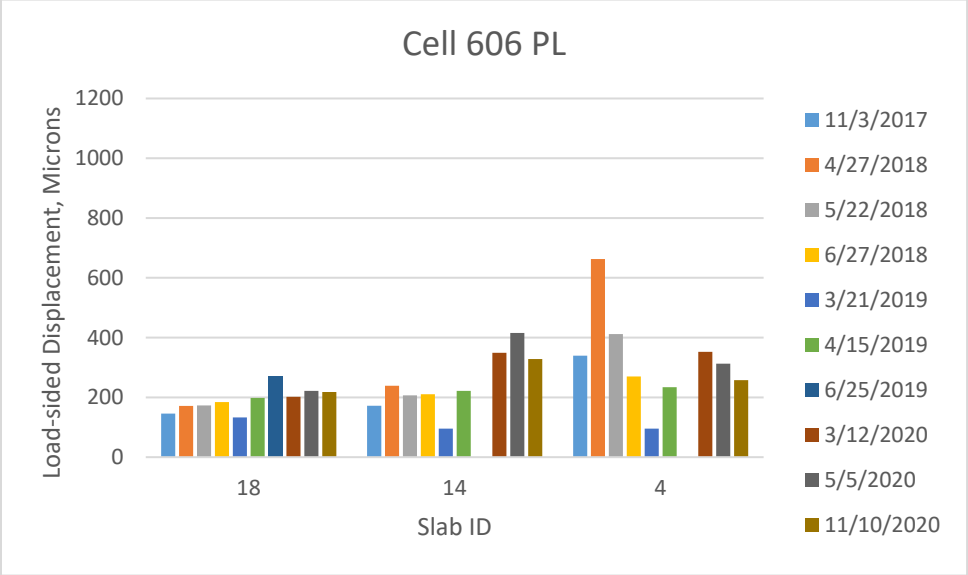

Figure 4-44. Loaded-side displacement of Cell 606 passing lane.

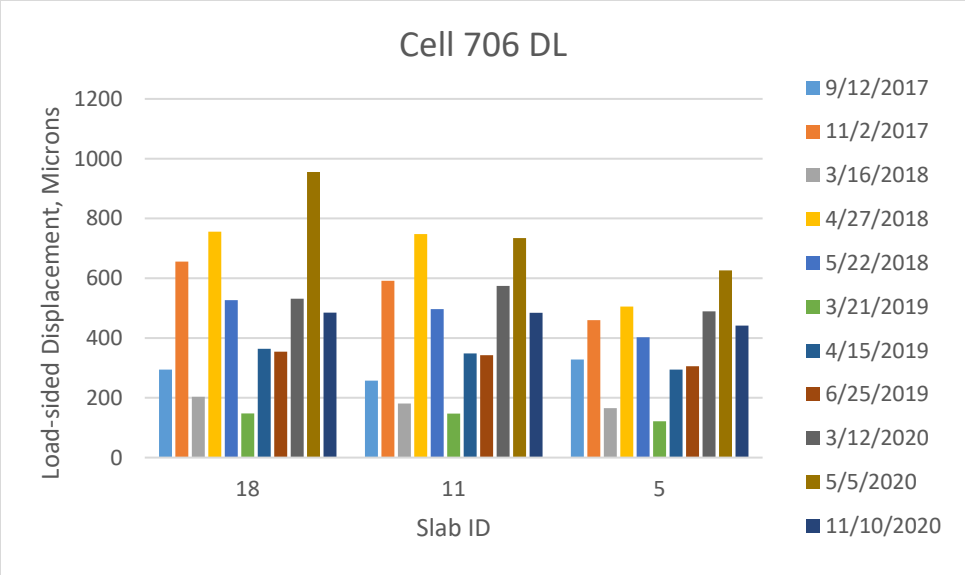

Figure 4-45. Loaded-side displacement of Cell 706 driving lane.

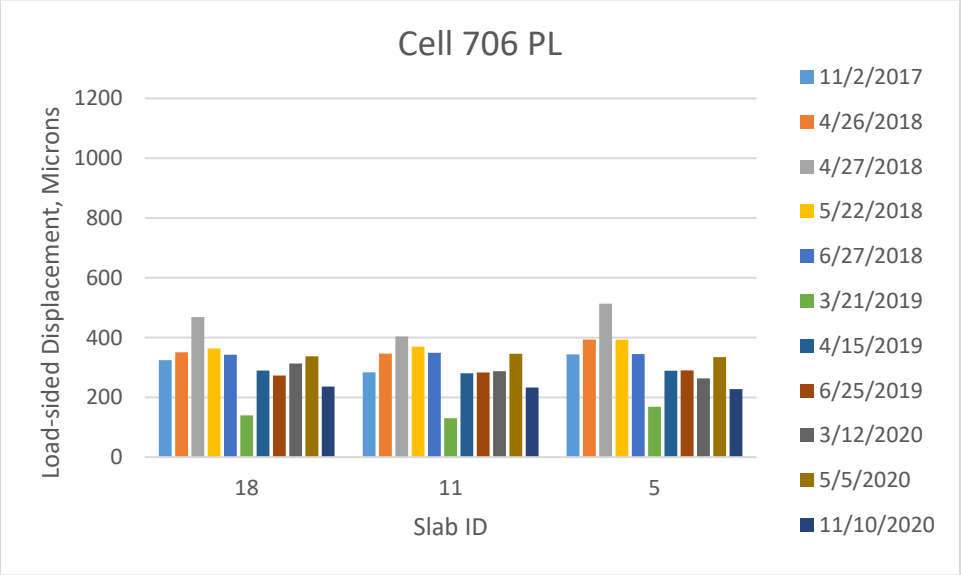

Figure 4-46. Loaded-side displacement of Cell 706 passing lane.

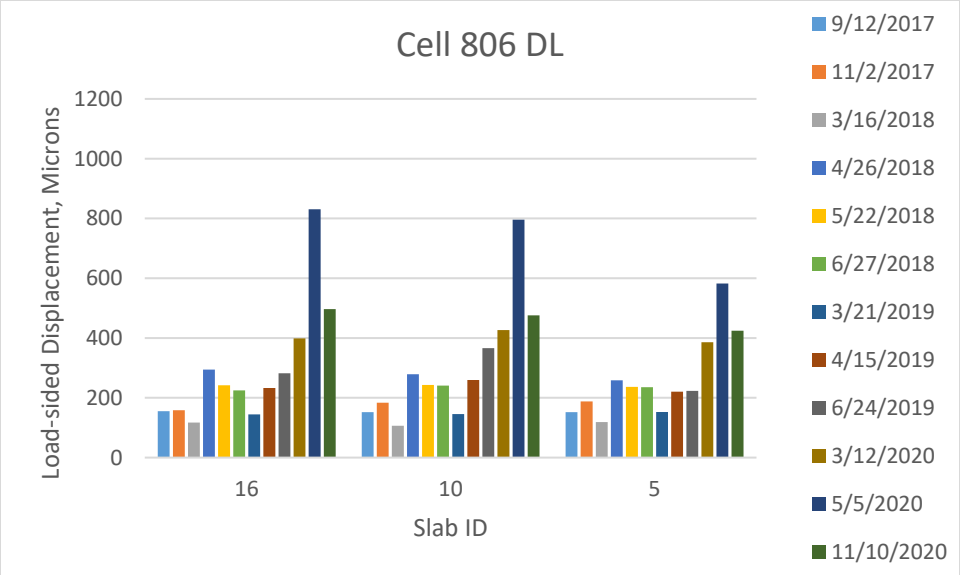

Figure 4-47. Loaded-side displacement of Cell 806 driving lane.

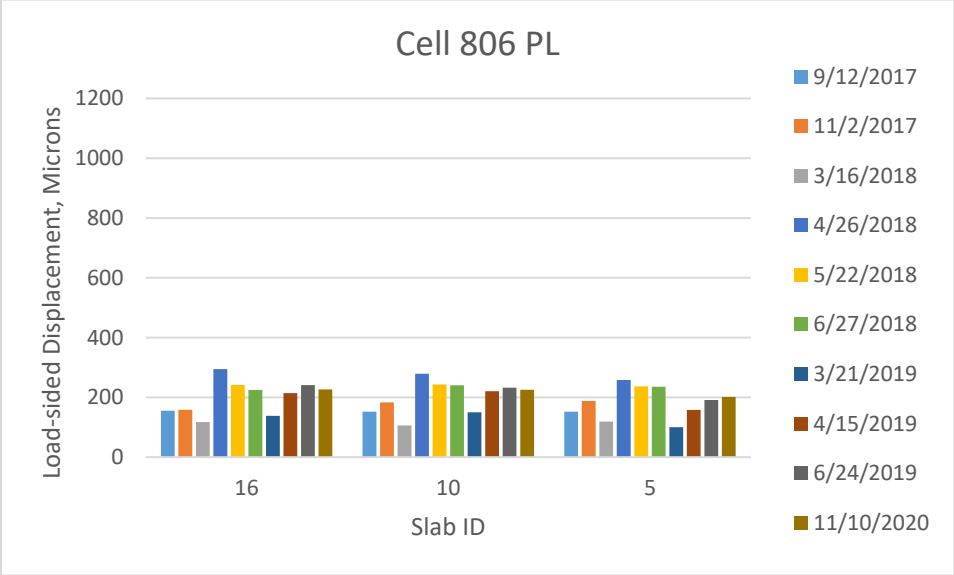

Figure 4-48. Loaded-side displacement of Cell 806 passing lane.

5 CONCLUSIONS

Fiber-reinforced concrete overlays had been constructed in the United States and many other countries for many decades. However, a comparison between the performances of fiber reinforced concrete pavements or overlays and their plain concrete counterparts was not available because of the lack of companion sections. The National Road Research Alliance funded and MnDOT constructed 2017 FRC research cells provided an excellent opportunity to draw such a comparison and quantify the contribution of structural fibers in mitigating cracks, faulting, and other distresses.

This report first presented a summary of the distresses observed in different cells during the first three years of service. The report then provided a discussion on the different sensor data collected during this period. The results of the joint performance tests conducted by using the falling weight deflectometer were discussed at the end of this report. The following major conclusions can be drawn from this report.

- Cracks and Spalling
  - In Cell 139, 75% slabs cracked with ~80,000 ESALs. The thickness of this cell was 3 inches, which is probably too extreme on a 6-inch un-stabilized aggregate base. The cracks observed in this cell were more like bottom-up fatigue cracks of asphalt pavement with shattered slabs along the wheel path.
  - The contribution of the fibers (@8lb/cy fiber, 30% RSR) on Cell 139 is not clear. Given the 3-inch thickness of the slab, it can be stated that the concrete or the overall pavement structure was too weak for yielding any fiber benefit. Although deflections were extremely high, the individual pieces of shattered concrete were somewhat contained by the connecting fibers.
  - Cell 239 (4-inch thick) has performed much better than Cell 139. It seems one-inch extra concrete could provide almost twice more life in Cell 239 compared to Cell 139. The dominant distress for this cell was the longitudinal crack along the wheel path. This observation concludes that such thin concrete pavement structures do not fail by the typical mid-slab

transverse fatigue cracks, unlike concrete pavements with more common thicknesses (> 6 inches). All the critical distresses appeared along the wheel path. While the distresses in Cell 139 relative to Cell 239 is more a function of the less thickness in the former, the early load application and weaker base condition might have played a role too.

- Wide-paneled (~12 ft wide, Cell 705) thin unbonded overlays experienced more longitudinal cracks compared to the narrow-paneled ones (~6 ft wide, Cell 805)- which experienced more transverse cracks. The transverse and corner cracks of Cell 805 and 705 were comparable.
- Compared to the pavement-on-grade cells, unbonded overlays experienced significantly higher fatigue cracks (Cells 705 and 805 vs. Cells 606 through 806). One theory for this behavior might be the ability for large thin slabs to freely curl up due to the lack of bonding between the old concrete and fabric interlayer. Also, the relatively thin fabric may not be able to provide the necessary cushioning needed to prevent breakage of the thin curled panels under heavy dynamic loads.
- With respect to cracking, Cells 506 through 806 are performing better than all other cells, with only a few cracks in three slabs of Cell 506 (no fiber); those slabs had to be replaced in the third year of service.
- Cell 506 experienced joint spalling in many locations. An investigation conducted in summer 2020 confirmed that the absence of fibers in this cell was not responsible for the spalling; instead, some hardened saw-cut residue stuck within the saw-cuts of the transverse joints was responsible.
- The cells in the mainline (Cells 705, 805, 506-806) had approximately 3.5 million ESALs on them by the end of 2020, well beyond the typical traffic load for low volume road designs. So many distresses that occurred in 2020 may be considered outside the typical design life.
- As Cells 506 through 806 (fiber dosage varied) have not experienced enough cracks yet, it is hard to quantify the contribution of fibers in mitigating fatigue cracks. These cells have successfully carried 3.5 million ESALs until December 2020. This observation indicates that the critical distress for the

small panel thin concrete pavements on the relatively stiff base layer may not be the fatigue cracking but other distresses like faulting. The fatigue cracking performance of these cells compared to the MnROAD's old thin concrete pavement cells (Cell 113-513) was better, probably because of the shorter panels.

- Joint Faulting
    - Cells 139, 239, 705, and 805 have experienced low faulting (1 to 2 mm)
    - Fibers' contribution was observed in Cells 506 through 806 in the faulting trend.
    - Cell 606, 706, and 806 showed lower faulting than Cell 506 (no fiber).
    - Cells 705 and 805 (overlay with nonwoven geotextile) experienced lower faulting than the concrete pavement cells (Cells 506 -806).
    - Cell 806 (11 lbs./cy fiber) showed higher LTE than Cell 506 (no fiber) until about 2.5 million ESALs, after which LTEs of all cells were comparable.
    - Cells 705 and 805 always showed low LTE even though these cells have not experienced significant faulting.
- Fibers helped in reducing the joint displacement (e.g., Cell 506 vs Cell 806) until about 2.5 million ESALs.
- The temperature gradient of all the cells was found to be linear to a great extent. As much as 60% of the time, slabs experienced a negative temperature gradient.
- The environmental strains measured showed that they possess a good relationship with the temperature, but no verifiable correlations with the fiber dosages and slab sizes (for Cell 705 and 805) were found.
- The dynamic strains were higher in general during the springtime when the base and subgrade support was weak. Strains in the ultra-thin cells (Cells 139 and 239) were higher than the other cells.
- Joint opening sensor data provided mixed results. Some cells showed greater joint openings than the other cells, irrespective of the fiber dosages and cell designs.

Lastly it should be cautioned that the results from this experiment represent the behavior of three dosages of one synthetic fiber and one concrete mixture. It should not be construed

that the results represent the behavior of other types and dosages of synthetic fibers or concrete mixtures for that matter.

6 REFERENCES

1. Barman, M., (2014). Joint Performance Characterization of Bonded Whitetopping Overlays. Ph. D Dissertation, Pittsburgh: University of Pittsburgh.Advisor: Vandenbossche, J.

2. Burnham and Tewfik (2007). Development of a Computer Program for Selecting Peak Dynamic Sensor Responses from Pavement Testing. Minnesota Department of Transportation. St. Paul, MN.

3. MnDOT (2018). Faultmeter-Joints. Version 2, Minnesota Department of Transportation, St. Paul, Minnesota. < http://www.dot.state.mn.us/mnroad/data/files/mnroad-faulting-2018-12.pdf>

4. MnDOT (2018). Report on 2017 MnROAD Construction Activities, Report Number: MN/RC 2018-16, Minnesota Department of Transportation, St. Paul, Minnesota.

5. Selezneva, O., Jiang, J., Tayabji, S. D. (1998). Preliminary Evaluation and Analysis of LTPP Faulting Data – Final Report., Federal Highway Administration, Virginia.

6. Burnham, T., & Izevbekhai, B. (2012). Performance of thin jointed concrete pavements subjected to accelerated traffic loading at the MnROAD facility. Advances in Pavement Design through Full-Scale Accelerated Pavement Testing, 289-297.

APPENDIX A

Third Year Distress Maps

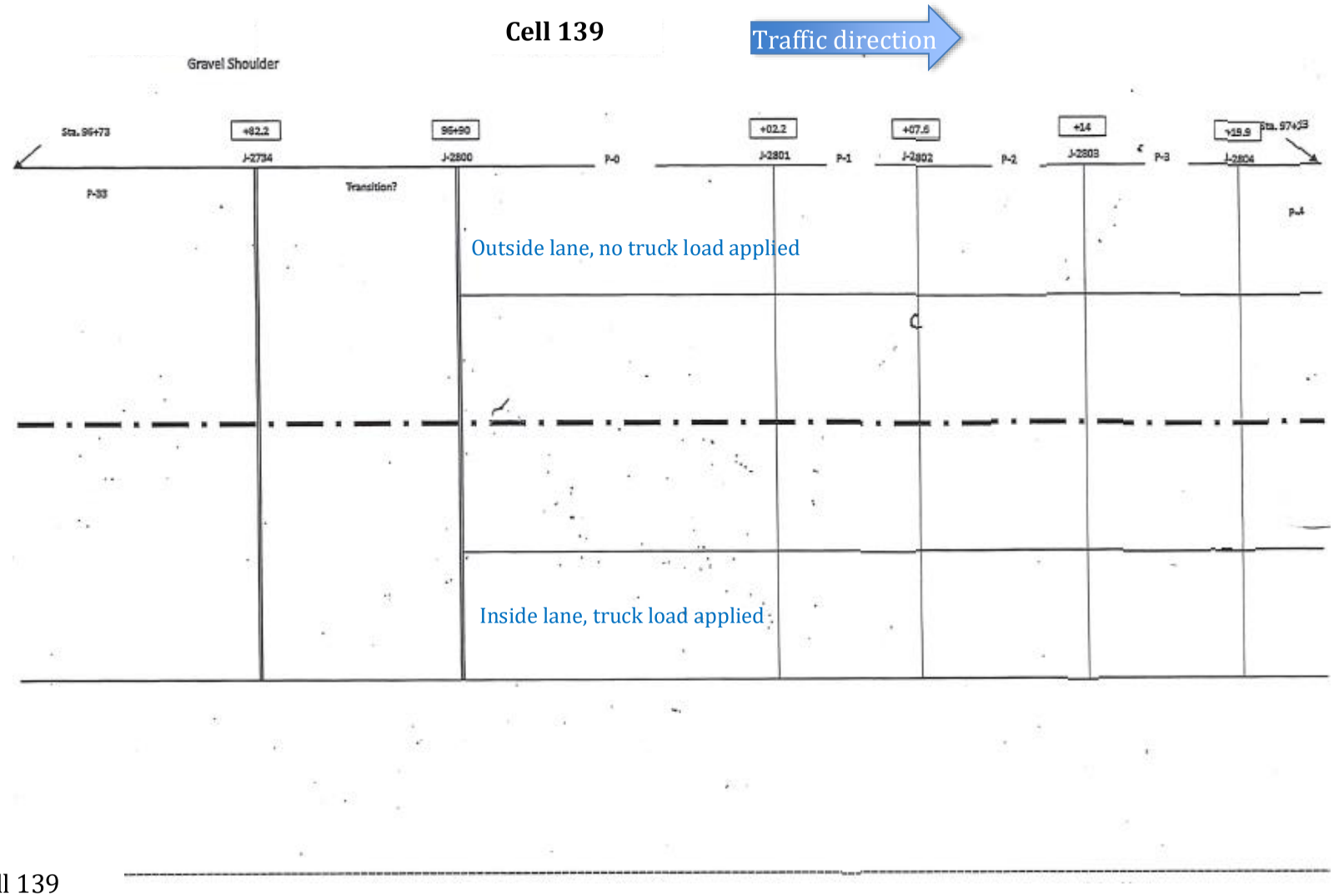

Figure A1: Distress map for Cell 139

Cell 139

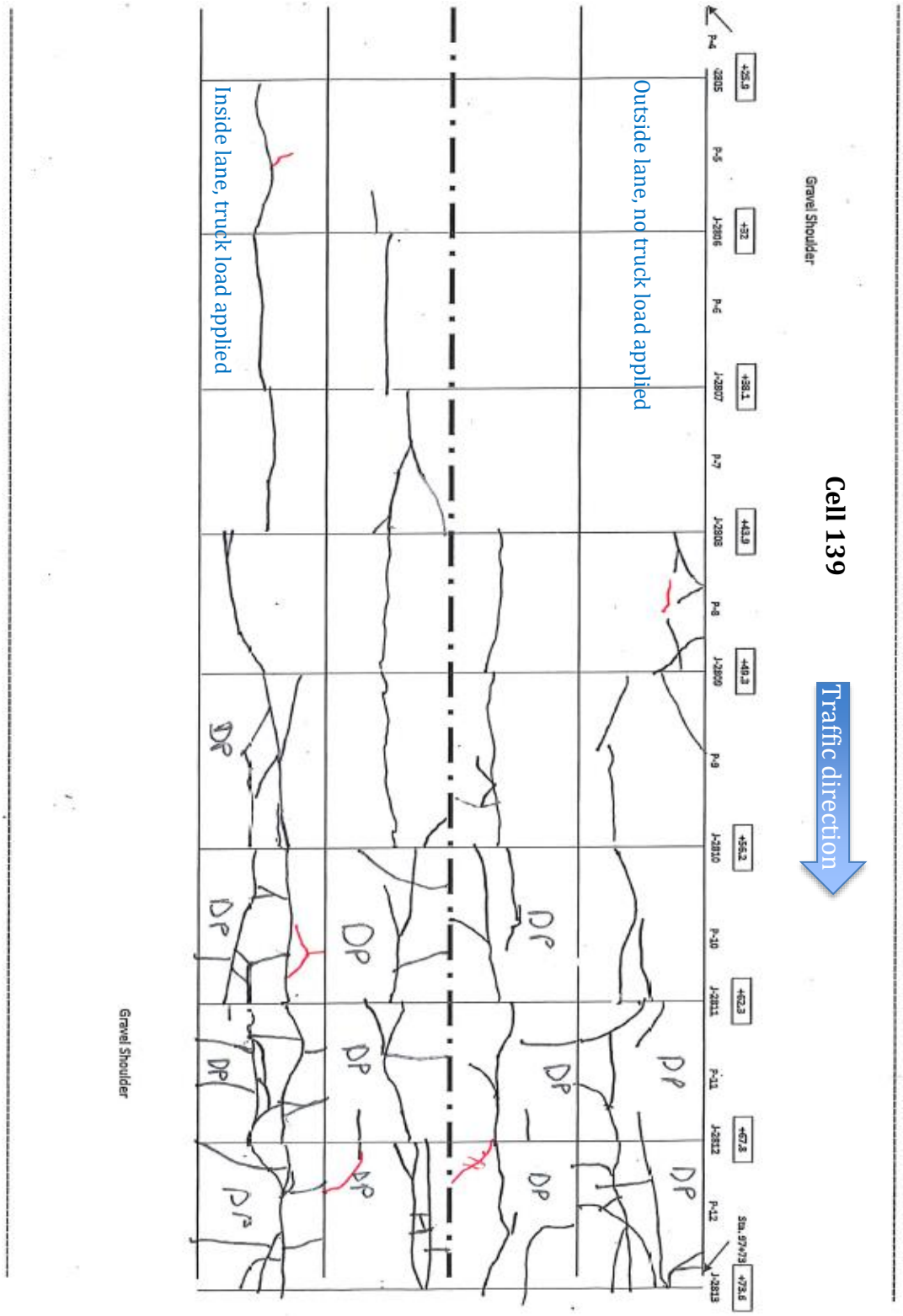

Cracks until March 2020; cracks colored red were documented on March 24, 2020.

Figure A2: Distress map for Cell 139 contd.

Cracks until March 2020; cracks colored red were documented on March 24, 2020.

Figure A3: Distress map for Cell 139 contd.

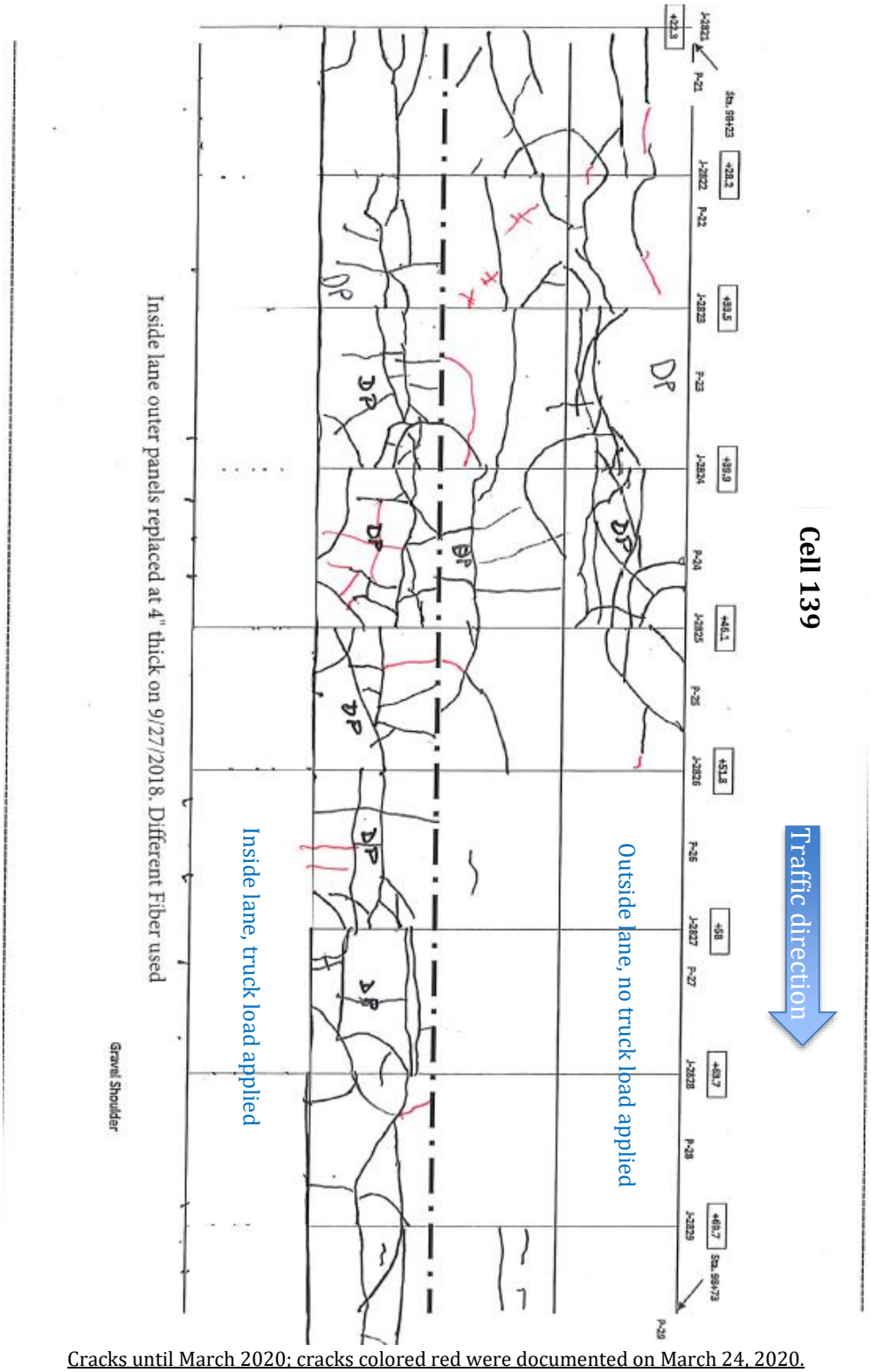

Cracks until March 2020; cracks colored red were documented on March 24, 2020.

Figure A4: Distress map for Cell 139 contd.

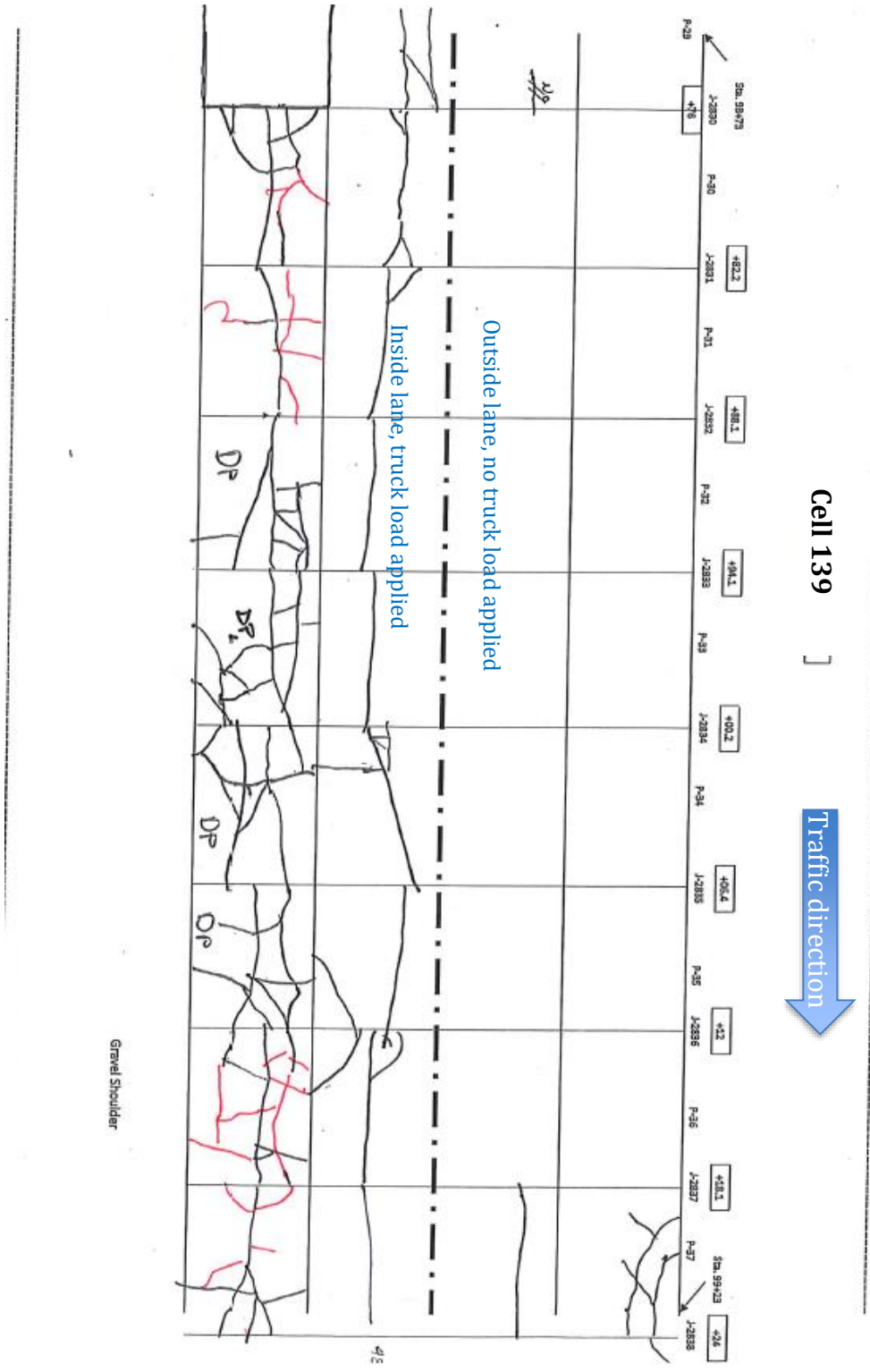

Cracks until March 2020; cracks colored red was documented on March 24, 2020.

Figure A5: Distress map for Cell 139 contd.

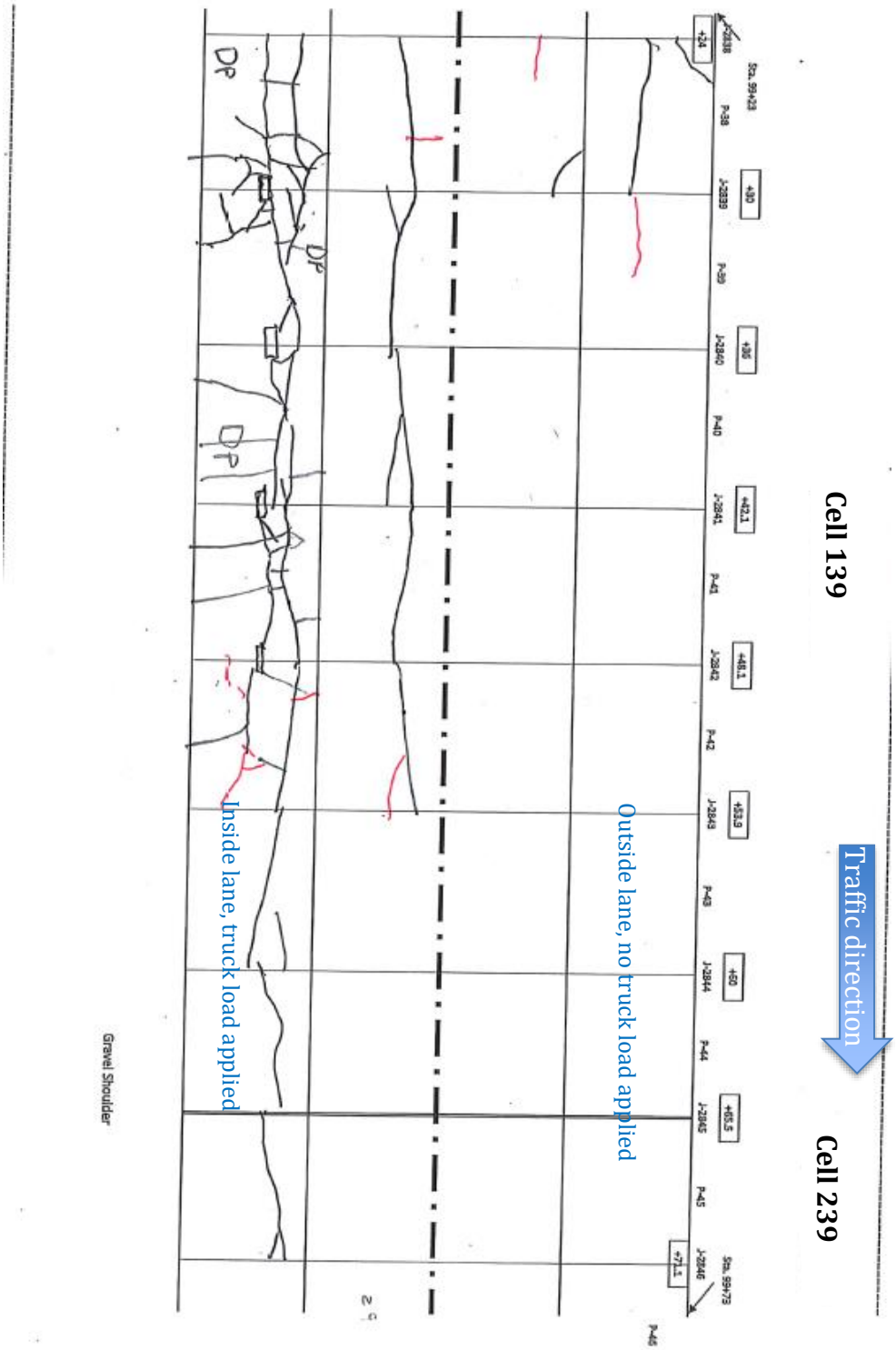

Cracks until March 2020; cracks colored red was documented on March 24, 2020.

Figure A6: Distress map for Cell 139 contd.

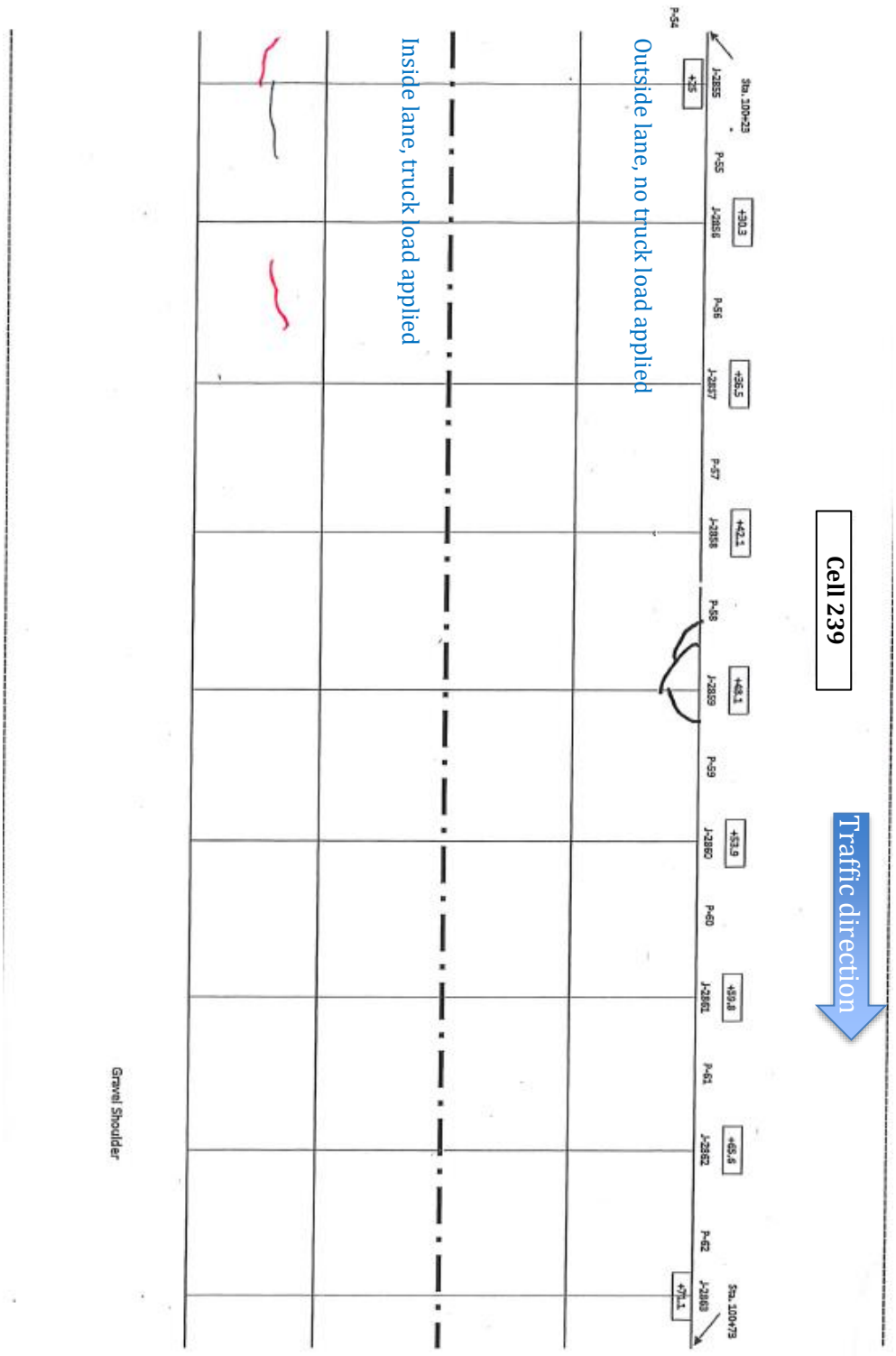

Figure A7: Distress map for Cell 239.

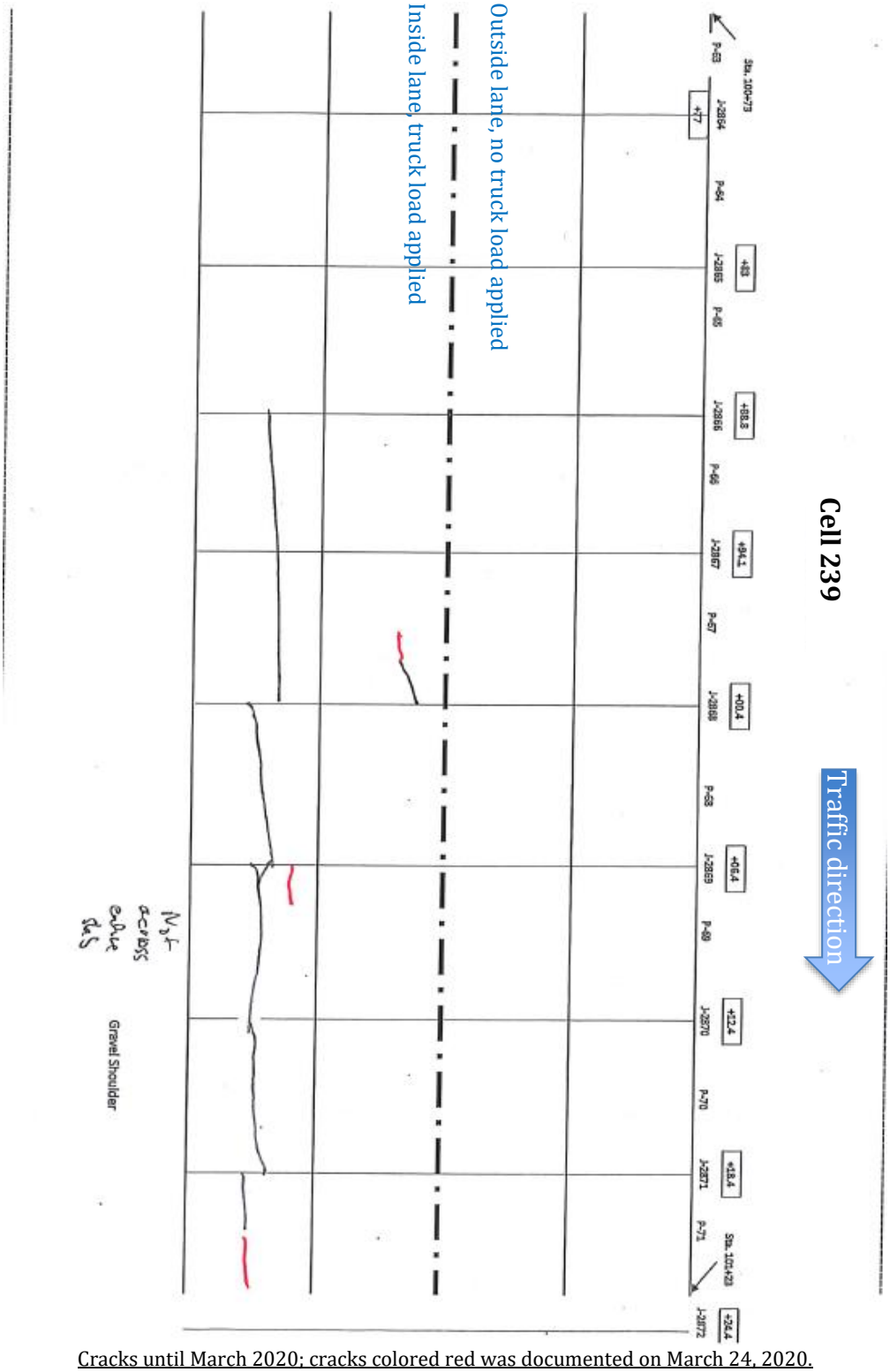

Cracks until March 2020; cracks colored red was documented on March 24, 2020.

Figure A8: Distress map for Cell 239 contd.

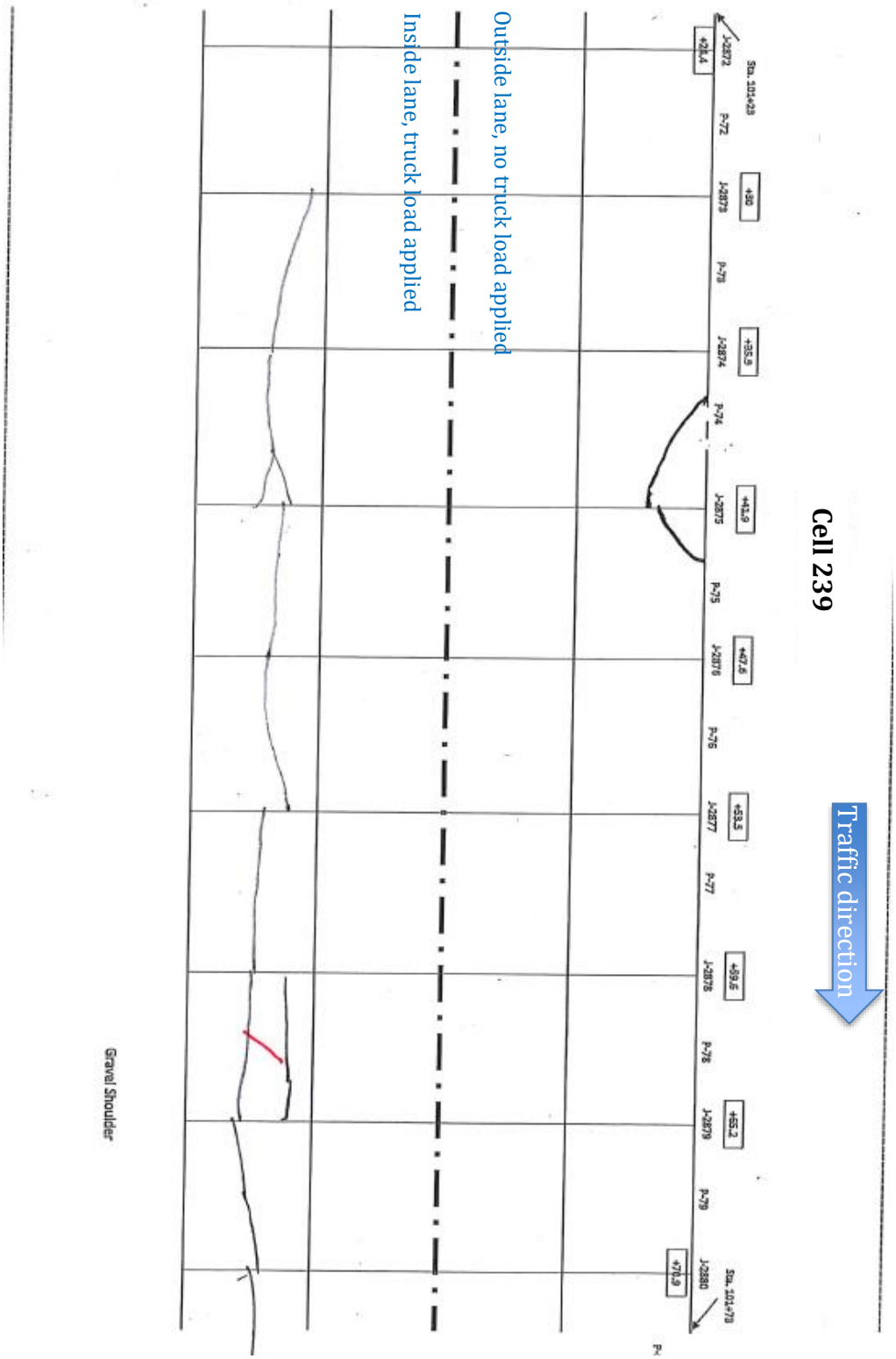

Cracks until March 2020; cracks colored red were documented on March 24, 2020.

Figure A9: Distress map for Cell 239 contd.

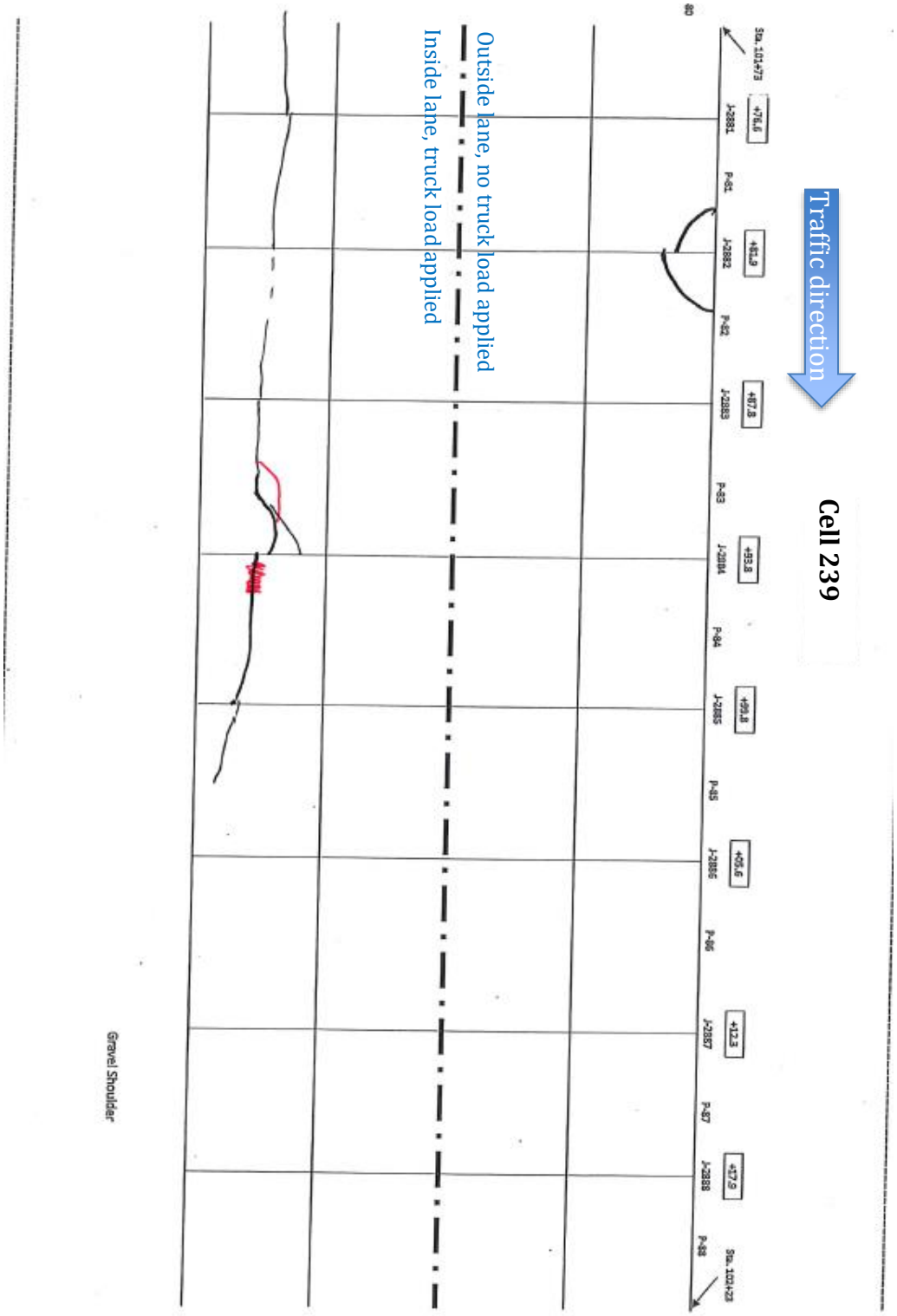

Cracks until March 2020; cracks colored red were documented on March 24, 2020.

Figure A10: Distress map for Cell 239 contd.

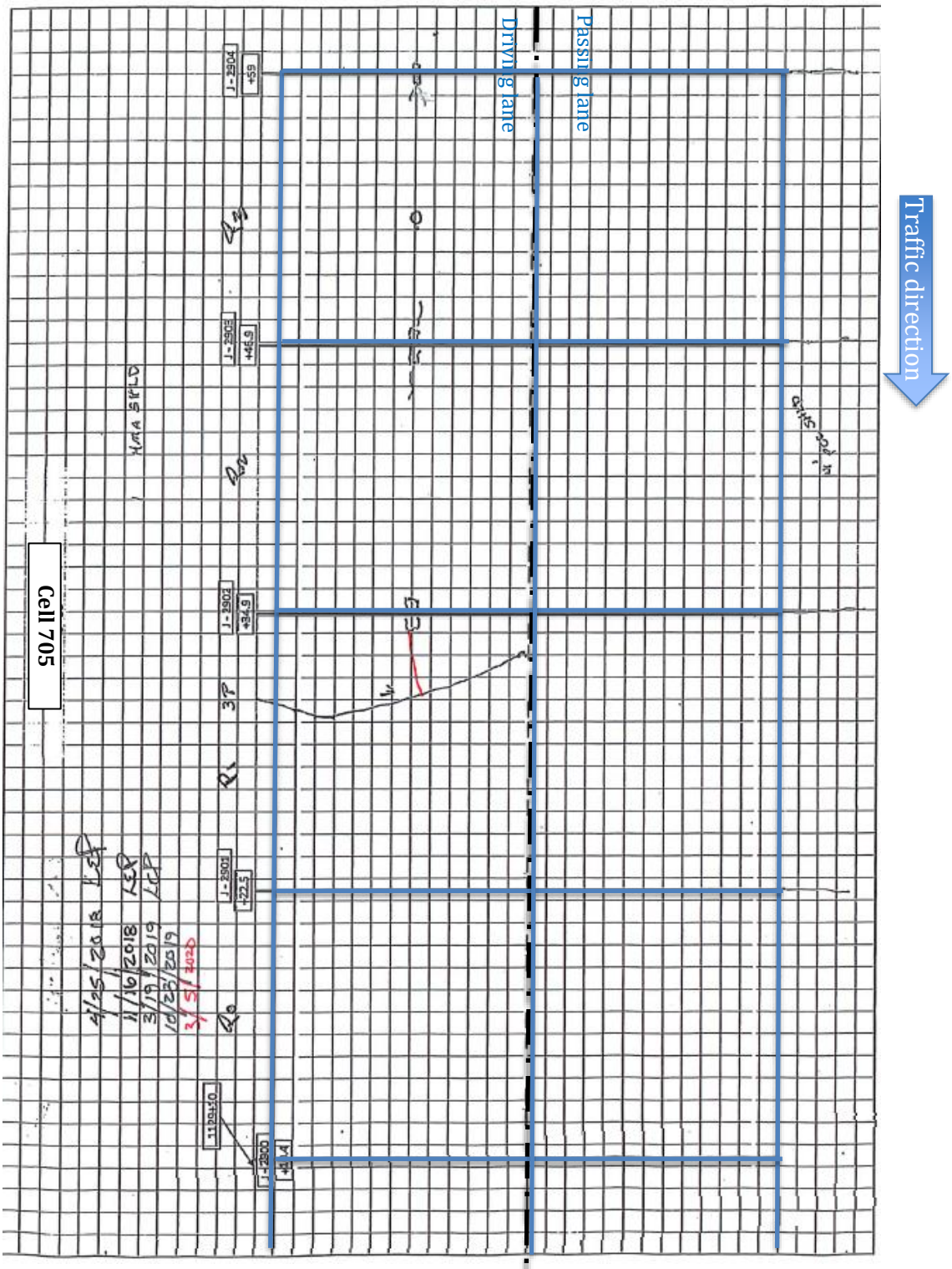

Cracks until March 2020; cracks colored red was documented on March 5, 2020.

Figure A12: Distress map for Cell 705.

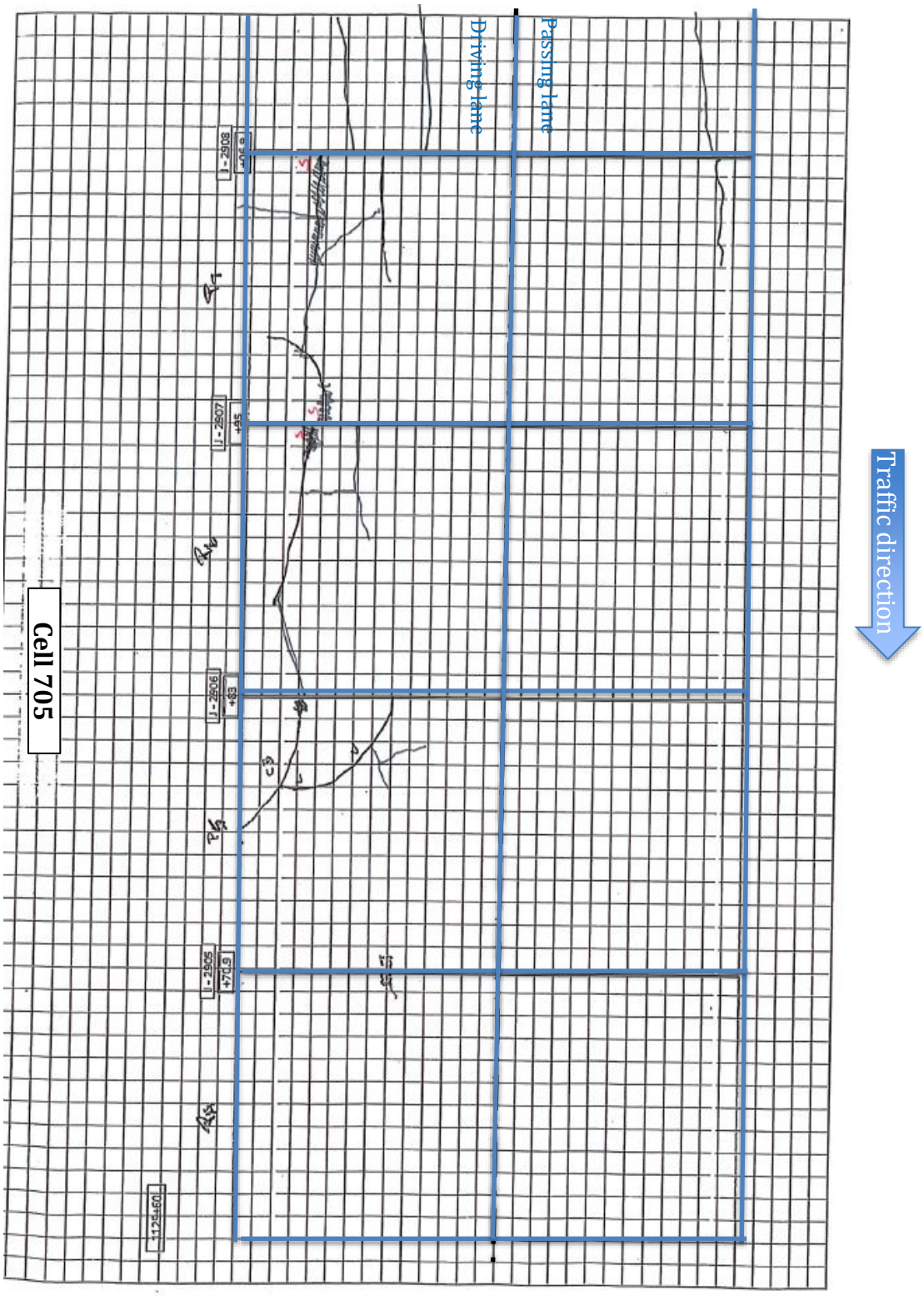

Figure A13: Distress map for Cell 705 contd.

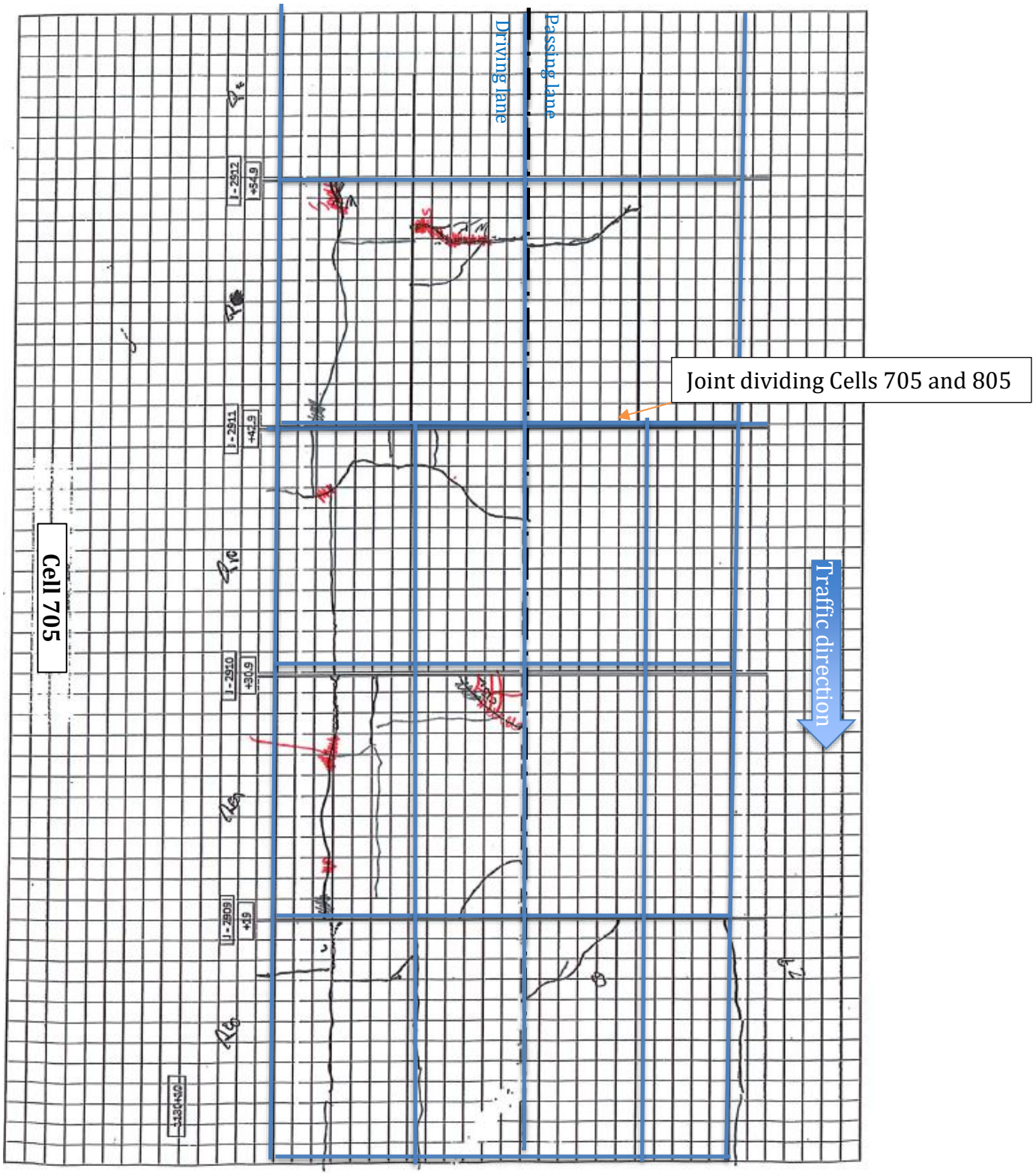

Cracks until March 2020; cracks/spalls colored red were documented on March 5, 2020 (not to scale).

Figure A14: Distress map for Cell 705 contd.

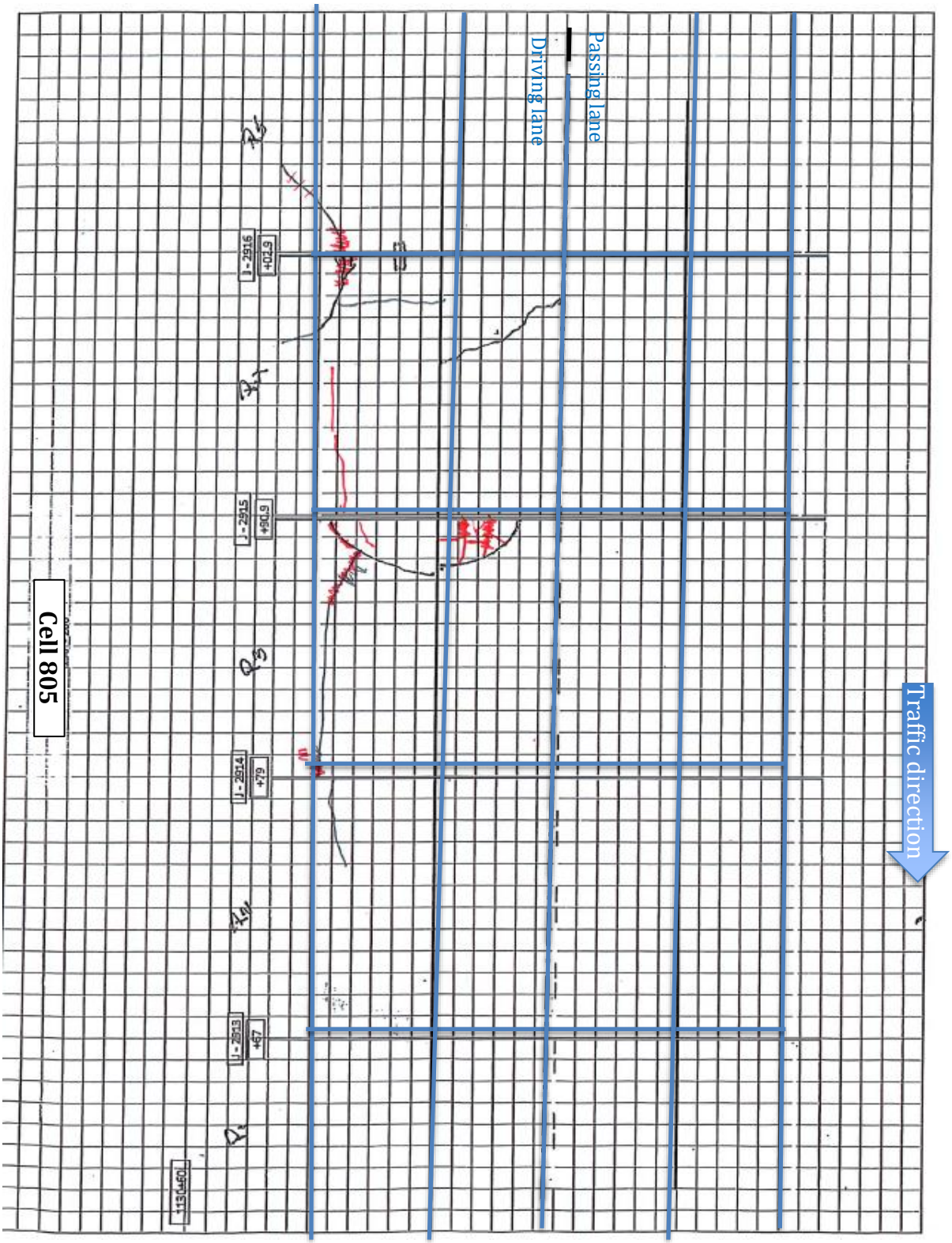

Cracks until March 2020; cracks/spalls colored red was documented on March 5, 2020
(not to scale, Driving:6' x 12' and 8' x 12';Passing:6' x 12' and 6' x 12').

Figure A15: Distress map for Cell 805.

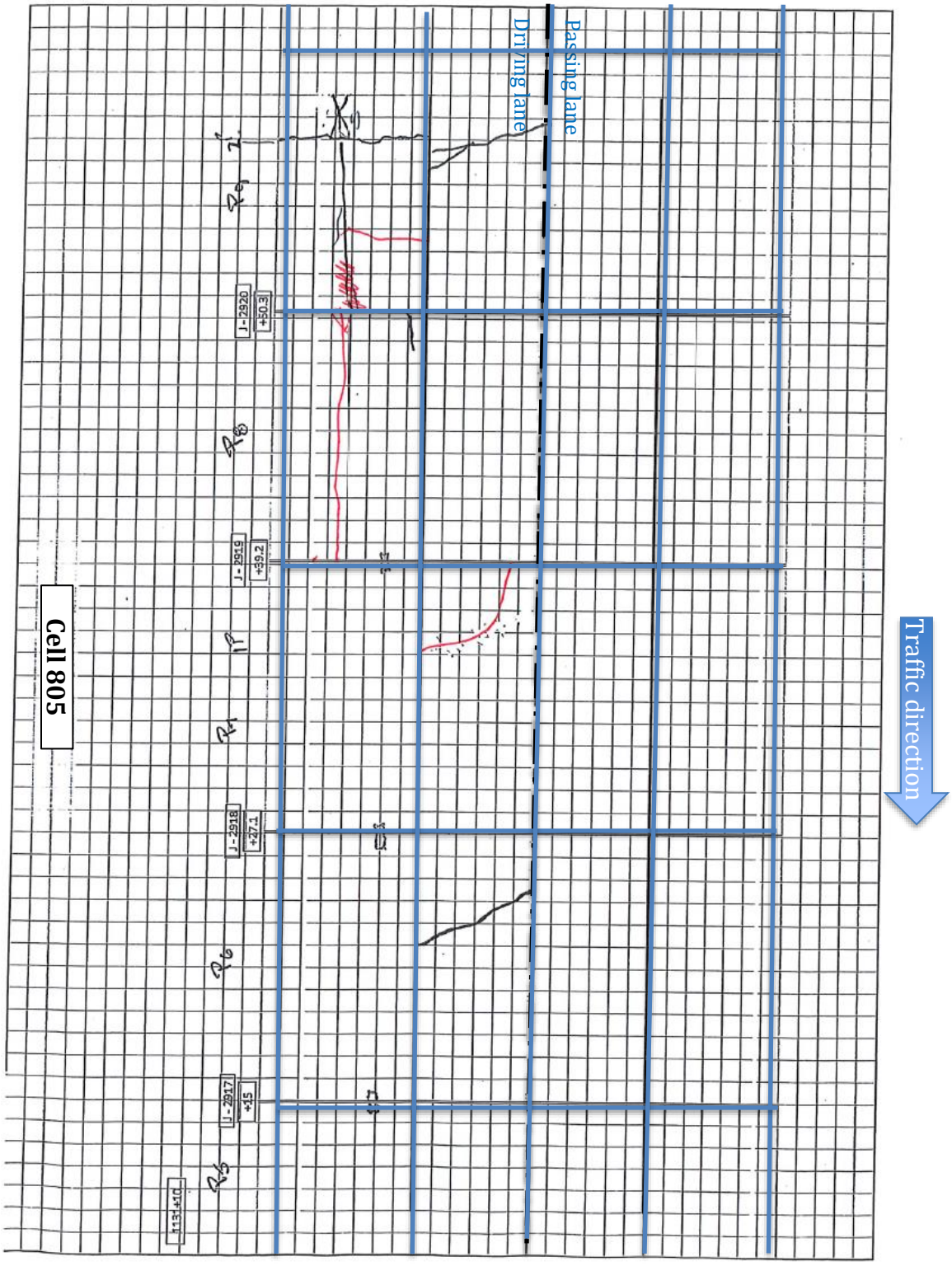

Cracks until March 2020; cracks/spalls colored red were documented on March 5, 2020
(not to scale, Driving:6' x 12' and 8' x 12';Passing:6' x 12' and 6' x 12').

Figure A16: Distress map for Cell 805 contd.

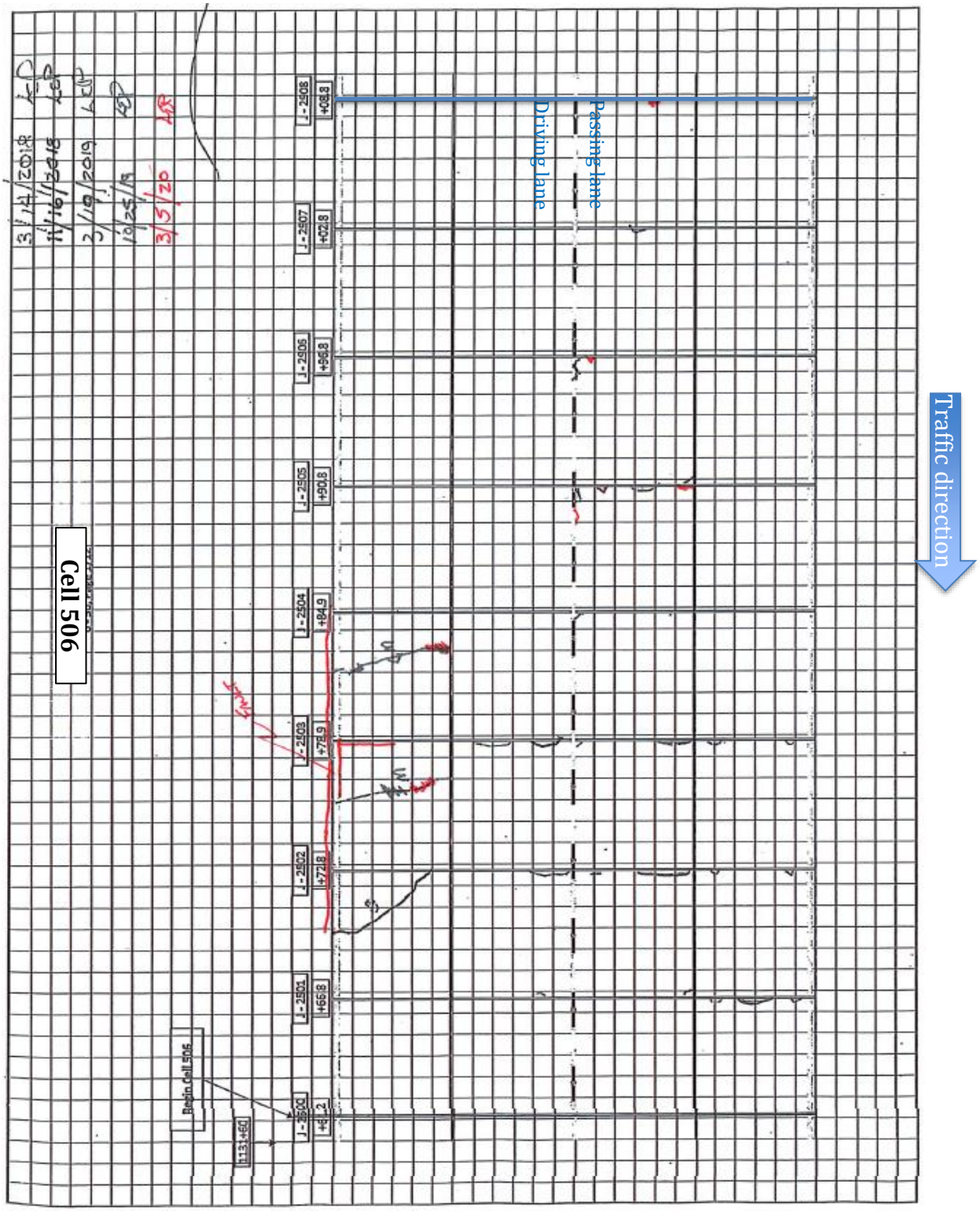

Cracks until March 2020; cracks/spalls colored in red were documented on March 5, 2020(not to scale).

Figure A17: Distress map for Cell 506.

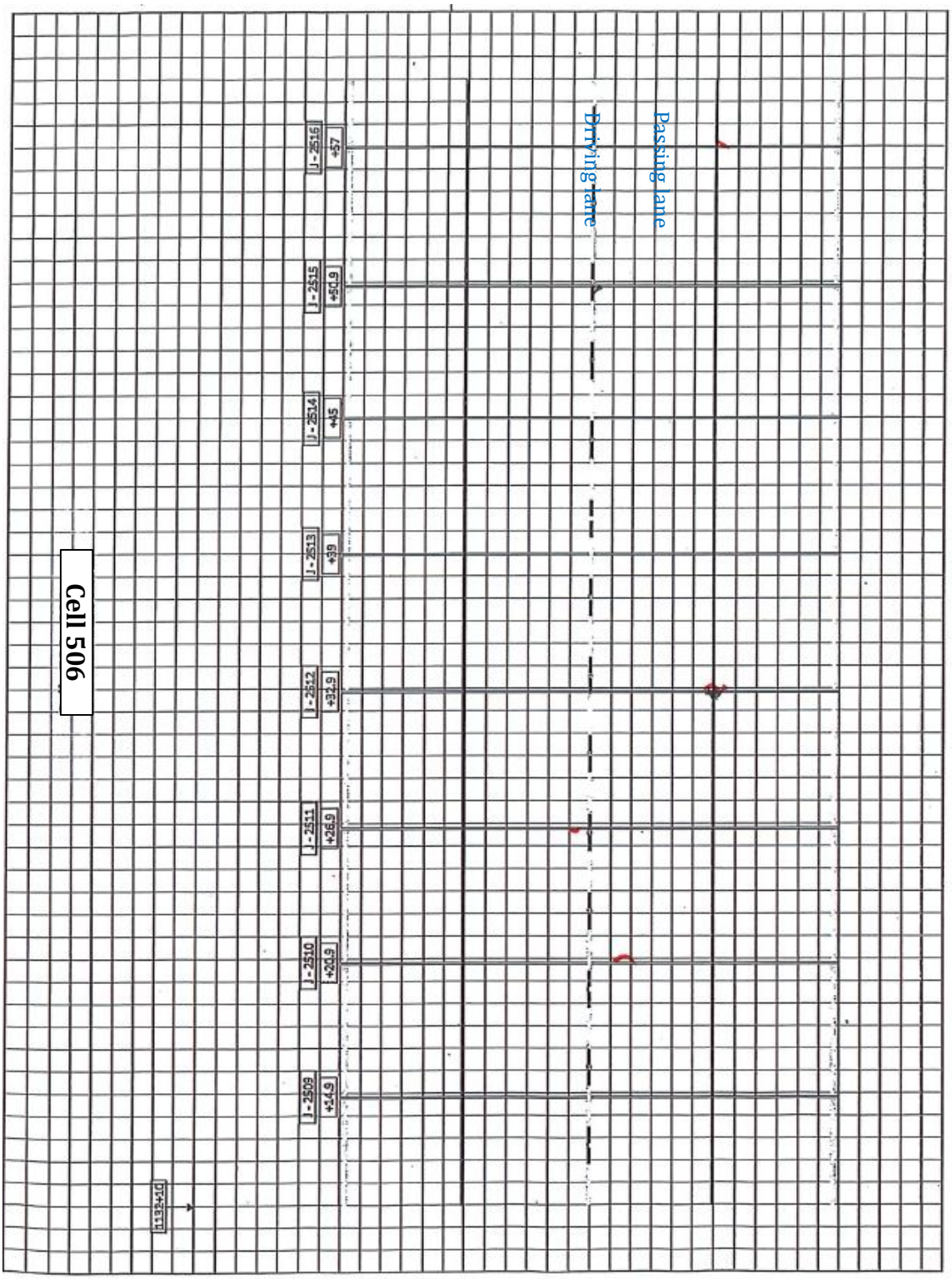

Cracks until March 2020; cracks/spalls colored red were documented on March 5, 2020.

Figure A18: Distress map for Cell 506 contd.

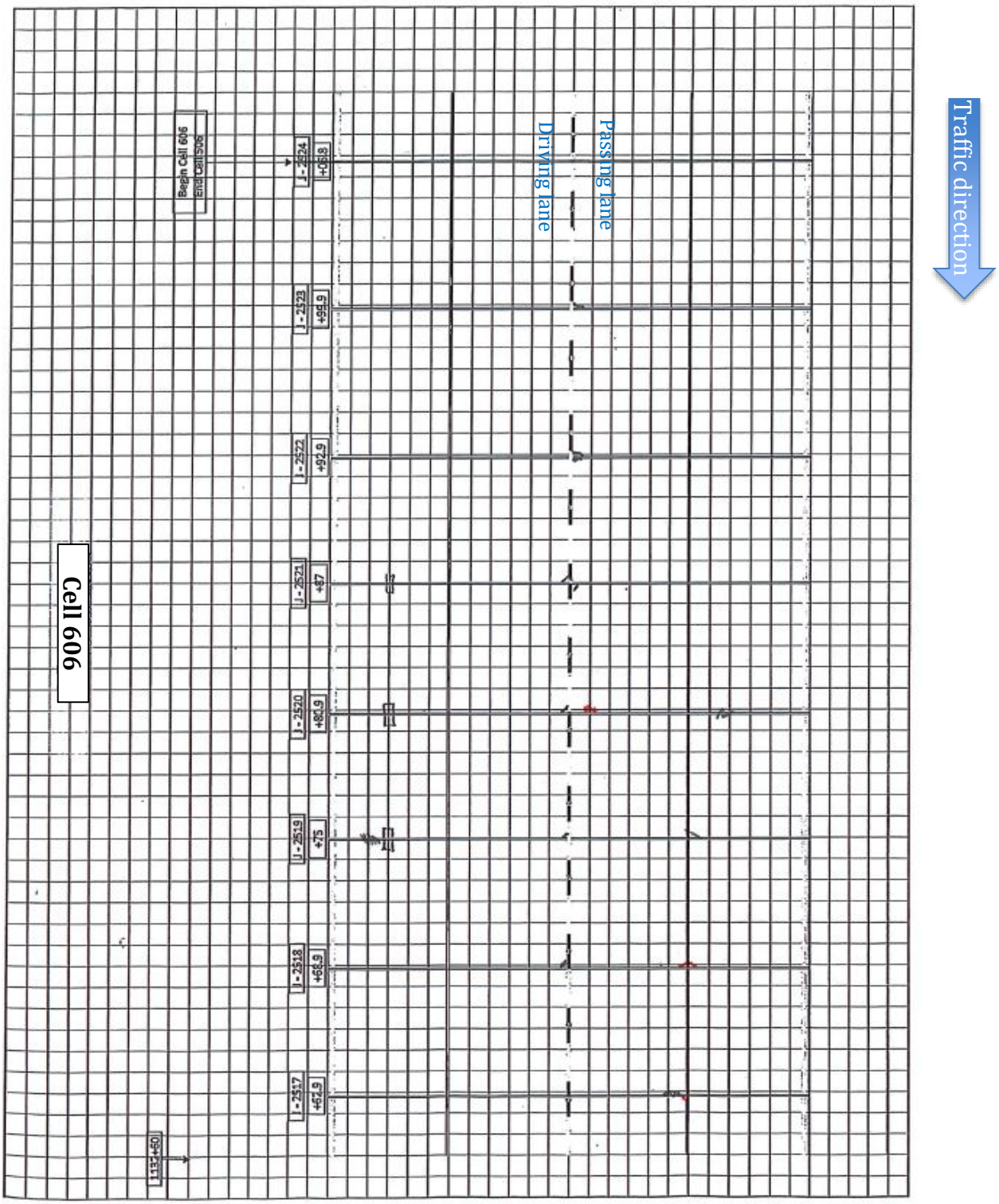

Figure A19: Distress map for Cell 606.

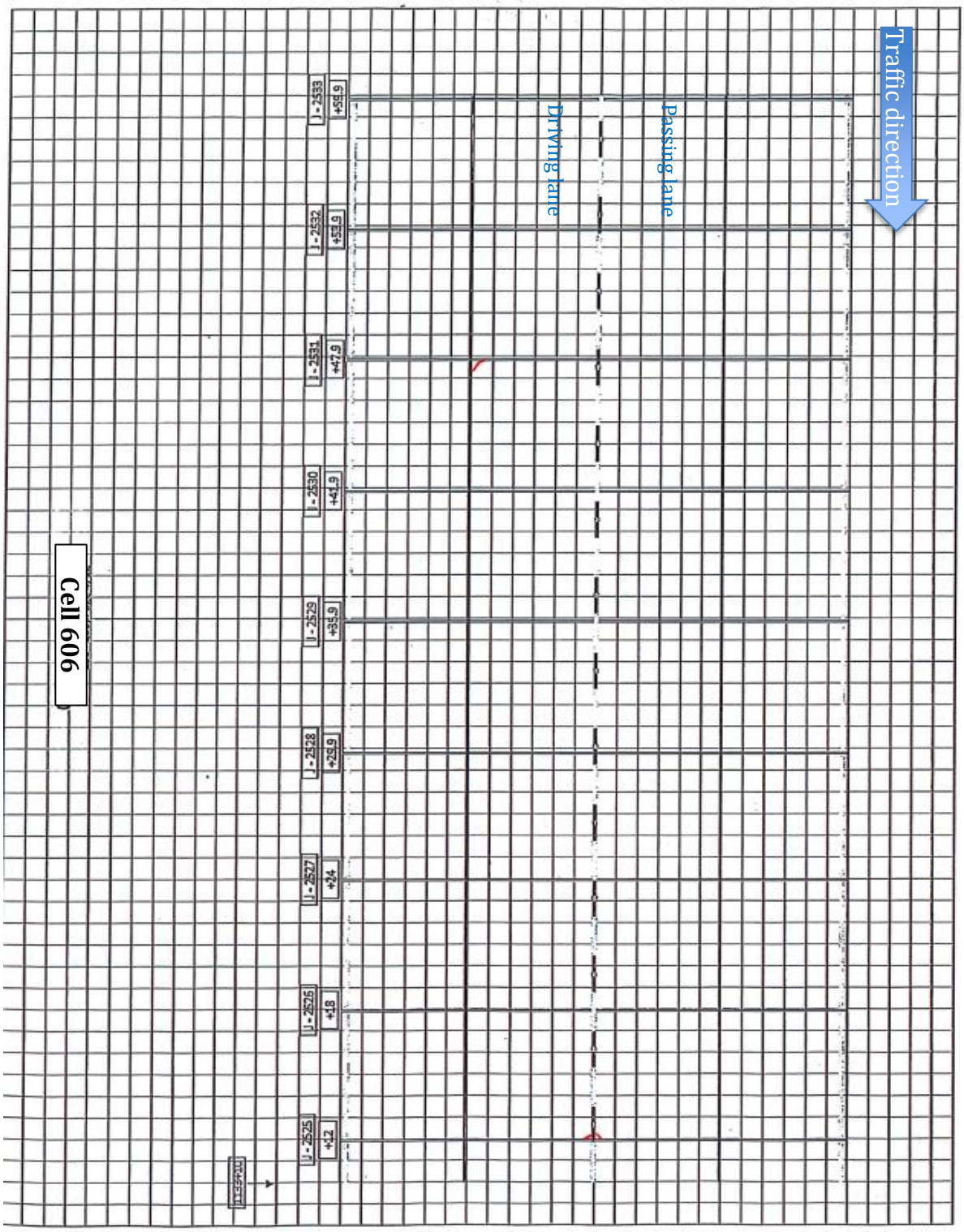

Cracks until March 2020; cracks/spalls colored red were documented on March 5, 2020.

Figure A20: Distress map for Cell 606 contd.

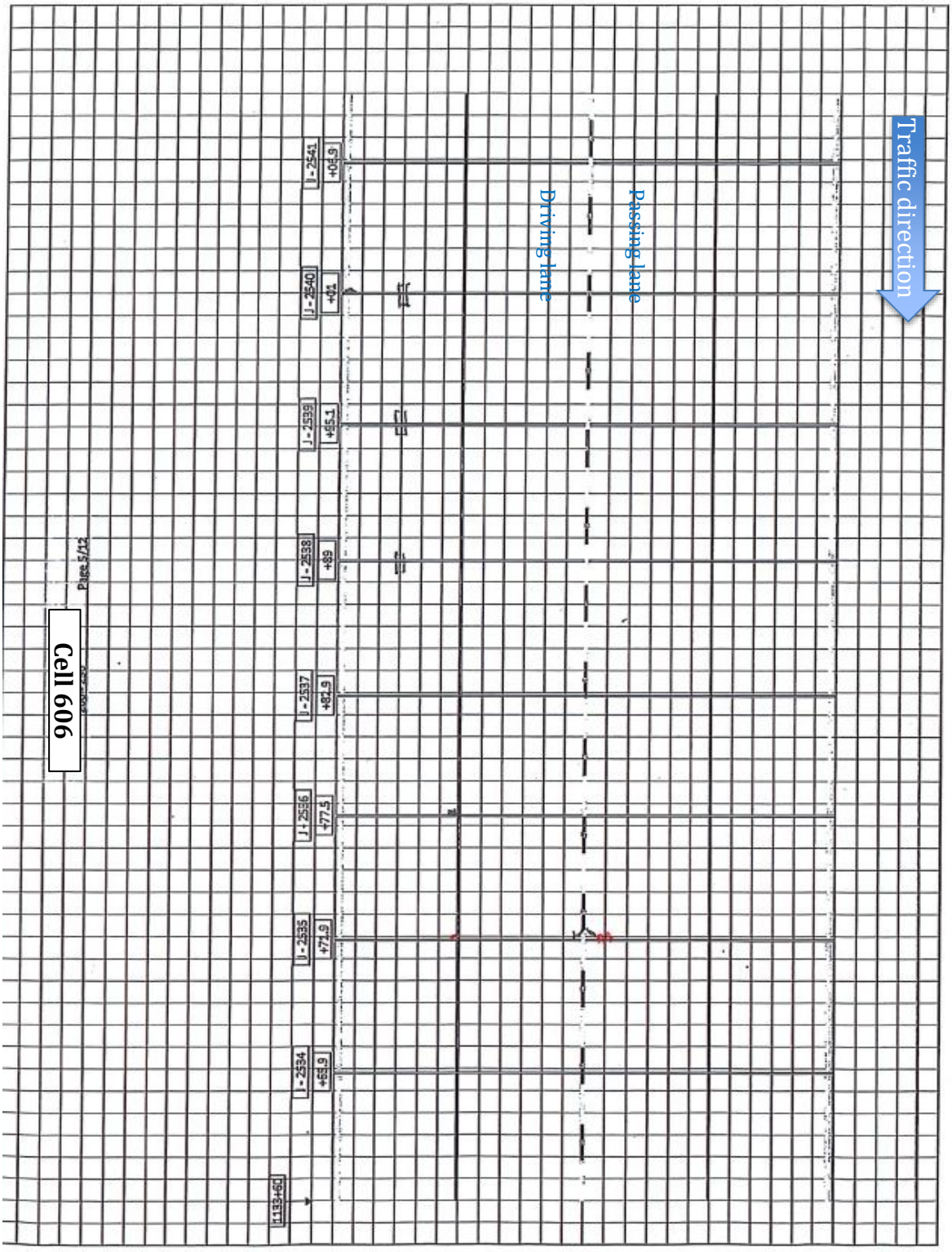

Cracks until March 2020; cracks/spalls colored red were documented on March 5, 2020.

Figure A21: Distress map for Cell 606 contd.

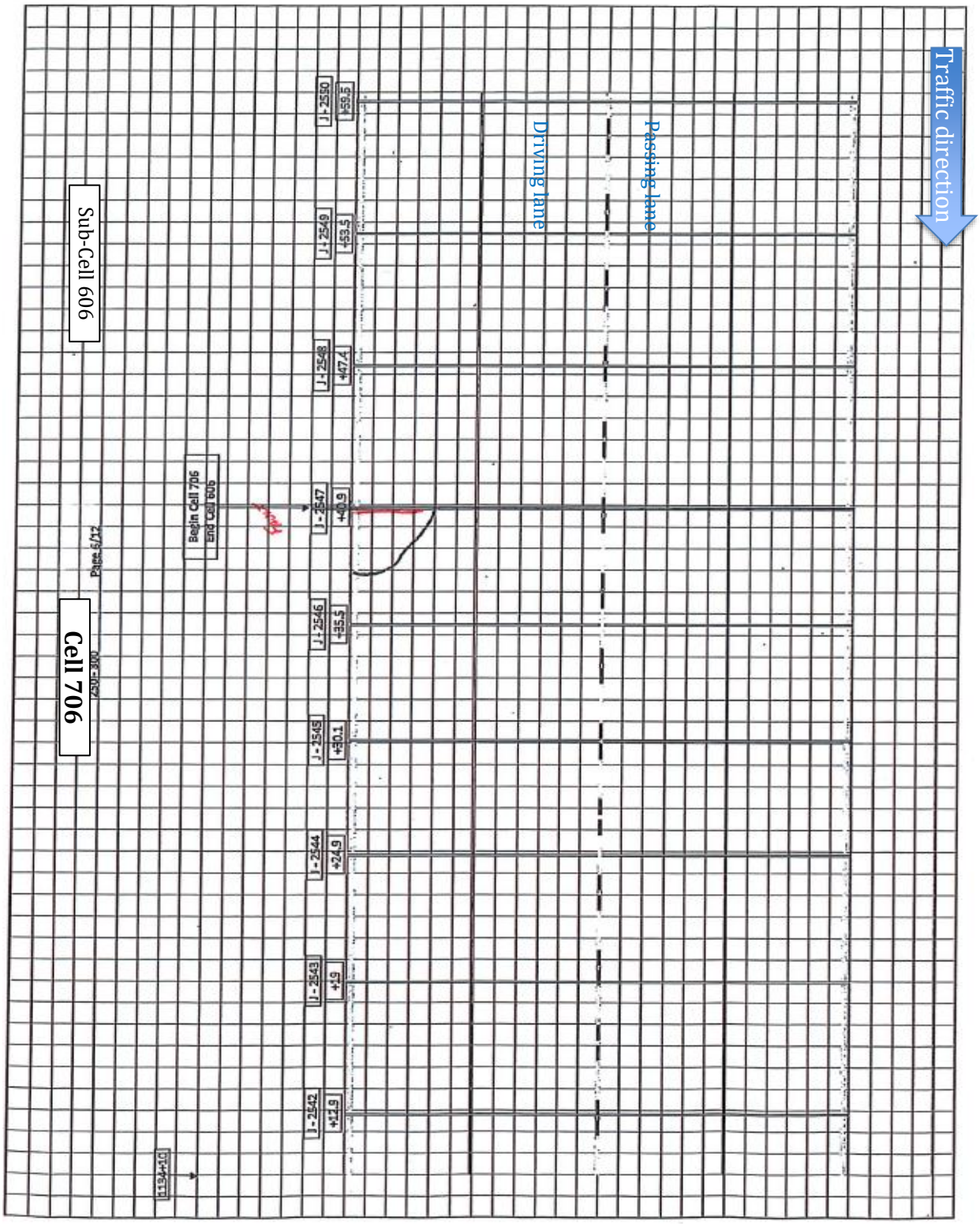

Cracks until March 2020; cracks/spalls colored in red were documented on March 5, 2020.

Figure A23: Distress map for Cells 606 through 706.

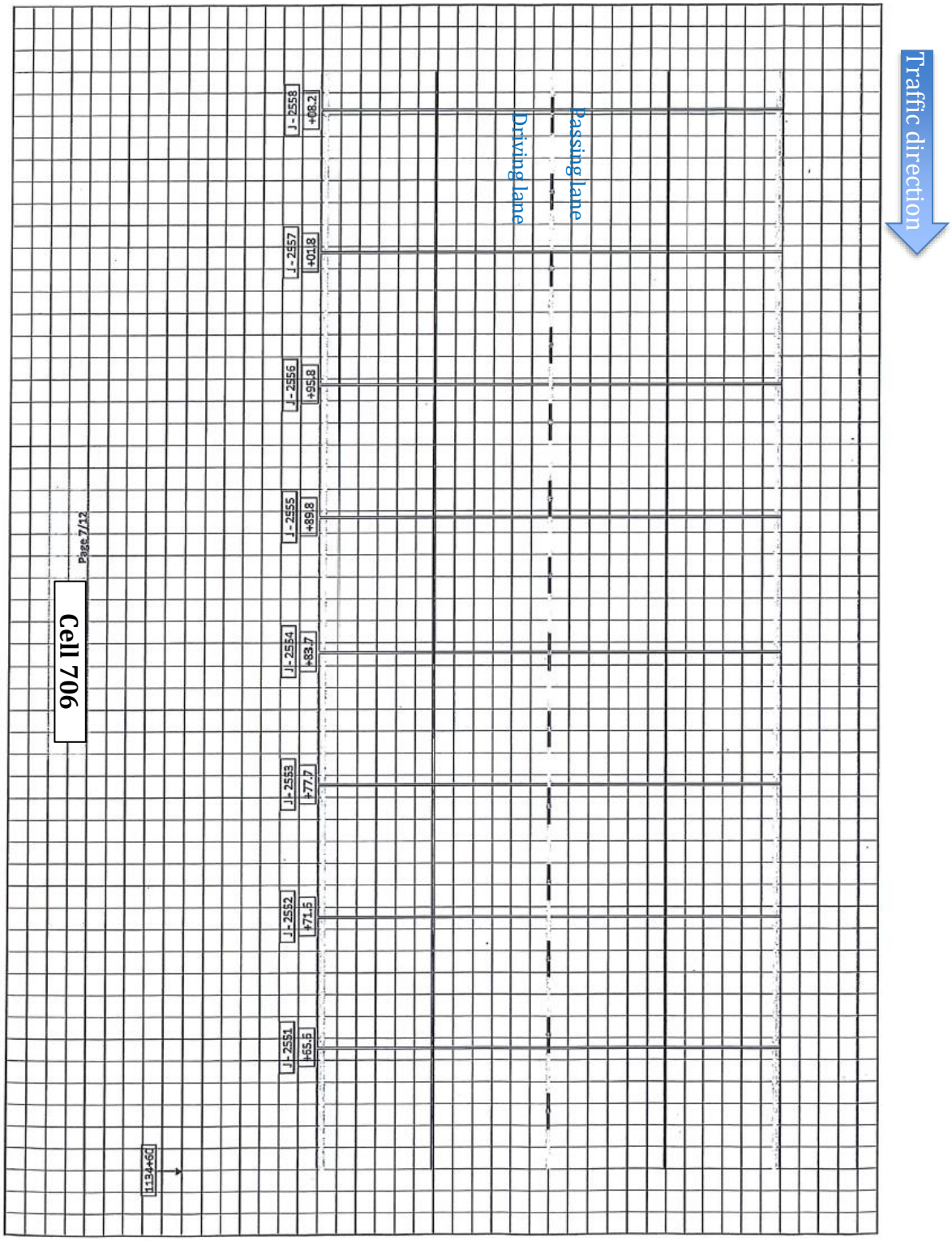

Figure A24: Distress map for Cells 706 contd.

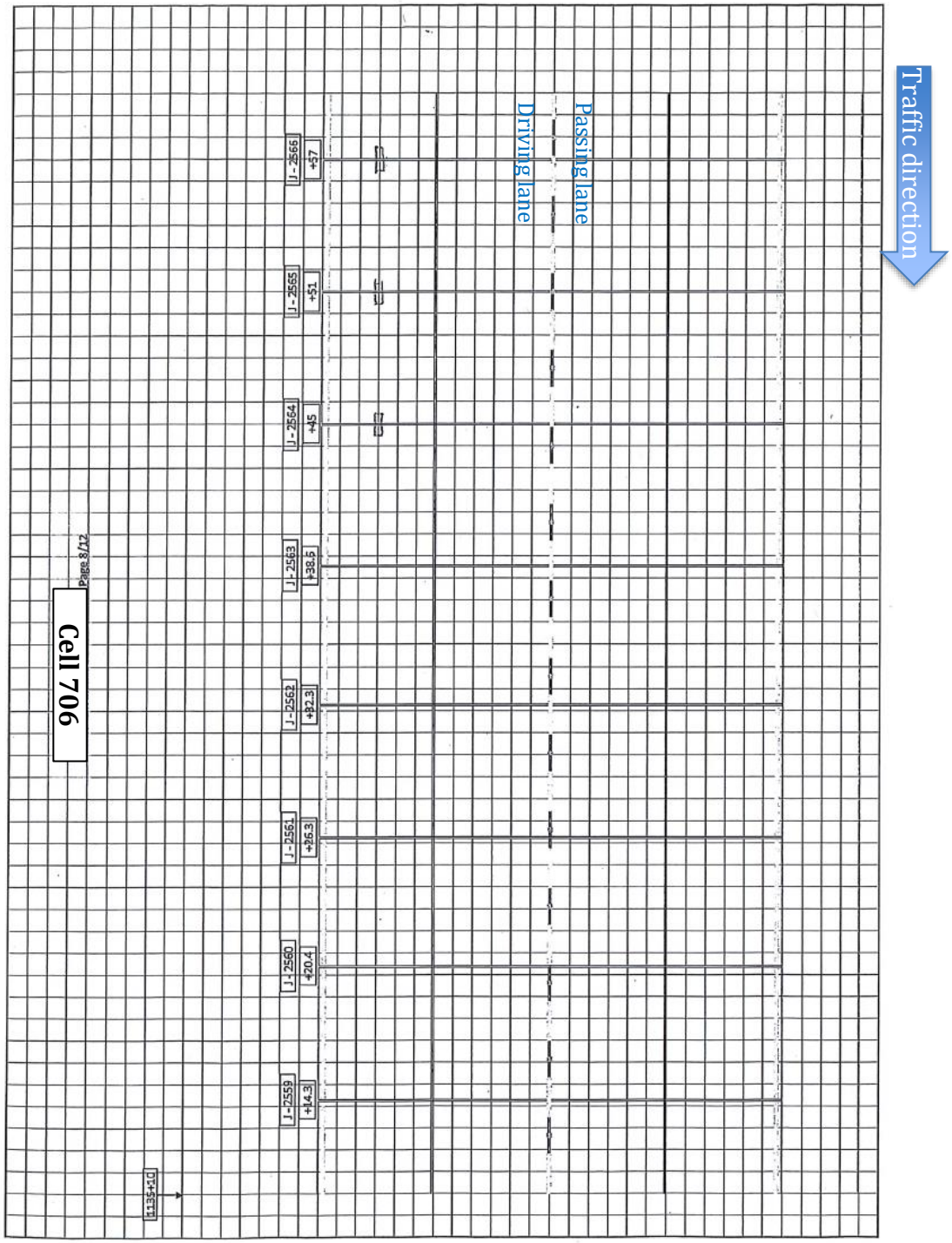

Figure A25: Distress map for Cell 706 contd.

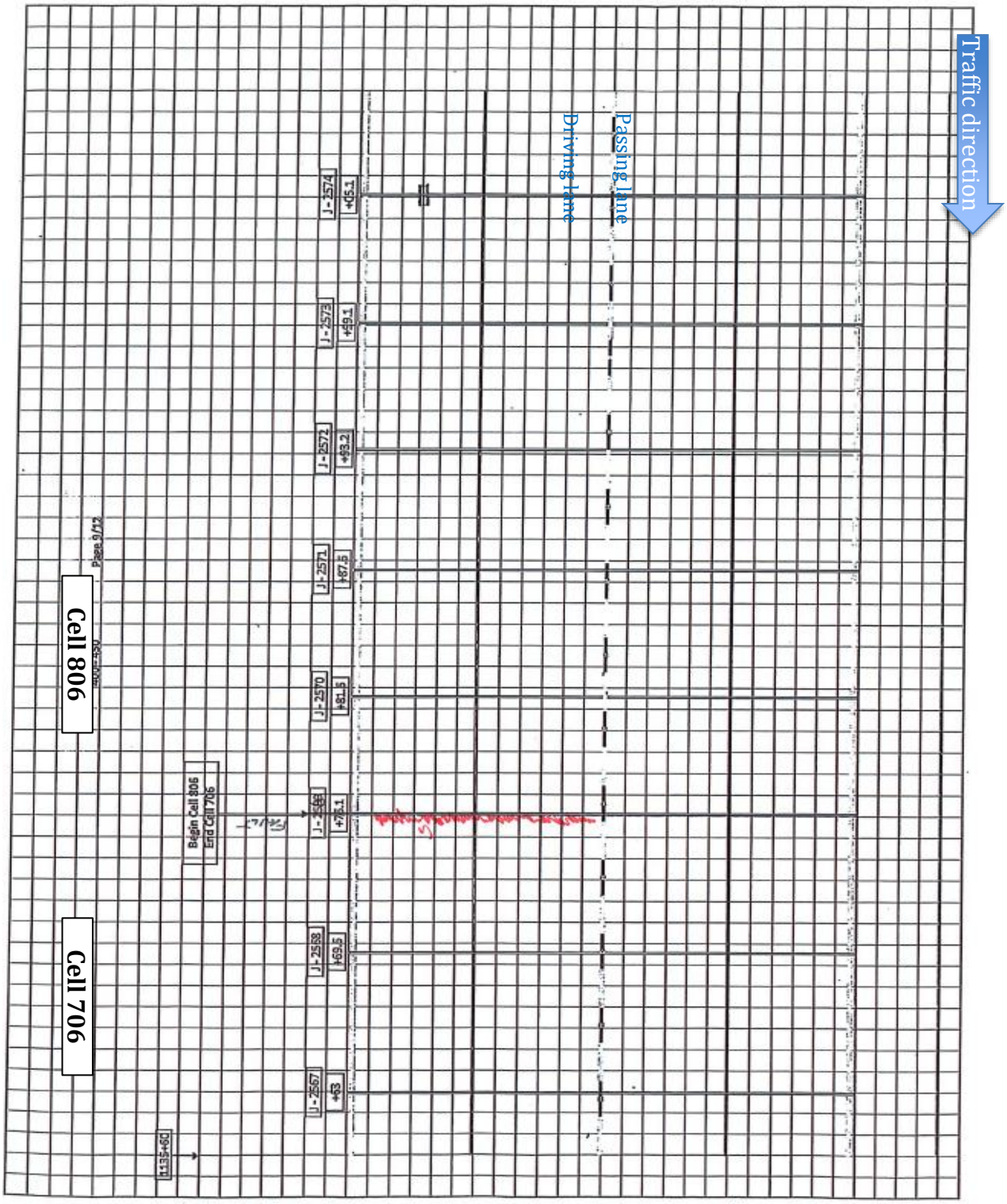

Cracks until March 2020; cracks/spalls colored in red were documented on March 5, 2020.

Figure A 26: Distress map for Cells 706 through 806 contd.

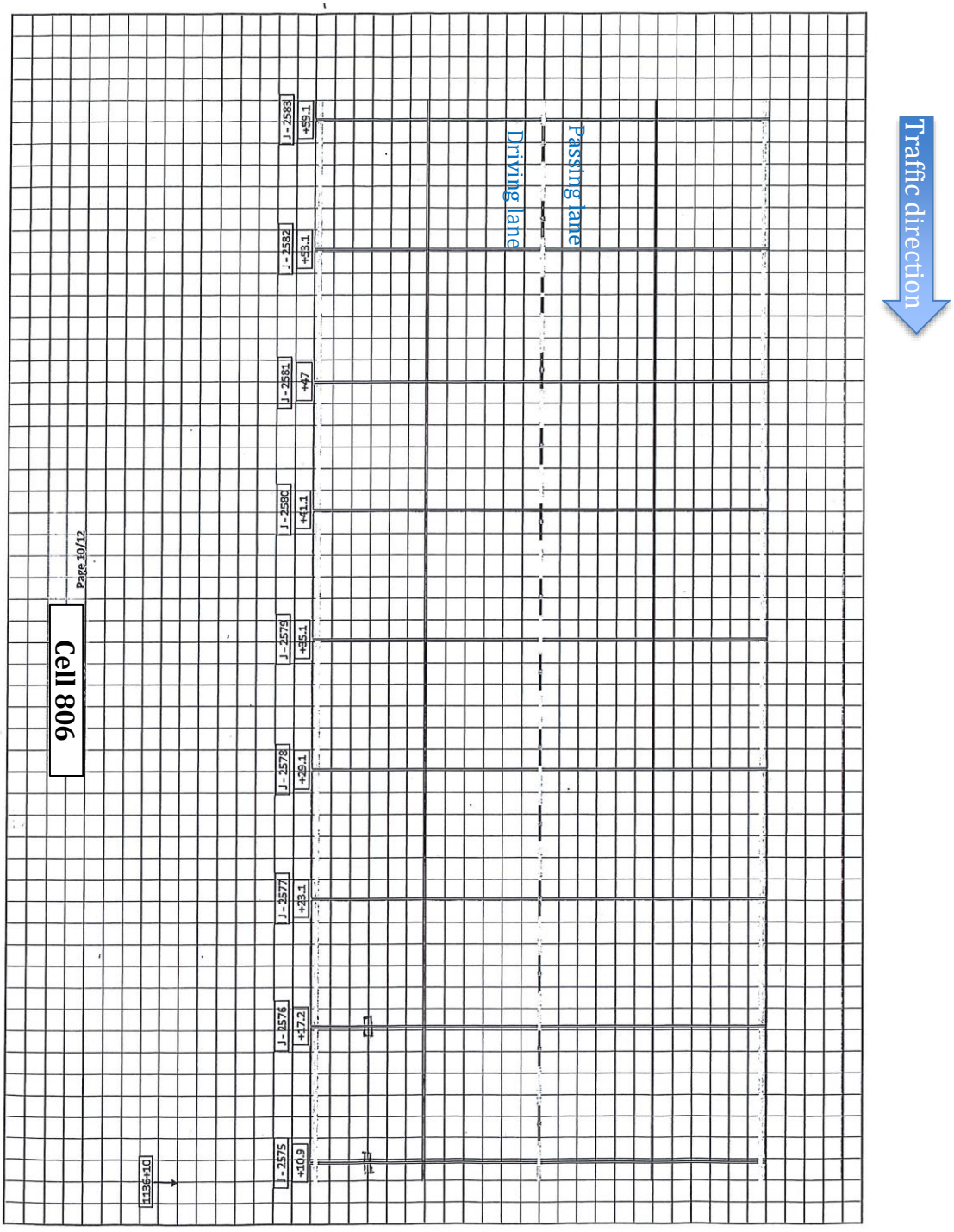

Figure A27: Distress map for Cell 806 contd.

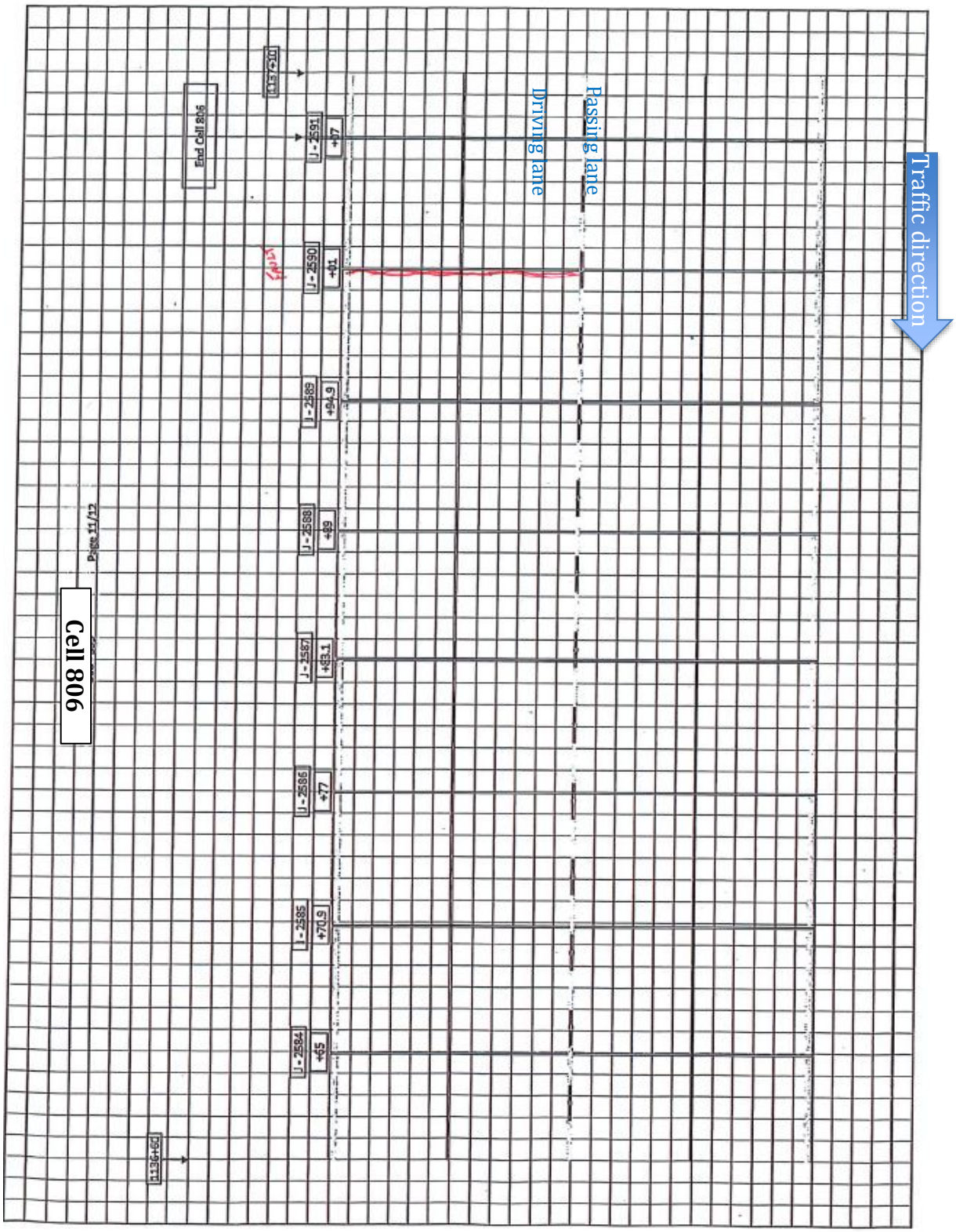

Cracks until March 2020; cracks/spalls colored in red were documented on March 5, 2020.

Figure A28: Distress map for Cell 806 contd.

APPENDIX B

Joint Movement Data from Spring Loaded Potentiometer

Note: This Appendix presents the joint movement data recorded by the spring-loaded potentiometers installed at different cells. Note that some of the data are appeared to be erroneous and not considered for any analysis.

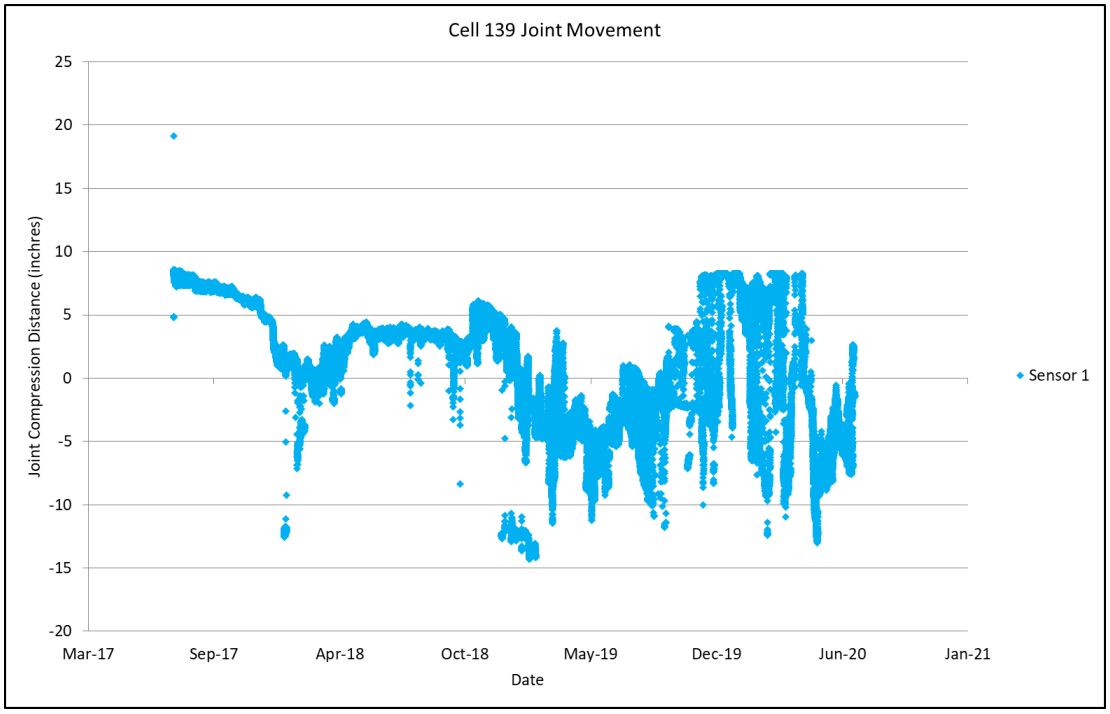

Figure B1. Joint movement data for Cell 139, Sensor 1.

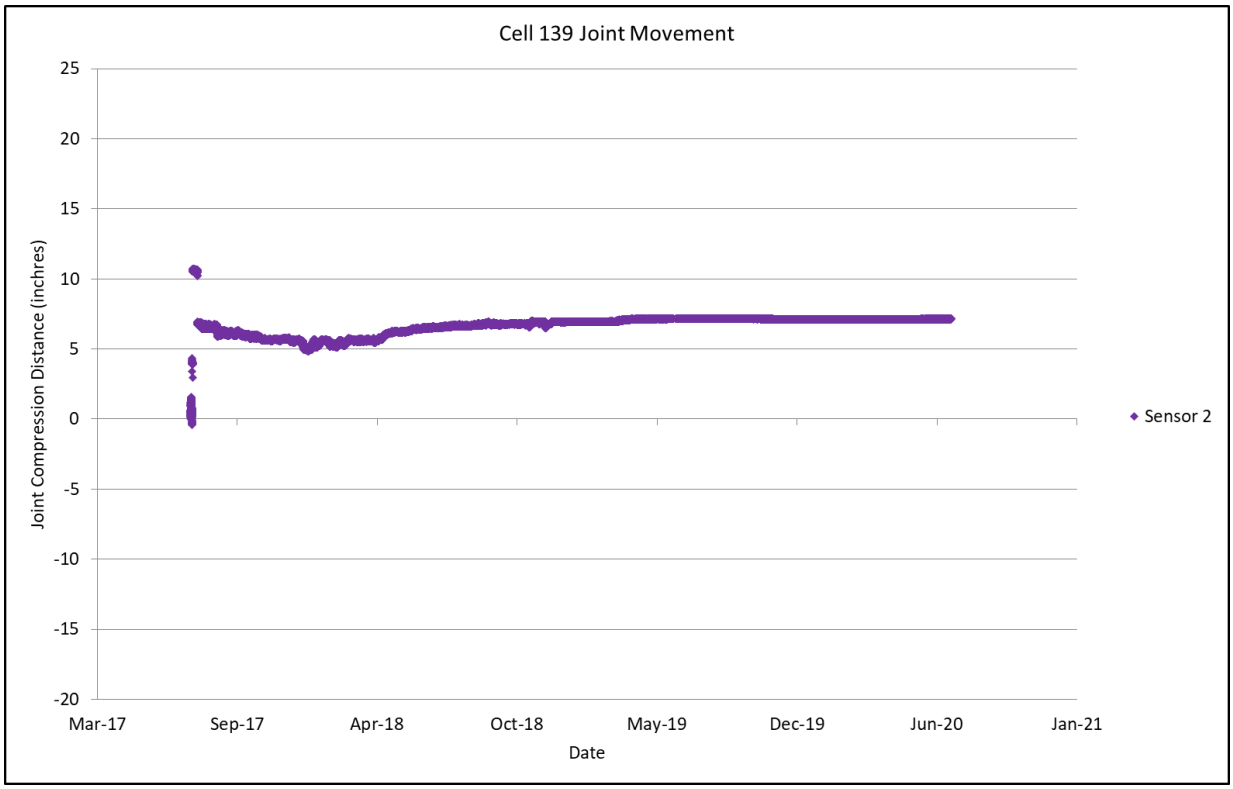

Figure B2. Joint movement data for Cell 139, Sensor 2.

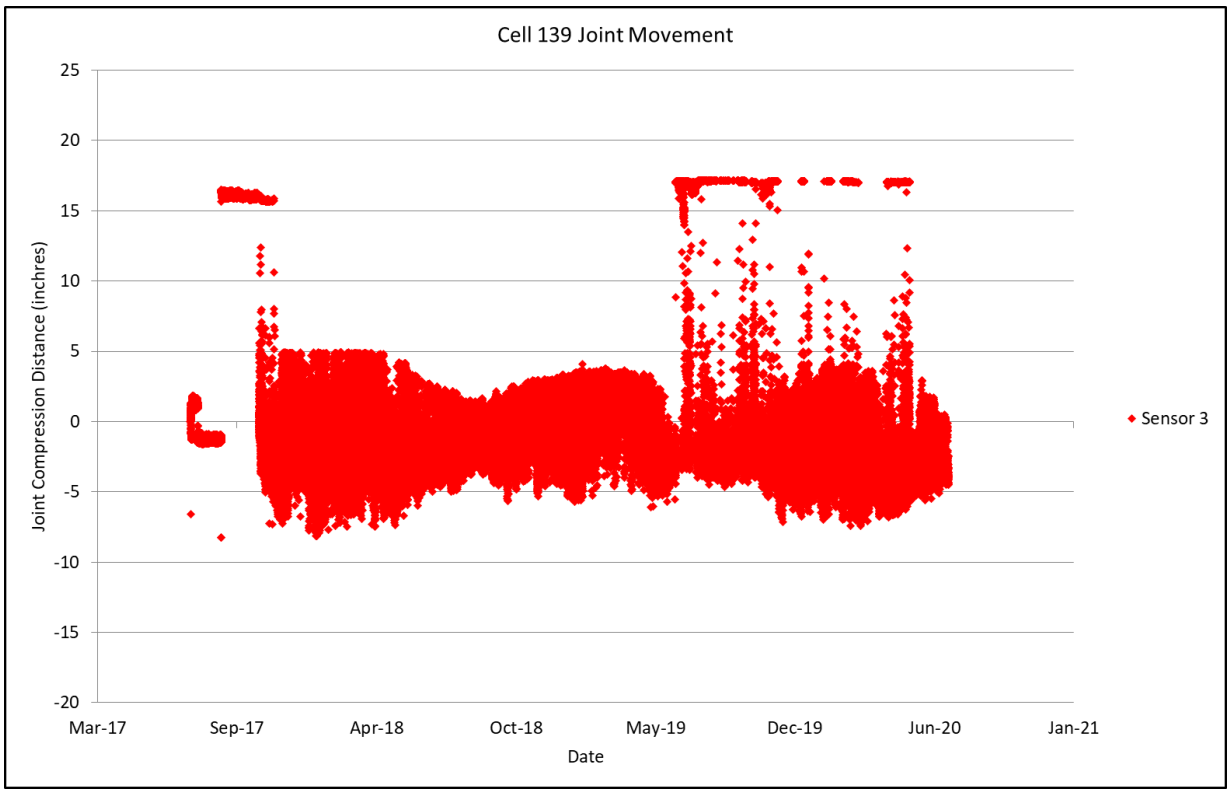

Figure B3. Joint movement data for Cell 139, Sensor 3 **(Bad sensor)**.

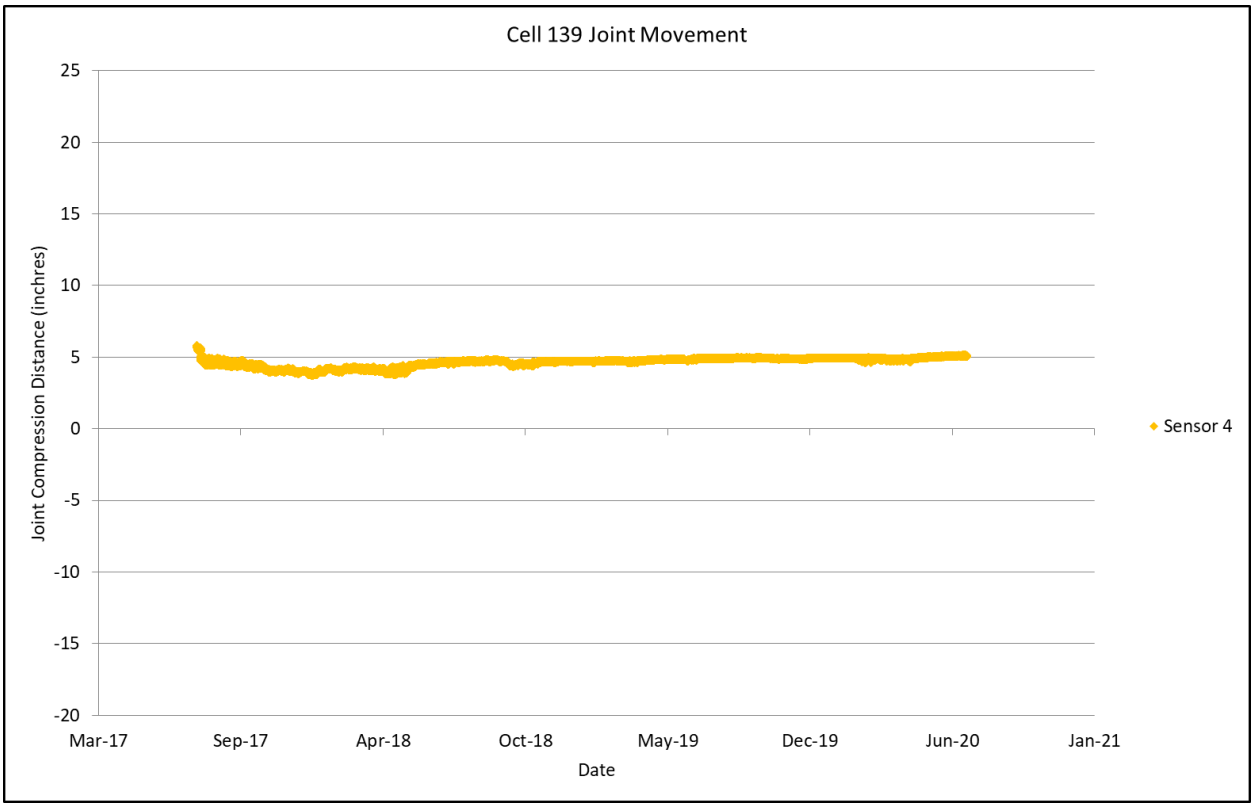

Figure B4. Joint movement data for Cell 139, Sensor 4.

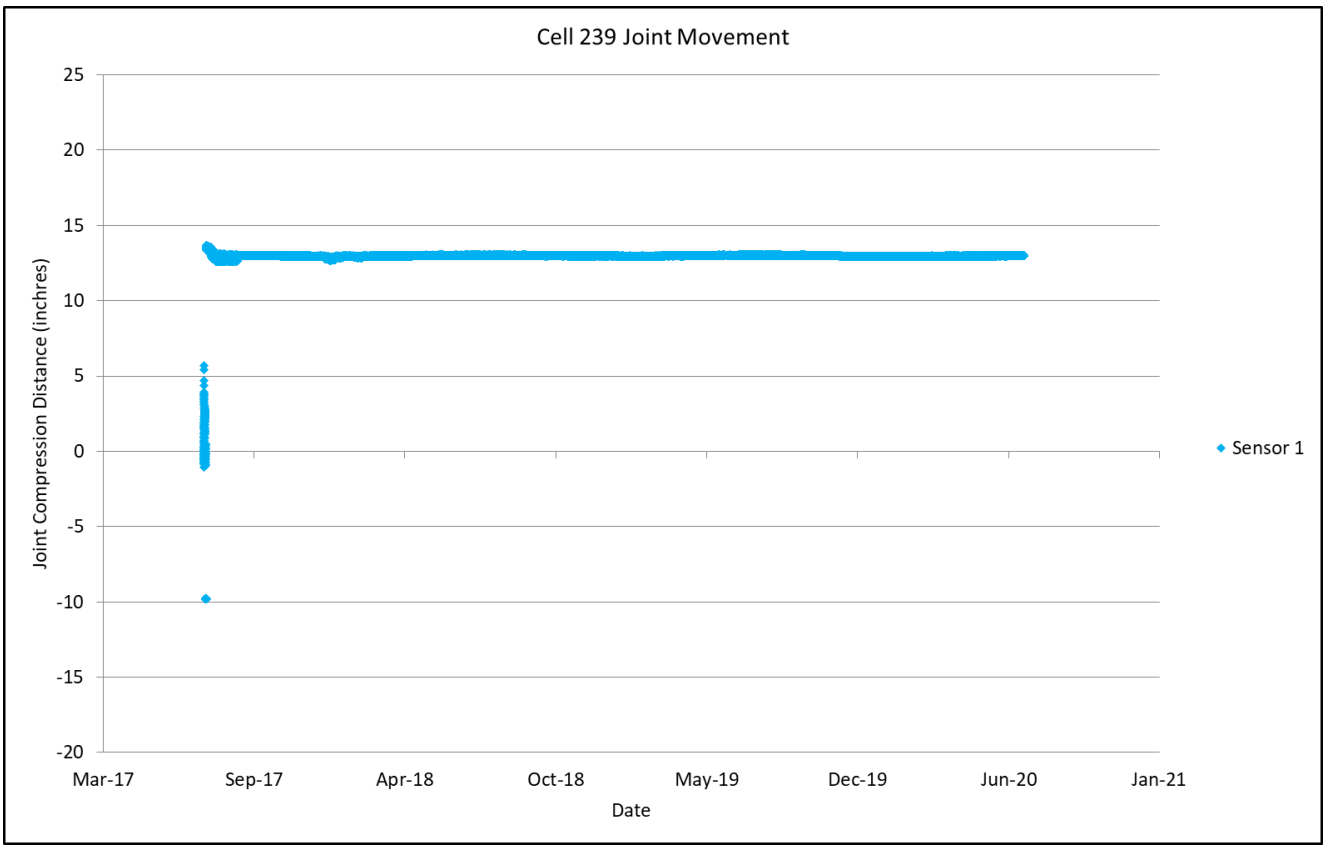

Figure B5. Joint movement data for Cell 239, Sensor 1.

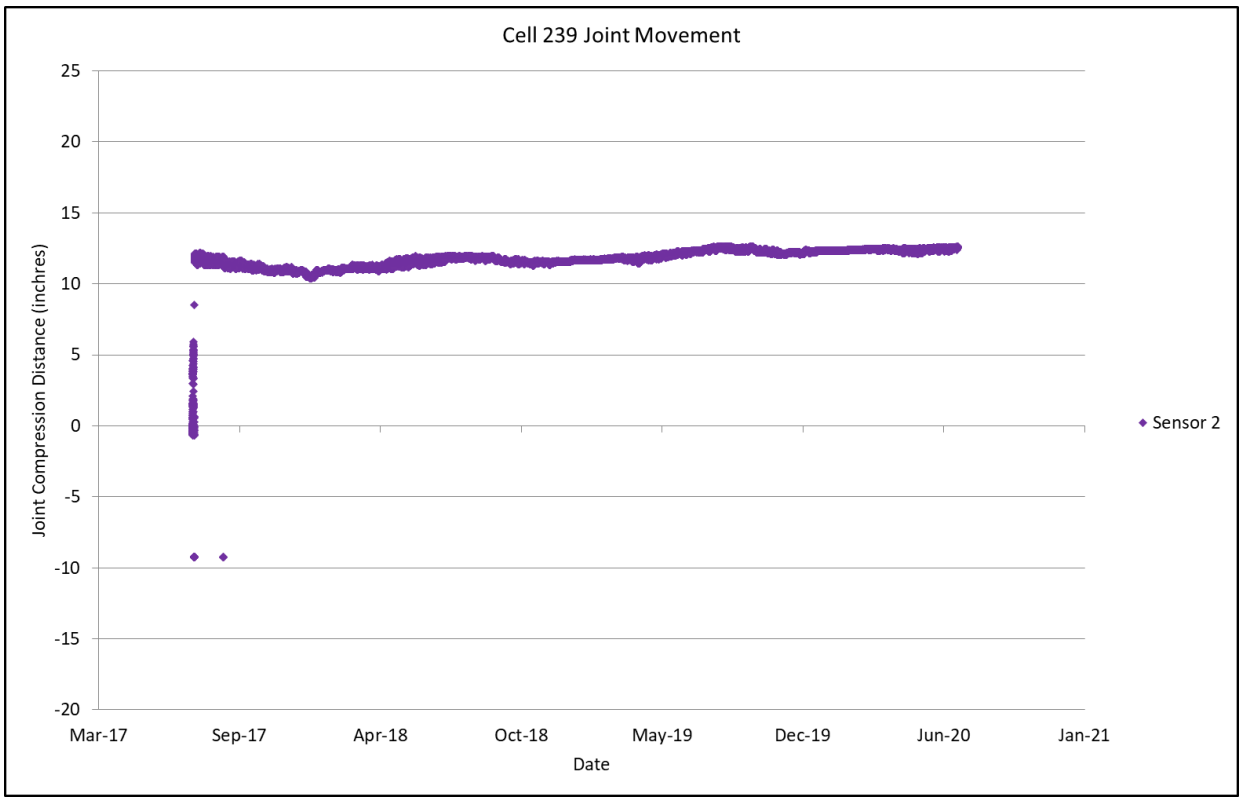

Figure B6. Joint movement data for Cell 239, Sensor 2.

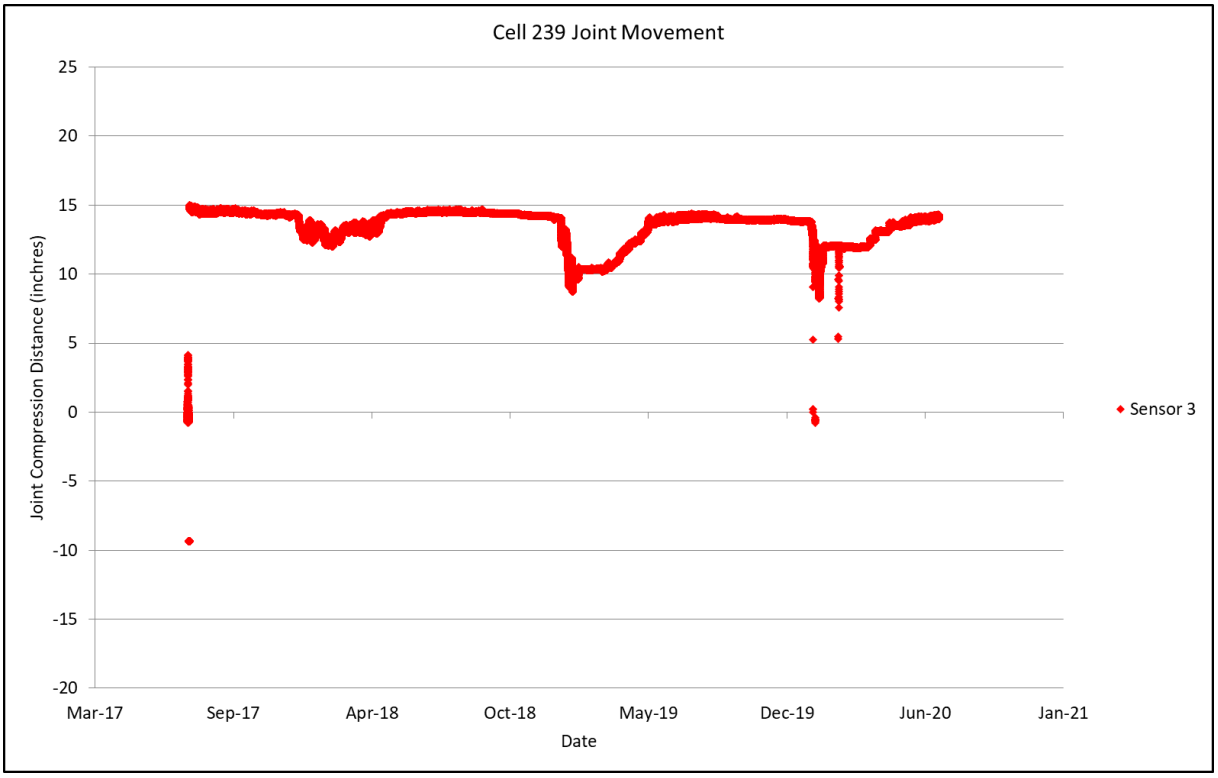

Figure B7. Joint movement data for Cell 239, Sensor 3.

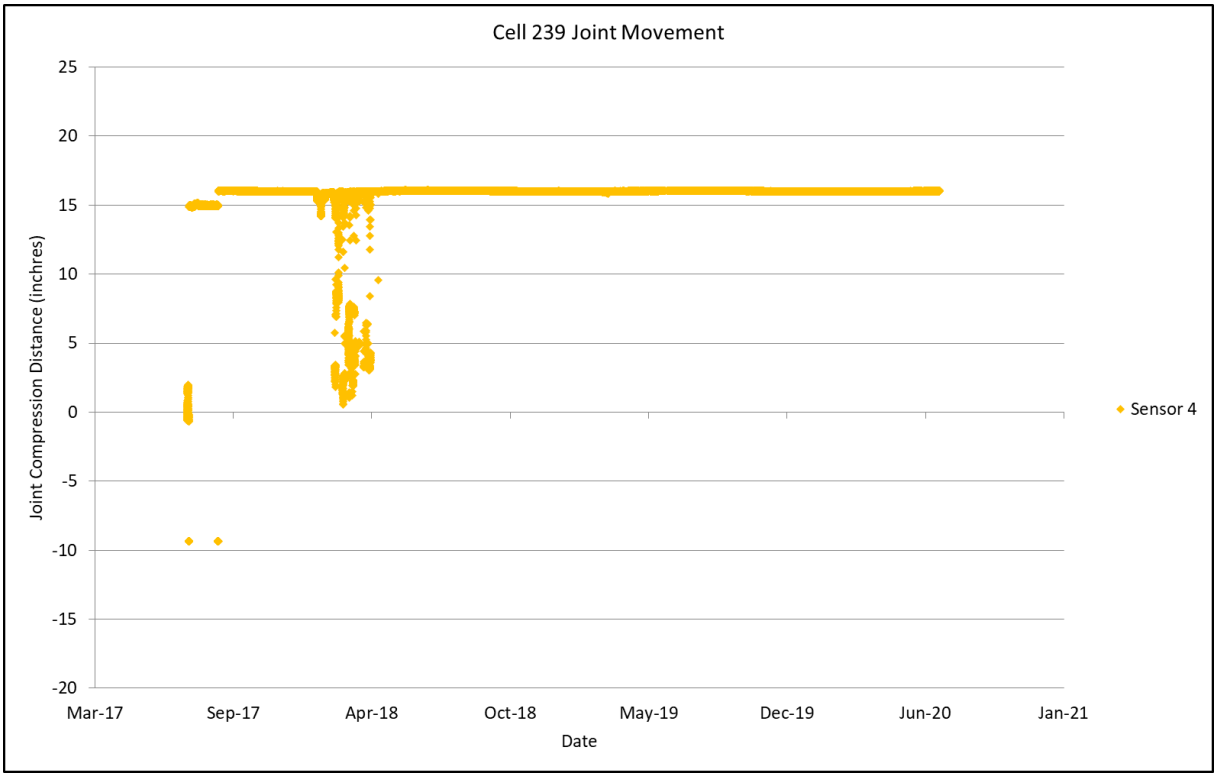

Figure B8. Joint movement data for Cell 239, Sensor 4.

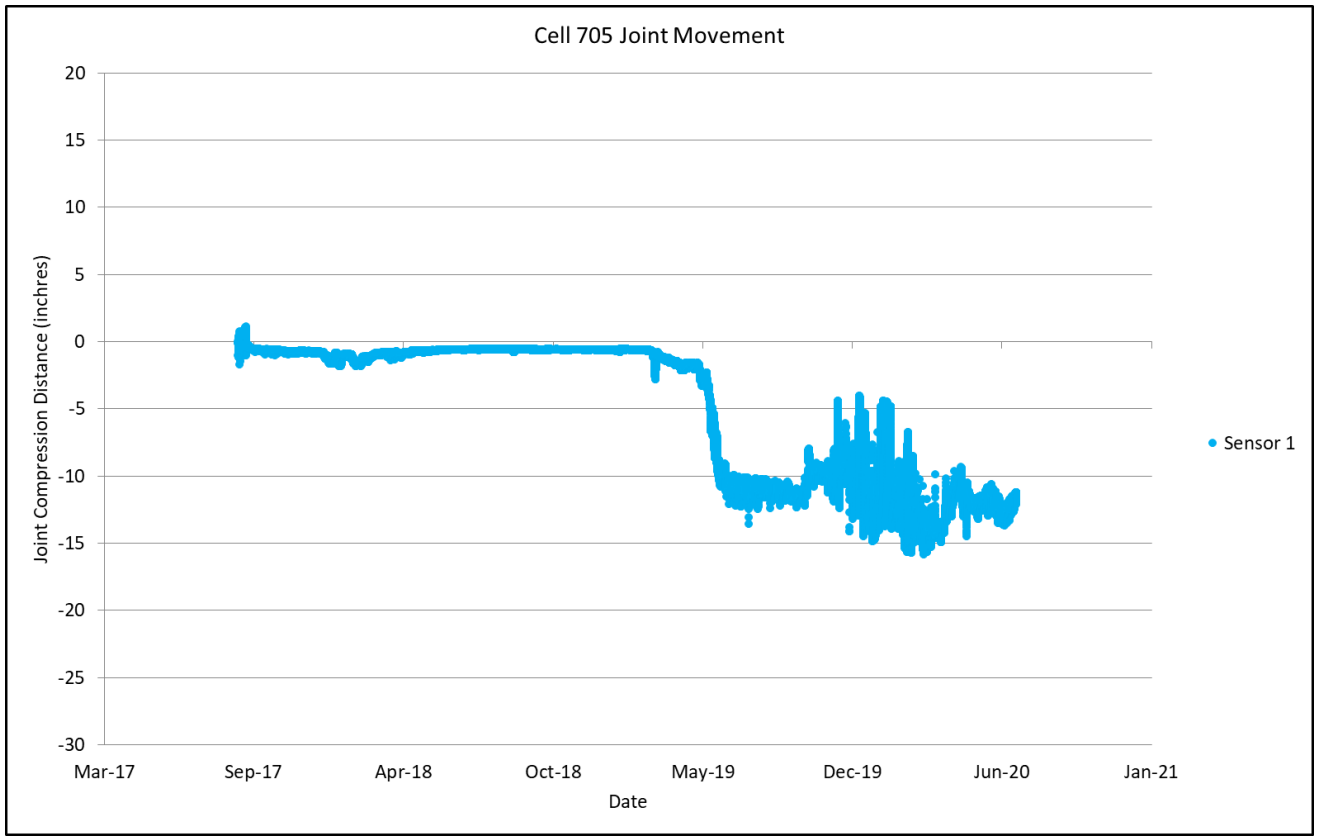

Figure B9. Joint movement data for Cell 705, Sensor 1.

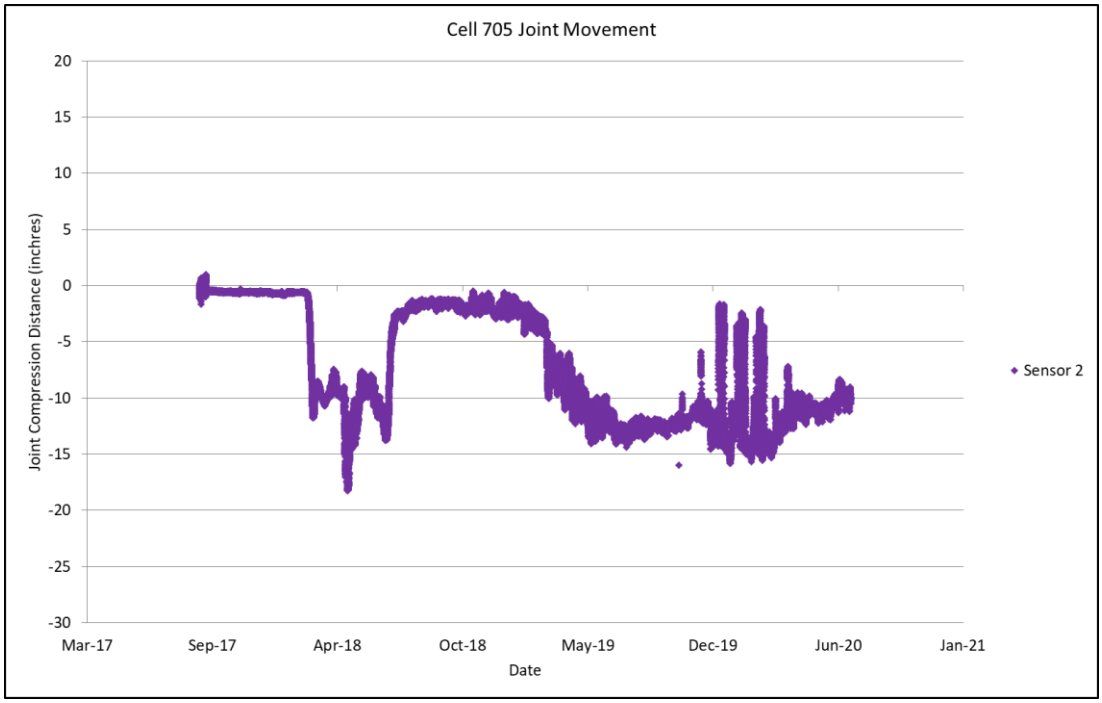

Figure B10. Joint movement data for Cell 705, Sensor 2.

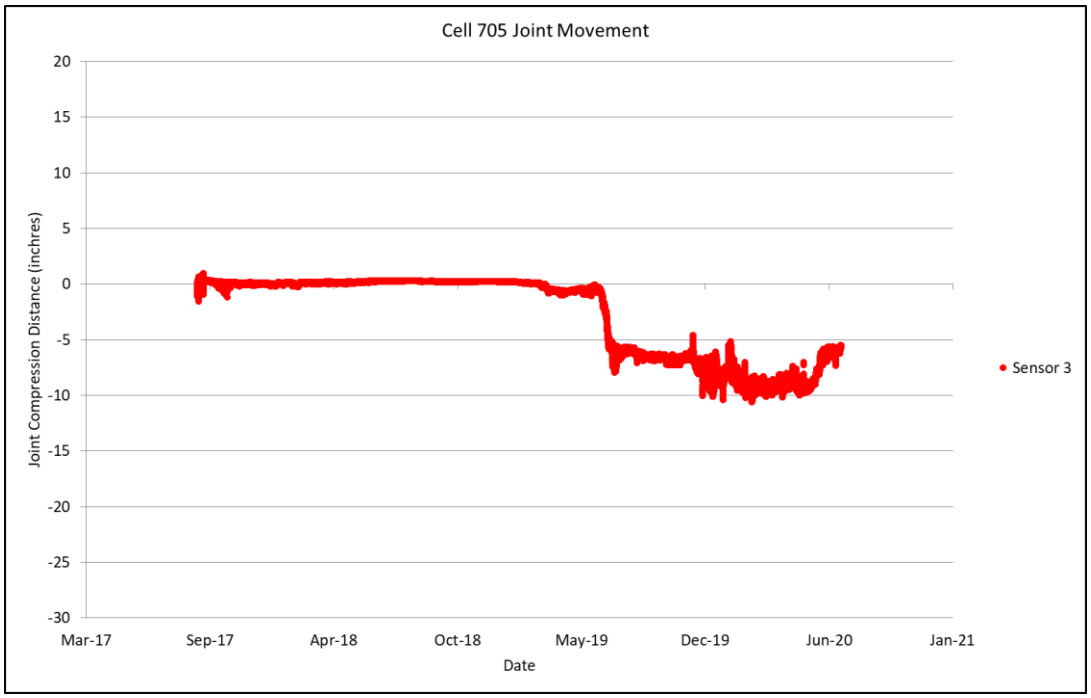

Figure B11. Joint movement data for Cell 705, Sensor 3.

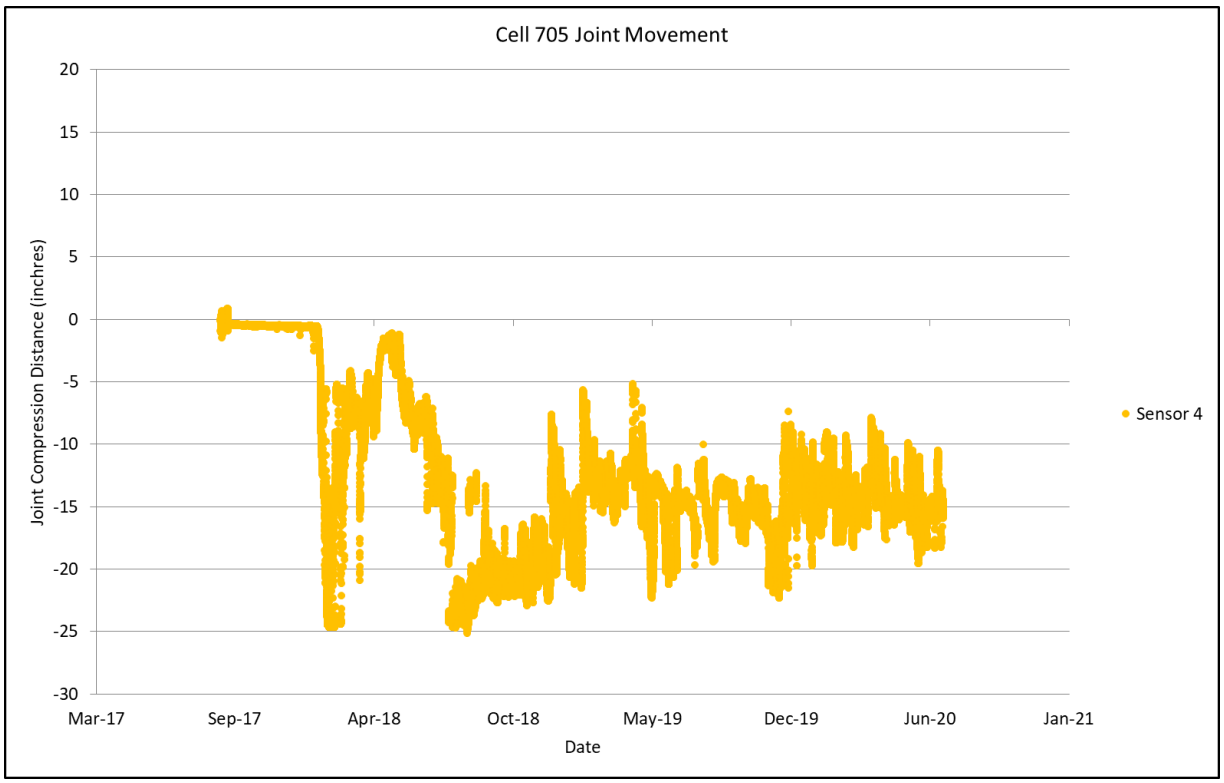

Figure B12. Joint movement data for Cell 705, Sensor 4.

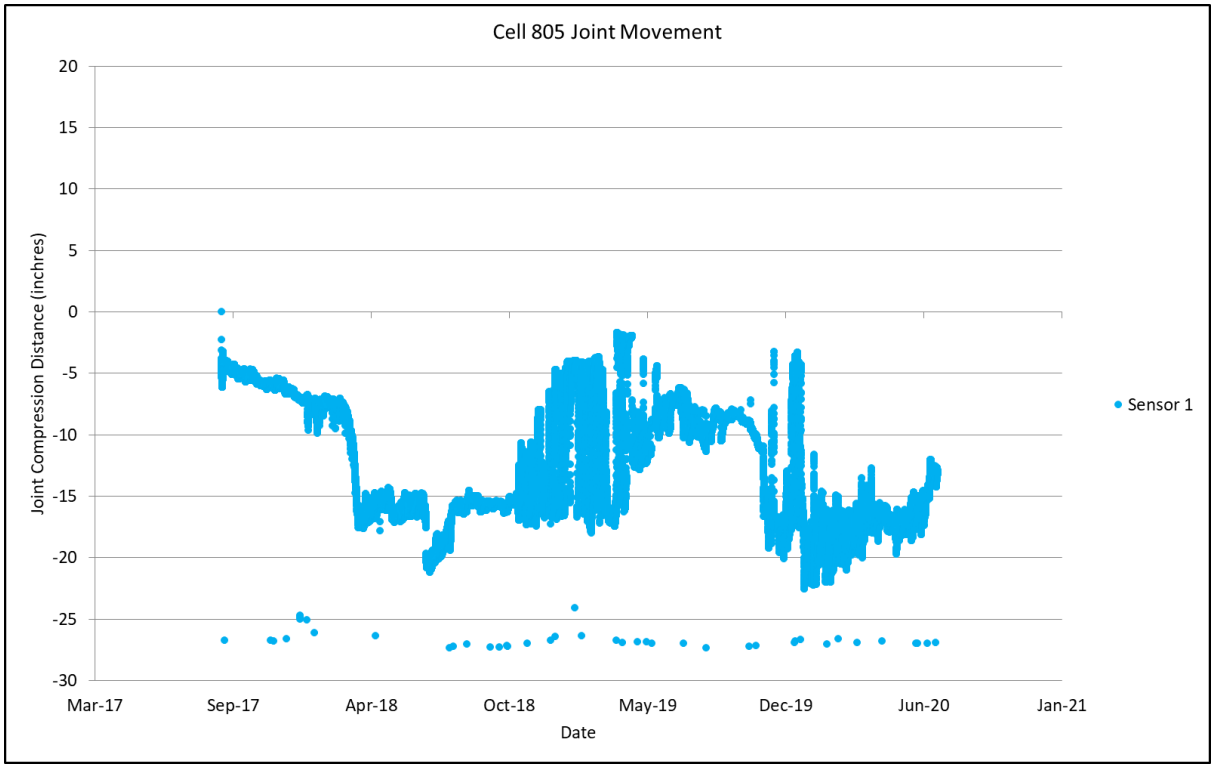

Figure B13. Joint movement data for Cell 805, Sensor 1.

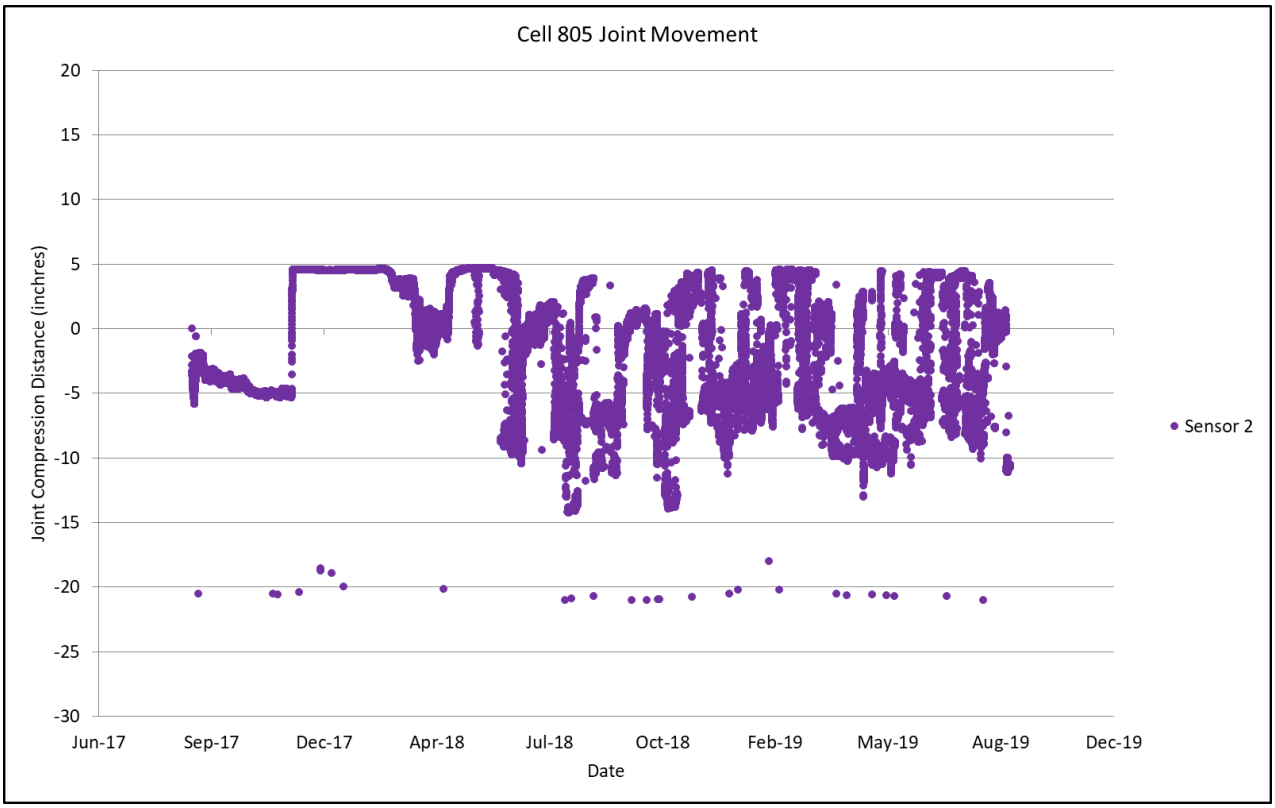

Figure B14. Joint movement data for Cell 805, Sensor 2.

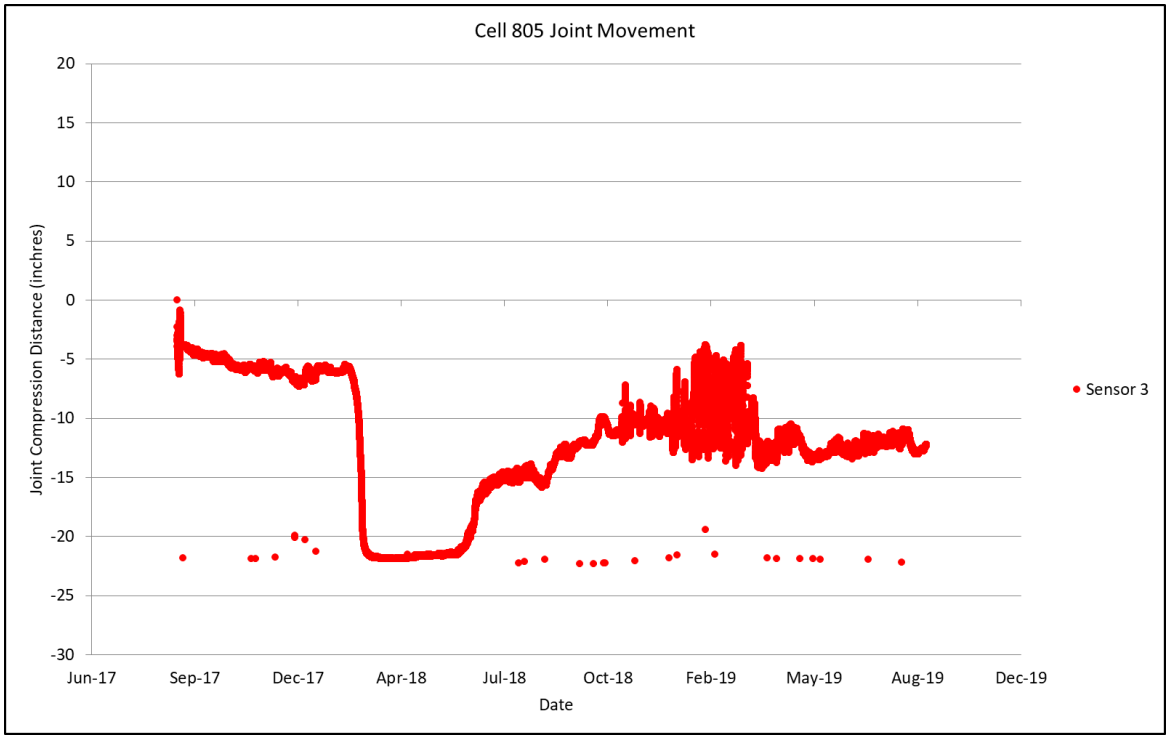

Figure B15. Joint movement data for Cell 805, Sensor 3.

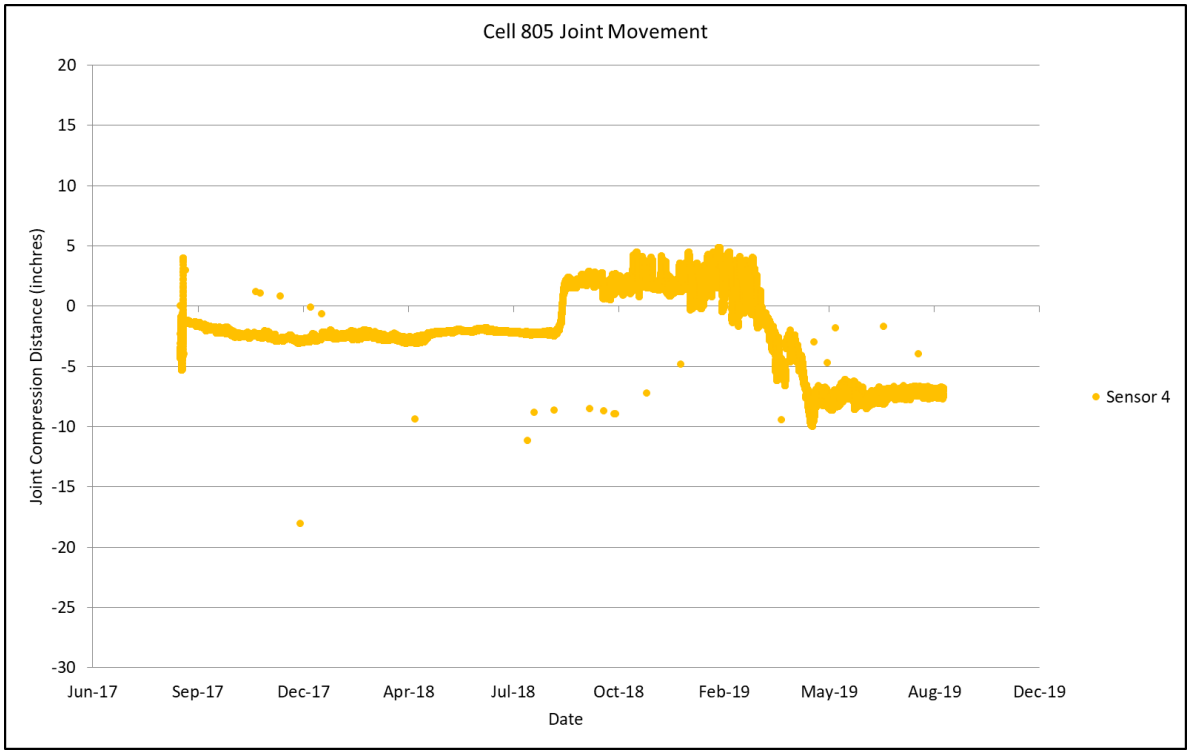

Figure B16. Joint movement data for Cell 805, Sensor 4.

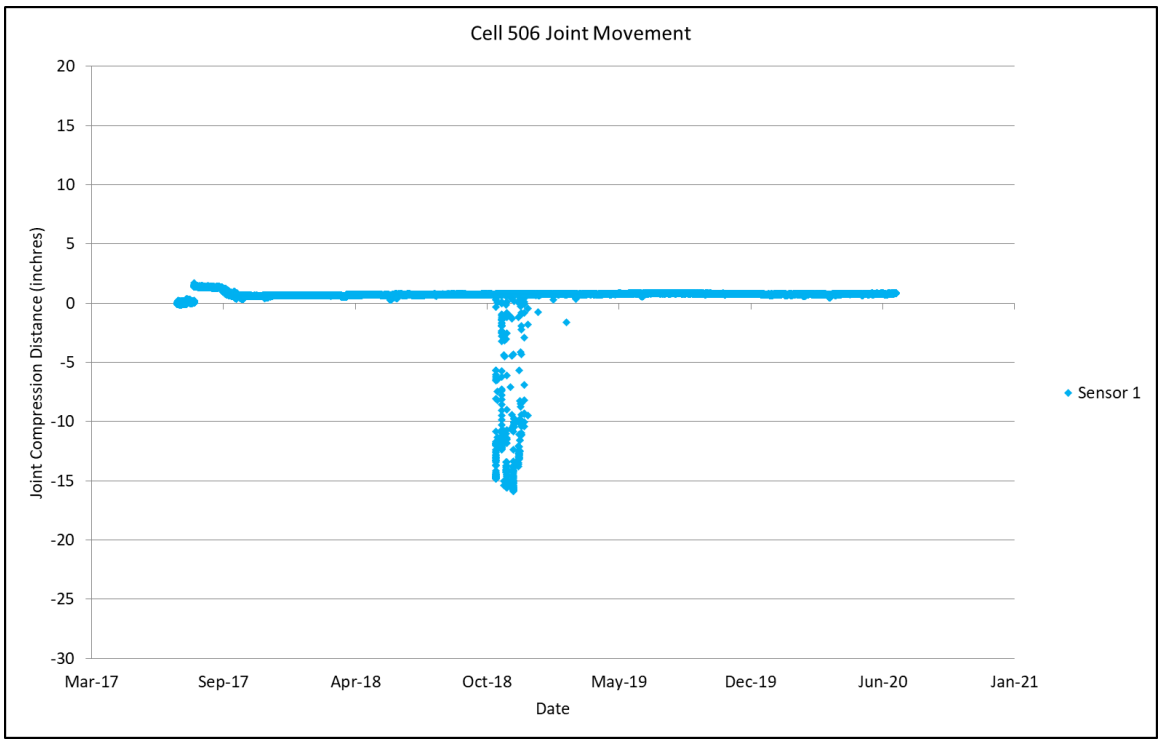

Figure B17. Joint movement data for Cell 506, Sensor 1.

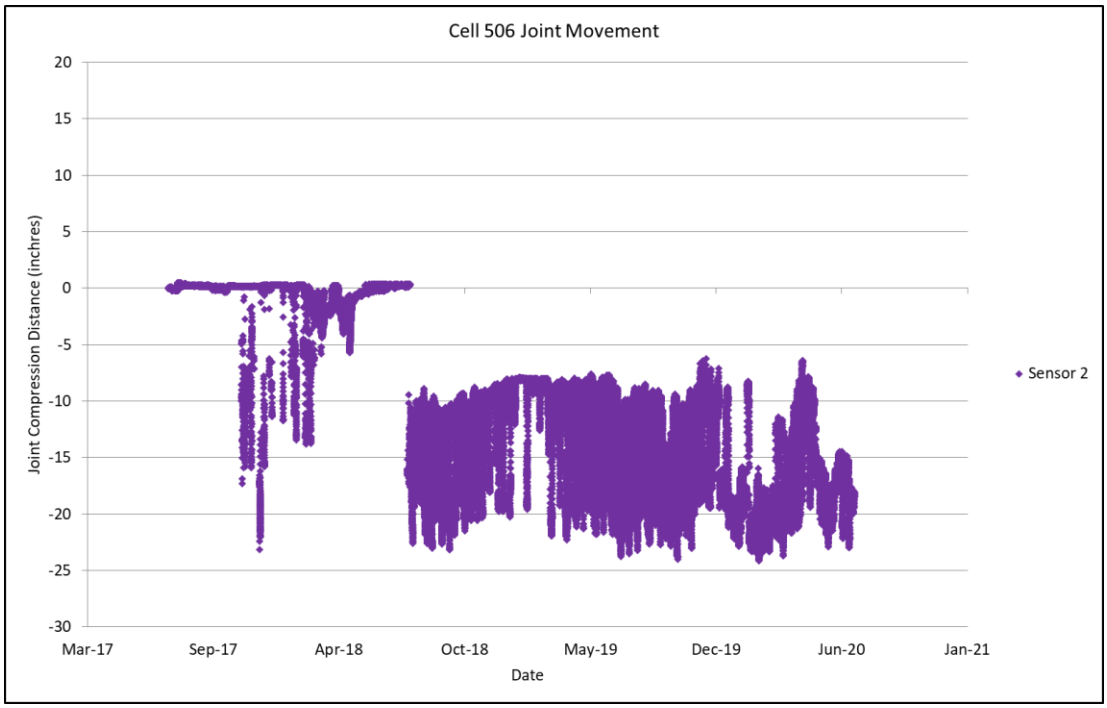

Figure B18. Joint movement data for Cell 506, Sensor 2.

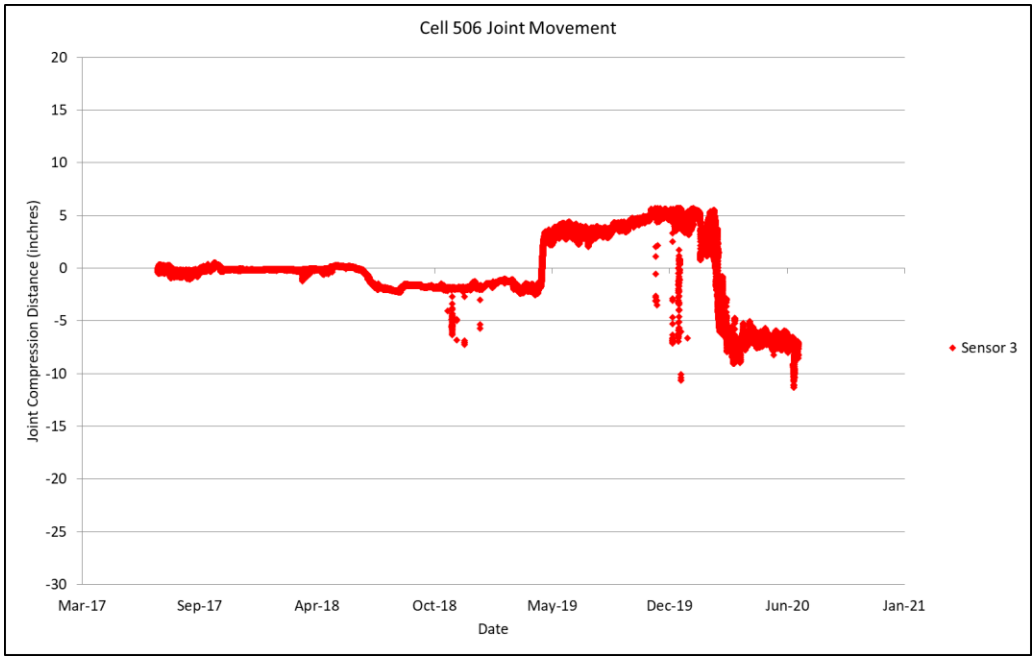

Figure B19. Joint movement data for Cell 506, Sensor 3.

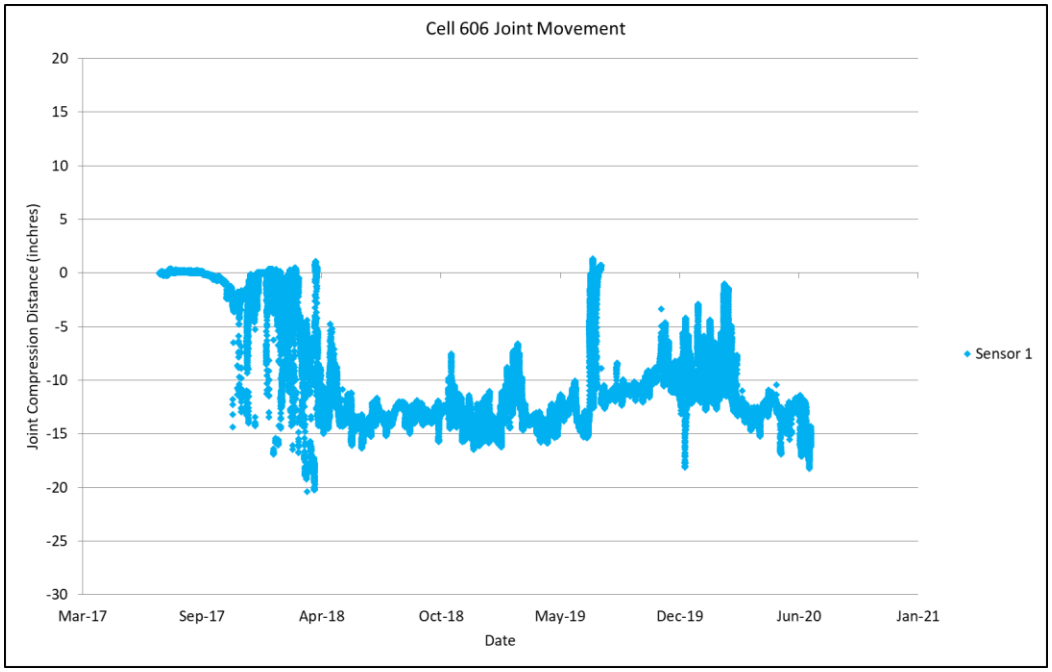

Figure B20. Joint movement data for Cell 606, Sensor 1.

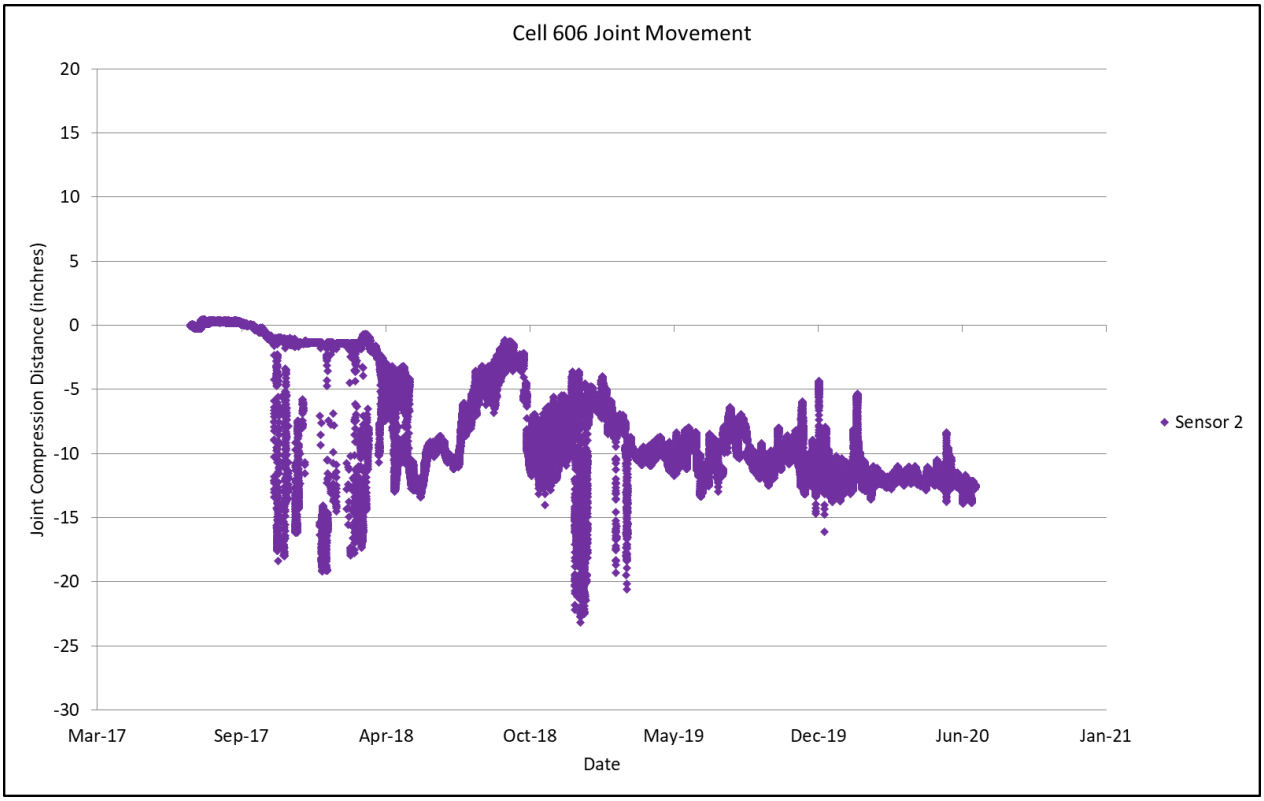

Figure B21. Joint movement data for Cell 606, Sensor 2.

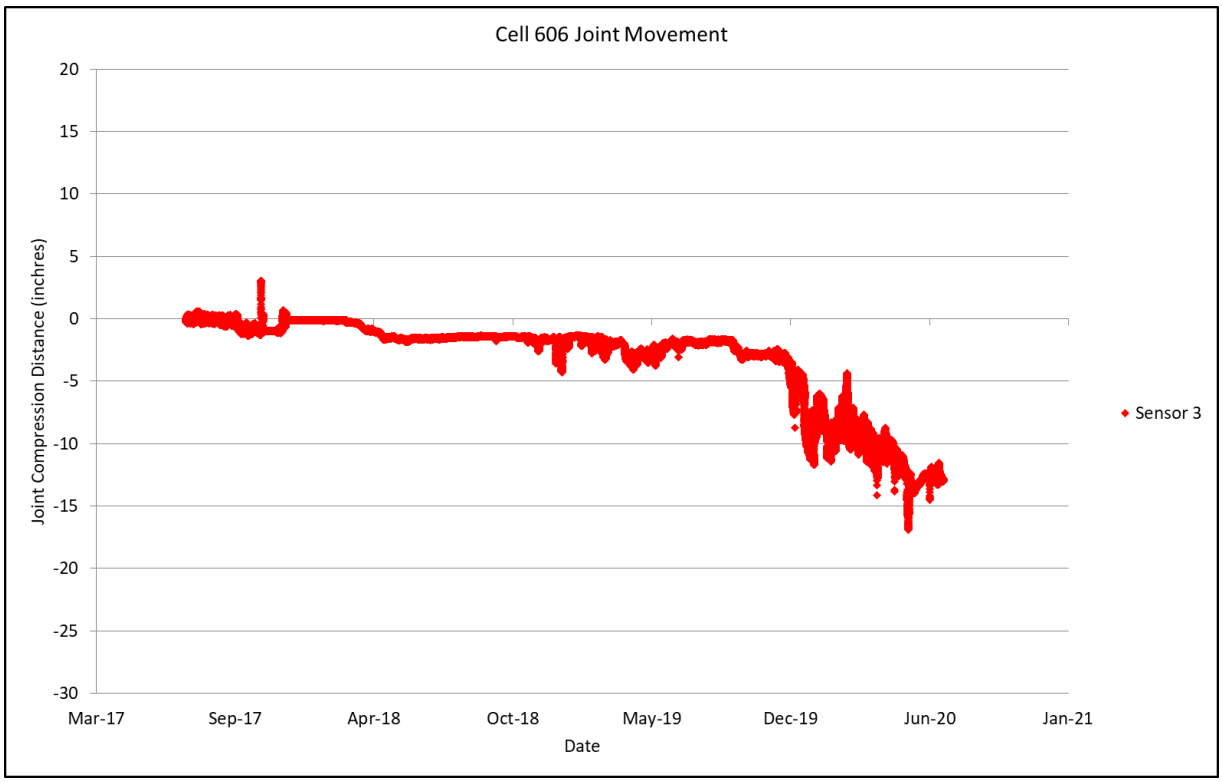

Figure B22. Joint movement data for Cell 606, Sensor 3.

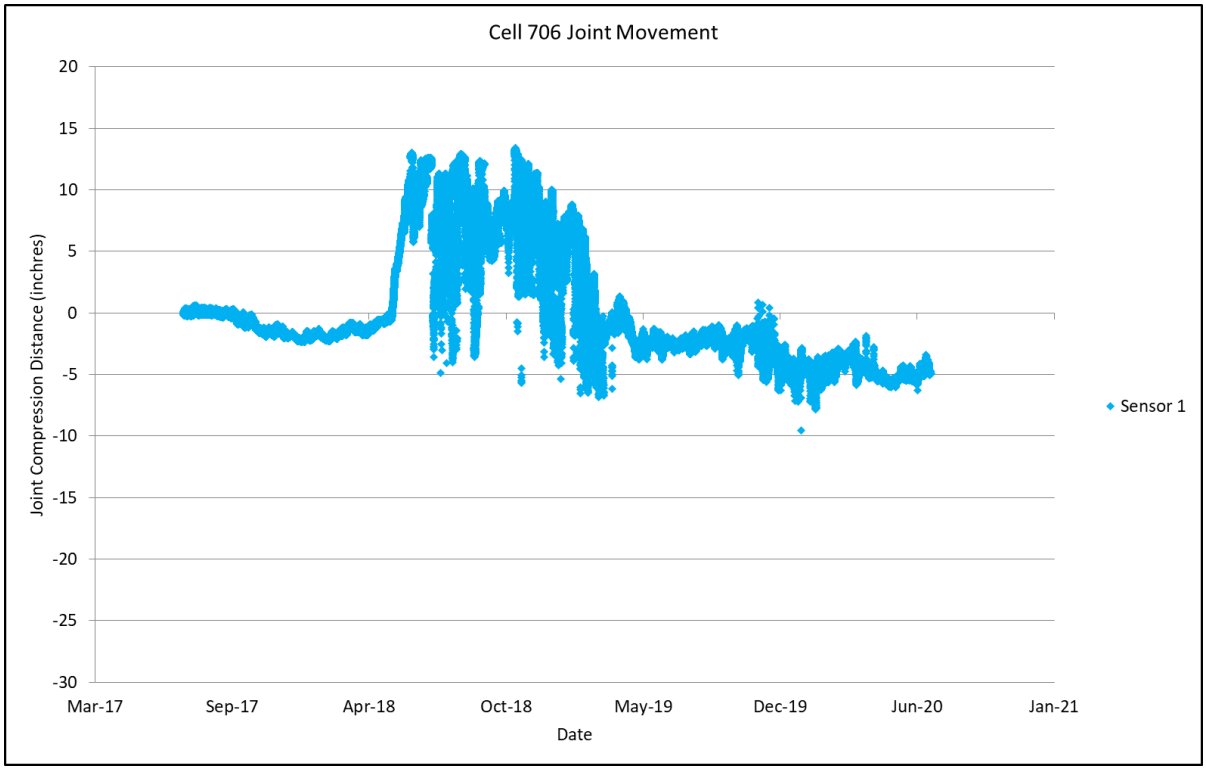

Figure B23. Joint movement data for Cell 706, Sensor 1.

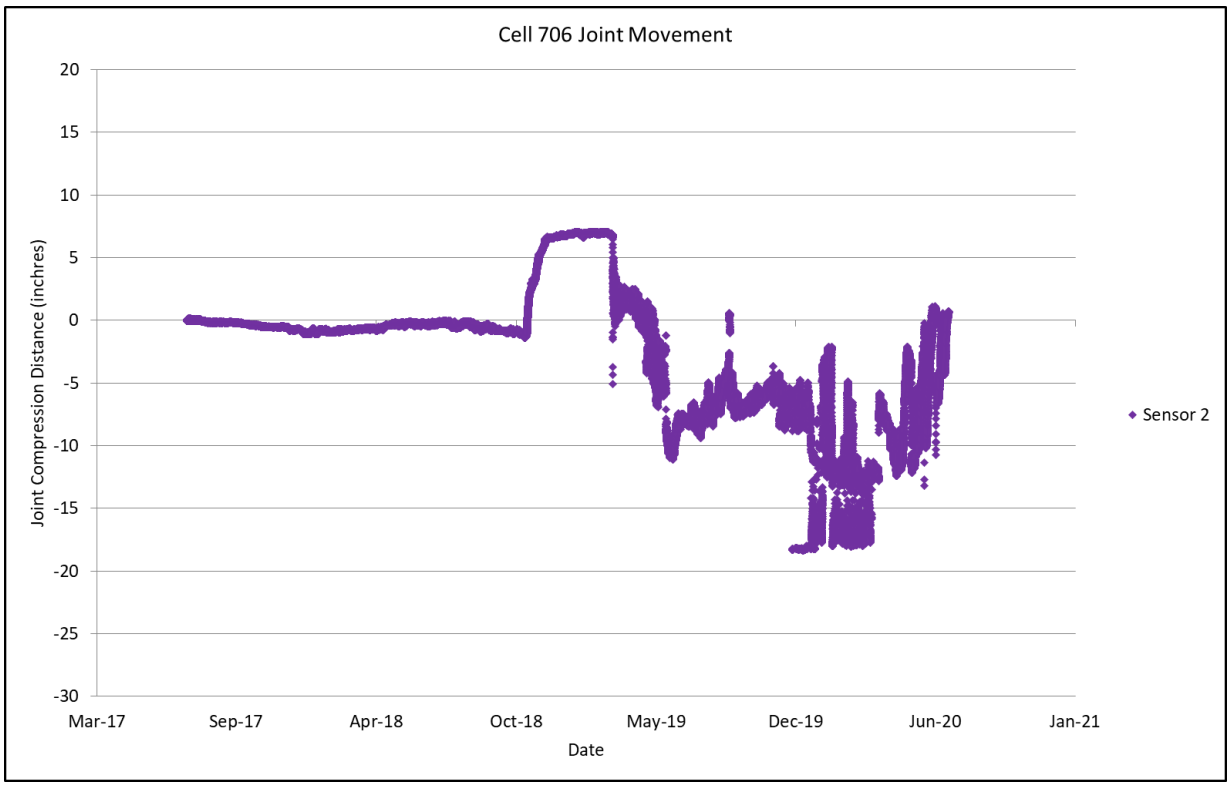

Figure B24. Joint movement data for Cell 706, Sensor 2.

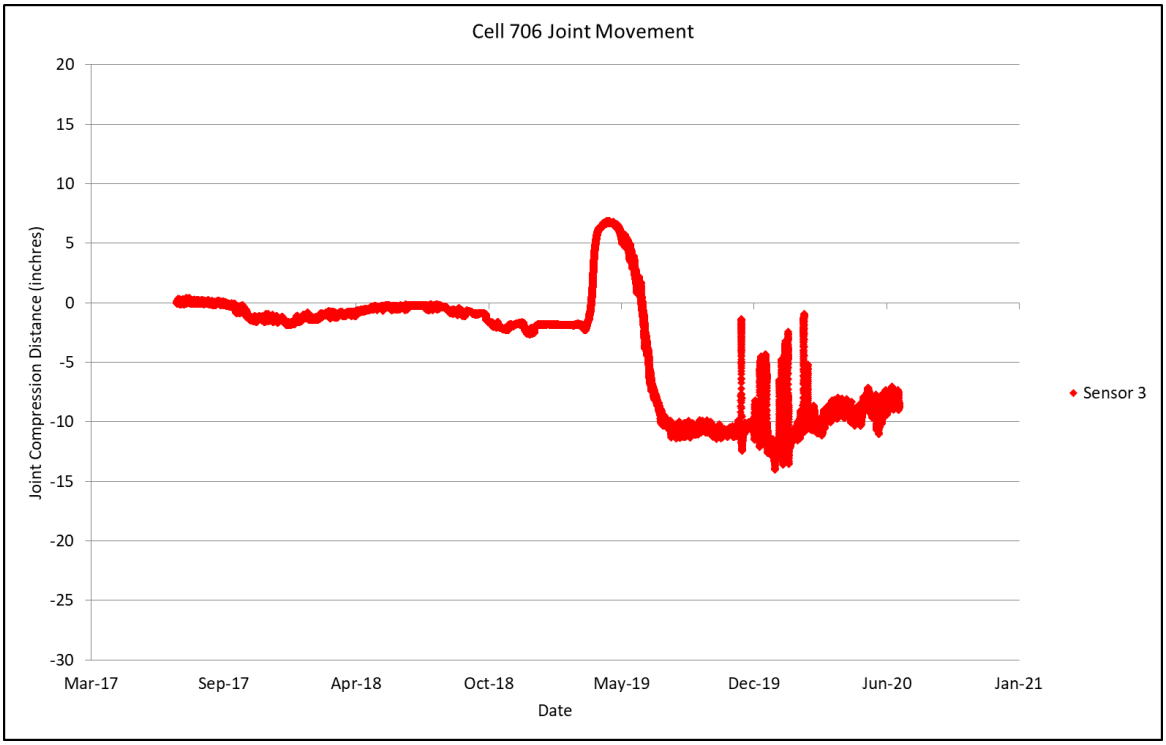

Figure B25. Joint movement data for Cell 706, Sensor 3.

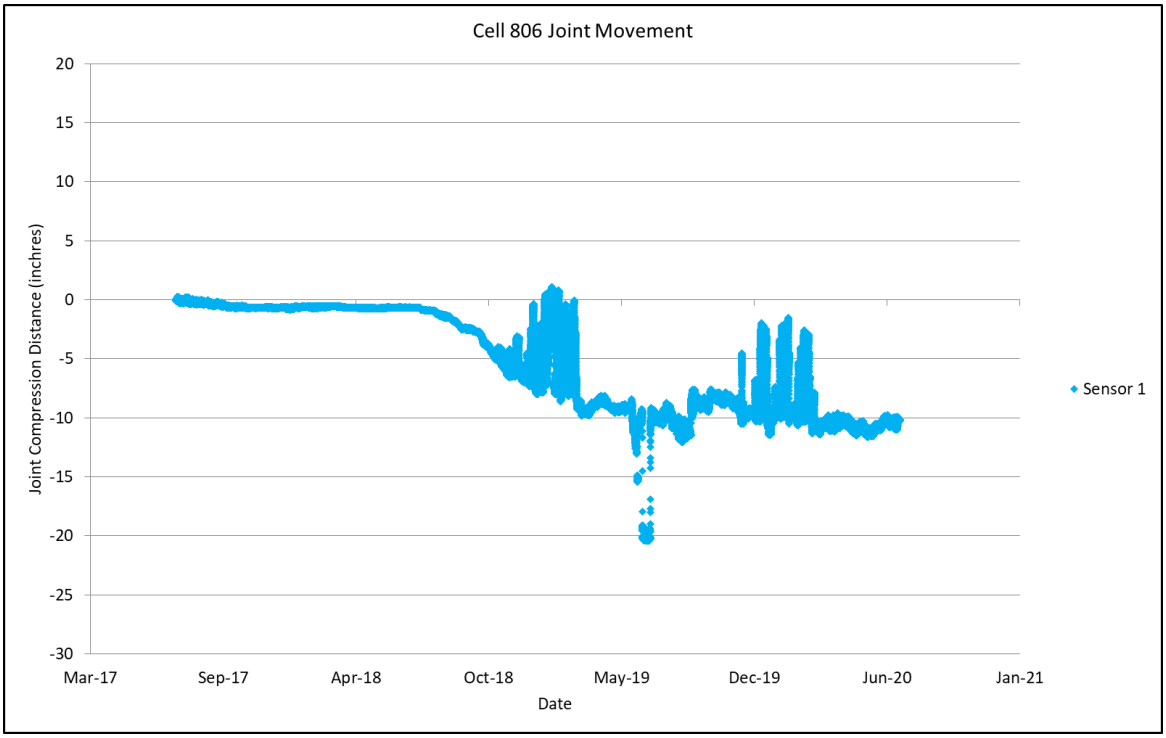

Figure B26. Joint movement data for Cell 806, Sensor 1.

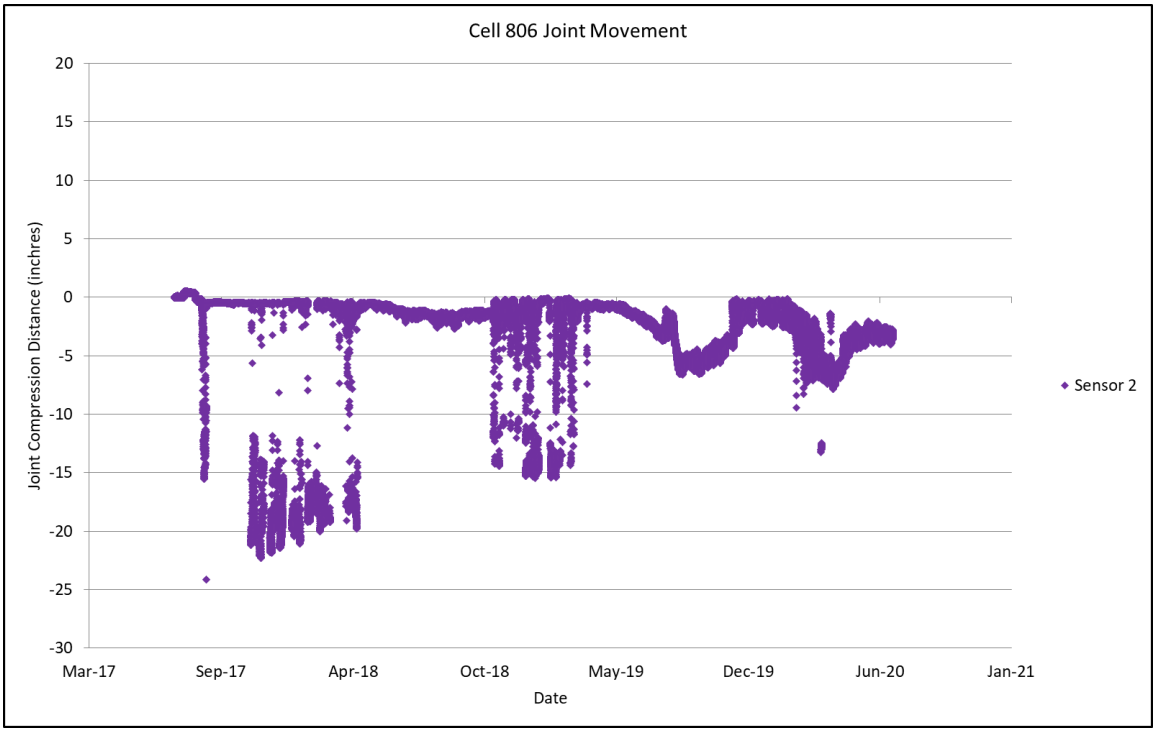

Figure B27. Joint movement data for Cell 806, Sensor 2 **(Bad sensor)**.

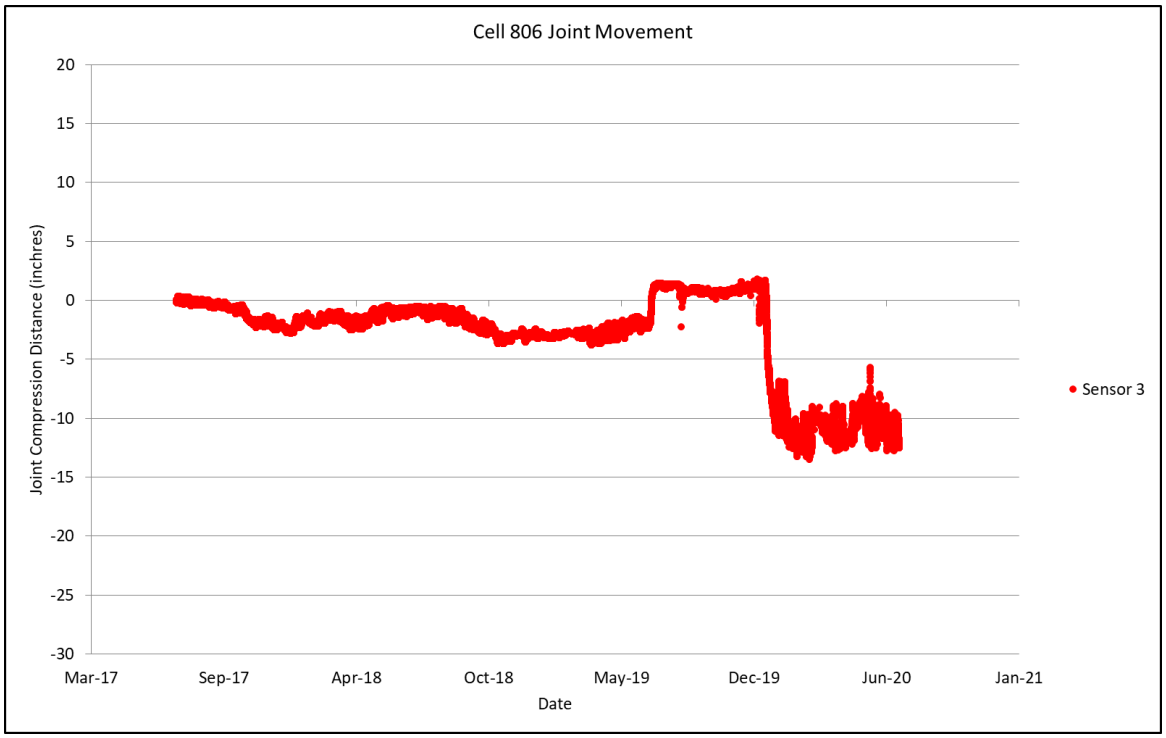

Figure B28. Joint movement data for Cell 806, Sensor 3.